

**INDUCTION HEATING OF SINTERED LOW ALLOY STEEL POWDER  
COMPACTS:**

An experimental and theoretical study of  
through-heating shaped parts for forging.

by

**ROBERT ANDREW COLVIN**

A thesis  
submitted for the  
Degree of  
**Doctor of Philosophy**  
to



**The University of Aston in Birmingham**

NOVEMBER 1982

# INDUCTION HEATING OF SINTERED LOW ALLOY STEEL POWDER COMPACTS

An experimental and theoretical study of  
through-heating shaped parts for forging.

Submitted by ROBERT ANDREW COLVIN

for the degree of Doctor of Philosophy

to The University of Aston in Birmingham

1982

## SUMMARY

An inter-disciplinary investigation of induction heating for forging of alloy steel, sintered, powder compacts of axi-symmetric shape is described, with attention to the importance of compact properties and shape complexity for induction coil design.

The present facility for coil design, using the equivalent circuit analogy for solenoidal coils, is assessed and compared with an industrial example; the limitations of the method are identified. The influence of powder and compact production stages on the material properties:- electrical resistivity,  $\rho$  ; thermal conductivity,  $k$  ; and magnetic permeability,  $\mu$  ; and the absence of reliable data on these properties, are shown in a literature review. Values of  $\rho$  ,  $k$  and  $\mu$  are measured against compact density, up to 1000°C, in specially developed apparatus and confirm semi-empirical relationships from the literature.

A simple method is advanced for simulating the temperature distribution with time and, from corroboratory tests on simple shaped compacts, it is deduced that sintered materials behave similarly to solid steel during induction heating.

The principal advantage of using powder compacts for forging applications lies in the reduced cost of machining, favouring parts of complex shape. Production coil options, for preforms of various degrees of complexity, are considered and the inductor configuration, the linear coil, proposed.

Measurements of current density distribution over simple billet surfaces in a linear coil provide preliminary evidence on the relationships between induced power and efficiency, and the number and position of coil inductors. No theoretical analysis of the heating behaviour of linear coils was hitherto available. Proposals are given for extending predictions to cover complex-shaped preforms, using computer simulations, for both linear and solenoidal coils.

An economic assessment of proposed production applications is presented, showing the impact of metal loss during heating, down-time costs and coil efficiency. Preforms are grouped, according to complexity, and recommendations made for the choice of inductor coil type.

## KEY WORDS

Induction Heating, Powder-Forging, Induction Coil Design,  
Powder Compact Properties



## ACKNOWLEDGEMENTS

I should like to acknowledge the invaluable guidance and support received throughout the duration of this project from my supervisors: Professor Davies (Main Supervisor) for his general help on the direction, and suggestions for the execution, of the research and for guidance with theoretical aspects of the work;

Mr. L.W. Crane (Associate Academic Supervisor) for introducing and advising me on the subject of Powder Metallurgy;

Dr. A.J. Cochran (I.H.D. Tutor) for his assistance in co-ordinating the numerous academic and industrial facets of this interdisciplinary study; and Mr. R.M. Gardner (Associate Industrial Supervisor) for easing my progress within the G.K.N. Forgings Sub-group, help in arranging assistance with the practical work and constant, cheerful support.

I am indebted to those at P. & P.D. Department of G.K.N. Forgings at Bromsgrove, for their suggestions, helpful co-operation and for constructing much of the apparatus, especially to John Wilkes for many a sympathetic talk about the problems of the project. I am grateful for the assistance provided at the G.K.N. Group Technology Centre, Wolverhampton: for the use of their excellent library service; for the help of staff and technicians in the Electrical Department; and to Dr.W.B. James for providing powder compact specimens. My thanks are due to Powder-Forgings Division, Redditch for much useful information and discussion.

To Ron Bentley (Technical Department, G.K.N. Sankey), and to Bill Flint (Mechanical Engineering) and Brian Harrison (Electrical Engineering, Research Workshops) at Aston, I owe much for their kind permission to use apparatus and facilities.

In the preparation of this thesis, I have had the willing co-operation of the I.H.D. office and many of my friends. I should like to thank Chris for her excellent typing of half of the first draft. To my sister, Margaret, for her professional layout of the remainder, thank you. Without the encouragement and support of my final year colleagues, especially Tony, Ian, Nigel and Binna, I might never have completed. I am very grateful to Janice, Nigel and Trev for proof-reading, and to Mark New, Della and Dasha of the Birmingham Word Centre for supervising the final, word processed version.

Finally, a special note of thanks to my flat-mates of the last three years for their company, understanding and encouragement: to Alec for mutual appreciation of the frustrations of research; to all at Bournbrook Road, especially Heather, Eileen, Derek and Mike; and to Ping and Dave for their friendly support.



T♥ Janice,

xxx → ∞

LIST OF CONTENTS



## CONTENTS

	<u>Page</u>
<u>LIST OF FIGURES</u>	xv
<u>LIST OF TABLES</u>	xxi
<u>LIST OF SYMBOLS</u>	xxiv
<u>Chapter 1 : INTRODUCTION</u>	1
1.1    The Collaborating Organization	2
1.2    The Problem	3
1.3    Project Definition	7
1.4    Organisation of the Research	9
1.4.1    Identification	11
1.4.2    Diagnosis	13
1.4.3    Results and their Evaluation	14
1.4.4    Conclusions	15
1.5    Summary of Principal Findings	15
1.5.1    On Current Methods used in Coil Design	15
1.5.2    On Powder Compacts	16
1.5.3    On Induction Heating of Cylindrical Powder Compacts	16
1.5.4    On Induction Heating of Shaped Metal Parts	16
1.5.5    On the Implications for G.K.N.	17
1.6    Observations	17

	<u>Page</u>
<u>Chapter 2 : AN INTRODUCTION TO INDUCTION HEATING</u>	19
2.1 Principles of Induction Heating	20
2.2 Applications of Induction Heating	22
2.3 Through-Heating for Forging	24
2.4 G.K.N. Production Layout	27
 <u>Chapter 3 : THEORY OF INDUCTION HEATING</u>	 31
3.1 Introduction	32
3.2 General Theory	33
3.2.1 Solution of the Electromagnetic Equations	33
3.2.2 Thermal Solution	37
3.2.2.1 Effect of Skin Depth	39
3.2.2.2 Effect of Radiation	40
3.2.2.3 Effect of Power Input Change	42
3.3 Equivalent Circuit Coil Design Method	45
3.4 Example of Equivalent Circuit Coil Design	49
3.4.1 Initial Specifications	49
3.4.2 Solution	51
3.5 Discussion of the Coil Design Method	55
3.6 Concluding Summary	59



	<u>Page</u>
<u>Chapter 4 : AN INTRODUCTION TO POWDER FORGING</u>	60
4.1 Introduction	61
4.2 Powder and Compact Production	65
4.2.1 Elemental Mix	65
4.2.2 Partially Pre-alloyed Powders	65
4.2.3 Fully Pre-alloyed Powders	65
4.3 Influence of Production Stages on Properties	68
4.3.1 Powder Production	68
4.3.2 Lubricant and Graphite Blending	69
4.3.3 Compaction	69
4.3.4 Sintering	70
4.3.5 Forging	73
4.4 G.K.N. Powders and Powder Compacts	73
4.5 Concluding Summary	79

	<u>Page</u>
<u>Chapter 5 : POWDER COMPACT PROPERTIES</u>	80
5.1    Introduction	81
5.2    Review of the Literature	83
5.2.1    Theoretical Predictions-Packing Models	83
5.2.2    Empirical Results	84
5.3    Measurements of Powder Compact Properties	97
5.3.1    Electrical Resistivity	97
5.3.2    Thermal Conductivity	99
5.3.3    Magnetic Permeability	100
5.4    Results and Discussion	101
5.4.1    Electrical Resistivity	101
5.4.2    Thermal Conductivity	102
5.4.3    Magnetic Permeability	103
5.5    Concluding Summary	105
 <u>Chapter 6 : SOLENOIDAL COIL DESIGN FOR SIMPLE SHAPES</u>	 135
6.1    Introduction	136
6.2    Revised Coil Design Calculation Method	137
6.2.1    Calculation of Power Density	137
6.2.1.1    First Section (sub-Curie)	137
6.2.1.2    First Section (super-Curie)	140
6.2.1.3    Second Section	141
6.2.2    Iterative Thermal Solution	143
6.3    Comparison of Calculated and Measured Temperatures	144
6.4    Concluding Summary	147



	<u>Page</u>
<u>Chapter 7 : SOLENOIDAL COIL INDUCTION HEATING OF SIMPLE SINTERED BILLETS</u>	148
7.1 Introduction	149
7.2 Method of Billet Temperature Measurement	150
7.3 Results of Temperature Measurements	152
7.3.1 Comparison of Predicted and Measured Results for Powder Materials	158
7.3.2 Comparison of Solid with Sintered Billet Heating	161
7.3.3 Effect of Density on Sintered Billet Induction Heating	162
7.4 Concluding Summary	164
 <u>Chapter 8 : PRODUCTION COIL OPTIONS-QUALITATIVE CONSIDERATIONS</u>	 166
8.1 Introduction	167
8.2 Solenoidal Coils	169
8.2.1 Advantages	169
8.2.2 Disadvantages	170
8.3 Coil Requirements	170
8.4 Coil Options	173
8.4.1 Conventional Straight-sided Solenoid	173
8.4.2 Shaped Solenoid	173
8.4.3 Multiple Shaped Solenoid Carousel	174
8.4.4 Transformer-type	174
8.4.5 Linear 'skate' coil	175
8.5 Concluding Summary	176

	<u>Page</u>
<u>Chapter 9 : LINEAR COIL INDUCTION HEATING OF SIMPLE SHAPES</u>	183
9.1    Introduction	184
9.2    Measurement of Current Density	187
9.2.1    Principle	187
9.2.2    Preparation of Test Billets	188
9.2.3    Experimental Method	189
9.3    Results	190
9.3.1    Cube Test Billet	191
9.3.2    Cylinder Test Billet	192
9.4    Discussion of Results	192
9.4.1    Cube Test Billet	192
9.4.2    Cylinder Test Billet	195
9.4.3    Cube and Cylinder Results Comparison	196
9.4.4    Efficiency	197
9.4.5    Uniformity of Heating	197
9.5    Concluding Summary	200
 <u>Chapter 10 : INDUCTION HEATING OF COMPLEX SHAPES</u>	 223
10.1    Introduction	224
10.2    Electromagnetic Solution for Solenoidal Induction Coils	226
10.2.1    Straight-sided Solenoidal Coils	226
10.2.2    Complex Geometries	237
10.3    Electromagnetic Solution for Linear Coils	237
10.4    Thermal Solution	239
10.5    Combination of Electromagnetic and Thermal Solutions	247
10.6    Concluding Summary	244



	<u>Page</u>
<u>Chapter 11 : IMPLICATIONS FOR G.K.N.</u>	246
11.1    Introduction	247
11.2    Cost Analyses	249
11.2.1    Induction Heating versus Conventional Heating	249
11.2.2    Powder-Forging versus Conventional Forging	249
11.2.3    Induction Heating of Sintered Preforms for Forging	250
11.3    Production Requirements	251
11.4    Coil Design	254
11.4.1    Heating of Ring and Disc Preforms	255
11.4.2    Heating of Stepped Billet Shaped Preforms	256
11.4.3    Heating of Gear Preforms	258
11.5    Other Factors	260
11.6    Concluding Remarks	263
 <u>Chapter 12 : SUMMARY, CONCLUSIONS AND                     RECOMMENDATIONS</u>	 264
12.1    Introduction	265
12.2    Summary of Results	266
12.2.1    Induction Coil Design	266
12.2.2    Induction Heating of Powder Compacts	268
12.2.3    Industrial Application of Induction Heating for Powder-Forging	269

	<u>Page</u>	
12.3	Conclusions	270
12.3.1	On Current Methods used in Coil Designs	270
12.3.2	On Powder Compact Properties	271
12.3.3	On Induction Heating of Cylindrical Powder Compacts	271
12.3.4	On Induction Heating of Shaped Metal Parts	272
12.3.5	On the Implications for G.K.N.	272
12.4	Industrial Implications of this Study	273
12.5	Recommendations for Further Study	276
 <u>Appendix 1 : METHOD OF DENSITY DETERMINATION</u>		 279
 <u>Appendix 2 : DERIVATION OF TEMPERATURE DISTRIBUTION AFTER CHANGE OF INPUT POWER DENSITY</u>		 281
A2.1	The Problem	281
A2.2	The Solution	281
A2.2.1	Initial Power Input	281
A2.2.2	Soak of Power Input $P_1$	283
A2.2.3	Power Input Density $P_2$	285
A2.2.4	Superposition of Temperature Distributions	285
 <u>Appendix 3 : DERIVATION OF EQUATION 5.13 FOR DETERMINING THERMAL CONDUCTIVITY</u>		 289
 <u>Appendix 4 : SUMMARY OF CALCULATIONS FOR SINTERED BILLETS OF CHAPTER 7, BY THE METHOD OF CHAPTER 6</u>		 292



	<u>Page</u>
<u>Appendix 5 : COST ANALYSIS OF INDUCTION HEATING FOR POWDER FORGING</u>	299
A5.1 Introduction	299
A5.2 Induction Heating versus Conventional Heating	301
A5.2.1 Furnace Comparisons	301
A5.2.1.1 Capital Costs	302
A5.2.1.2 Running Costs	303
A5.2.2 Heating for Forging Comparisons	305
A5.2.3 Concluding Summary	308
A5.3 Powder-Forging versus Conventional Forging	308
A5.3.1 Energy Consumption	308
A5.3.1.1 Conventional Forging	309
A5.3.1.2 Powder-Forging	310
A5.3.2 Advantages of Powder-Forging	310
A5.3.3 Other Factors	312
A5.3.4 Concluding Summary	312
A5.4 Induction Heating of Sintered Preforms for Forging	314
A5.4.1 Billet Heating	314
A5.4.2 Heating of Shaped Parts	314
<u>LIST OF REFERENCES</u>	330

LIST OF FIGURES



## LIST OF FIGURES

<u>Figure</u>	<u>Title</u>	<u>Page</u>
1.1	Typical Linear or "Skate" Coil	4
1.2	Block Diagram of Thesis Arrangement	10
2.1	Induction Heating of Cylindrical Load showing Flux Paths	21
2.2	Transformer Analogy of Induction Heating	21
3.1	Solid Cylindrical Workload within a Solenoidal Coil	35
3.2	$p$ and $q$ functions for a Solid Cylinder	35
3.3	Temperature Distribution with Radius of Solid Cylinder with time $\tau$ , Surface Power Input Assumed	38
3.4	Temperature Distribution with Radius of Solid Cylinder, modified for Finite Current Depth	40
3.5	Radiation Correction Factor for Equation (3.17)	42
3.6	Surface and Centre Temperature Variation during Soaking	43
3.7	Physical Properties $\rho$ , $k$ and $\mu$ of Solid En8 Steel, with Temperature	48
3.8	Specific Heat Capacity of En8 Steel, with Temperature	52
3.9	Phase Diagram of Power Factor Correction	55
4.1	Production Routes for Powder Forged Steel Parts	64
4.2	Typical G.K.N. Preform Shapes with the corresponding Finished Part	74
4.3	Measured Density Distribution of Selected G.K.N. Preforms	76
4.4	Scanning Electron Microscope Photograph of Compacted 'W4' Powder	77
5.1	Variation of Thermal Conductivity of Steel and Copper with Powder Density, with Predicted Curves	107
5.2	Electrical Resistivity of Steel and Copper with Powder Density, with Predicted Curve	108

<u>Figure</u>	<u>Title</u>	<u>Page</u>
5.3	Electrical Resistivity of Iron with Powder Density,with Predicted Curve	109
5.4	Magnetic Permeability of Iron with Powder Density, with Predicted Curves	110
5.5	Preparation of Test Bar for Electrical Resistivity Measurements	111
5.6	Apparatus for Electrical Resistivity Measurements	112
5.7	Preparation of Test Bar for Thermal Conductivity Measurements	113
5.8	Apparatus for Thermal Conductivity Measurements	114
5.9	Preparation of Test Toroid for Magnetic Permeability Measurements	115
5.10	Apparatus for Magnetic Permeability Measurements	115
5.11	Measured Electrical Resistivity with Temperature for 'W4' Powders, with Predicted Curves	116
5.12	Measured Electrical Resistivity with Temperature for 'W78' Powders, with Predicted Curves	117
5.13	Electrical Resistivity with Temperature for Standard Solid Test Bars, with Predicted Curves	118
5.14	Ratios of Measured "W4" Powder Resistivity to Solid Resistivity, with Predicted Ratios	119
5.15	Ratios of Measured "W78" Powder Resistivity to Solid Resistivity, with Predicted Ratios	120
5.16	Measured Thermal Conductivity with Temperature for "W4" Powders, with Predicted Curves	121
5.17	Measured Thermal Conductivity with Temperature for "W78" Powders, with Predicted Curves	122
5.18	Ratios of Measured "W4" Powder Conductivity to Solid Conductivity with Predicted Ratios	123



<u>Figure</u>	<u>Title</u>	<u>Page</u>
5.19	Ratios of Measured "W78" Powder Conductivity to Solid Conductivity, with Predicted Ratios	124
5.20	Magnetic Permeability with Magnetic Field for "W4" Powder, $\nu/\nu_0 = 0.74$	125
5.21	Magnetic Permeability with Magnetic Field for "W4" Powder, $\nu/\nu_0 = 0.79$	126
5.22	Magnetic Permeability with Magnetic Field for "W4" Powder, $\nu/\nu_0 = 0.82$	127
5.23	Magnetic Permeability with Magnetic Field for "W78" Powder of 0.74 relative density	128
5.24	Magnetic Permeability with Magnetic Field for "W78" Powder of 0.79 relative density	129
5.25	Magnetic Permeability with Magnetic Field for "W78" Powder of 0.82 relative density	130
5.26	Relative Magnetic Permeability with Temperature for "W4" Powder of 0.74 relative density	131
5.27	Magnetic Permeability with Magnetic Field for "W4" and "W78" Powders of 0.74 relative density, with Predicted Curves	132
5.28	Magnetic Permeability with Magnetic Field for "W4" and "W78" Powders of 0.79 relative density, with Predicted Curves	133
5.29	Magnetic Permeability with Magnetic Field for "W4" and "W78" Powders of 0.82 relative density, with Predicted Curves	134
6.1	Measured and Calculated Temperature with Time at various radii of solid En8 Billet	145
7.1	Preparation of Cylindrical Test Billet and Apparatus for Temperature Measurements	151
7.2	Measured and Calculated Temperatures with Time for Solid En8 Billet	153
7.3	Measured and Calculated Temperatures with Time for Powder Billet, $\nu/\nu_0 = 0.74$	154
7.4	Measured and Calculated Temperatures with Time for Powder Billet, $\nu/\nu_0 = 0.79$	155

<u>Figure</u>	<u>Title</u>	<u>Page</u>
7.5	Measured and Calculated Temperatures with Time for Powder Billet, $V/V_0 = 0.82$	156
8.1	Conventional Straight-sided Solenoidal coil	178
8.2	Shaped Solenoidal Coil	178
8.3	Multiple Shaped Solenoidal Coil Carousel	179
8.4	Transformer-type Coil, with Internal Flux Concentration	180
8.5	Linear "skate" Coil	181
8.6	Sections of the range of G.K.N. Powder-Forged Preforms	182
9.1	Adjustable Coil and Apparatus for Linear Coil Experiments	203
9.2	Preparation of Cube Test Billet for Current Density Measurements	204
9.3	Preparation of Cylinder Test Billet for Current Density Measurements	205
9.4	Measured Current Density on Cube Billet in a Single Conductor Pair Coil	206
9.5	Measured Current Density on Cube Billet in a Two Conductor Pair Linear Coil	207
9.6	Measured Current Density Distribution on Cube billet in a Three Conductor Pair Linear Coil	208
9.7	Generalized Current Density Distribution on Cube Test Billet Measurement Faces	209
9.8	Generalized Current Density over Cube Billet in relation to conductor position	210
9.9	Power Density at Selected Positions on Cube Face A, with Linear Coil spacing $d$	211
9.10	Power Density at Selected Positions on Cube Face B, with Linear Coil spacing $d$	212
9.11	Power Density at Selected Positions on Cube Face C, with Linear Coil spacing $d$	213
9.12	Power Density at Selected Positions on Cube Face A, with Number of Linear Coil Pairs	214



<u>Figure</u>	<u>Title</u>	<u>Page</u>
9.13	Power Density at Selected Positions on Cube face B, with Number of Linear Coil Pairs	215
9.14	Power Density at Selected Positions on Cube Face C, with Number of Linear Coil Pairs	216
9.15	Current Density on Cylindrical Billet in a single conductor pair Linear Coil	217
9.16	Current Density of Cylindrical Billet in a two conductor pair Linear Coil	218
9.17	Current Density of Cylindrical Billet in a three conductor pair Linear Coil	219
9.18	Generalized Current Density Distribution on Cylinder Billet Measurement Faces	220
9.19	Generalized Current Density Distribution on Cylindrical Billet in relation to Conductor Position	220
9.20	Power Density on Cylindrical Test Billet, with Linear Coil spacing $d$	221
9.21	Power Density on Cylindrical Test Billet, with number of Linear Coil pairs	222
10.1	Mesh Segmenting of Coil and Billet for Finite Difference Analysis	229
10.2	Equivalent Circuit Representation of Mesh	232
10.3	Flow Diagram for Computer Solution	236
A2.1	Variations of Parabolic Temperature Profile During Soaking Period	282
A2.2	Example of the Change in Temperature Profile during the Curie Transition	287
A2.3	Example of the Change in Temperature Profile during Transition between Coil Sections	288
A5.1	Cost Comparison on Induction Heating and Gas-Fired Furnaces, with Operation Time	317
A5.2	Typical Features that may not be incorporated in Powder Preforms	318
A5.3	Linear Coil Configuration used for Results of Tables A5.12 and A5.13	319

LIST OF TABLES



## LIST OF TABLES

<u>Table</u>	<u>Title</u>	<u>Page</u>
1.1	Companies of the G.K.N. Forgings Ltd. Sub-Group	2
2.1	Induction Heating Systems and Applications	24
2.2	Frequencies for Through-heating Steel for Forging	26
2.3	Recommended Air-gaps for Through-heating in Solenoidal Coils	28
3.1	Worked Example of Coil Design for a Two-section Production Coil	50
3.2	Equivalent Circuit Calculations for the Coil Design of Table 3.1	53
4.1	G.K.N. Powder Chemical Compositions and Particle Sizes	72
4.2	Properties of Compacted "W4" and "W78" powders and Mechanical Properties	78
6.1	Summary of Temperature Distribution Calculations for Solid En8 Billet	142
7.1	Recorded Voltage, Current, Reactive Power and Coil Power during Temperature Measurements on Solid and Powder Billets	157
8.1	Ability of Various Coil Types to meet Desired Coil Attributes	171
9.1	Calculated $P_C$ , $\mathcal{P}$ and $\eta$ of Cube and Cylinder Billet Tests	202
A4.1	Summary of Equivalent Circuit Calculations for Powder Billet, $v/v_0 = 0.74$	293
A4.2	Summary of Equivalent Circuit Calculations for Powder Billet, $v/v_0 = 0.79$	294
A4.3	Summary of Equivalent Circuit Calculations for Powder Billet, $v/v_0 = 0.82$	295
A4.4	Temperature Distribution Calculations for Powder Billet, $v/v_0 = 0.74$	296
A4.5	Temperature Distribution Calculations for Powder Billet, $v/v_0 = 0.79$	297

<u>Table</u>	<u>Title</u>	<u>Page</u>
A4.6	Temperature Distribution Calculations for Powder Billet, $\gamma/\gamma_0 = 0.82$	298
A5.1	Power Input Density Comparison for Various Methods of Heat Transfer	320
A5.2	Capital Cost Comparisons for Major Furnace Types.	320
A5.3	Fuel Costs (May 1981)	320
A5.4	Energy Consumption and Start-up Conditions for Indirect Gas-Fired Furnace.	321
A5.5	Cost Analysis of Induction Heating and Gas for Billet Heating	322
A5.6	Cost Analysis of Induction Heating and Gas; Complete Production Process	323
A5.7	Energy Consumption for Steel Billet Production used in Conventional Forging	324
A5.8	Energy Consumption for Conventional Forging and Machining	325
A5.9	Energy Consumption for G.K.N. Powder Production	325
A5.10	Energy Consumption for G.K.N. Powder-Forging	326
A5.11	Linear Coil Performance in heating Powder Preforms	327
A5.12	Predicted Cost Estimates for Induction Heating of Ring-shaped Powder Preforms	328
A5.13	Predicted Cost Estimates for Induction Heating of Gear Powder Preforms	329



LIST OF SYMBOLS

LIST OF SYMBOLS

<u>Symbol</u>	<u>S.I.Units</u>	<u>Quantity</u>
A	m <sup>2</sup>	area
A'	Wb/m	magnetic vector potential
a	m	length; thickness
B	T	magnetic flux density
B <sub>s</sub>	T	saturation magnetic flux density
C		constant
c	J/(kgK)	specific heat capacity
d	m	diameter; air-gap
E	V/m	electromotive force
e		natural logarithms base 2.71828
F		correction factor to equation 3.13 for radiation and finite current depth
F <sub>v</sub>	W/m <sup>3</sup>	heat flux density
f	Hz	frequency
H	A/m	magnetic field strength
H <sub>Rm</sub>	A/m	maximum field at R
I	A	current
I <sub>p</sub>	A	primary current
I <sub>s</sub>	A	secondary current
J	A/m <sup>2</sup>	current density
J <sub>0</sub> , J <sub>1</sub> , J <sub>2</sub>		Bessel functions of the first kind of order of subscript
j		- imaginary quantity
K	Ω/m <sup>2</sup>	equivalent circuit constant
k	W/(mK)	thermal conductivity
k <sub>m</sub>	W/(m <sup>2</sup> K)	thermal conductance
k <sub>r</sub>		coil turn spacing correction factor



<u>Symbol</u>	<u>S.I.Units</u>	<u>Quantity</u>
$l$	m	length
m	kg	mass
$m_a$	kg	mass in air
$m_w$	kg	mass in water
$m_d$	kg	mass difference
$m'_a$	kg	mass in air with absorbed water
$N_c$		number of coil turns
n		constant
P	W	power
$\mathcal{P}$	W/m <sup>2</sup>	power density, power per unit area
$p'$	m	perimeter
p		equivalent circuit p function
q		equivalent circuit q function
Q	W	reactive power
R	$\Omega$ ;m	resistance; billet radius
r	m	radius
$r_c$	m	radius of particle contact
s		constant
T	K	absolute temperature
t	s	time
V	V ; m <sup>3</sup>	potential difference, voltage ; volume
$\bar{W}$	W/m <sup>3</sup>	power density, power per unit volume
X	$\Omega$	reactance
Z	$\Omega$	impedance

<u>Symbol</u>	<u>S.I.Units</u>	<u>Quantity</u>
$\alpha$	1/m	inverse of penetration depth
$\beta_n$		positive roots of $J(\beta) = 0$
$\gamma$	kg/m <sup>3</sup>	density
$\Delta$		a difference
$\delta$	m	penetration depth
$\epsilon$		emissivity
$\eta$		efficiency
$\theta$	°C	temperature degrees Celsius
$\theta_s$	°C	surface temperature
$\theta_c$	°C	centre temperature
$\mu$	H/m	absolute permeability
$\mu_r$		relative permeability
$\mu_0$	H/m	permeability of free space
$\mu_s$		permeability of solid material
$\xi$		porosity
$\rho$	$\Omega\text{m}$	resistivity
$\sigma$	Pa	tensile strength
$\sigma_k$	mK/W	thermal resistivity
$\sigma_s$	W/(m <sup>2</sup> K <sup>4</sup> )	Stefan's constant, $5.669 \times 10^{-8}$
$\tau$		normalised time
$\varphi$	Wb	flux linkage
$\cos \varphi$		power factor
$\omega$	rad	angular frequency
$\psi$	rad	spherical polar coordinate, angle of inclination



General Subscripts

Unless given above, subscripts assume the following meanings:-

c	coil
curie	at the Curie magnetic transition temperature
e	external, environment
g	air-gap
h	horizontal
i	initial value
m	mean
max	maximum
min	minimum
n	net value
o	solid
R	radiated
T	total
V	vertical
w	work
x y z	} cartesian co-ordinates
1 2 3	} induction coil section or temperature
~	matrix

CHAPTER ONE

INTRODUCTION



## CHAPTER 1 : INTRODUCTION

### 1.1 The Collaborating Organisation

Guest, Keen and Nettlefolds (G.K.N.) Ltd is the largest international company in Britain specialising in most metal production and forming applications. This project is sponsored by G.K.N. Forgings Ltd, a wholly owned subsidiary of G.K.N., consisting of six companies, Table 1.1, currently employing over 6000 people, with an annual turnover of £185m.[1]

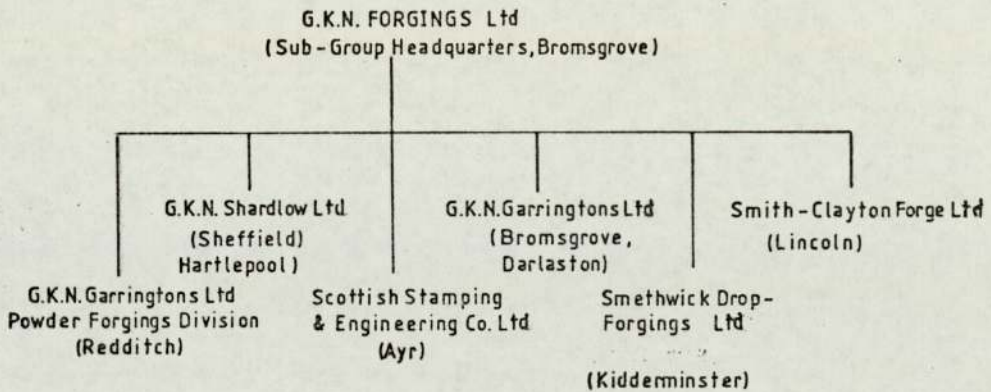


TABLE 1.1: Companies of the G.K.N. Forgings Ltd. Sub-group.

Production capacity of 300 000 tonnes per annum within the Sub-Group of as-forged items for the automotive, agricultural, aerospace and allied industries constitutes about half of the total output of the British forging industry. High-volume production installations produce forgings of 16g to 1t from carbon and alloy steels in the form of axle beams, crankshafts, connecting rods, suspension and transmission parts, compressor and turbine blades, air frames and undercarriage components. The Sub-Group's major customers are other U.K. companies, although some components are sold within the Group for finishing and assembly and approximately

16% of production is exported to the U.S.A. and Europe. To maintain this position in the forging industry, G.K.N. Forgings Ltd is backed by its own Process and Product Development Department (P. and P.D.) at Bromsgrove, which carries out a continuous programme of modernisation and development in both forging and ancillary processes on behalf of the Sub-Group companies. The P. and P.D. programme is geared to up-date production methods and technology to meet the increasing needs and growing sophistication of major markets. In addition, the Group has access to research facilities at the G.K.N. Group Technological Centre at Wolverhampton, whose function it is to perform more fundamental research and development work on metallurgy, materials and equipment used by all G.K.N. companies.

Recently the P. and P.D. department has developed the Powder-Forging technique for producing "near-finished" forgings from compacted powder compact "preform" shapes (of approximate dimensions of the final component). The process was advanced to give an operational production process set up at Redditch in 1977, G.K.N. Powder-Forgings Division, now a division of Garringtons.

## 1.2 The Problem

Production of powder forgings was begun after development work at P. and P.D. department had shown [2] that the process was viable. It was estimated that considerable savings could be made using the



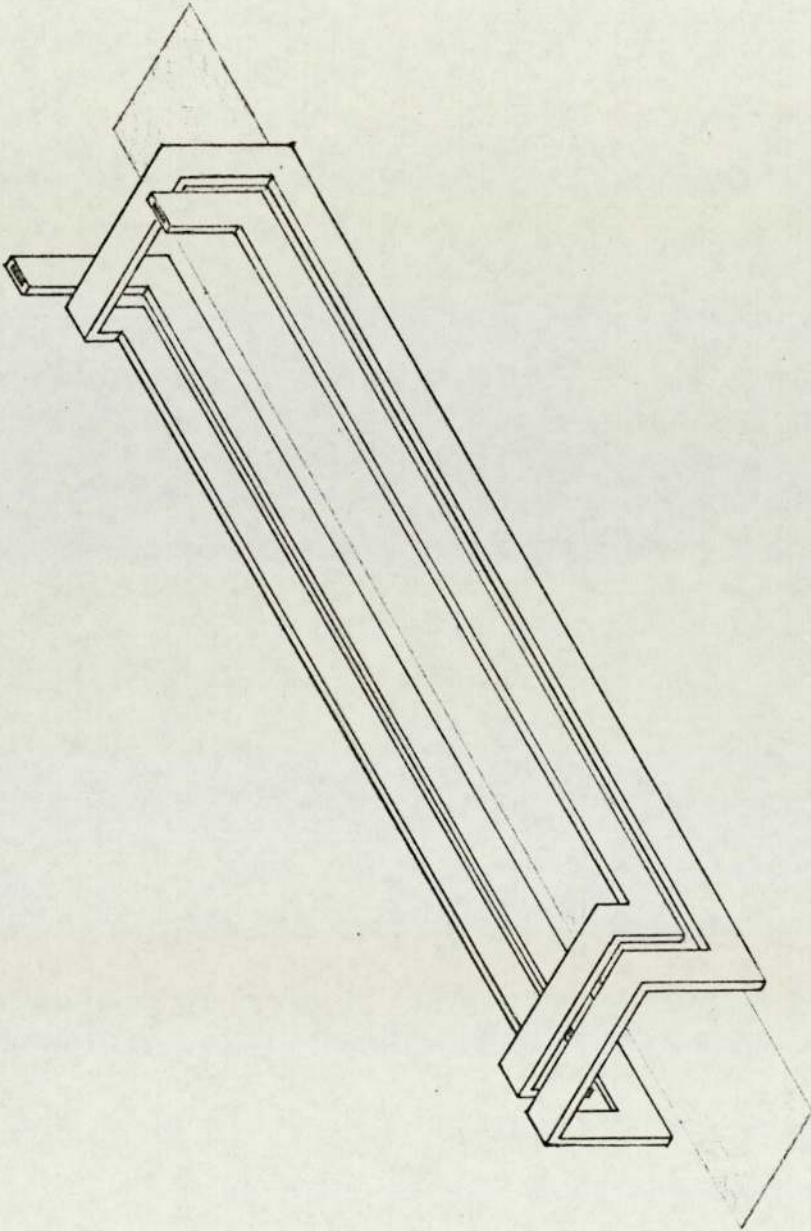


Figure 1.1 : Typical linear or "skate" coil consisting of two pairs of parallel conductor tubes. Preforms are moved through the coil on a mesh belt, shown shaded.

powder route; material utilization, from powder to finished product, was increased to over 90%, compared with 40% for conventional forging; machining operations were considerably reduced or eliminated; and press and die lives were increased, as fewer forging operations were necessary for powder-forged parts. Further development studies, and the experience of some American manufacturers, indicated that choice of the heating method used was crucial in maintaining the consistency, performance and reliability of powder-forged components. Induction heating was considered desirable to give greater efficiency and flexibility of heating with units of reduced size and better compatibility with automatic handling equipment than conventional furnaces.

A novel production heating system was developed [3] by G.K.N. from research by the Electricity Council Research Centre, Capenhurst [4]. The principle is that components are moved on a mesh belt between a number of straight rectangular-sectioned tubes usually arranged in pairs, conducting medium frequency current. This constitutes the induction heating coil (figure 1.1); this design is commonly referred to as a "skate" coil within G.K.N.

Compacted preforms require three stages of heating (Chapter 4). During the first stage the lubricant, which is added for ease of compaction and die longevity, is evaporated or "burned-off". Secondly, consolidation and extension of the interparticle bonds occurs



in the sintering stage. Finally, the compact is heated to the high temperature required for forging.

It was found that difficulties were experienced in applying induction heating to powder-forging during the first and second stages. Due to inefficient burn-off, the final mechanical performance was reduced, due to contamination by lubricant residue after combustion, and non-uniform heating and localized melting occurred during sintering. The present Powder-Forging production line was established where de-waxing and sintering occur in conventional gas-fired furnaces, and heating for forging is performed by the "skate" coil induction heater. However, the processing of parts in a gas furnace is incompatible with the continuous heating of the induction coil: Sintered parts are therefore cooled before being re-heated to forging temperature in the coil. G.K.N. are committed to developing a complete induction heating process from compaction to forging in order to eliminate this energy waste.

This project was initiated after Powder-Forging Division found difficulty in the induction heating of preform shapes, other than simple rings and flat discs, in the "skate" coil. Non-uniform heating occurred, resulting in local melting of the preform surface or failure to achieve forging temperature.

The aim of the project is to improve the technique of heating complex shapes. The project would be a theoretical and experimental

study of the induction heating of powder-compact preforms, to establish factors and relationships to aid coil design.

### 1.3 Project Definition

It became clear at the beginning of this investigation that the Company had little information on induction heating and powder metallurgical concepts that would lead to improvements in their coil design methods. Experienced personnel had been lost when an independent company, Birwelco\* (Newport) Ltd, had been formed and all induction coil specifications had to be bought from that organisation. Birwelco's reluctance to consider "skate" systems, and the requirement to independently assess the design of conventional solenoidal coils, have prompted the instigation of this project.

This project aims to increase company knowledge, to inject a more rational and theoretical approach to coil design, and to preserve G.K.N.'s lead in this technology.

A full solution to the problem of coil design for the heating of powder preforms demands evaluation of the interaction of a number of factors relating to the preform and to the coil. The preform factors are:-

- powder composition (constituents and particle sizes)
- heating atmosphere

\*Now re-named Newelco.



- preform density distribution
- preform state (unsintered (known as green), or sintered)
- preform shape

The coil factors are:-

- operating frequency or frequencies
- power input levels
- coil shape and size
- method of preform support and transport
- coil insulation

It is impossible for a study of this type to cover all aspects of this problem in the time available. The first requirement is that any present theory available for induction heating coil design for solid materials needs to be identified. The degree of application of induction heating theory to powder compact material heating may then be determined. From here, extensions to the coil design theory may be considered for G.K.N. applications. This study endeavours to overcome the problems of coping with the wide range of factors influencing coil design, by generating new knowledge based on typical G.K.N powders and powder preforms in the sintered state. The conclusions drawn may be applied to metal powder preforms generally, provided that the physical properties of the specific cases are known. Similarly, the coil design methods proposed may be used, with care, to predict for wider industrial applications than are explicitly derived in the thesis. This work forms a case study for the application of induction heating to powder-forging.

Criteria for assessing the value of the results may be stated quite simply. Study of existing methods of coil design will provide G.K.N. with the necessary knowledge of induction heating design, with guides for its application in practice. Comparison of these methods with practical experience of production coil systems will pin-point the limitations of present calculations, and surmount present problems of coil under-performance by expanding the theory. Success of the refinements will be measured by the accuracy of predictions compared with experimental tests. A similar principle may be applied to comparable trials using sintered metal parts to assess whether preform heating theory may be compared to the known behaviour of solid materials of simple shape.

Further investigation of the effects of heating coil and preform shape will be judged by the correlation of experimental measurements and extensions to theory, and by greater facility for coil design.

#### 1.4 Organisation of the Research

This thesis describes the development of the study through the following stages;-

IDENTIFICATION of the current state of knowledge and the nature of the problem,

DIAGNOSIS of the areas where new knowledge is needed and attempts to generate this,

RESULTS, and their discussion,



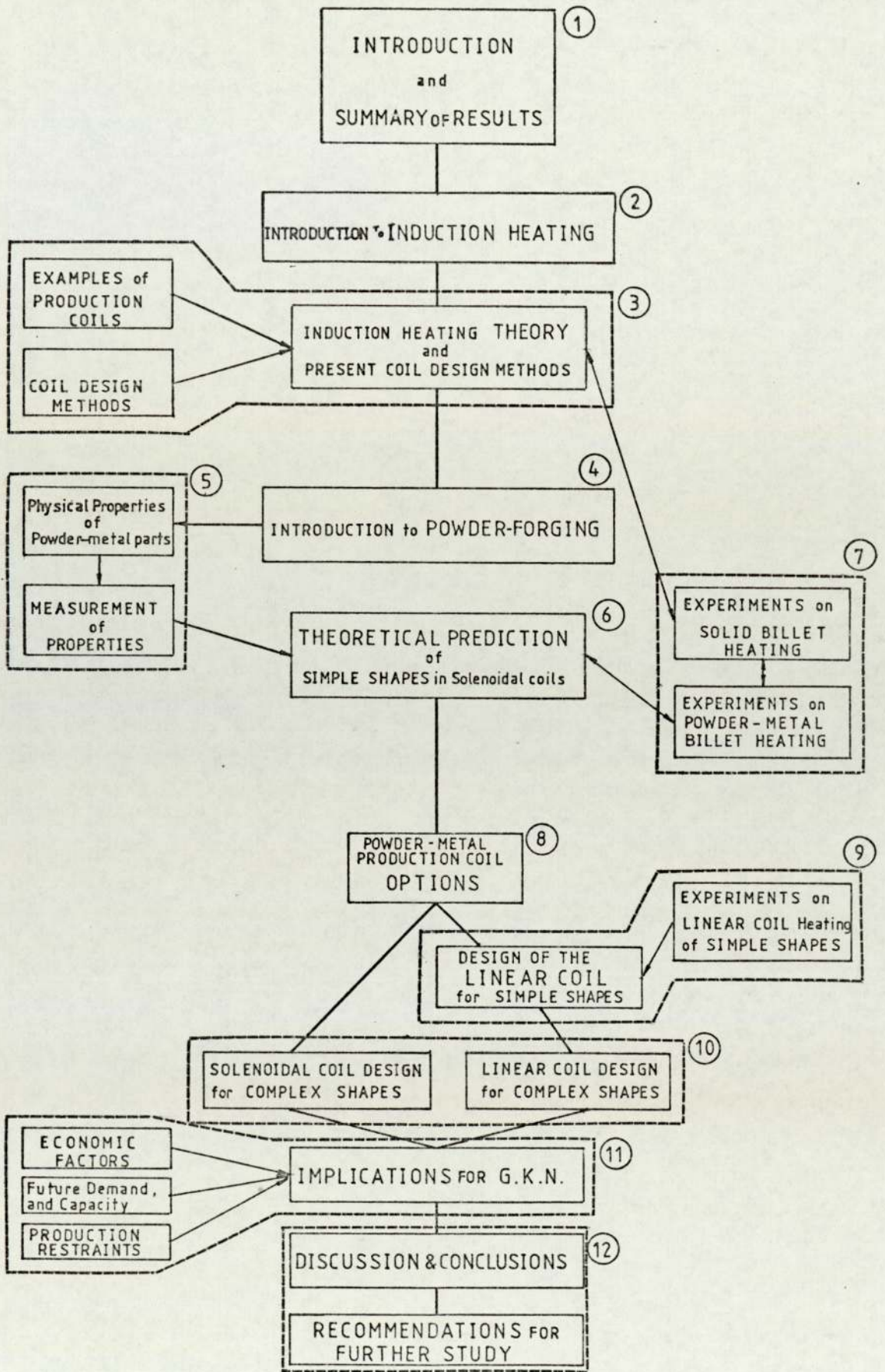


FIGURE 1.2: Thesis arrangement:- Project topics are in solid boxes. Chapters are circled. Chapters with many topics are in dashed boxes.

CONCLUSIONS that may be drawn.

This project consists of a number of related but separate topics, each requiring some consideration of all four stages independently. An outline plan is contained in block diagram form in figure 1.2, which shows the relationship between parts of this study.

#### 1.4.1 Identification

This stage is considered in Chapters 1 to 4. These chapter contents may be briefly summarized in the following sub-sections.

The basic principles of induction through-heating of steels for forging will be briefly presented in Chapter 2, highlighting:-

- a) The importance of the strength and distribution of the magnetic field produced by coil conductor configurations.
- b) The effect of the heated material's relative magnetic permeability and its variation with temperature on the induced field.
- c) The limits imposed by electrical resistivity and thermal conductivity of the heated material on heat generation and transfer.

Chapter 3 will develop a more detailed treatment of the theory in the section below.



Chapter 3 is an examination of the mathematical basis of induction heating. The solution of the magnetic flux equations will be produced to derive the equivalent circuit calculations for coil design. The methods, as described in the literature, will be compared with practical experience drawn from production coils and the limitations of the methods shown.

The heat transfer equations governing temperature distribution will be developed, and the importance of skin effect, metal properties and radiation on the heating pattern demonstrated.

The basic principles of powder metallurgy will be briefly presented in Chapter 4, highlighting :

- The production of powder compacts and its influence on properties (micro-and macroscopic);
- The influence of forging and heat treatment stages on compact density, and its importance;
- Preform shape and complexity with respect to physical properties.

The contents of Chapters 2 and 4 contain short résumés of both subjects. It is intended that these be of sufficient general and detailed nature to satisfy workers in the respective fields of study, while directing attention to the relevant topics of specific interest. The current state of knowledge of coil design in the literature and in industrial practice is defined and the need for quantifying powder compact properties shown.

#### 1.4.2 Diagnosis

Diagnosis of areas where new knowledge is required and attempts to generate the information are described in Chapters 5,6, 8 and 9.

A literature survey of powder compact physical properties contained in Chapter 5, shows the need for measurement of electrical resistivity, thermal conductivity and magnetic permeability. The chapter will then describe experiments to determine values for those quantities. These values will be related to information gained by referring to the literature.

Chapters 6 and 7 are written to link Chapters 3,4 and 5. This section will consider induction heating of sintered parts with reference to existing coil design theory and the extensions of the theory as shown in Chapter 6. Important differences in the heating of solid and sintered parts (relating to properties) will be described. Predictions of the heating performance of powder-metal parts in solenoidal coils will be compared with the performance of solid material. Identified also in Chapter 6 are the limitations of coils in current use for heating the full range of G.K.N. shaped preforms. The need for more elaborate designs is considered in the following section.



"Coil Options for production" (Chapter 8) introduces the second part of the thesis which concentrates on "skate" coil work. It indicates the limits and advantages of solenoidal coils for G.K.N. production, and presents alternatives. Of these the linear "skate" coil is favoured by G.K.N., chiefly for reasons of production convenience and simplicity.

Two further topics of the remainder of the thesis, solenoidal and linear coil development, are directed in Chapter 10 towards the heating of complex shapes.

A literature review of theoretical methods for predicting induction heating of shaped parts is presented in Chapter 10. This introduces the need for further development of methods applicable to more complex geometries, and identifies a deficiency in experimental results for comparison with calculations.

#### 1.4.3 Results and their Evaluation

The presentation of results occurs at strategic positions within Chapters 5,6,7 and 9 after discussion of the following information:-

Powder compact properties (Chapter 5);

Induction heating of solid and compacted powder billets (Chapters 6 and 7);

Induction heating of shaped parts (Chapter 9).

Evaluation of these results and their implications for the sponsoring Company appears in Chapter 11. Some discussion inevitably follows chapters reporting experimental results since correlation between these values and theoretical study provides justification for the subsequent chapters.

#### 1.4.4 Conclusions

Overall discussion and the conclusions that may be drawn from the results are shown in Chapter 12.

Recommendations for further studies in the field of induction heating of powder compacts are also discussed in this final chapter.

### 1.5 Summary of Principal Findings :

#### 1.5.1 On Current Methods used in Coil Designs

- These methods are limited to considering the heating of cylindrical shaped parts in solenoidal coils.
- Present methods fail to enable production coil systems to be designed with sufficient accuracy.
- New modifications are presented for improving the methods.
- Guide - lines for their use for practical coil designs used in production are given.
- Comparison of the improved method with experimental verification shows a distinct increase in prediction accuracy.



#### 1.5.2 On Powder Compacts

- Absence of reliable information on the physical properties (i.e. magnetic permeability, electrical resistivity and thermal conductivity) of G.K.N. powders was identified.
- Apparatus was designed, built and used to determine the powder compact properties.
- A relationship between the powder compact properties and density was found and compared with predictions presented in the literature.

#### 1.5.3 On Induction Heating of Cylindrical Powder Compacts

- Temperature measurements were made during heating of simple preforms in a production solenoidal coil.
- Comparison between predicted performance and experimental results shows excellent agreement.
- Similar heating characteristics of solid and sintered metal parts under the influence of induction heating is established.

#### 1.5.4 On Induction Heating of Shaped Metal Parts

- The range of theoretical models is reviewed and their limitations to the solution of simple two-dimensional non-magnetic cases shown.
- The feasible options for production coil systems are identified.
- Further theoretical modelling for the solenoidal and linear "skate" coil is proposed , with attention to varying

material properties and various ferro-magnetic materials.

- Predictions of coil performance for heating shaped parts are made and compared with preliminary tests on linear coil heating. The effect of coil proximity and field strength is shown.

#### 1.5.5 On the Implications for G.K.N.

- An economic assessment of induction heating of powder-forgings presents the advantages of the route over conventional heating processes.
- All calculation methods are presented in a form that facilitates the extension of these findings for general consideration of other shapes. Methods of elaborating the predictions for more complex shaped parts are discussed.

### 1.6 Observations

The fundamental relationships for the solution of magnetic field equations and the principles of heat transfer have been well understood since before the turn of the century. Analytical solutions to these equations for induction heating applications exist only for the most simple cases [5]. It is not surprising therefore, that progress towards solution of actual induction coil design problems has been slow.

Approximate coil design methods have been available for some time. However, it was not until the introduction of the computer,



making available fast calculation speeds and large amounts of information storage, that numerical solutions could be developed to approximate more closely to practical systems.

The delicate energy balance of induced power input to a part being heated, and heat transfer within the part may now be more accurately predicted. The prediction allows for the changing magnetic and thermal conditions prevailing at each stage of heating. However, it appears that the practicalities and realistic application of these methods have been largely ignored, with the assumptions required for approximate solutions.

This study utilizes theoretical and practical approaches from fundamental roots, and develops potential solutions for a practical case study within the constraints of an industrial setting. These principles may also be generally applied to a new application where induction heating is considered.

CHAPTER TWO

AN INTRODUCTION TO INDUCTION HEATING



## CHAPTER 2 : AN INTRODUCTION TO INDUCTION HEATING

### 2.1 Principles of Induction Heating [6-18]

A metal object placed within a pulsating magnetic field has an electromotive force (V) induced within it to oppose the initiating magnetic flux change. The associated flow of current is resisted by the metal, and heat is generated by the Joule heating effect (where  $I^2R$ =power induced). This phenomenon is the basis of induction heating.

The magnetic field is produced within a water-cooled copper coil by connection to an alternating current supply. Careful location of the coil and the metal to be heated (commonly referred to as the work, workload, load or workpiece) ensures that most flux paths encounter the workpiece, thus minimizing wasteful flux leakage (figure 2.1). The basic arrangement is similar to a transformer, differing only in that the secondary winding is a shorted single turn (figure 2.2), separated from the primary coil by a small air-gap.

A non-uniform current distribution is induced in the metal; the current density decreases from the surface to the centre of the load as the magnetic flux is exponentially reduced by the opposing field developed in the part. A characteristic penetration or "skin" depth is defined where the current density is reduced to  $1/e$  times (approximately one third) the surface value,

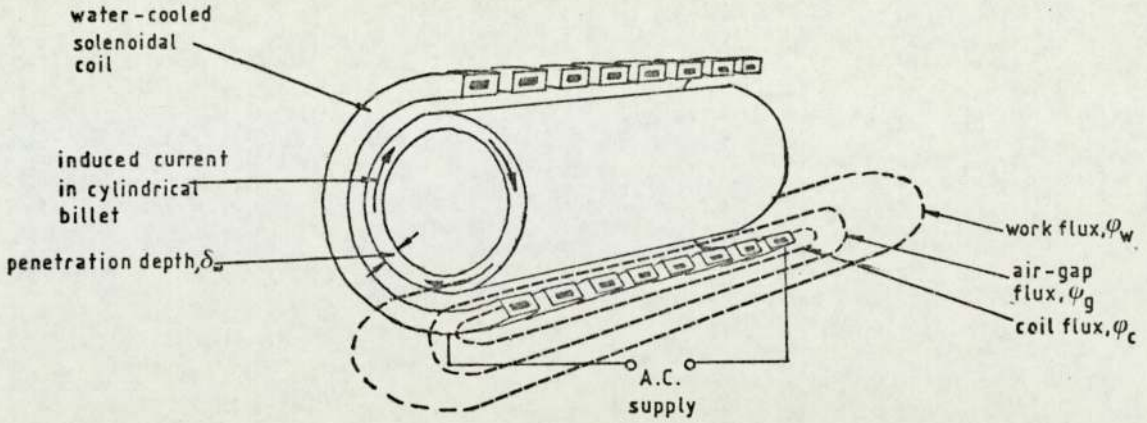


FIGURE 2.1: Induction heating of a cylindrical load in a solenoidal coil. The flux paths linking the work, the coil and the air-gap are shown.

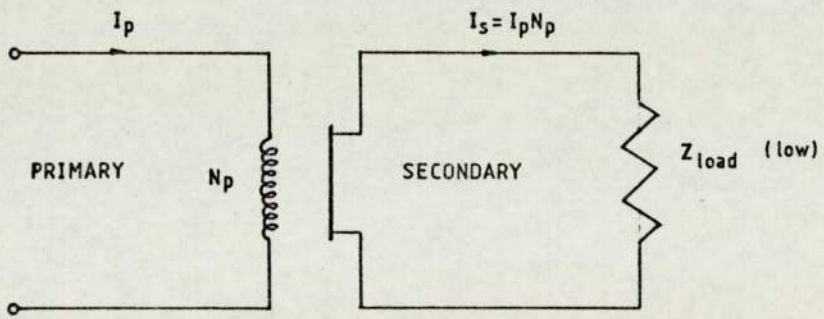


FIGURE 2.2: Transformer analogy of induction heating. Large currents flow in the shorted secondary circuit.



$$\delta = \sqrt{\frac{\rho}{f \pi \mu}} \quad (2.1).$$

This depth is dependent on the frequency  $f$  of the primary flux change and two properties of the workload material, the electrical resistivity  $\rho$  and the magnetic permeability  $\mu^*$ . Power developed by current flow in the primary coil is also governed by the same principles.

For greatest induction heating efficiency, the power induced in the workload must be at a maximum and the coil losses kept to a minimum. Heat is transferred to the surroundings from the workload surface by conduction, which is determined by the material thermal conductivity  $k$ , and by radiation. The relationship between the induced power density and dispersal of the heat within the load is complex. The temperature profile may be altered by control of the penetration depth, by altering frequency and primary current input with time, to suit a particular application.

## 2.2 Applications of Induction Heating

Induction heating is used for a wide variety of applications [19] since the process has major advantages in comparison with fuel-fired furnace installations. These advantages for steels are summarized

\*  $\mu$  is a product of the material relative magnetic permeability  $\mu_r$  and the permeability of free space  $\mu_0$  (defined as

$$\mu_0 = 4 \pi \times 10^{-7} \text{ H/m } )$$

here and considered in greater detail later.

High heating rates, resulting in short heating times, reduce the amounts of scaling and decarburization produced on the surface. The greater speed and improved control of temperature lends the induction heating process to automated production lines. The better overall efficiency is enhanced when the more rapid start-up associated with induction heaters is considered. This feature is highly relevant in relation to meal breaks and production stoppages for tool attention etc. Fuel-fired equipment, at best, can only be switched to a "stand-by" during these periods. Because heat is generated more efficiently within the workload, rather than from an external fuel source, a cooler working environment exists and greater utilization of floor space is possible. The absence of noxious combustion products allows better metallurgical control of the metal surface conditions to be achieved. By a more precise control of workload temperature relative to time, metallurgical structure can be closely controlled.

Applications may be divided into three categories in order of increasing frequency. In the first, localized surface heating within a shallow skin depth  $\delta$  is used for surface hardening, soldering, brazing and tube-welding [16]. High power densities are delivered at medium to high frequencies (keeping  $\delta$  small), using coils of few turns to confine the heated area. This study concerns the second application, through-heating of steels for forging. In this application, uniform



heating is achieved using long coils with lengthier heating times, and arranging deeper penetration depths using low to medium frequency supplies. Finally, induction heating is used extensively for steel smelting. The three categories are shown in table 2.1, with typical frequencies used.

This thesis concentrates on through-heating applications for forging, especially those related to the needs of G.K.N.

### 2.3 Through-heating for Forging

Most applications involve the heating of cylindrical or square-sectioned steel billets of between 50mm and 150mm diameter or side length. Billet length lies between 50mm and 2000mm. Forging temperatures are between 1100°C and 1250°C, depending on application, with temperature uniformity in an individual workload within  $\pm 25^{\circ}\text{C}$ .

TYPE	APPLICATION	FREQUENCY (Hz)							
		10	100	1k	10k	100k	1M	10M	
MELTING	STEEL SMELTING	-----							
THROUGH HEATING	STEEL FORGING	-----							
SURFACE HEATING	SURFACE HARDENING			-----					
	TUBE WELDING					-----			
	BRAZING & JOINING	-----							

Table 2.1 : Induction heating systems and applications.

For maximum heating efficiency, Chapter 3 shows that the medium frequency supply should be chosen as shown in table 2.1. The penetration depth is related to the workload diameter  $d$  by the equation

$$d \geq 3.5 \delta \quad (2.2).$$

For square-sectioned billets of side  $a$ , the relationship  $1.28 a \geq 3 \delta$  is used.

However, the skin depth alters significantly as the steel is heated, due to changes in the relative magnetic permeability of the material. Materials which are magnetic at room temperature, having a high  $\mu_r$  value, become non-magnetic ( $\mu_r = 1$ ) at a particular temperature  $\theta_{\text{curie}}$ , known as the Curie temperature.  $\theta_{\text{curie}}$  lies between  $720^\circ\text{C}$  and  $760^\circ\text{C}$  for steel, depending on carbon content. It is therefore necessary to induction heat using two frequencies, one below and the other above Curie, or suffer the consequence of reduced efficiency above  $\theta_{\text{curie}}$  when equation 2.2 is not met. Table 2.2 shows typical frequencies for various workload diameters.



BILLET DIAMETER (mm)	FREQUENCY	
	Below Curie Temperature	Above Curie Temperature
6 to 12	3kHz	8 to 10 kHz
12 - 25	1kHz	8 to 10 kHz
25 - 38	1kHz	3 to 10 kHz
38 - 50	50/60 Hz	1 to 3 kHz
50 - 150	50/60 Hz	1 kHz
over 150	50/60 Hz	50/60 Hz

Table 2.2 : Frequencies for through-heating steel of various diameters for forging at 1250°C. [18].

Power supply systems for delivering the primary current supply are of three types. For larger diameter workloads, mains supply heaters are used, needing no frequency conversion and requiring only transformers, switchgear and load-matching capacitors. These low-maintenance units are the cheapest induction heaters in terms of kilowatt installed. The second type is the use of electric motor-alternators to supply fixed frequency between 500Hz and 1kHz. These alternators are normally driven by an induction motor and loads are matched by switchable capacitors. The system is extremely reliable and easy to maintain by production workshops. Except where constant frequency output is desirable, the motor-alternator is rapidly being superseded by the third type, the static inverter. The static inverter is a solid-state device, operating between 500Hz and 50kHz. Load

matching occurs as the output frequency automatically alters and so maintaining efficiency by continuously matching frequency to the changing load impedance during heating. Although solid-state alternating current supply for induction heaters represents the biggest recent advance in the field, it may be some time before they completely replace motor-alternators on established production lines. The following section describes a typical through-heating arrangement for production forging at G.K.N.

#### 2.4 G.K.N. Production Layout

The industrial production system produces 2.7kg/kWh (6lb/kWh) (typically) of steel at forging temperature and consists of a motor-alternator set or sets, delivering between 140kW and 1700kW, connected to the induction heater. To reduce noise and release space for the actual production line, the power generator is often sited away from the heater. The heater unit comprises the following:-

- power control switch-gear
- power-factor correction capacitors
- voltage, current, power and reactive power meters
- the induction heater process timer
- water-cooling supply tanks and manifolds
- coil
- coil electrical and water-cooling connections
- workload handling equipment.

The heater often serves as a platform for the induction coil, so that heated billets may be gravity fed to the forging press.



Billets are normally supplied to the coil via an automatic feed magazine, cycled by the process timer on the heater. The work-handling equipment includes compressed air pistons which push the billet column into the coil; the coil is fitted with internal longitudinal guide rails of stainless steel with a hard coating on which the billets travel. The purpose of a through-heating coil is to electrically couple as close as possible with the workload shape, taking into account loading and unloading clearances, adequate thermal and electrical insulation and mechanical rigidity. Typical air-gaps for good working practice are indicated in table 2.3.

	FREQUENCY								
	50/60 Hz			1kHz		3kHz		10kHz	
BILLET TEMPERATURE(°C)	550	850	1250	850	1250	850	1250	850	1250
WORKLOAD DIAMETER (mm)	AIR-GAP (mm)								
0 - 60	25	25	50	50	62	50	62	50	62
60 - 125	25	38	50	62	75				
125 - 250	25	38	80	75	80				

Table 2.3 : Typical air-gaps for through-heating in solenoidal coils [18].

The coil is constructed of high-conductivity copper tubing of round or rectangular section, wound on a former; this is cast in refractory cement within an asbestos-type (Syndanyo) box. Multiple water circuits within the coil tubes are provided to ensure adequate cooling.

As discussed above, the power input to the billet alters at the Curie temperature. There may also be a "soaking" stage at the end of the heating cycle to reduce the temperature gradient through the section which is due to the use of high power densities at the surface. For these reasons, production coils often consist of as many as four sections [17,20]. The first, "sub-Curie" section, contains a high density of coil turns giving high power input to efficiently heat the billet quickly to the Curie temperature. A second section may be present to heat the billet through the Curie point where power is absorbed to supply latent heat for the magnetic transition. The next, "super-Curie", stage brings the billet to forging temperature at a less efficient rate. A higher frequency supply may power this section for more efficient heating by providing a closer approximation to the  $d/\delta \geq 3.5$  relationship. Finally, a "zero-energy" section is provided to overcome radiation losses from the surface, whilst the temperature distribution becomes uniform. Division of the coil into these sections and adjustment of the power input to each, allows various heat patterns to be obtained in the load. It also provides the nearest approximation to a continuously variable coil, ideally matched to the changing properties of the workload during heating.

The inter-relationship between the coil shape and the distribution of heat within the part is complex. The coil designer's problem



lies in developing a coil to raise the billet temperature efficiently and at the maximum rate to a uniform temperature distribution, without overconcentration of thermal stresses, or locally overheating or even melting the workload.

The next chapter considers the theory of induction heating and develops the existing state of coil design methods for production systems. An example is given of a G.K.N. coil and the degree to which prediction methods accord with practical experience is discussed.

CHAPTER THREE

THEORY OF INDUCTION HEATING



## CHAPTER 3 : THEORY OF INDUCTION HEATING

### 3.1 Introduction

This chapter introduces the theory of induction heating and shows how an approximate solution for industrial coil design has been developed from the theory. The general theory described in section 3.2 is divided into two parts. First, the electromagnetic solution may be solved from first principles for a metal part subjected to an external magnetic field, leading to the derivation of the flux, current and power distributions. Secondly, the principles of heat transfer are applied to describe the flow of this energy within the workload and the resulting temperature distribution.

Application of the theory for coil design is described in section 3.3 and the calculation method shown. The major coil and supply parameters may be calculated from the values obtained. The method only approximates to the physical conditions, however, and section 3.4 summarises the extent to which these predictions agree with an example of G.K.N. production coil design.

Section 3.5 gives the limitations of existing design practice and shows where the calculation method may be significantly improved.

## 3.2 General Theory

### 3.2.1 Solution of the Electromagnetic Equations [18]

The distribution of the magnetic field  $H$ , the electric field  $E$  and the current density  $J$  in metals within the frequencies used for electroheating are described by the diffusion equations

$$\nabla^2 H = \frac{\mu}{\rho} \frac{\partial H}{\partial t} ; \quad \nabla^2 E = \frac{\mu}{\rho} \frac{\partial E}{\partial t} ; \quad \nabla^2 J = \frac{\mu}{\rho} \frac{\partial J}{\partial t} . \quad (3.1)$$

For a sinusoidally varying magnetic field the first expression in equation 3.1 may be written (depending on the appropriate form for the workload shape), in rectangular co-ordinates,

$$0 = \frac{\partial^2 H}{\partial x^2} + \frac{\partial^2 H}{\partial y^2} + \frac{\partial^2 H}{\partial z^2} - j \frac{\mu \omega}{\rho} \{H_x + H_y + H_z\} \quad (3.2)$$

or in cylindrical polar co-ordinates,

$$0 = \frac{\partial^2 H}{\partial r^2} + \frac{1}{r} \frac{\partial H}{\partial r} - j \frac{\mu \omega}{\rho} H . \quad (3.3)$$

Similar expressions exist for  $E$  and  $J$ . These equations may be solved with applicable boundary conditions for the problem. The simplest solution, in mathematical terms, occurs for a flat slab, and is given by Davies and Simpson [18]. However, practical G.K.N. workloads are of cylindrical symmetry and are heated within a solenoidal coil by an applied  $H = H_{0m} \cos \omega t$ .



The Bessel function solution of equation (3.3), [18]

$$H = A I_0(kr) + B K_0(kr) , \quad (3.4)$$

where  $I_0$  and  $K_0$  are Bessel functions of zero order, may be shown [21] using Maxwell's equations [22] to give

$$J = \text{curl } H = \sqrt{2} \alpha H_R \frac{\text{ber}'\sqrt{2}\alpha r + j \text{ber}'\sqrt{2}\alpha r}{\text{ber}\sqrt{2}\alpha R + j \text{ber}\sqrt{2}\alpha R} \quad (3.5)$$

at a radial distance  $r$  within a solid cylinder of radius  $R$  (figure 3.1). Here  $\alpha$  is the inverse of penetration depth, i.e.

$$\alpha = \sqrt{\frac{\mu \omega}{2 \rho}} .$$

The total magnetic flux  $\phi_w$  within the cylinder,

$$\phi_w = \int_0^R B \cdot dr \quad (3.6)$$

is rationalized to give

$$\phi_w = \mu H_{Rm} A_w (q - j p) \quad (3.7)$$

where  $A_w$  is the cross section area of the workload,

$$q = \frac{\sqrt{2}}{\alpha R} \left. \begin{array}{l} \text{ber}'\sqrt{2}\alpha R \text{ber}\sqrt{2}\alpha R - \text{ber}'\sqrt{2}\alpha R \text{ber}\sqrt{2}\alpha R \\ \text{ber}^2\sqrt{2}\alpha R + \text{ber}^2\sqrt{2}\alpha R \end{array} \right\} \quad (3.8)$$

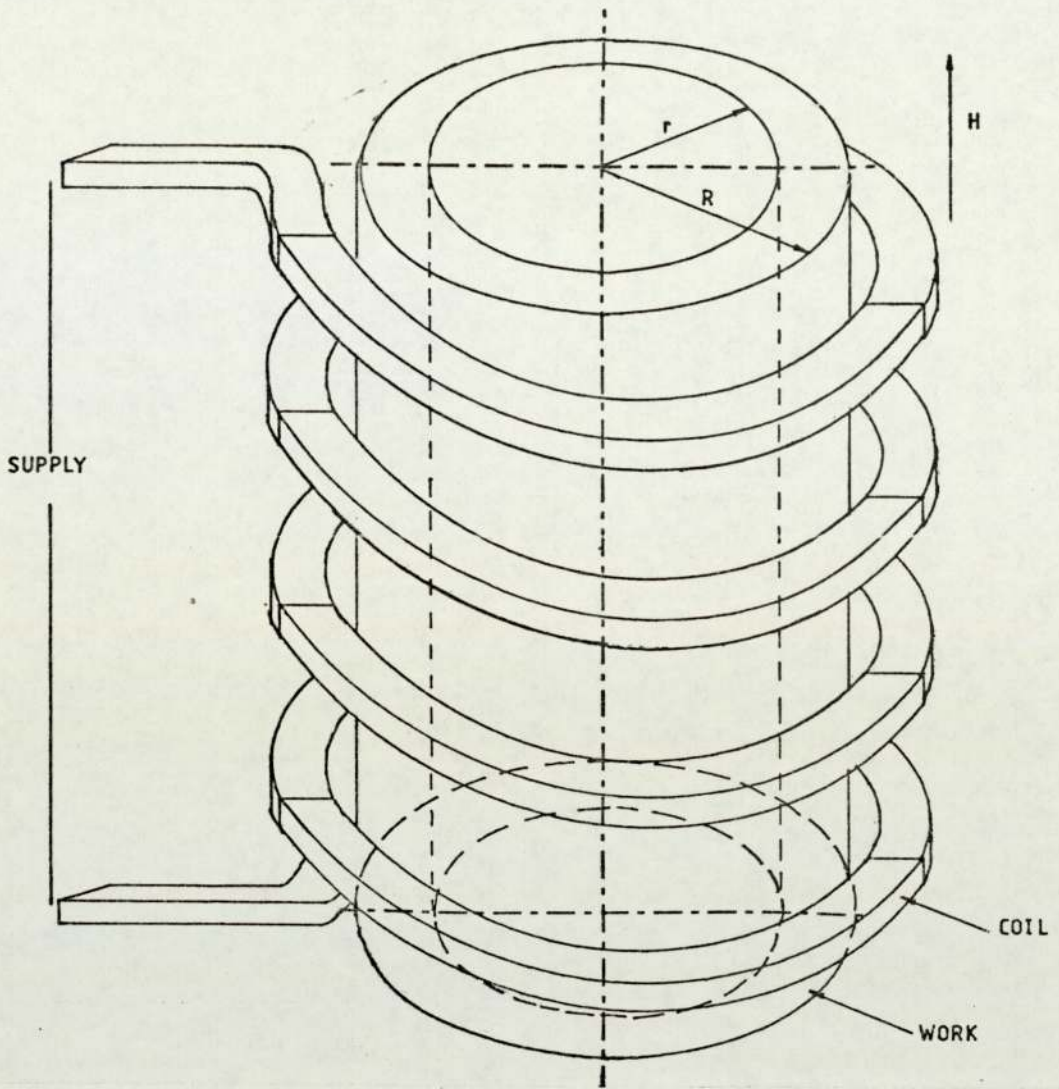


FIGURE 3.1: Solid Cylindrical workload within a solenoidal coil.

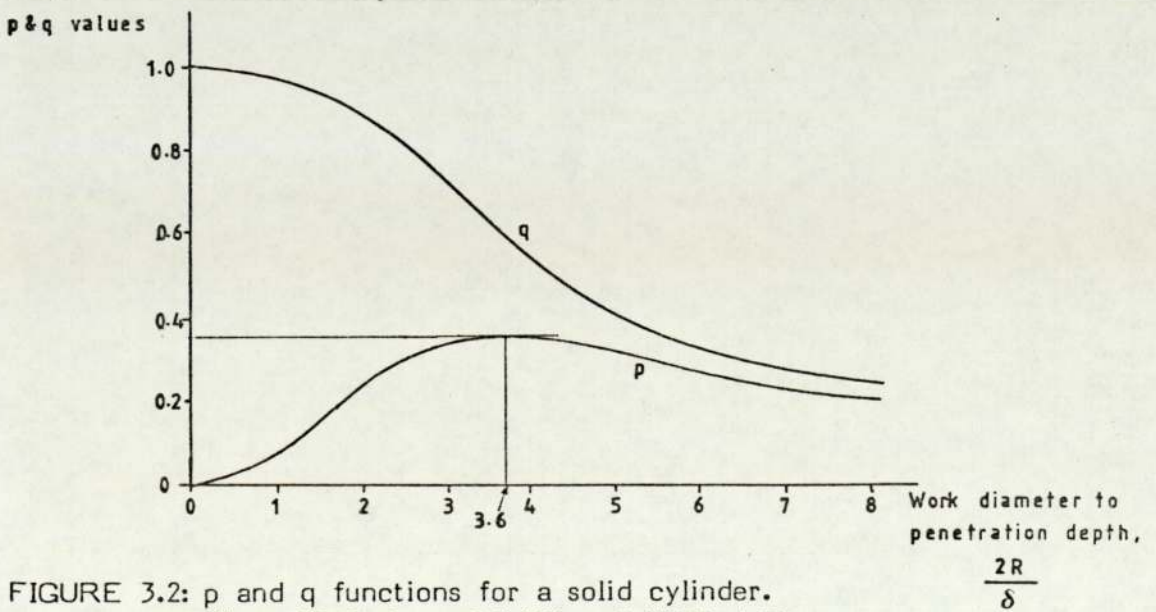


FIGURE 3.2:  $p$  and  $q$  functions for a solid cylinder.  
 When  $2R/\delta > 8$ ,  $q = 2/(d/\delta)$ ;  $p = 2/(1.23 + d/\delta)$



and

$$p = \frac{\sqrt{2}}{\alpha R} \frac{\text{ber}'\sqrt{2}\alpha R \text{ber}\sqrt{2}\alpha R + \text{ber}\sqrt{2}\alpha R \text{ber}'\sqrt{2}\alpha R}{\text{ber}^2\sqrt{2}\alpha R + \text{bei}^2\sqrt{2}\alpha R} \quad (3.8)$$

The  $p$  and  $q$  values are plotted in figure 3.2 as functions of  $d/\delta$ , the work diameter divided by the skin depth. The simplified expression for the flux (equation 3.7) has been solved for other simple cases and similar  $p$  and  $q$  graphs may be found for a slab and various hollow cylinders [18,23].

The power  $P_w$  developed in the load is, per metre length

$$P_w = \sqrt{2}\pi\rho\alpha H_{Rm}^2 R \left\{ \frac{\text{ber}\sqrt{2}\alpha R \text{ber}'\sqrt{2}\alpha R + \text{ber}'\sqrt{2}\alpha R \text{ber}\sqrt{2}\alpha R}{\text{ber}^2\sqrt{2}\alpha R + \text{bei}^2\sqrt{2}\alpha R} \right\} \quad (3.9)$$

which can be defined in terms of  $p$ ;

$$P_w = \mu \pi f H_{Rm}^2 p (\ell_w A_w) \quad (W/m)$$

where  $\ell_w$  is the workload length. The Power density  $\mathcal{P}_w$  is then

$$\mathcal{P}_w = \mu \pi f H_{Rm}^2 \frac{R}{2} p \quad (W/m^2) \quad (3.10)$$

It will be noticed that power loss within the workload is directly proportional to the value of  $p$ . Figure 3.2 shows that, for the solid cylinder, the maximum value of  $p$  occurs at  $d/\delta \approx 3.5$  and declines slowly for larger  $d/\delta$  ratios. Clearly, for efficient induction heating  $\mathcal{P}_w$  should be

maximized by adhering to the relationship

$$d \geq 3.5 \delta \quad .$$

The fundamental equations above are developed for coil calculations in section 3.3.

### 3.2.2 Thermal Solution

The principles of heat transfer are well established and various authoritative works [24,25] exist for the explicit solution of simple problems. Here, the theory related to cylindrical billets only will be shown. Expressions may be derived from the theoretical formulae that demonstrate the effects of induction heating variables on the billet temperature distribution, and are therefore useful for coil design. If the power input (equation 3.10) to the work is derived from a constant magnetic field strength and assumed to be concentrated at the billet surface, then the temperature distribution within a cylindrical billet can be solved [18] to give

$$\theta = \frac{\mathcal{P}R}{k} \left\{ 2\tau + \frac{r^2}{2R^2} - \frac{1}{4} - 2 \sum_{n=1}^{\infty} \exp\left(-\beta_n^2 \tau\right) \frac{J_0(\beta_n(r/R))}{\beta_n^2 J_0(\beta_n)} \right\} \quad (3.11) .$$

$\theta$  is the temperature rise at radius  $r$  after time  $t$  seconds and  $\tau$ , the dimensionless normalized time, is given by

$$\tau = \frac{kt}{\rho c R^2} \quad . \quad (3.12)$$



The summation term (  $\sum$  term) describes the transient temperature rise that disappears after  $\tau = 0.25$ , giving a steady parabolic temperature distribution with a constant surface-to-centre difference

$$\theta_s - \theta_c = \frac{\mathcal{P} R}{2k} \quad (3.13)$$

The normalized temperature is obtained by dividing equation 3.11 by equation 3.13 and is plotted in figure 3.3.

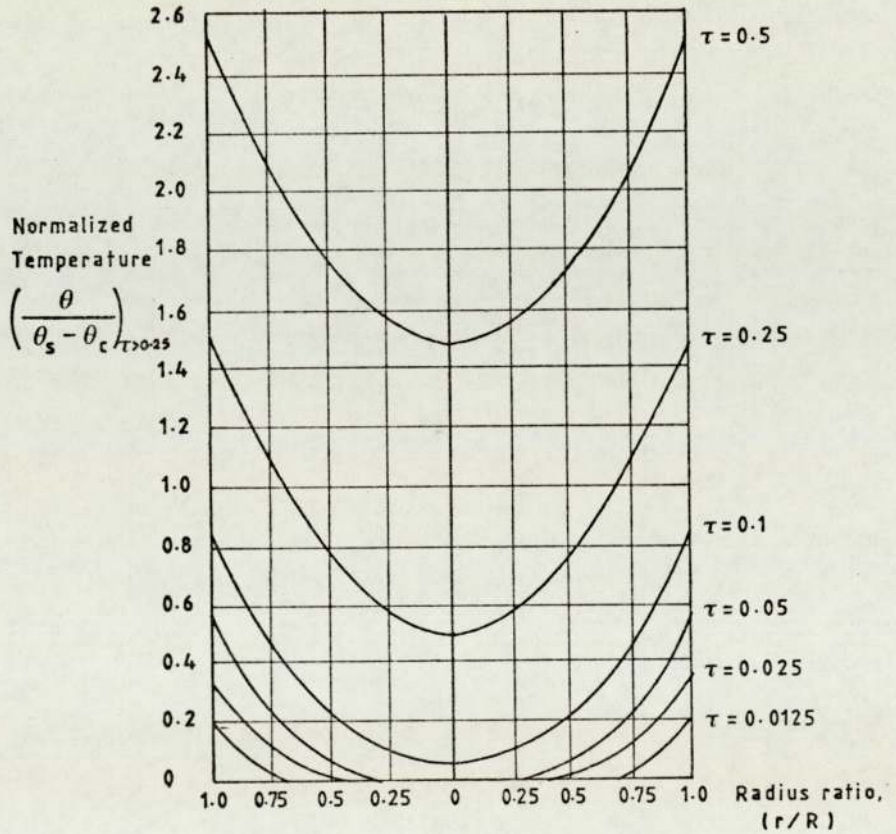


FIGURE 3.3: Distribution of temperature with radius in a solid cylinder, with normalized time  $\tau$ . Surface power input is assumed. All temperatures are normalized with respect to  $(\theta_s - \theta_c)_{\tau=0.25} = \mathcal{P} R/2k$ , See equation 3.11

After the initial transient has decayed, the temperature distribution assumes the following form,

$$\theta = \frac{\mathcal{P}_R}{k} \left( 2\tau + \frac{r^2}{2R^2} - \frac{1}{4} \right) \quad (3.14) .$$

(Equation 3.13 is derived by substituting  $r = 0$  and  $r = R$  in equation 3.14)

In practice, however this expression of steady temperature rise is modified by the following factors; the presence of some heating power developed below the surface, within the penetration depth; radiation losses from the billet surface; and changes in the power input.

#### 3.2.2.1 Effect of Skin Depth

In section 3.2.2. and equation 3.11 the power was assumed to be concentrated at the surface. In fact, power is also generated below the surface by a current of exponentially decaying magnitude. It has been shown [18] that a full solution modifies the temperature profile as shown in figure 3.4.



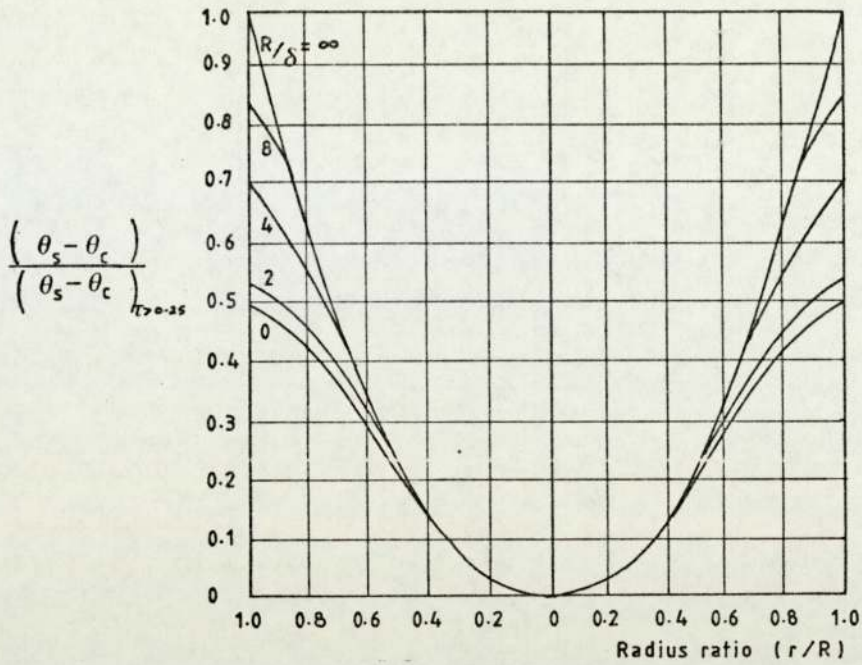


FIGURE 3.4: Distribution of temperature with radius in a solid cylinder, modified from the steady-state curves of figure 3.3 to account for the effect of skin depth. Curves plotted are for various values of  $R/\delta$ ,  $R/\delta = \infty$  corresponds to the steady curves of figure 3.3, where  $\tau > 0.25$ .

### 3.2.2.2 Effect of Radiation

Radiation losses from the billet surface (at absolute temperature  $T_s$ ), to the coil refractory lining at absolute temperature  $T_e$  may be calculated from the Stefan-Boltzmann law,

$$\mathcal{P}_R = \sigma_s \epsilon \left\{ T_s^4 - T_e^4 \right\} \quad (3.15)$$

where Stefan's constant  $\alpha_s = 5.67 \times 10^{-8} \text{ W/m}^2\text{K}^4$  and  $\epsilon$  is the emissivity coefficient of the surface.

If the refractory temperature is unknown, radiation loss may be adequately approximated by taking 75% of the free air radiation ( $T_e=293\text{K}$ ) to give a net power density,  $\mathcal{P}_n$ . A mean radiated power density  $\mathcal{P}_{Rm}$  over the temperature range  $T_1$  to  $T_2$ ,

$$\mathcal{P}_{Rm} = \frac{1}{5} \alpha_s \epsilon \left\{ \frac{T_2^5 - T_1^5}{T_2 - T_1} \right\} \quad (3.16)$$

may also be used. However section 3.2.2.1 was based on the assumption that the power density in the billet is uniform. Davies and Simpson [18] and Simpson [21] show that the surface-to-centre differential may be approximated by

$$\theta_s - \theta_c = \frac{\mathcal{P}_n R}{2k} \left[ 1 - \frac{\mathcal{P}}{\mathcal{P}_n} \left( \frac{X(k_2) - 1}{k_2 Z(k_2)} \right) \right] \quad (3.17)$$

where

$$Z(k_2) = \text{ber}\sqrt{2\alpha}R\text{ber}'\sqrt{2\alpha}R + \text{bei}\sqrt{2\alpha}R\text{bei}'\sqrt{2\alpha}R$$

and where

$$X(x) = \text{ber}^2x + \text{bei}^2x$$

The correction factor to equation (3.13) within square brackets in equation (3.17), is plotted in figure 3.5.



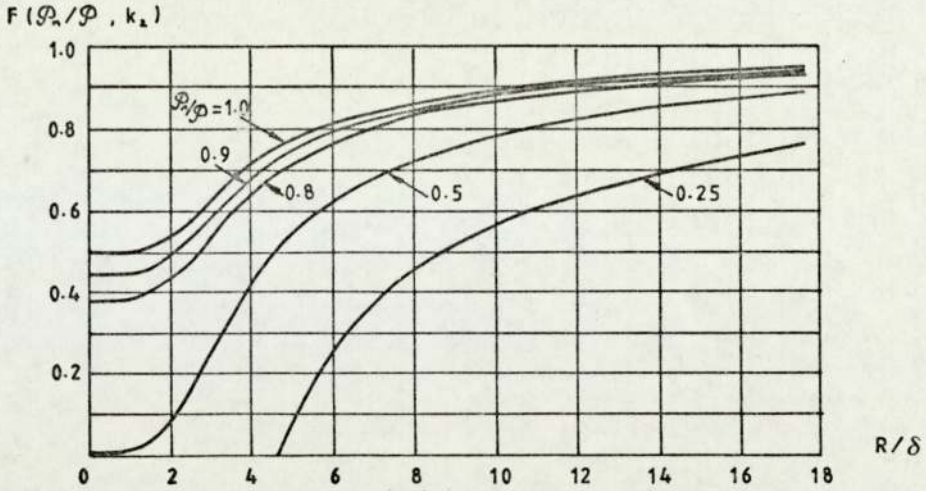


FIGURE 3.5: Correction factor of equation 3.17 (within square brackets) for temperature distribution due to radiation for a cylinder. The effect of finite current depth is also accounted for.

### 3.2.2.3 Effect of Power Input Change

The power input to the billet will be modified by three factors. When the billet emerges from the coil (or in a part of the coil where the power input is only sufficient to overcome radiation losses) the temperature distribution  $\theta=f(r)$  begins to equalize. This soaking period may be represented by the equation [26],

$$\theta_r = \frac{2}{R^2} \left[ \int_0^R r f(r) dr + \sum_{n=1}^{\infty} \exp(-\alpha_n^2 \tau) \frac{J_0(\alpha_n R/R)}{J_0^2(\alpha_n)} \int_0^R r f(r) J_0(\alpha_n r/R) dr \right] \quad (3.18)$$

The transient (  $\sum$  ) term describes the diminution of the temperature differential towards the final uniform temperature, represented by the integral. Figure 3.6 shows the normalized surface and centre temperatures

with time for a parabolic initial distribution, with the asymptote at the mean value of  $(\theta_s + \theta_c)/2$ .

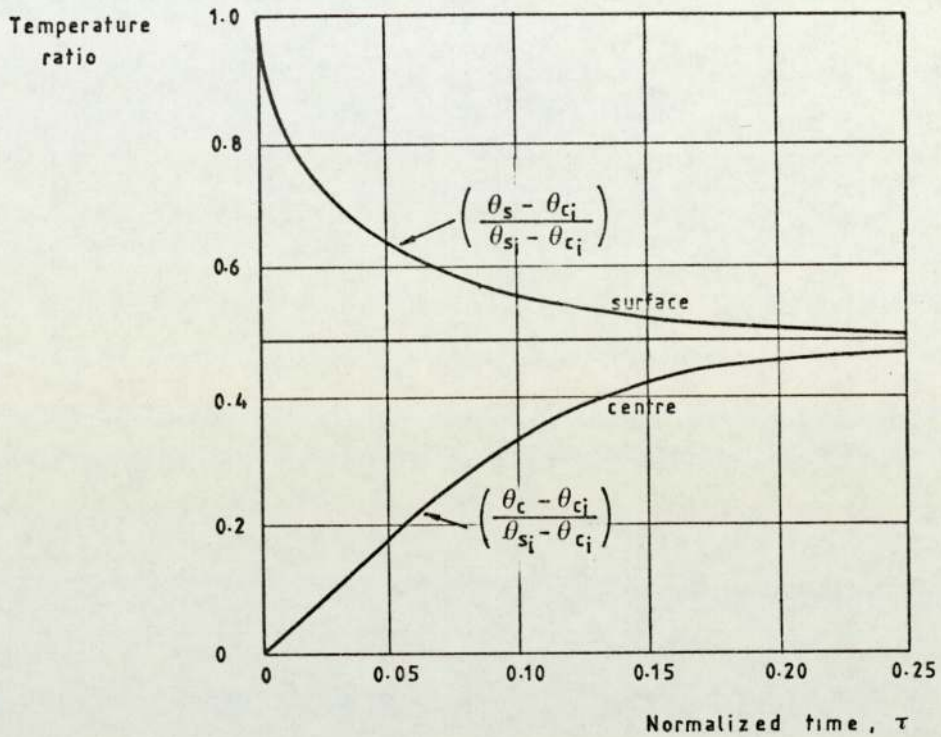


FIGURE 3.6: Variation of surface temperature  $\theta_s$  and centre temperature  $\theta_c$  during soaking period.  $\theta_{si}$  and  $\theta_{ci}$  are the initial temperatures of the parabolic distribution. (Also Appendix 2)

The second change, in multi-section coils, occurs when the power input will alter as the billet progresses from one section to another. Appendix 2 derives the mathematical equations to describe this change and shows graphically the temperature profile with time. The effect is somewhat complex but may be considered as a superposition of a transient rise, according to



equation (3.11), with the new power density over a soaking period of the temperature profile of the original section.

The third major power input density change occurs during the Curie transition. When a portion of the metal becomes non-magnetic, the power loss falls dramatically. This is extremely difficult to describe quantitatively since the surface regions of the billet become non-magnetic before the interior, which is still absorbing power at the below-Curie rate. The effect may be visualized by imagining a high power input band of thickness equal to the skin depth  $\delta$ , passing from the billet surface to the centre as the region outside the band exceeds the Curie temperature. In practice a soak period for a transition time  $t_{\text{curie}}$  is defined [18] as

$$t_{\text{curie}} = \frac{(\text{Energy for Magnetic Transition}) R}{2 \mathcal{P}'_1} \quad (3.19)$$

where  $\mathcal{P}'_1$  is the super-Curie power density to the billet.

Heat transfer theory has also been applied to calculations for the water cooling of the induction coil itself. Much experimental work has been done to verify the well-established theory. The coil designer need only refer to standard works [27,28] on fluid flow to find graphs of the water quantity required to give a desired rate of cooling

for most tube shapes and dimensions. Care must be exercised to ensure that the pressure drop in the water cooling circuits is not excessive and that the cooling paths are arranged so that sufficient coil surface area is presented to the water.

### 3.3 Equivalent Circuit Coil Design Method

In section 3.2.1 the workload r.m.s. flux  $\phi_w$  was stated,

$$\phi_w = \mu H_{pm} A_w (q - j p) \quad (3.7)$$

In practical coils, not all the flux is linked solely with the workload and the coil; some appears within the air-gap of even the most closely coupled coils. The total flux  $\phi_o$  is the sum of the total workpiece flux  $\phi_w$ , coil flux  $\phi_c$  and air-gap flux  $\phi_g$ , shown in figure 2.1. Davies and Simpson [18], page 44, show that the remaining terms may be written,

$$\phi_c = \frac{k_r \mu_o \delta_c (\pi d_c)}{2} H_{pm} (1 - j) \quad (3.20)$$

\*  $k_r$  is a correction factor that allows for the spacing between the coil turns.



and 
$$\phi_g = \mu_o H_{om} A_g \quad (3.21)$$

where

$$H_{om} = \sqrt{2} \frac{I_c N_c}{l_c} \quad (3.22)$$

$\delta_c$  and  $d_c$  are the coil penetration depth and diameter, respectively. Since the r.m.s. coil voltage is given by

$$E_c = j \frac{2\pi f N_c \phi_o}{\sqrt{2}}$$

by substitution and collecting terms, this may be written as

$$E_c = \frac{2\pi f \mu_o N_c^2 I_c}{l_c} \left\{ \left( \mu_r p A_w + \frac{\pi k_r d_c \delta_c}{2} \right) + j \left( A_g + \mu_r q A_w + \frac{\pi k_r d_c \delta_c}{2} \right) \right\} \quad (3.23)$$

It has been common practice, following Baker [23], Vaughan and Williamson [29,30] to represent equation (3.23) by an equivalent series circuit where the coil and workload resistances and reactances  $R_c$ ,  $R_w$ ,  $X_c$ ,  $X_w$  and air-gap reactance  $X_g$  are given by

$$\left. \begin{aligned} R_w &= K (\mu_r p A_w) \\ R_c &= K (k_r \pi d_c \delta_c / 2) \\ X_g &= K A_g \\ X_w &= K (\mu_r q A_w) \\ X_c &= K (k_r \pi \delta_c d_c / 2) \end{aligned} \right\} \quad (3.24)$$

where

$$K = (2\pi f \mu_o N_c^2 / l_c)$$

and

$$Z^2 = (R_w + R_c)^2 + (X_g + X_w + X_c)^2$$

As the physical analogy of the equivalent circuit is the subject of some debate for coil design, only the basic equations (3.24) will be used here.

It is a simple matter to calculate the major coil properties from the above. Coil efficiency  $\eta$  is given by

$$\eta = \frac{R_w}{R_c + R_w} \quad (3.25)$$

Coil power factor,  $\cos \phi$ , given by

$$\cos \phi = \frac{R_w + R_c}{Z} \quad (3.26)$$

is used for calculating the capacitive load required to match the coil and workload to the electrical supply. Coil power  $P_c$  is found from the workload power  $P_w$  which is the power required to heat the metal to temperature (see section 3.4)

$$P_c = \frac{P_w}{\eta} \quad (3.27)$$

Coil volt-amps  $(VA)_c$  is given by

$$(VA)_c = \frac{P_c}{\cos \phi} = I_c^2 Z \quad (3.28)$$

Coil volts per turn  $E_c/N_c$  and r.m.s. ampere-turns  $I_c N_c$  follow,

$$\left. \begin{aligned} E_c/N_c &= \sqrt{(VA)_c Z/N_c^2} \\ I_c N_c &= \sqrt{\frac{(VA)_c}{Z/N_c^2}} \end{aligned} \right\} \quad (3.29)$$



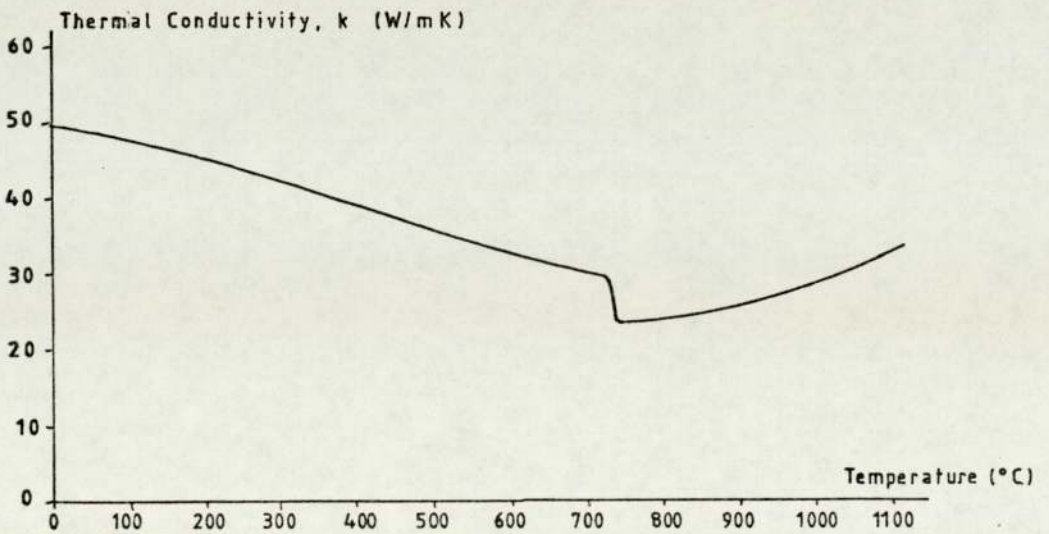
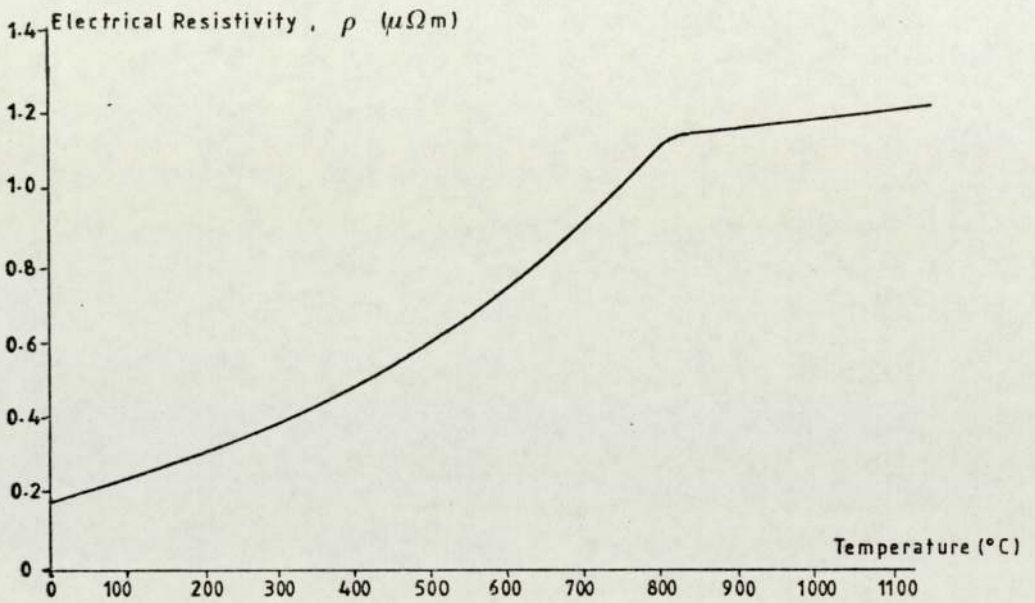
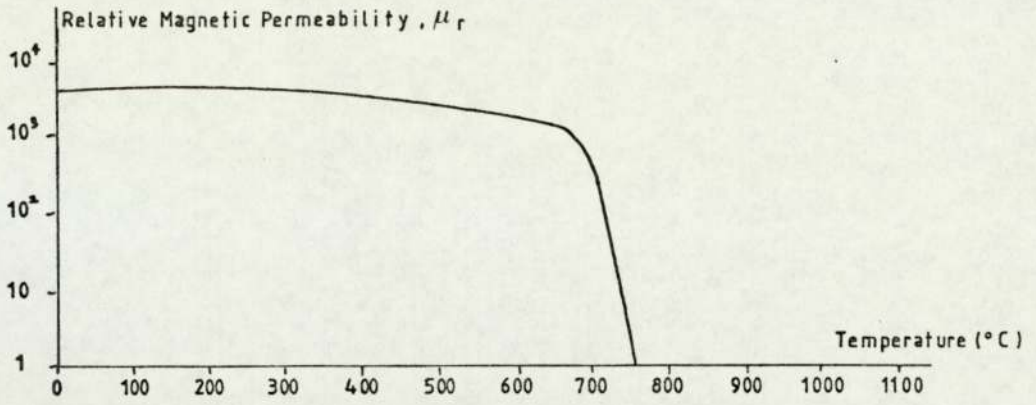


FIGURE 3.7: Physical properties of solid (En8) steel with temperature  
 a) Relative Magnetic permeability  $\mu_r$  b) Electrical Resistivity  $\rho$  and c) Thermal Conductivity  $k$ . See p49.

The coil dimensions and heater connections may now be calculated with the power requirements from the electrical supply. The following section gives an example of this design method for a G.K.N. production coil.

### 3.4 Example of Equivalent Circuit Coil Design

Numerical values for the example are given in tables 3.1 and 3.2. The two section coil heats billets of 51 mm (2") diameter and is also used later in this study (see Chapters 6 and 7).

#### 3.4.1 Initial Specifications

For through-heating, the required through-put, the dimensions and physical properties of the workload and the temperature rise in each section are needed. The physical properties  $\rho$ ,  $k$  and  $\mu$  for steel are given with temperature in figure (3.7). The electrical resistivity is usually taken as the mean integrated value\* over the coil section temperature range. The power per tonne over the temperature rise required may be found from the heat content, plotted in figure 3.8.(p52)

\* The integrated resistivity  $\rho_m$  is found from the corresponding values  $\rho_1$  and  $\rho_2$  over the temperature range and given [18] by

$$\rho_m = \frac{\{\sqrt{\rho_2} + \sqrt{\rho_1}\}^2}{4} \quad (3.30)$$



ITEM	QUANTITY	METHOD OF CALCULATION	VALUE	UNITS
1	Required Through-put		245	kg/h
2	Billet Mass		0.613	kg
3	Billet Length, $l_w$		38	mm
4	Billet Diameter, $d_w$		51	mm
5	Metal Density, $\rho_w$	$(2)/((3) \times \frac{\pi}{4} (4)^2)$	7860	kg/m <sup>3</sup>
FIRST SECTION - Sub Curie				
6	Temperature Rise	20°C to 760°C	740	K
7	Maximum $\theta_s - \theta_c, \Delta\theta$		310	K
8	Metal Resistivity, $\rho_w$	equation (3.30)	0.57	$\mu\Omega\text{m}$
9	Kilo-watt hrs/tonne	fig. 3.8	137	kWh/t
10	Work Power, $P_{w1}$	(9).(1)	33.5	kW
11	Frequency, $f_1$	supply available	4	kHz
12	Relative Permeability, $\mu_r$	estimate	11	
13	Penetration Depth, $\delta_w$	equation 2.1	1.81	mm
14	$d/\delta$	(4)/(13)	28.15	
15	Power Density, $\mathcal{P}_o$	eqn. 3.17 & (7)	728	kW/m <sup>2</sup>
16	Minimum surface area	(10)/(15)	$4.6 \times 10^{-2}$	m <sup>2</sup>
17	Minimum Length	(16)/ $\pi$ .(4)	0.287	m
18	No. of Billets	(17)/(3)	7.5~8	
19	Billet Heating Time	(18).(2).3600/(1)	72	secs
CURIE TRANSITION				
20	Transition Time	Fig. 3.8	8.8	secs
SECOND SECTION - Super Curie				
21	Temperature Rise	(1250°C-760°C)	490	K
22	Maximum $\theta_s - \theta_c, \Delta\theta$		75	K
23	Resistivity, $\rho_w$	equation 3.30	1.18	$\mu\Omega\text{m}$
24	Kilo-watt Hrs./t	fig. 3.8	100	kWh/t
25	Work Power, $P_{w2}$	(24)x(1)	24.5	kW
26	Frequency, $f_2$	supply available	4	kHz
27	Relative Permeability, $\mu_r$	equation 2.1	8.64	mm
28	$d/\delta$	(4)/(27)	5.9	
29	Ratio of $\theta_s - \theta_c$ to ideal	Fig. 3.4	0.75	
30	Power density, $\mathcal{P}_o$	equation 3.17	460	kW/m <sup>2</sup>
31	Radiation Power Density $\mathcal{P}_r$	(22).(29)	97	kW/m <sup>2</sup>
32	Minimum Surface Area	(25)/((30)+(31))	$4.4 \times 10^{-2}$	m <sup>2</sup>
33	Minimum Length	(32)/(4). $\pi$	0.275	m
34	No. of Billets	(33)/(3)	7.3~8	
35	Billet Heating Time	(34).(2).3600	72	secs
SUMMARY				
36	Total Heating Time	(19)+(20)+(35)	153	secs
37	No. of Billets/Hour	$((18)+(34)).3600$ (36)	377	1/h
38	Actual Through-put	(37)x(2)	231	kg/h
39	Total No. of Billets in coil	(18)+(34)	16	
40	Power Density Total	(15)+(30)+(31)	1285	kW/m <sup>2</sup>
41	Total Work Power	(40). $\pi$ .(4).(39)(3)	125	kW
42	Billet Speed	(1)/( $\frac{\pi}{4}(4)^2$ ).(5)	4.24	mm/sec
43	Active Length, 1st section	(42).(19)	30.5	mm
44	Active Length, 2nd section	(42).((35)+(20))	34.25	mm
45	Coil Internal Diameter	(4)&Table 2.3,ave.	10.3	mm
46	Work Power, 1st section	(15).(43).(4)	35.5	kW
47	Work Power, 2nd Section	(30).(44).(4)	35.25	kW

Table 3.1 : Worked Example of coil design (section 3.4) for a two-section series-connected production coil specification.

### 3.4.2 Solution

The frequency is chosen from table 2.2 and the recommended air-gap from table 2.3. The thermal power is found from the coil through-put and the power per tonne required. The maximum allowable temperature differential defines the power density which is found from section 3.2.2.1, allowing for the finite current depth, and subtracting radiation losses according to section 3.2.2.2, equation 3.16. From the power density and the thermal power, a minimum heated area is calculated and thus a coil minimum length. Due allowance is made for the Curie transition by including a period calculated from equation 3.19, using the transition energy indicated by figure 3.8. The billet heating time follows and the total power to the workload  $P_w$  then found. Final coil diameters may be estimated from table 2.3.



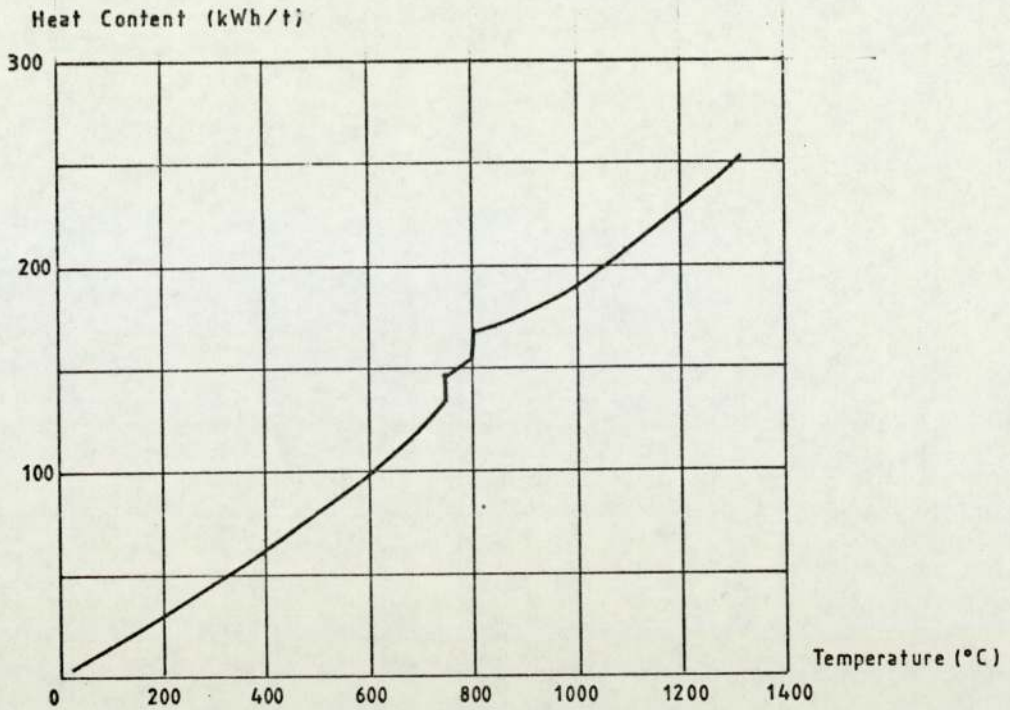


FIGURE 3.8: Specific heat capacity for (En8<sup>\*</sup>) steels, from 20<sup>o</sup>C.

\* Note:- British standards (B.S.970, 1950) En8 steel is superseded by B.S. 970: 1972: 080M40 specification.

Taking the data above, the equivalent circuit method follows, for calculation of the coil variables. Due regard for available power supplies may influence the choice of supply frequency, voltage and current.

For ferrous materials an immediate problem arises in calculating the equivalent impedances below the Curie temperature; in that a value of  $\mu_T$  is needed for  $R_w$  and  $X_w$ . The coil current however, and hence the magnetic field  $H$ , upon which  $\mu$  is dependent (equation 3.29), has yet to be derived. In practice the calculations of equations 3.24 to 3.29 are iterated with various initial  $H$  values until agreement is achieved.

ITEM	QUANTITY	METHOD OF CALCULATION	VALUE	UNITS
<b>FIRST SECTION - Sub-Curie</b>				
1	Magnetic Field, $H_{om}$	estimate	105	KA/m
2	Work Penetration Depth, $\delta_w$	Table 3.3, (13)	1.81	mm
3	Coil Penetration Depth, $\delta_c$		1.20	mm
4	p and q values	figure 3.2	p=0.068	
5	Work Resistance/Turn <sup>2</sup>	equation 3.24	q=0.071 K. $1.53 \times 10^{-3}$	$\Omega$
6	Coil Resistance/Turn <sup>2</sup>		K. $2.59 \times 10^{-4}$	$\Omega$
7	Coil Reactance/Turn <sup>2</sup>		K. $2.59 \times 10^{-4}$	$\Omega$
8	Work Reactance/Turn <sup>2</sup>		K. $1.56 \times 10^{-3}$	$\Omega$
9	Gap Reactance/Turn <sup>2</sup>		K. $6.23 \times 10^{-3}$	$\Omega$
10	K Factor		$0.104 \cdot N_c^2$	$\Omega/m^2$
11	Total Impedance, Z	equation 3.24	K. $8.0 \times 10^{-2}$	
12	Coil Efficiency, $\eta$	equation 3.25	0.856	
13	cos $\phi$	equation 3.26	0.215	
14	Coil Power, $P_{c1}$	equation 3.27	39.1	kW
15	Coil Volt-Amps	equation 3.28	182	KVA
16	Coil Volts per Turn	equation 3.29	12.6	V
17	Coil Amp-Turns	equation 3.29	14.5	KA
<b>SECOND SECTION - Super Curie</b>				
18	Work penetration Depth, $\delta_w$		8.64	mm
19	p and q values	figure 3.2	p= 0.28 q= 0.33	
20	Work Resistance/Turn <sup>2</sup>	equation 3.24	K. $5.72 \times 10^{-4}$	$\Omega$
21	Coil Resistance/Turn <sup>2</sup>		K. $2.76 \times 10^{-4}$	$\Omega$
22	Coil Reactance/Turn <sup>2</sup>		K. $2.76 \times 10^{-4}$	$\Omega$
23	Work Reactance/Turn <sup>2</sup>		K. $6.74 \times 10^{-4}$	$\Omega$
24	Gap Reactance/Turn <sup>2</sup>		K. $6.23 \times 10^{-4}$	$\Omega$
25	K Factor		$0.100 \cdot N_c^2$	$\Omega/m^2$
26	Total Impedance, Z	equation 3.24	K. $7.31 \times 10^{-2}$	
27	Coil Efficiency, $\eta$	equation 3.25	0.675	
28	cos $\phi$	equation 3.26	0.116	
29	Coil Power $P_{c2}$	equation 3.27	36.3	kW
30	Coil Volt-Amps,	equation 3.28	313	kVA
31	Coil Volts per Turn	equation 3.29	15.1	V
32	Coil Amp-Turns	equation 3.29	20.7	kA
33	Ratio of Voltages	$= (P_{c1}/P_{c2})$	1.07	
34	Generator Voltage		340	V
35	Coil Total Voltage	(34)-transmission loss 5%	323	V
<b>SUMMARY</b>				
36	Volts Drop for section		$V_1 = 167$	V
37		(35) = $V_2 + 1.07V_2$	$V_2 = 156$	V
38	No. of Turns in 1st sect.	(36)/(16)	13	
39	No. of Turns in 2nd sect.	(37)/(31)	10	
40	Coil Current, 1st Section	(17). (13)/(38)	240	V
41	Coil Current, 2nd section	(32). (28)/(39)	240	V

Table 3.2 : Equivalent circuit calculations for the two-section production coil design of Table 3.1, described in section 3.4.



The equivalent circuit is repeated for both sections and compared with the supply voltage (less 5% for transmission losses in the connections between motor-alternator, heater and coil) to give the coil turns. Consideration of the coil cooling then dictates the coil tube cross-section to be used. For optimum electrical efficiency, the combined coil and work volt-amps should share the same phase angle as the electrical supply e.g., Midlands Electricity Board (M.E.B) power factor,  $\cos \phi = 0.98$  lagging [31]. Before correction the coil represents

$$(\text{kVAR})_T = \sqrt{(\text{VA}_c)_T^2 - (\text{P}_c)_T^2} \quad (3.31)$$

of lagging reactive power, as shown in the phase diagram in figure 3.9, where the T suffix represents the totals for all coil sections. Capacitors\* are needed [31] to alter the electrical load presented to the supply to give, after correction,

$$(\text{kVAR})'_T = (\text{P}_c)_T \tan(\cos^{-1} 0.98) \quad (3.32)$$

of lagging reactive power.

\* If the correction capacitors are rated at  $V_1$  volts and  $f_1$  hertz and used at a lower  $V_2$  voltage and  $f_2$  frequency then they should be derated, according to the formula

$$(\text{kVAR})_{V_2, f_2} = (\text{kVAR})_{V_1, f_1} \cdot \left[ \frac{V_2}{V_1} \right]^2 \cdot \left[ \frac{f_2}{f_1} \right] \quad (3.33)$$

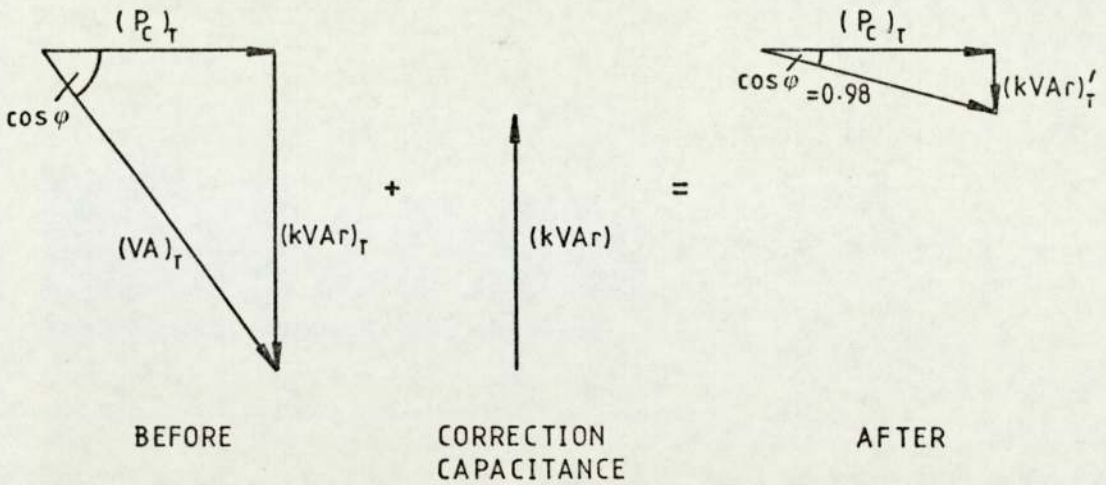


FIGURE 3.9: Phase diagram of power factor correction.

### 3.5 Discussion of the Coil Design Method

As an approximate method of coil design, the equivalent circuit method and associated calculations (Tables 3.1 and 3.2) provide the designer with a ready tool for practical purposes. This approach is of limited value to understanding the physical reality of billet heating however, due to the assumptions made. Although the temperature profile has been shown to rise parabolically, design calculations assume that the billet temperature is uniform at the start and end of each coil section. This supposition introduces errors in calculating the material properties in force at a particular position and time. The work power, and hence coil length and heating time, is also erroneous since parts of the billet are above the assumed end temperature.



VERTICAL COIL DESIGN FOR 51mm DIAMETER BILLETS TO  
MATCH 150kW, 340V, 4000Hz MOTOR ALTERNATOR

Coil Length	0.610m
Copper internal diameter	0.103m
Refractory internal diameter	0.060m
Inside of guide rails at diameter	0.572m

First coil section 30.5cm long, 13 turns of 19mm by 9.5mm high conductivity copper tube, wound flat.

Second coil section 30.5cm long, 9 turns of 25mm by 11mm high conductivity copper tube, wound flat.

Anticipated operating conditions

340 volts, 140kW, 350kg/hr of 51mm diameter steel heated to 1250°C.

Capacitors 120 kVAr at 400 volts.

Table 3.3 : Two-section production coil specification for 350 kg/hr through-put used as a coil design example in section 3.4 for a 245 kg/hr through-put. See p57.

The material electrical and thermal properties vary with temperature, but are incorporated in the calculations using mean values. The maximum surface-to-centre temperature difference,  $\Delta\theta$  however, will be exceeded when the thermal conductivity falls below the mean value. The designer must ensure that the maximum value of  $\Delta\theta$  is a sufficiently conservative estimate.

The Curie transition is not well represented by the simple inclusion of a heating time to allow the metal to absorb the transition energy. The calculation method also assumes that the whole billet is at uniform Curie temperature at the start of the second section. In practice, the billet surface achieves super-Curie temperatures before the centre and continues to absorb power in the first coil section at a rate, which is not calculated, while the remainder of the billet becomes non-magnetic. Davies and Simpson give experimental and theoretical evidence for modifying the power absorbed in the work load, to account for the non-linear relationship between H and B for magnetic materials. For a sub-Curie coil, multiplication by the factor 1.47 gives good results but the value of this factor, for coil sections where heating both below and above the Curie point occurs, is unclear.

The production coil, from which the initial values of Table 3.1 were taken, is specified for a through-put of 350 kg/hr in table 3.3.



Comparisons between the calculated and true performances follow.

The calculated dimensions compare well to the actual values. Coil section lengths are exact, apart from a calculated 37.5mm length for the Curie transition in the second section. The number of coil turns differs only by one in the second section, also caused by the Curie approximation. This also accounts for the slight difference in calculated and specified heating times and through-put. The air-gap is within the range specified in table 2.3 at the average billet temperature.

The ratio of coil power to the specified value for 350 kg/hr through-put is within 7% of the coil current and  $(VA)_T$  ratios. It is interesting to note that the first section efficiency is far higher than that of the second coil section. However,  $\eta$  would be significantly improved if ratio  $d/\delta$  were to be reduced from its high value of  $d/\delta \approx 28$  towards the optimum (equation 2.2) by using a more suitable frequency (table 2.2) for sub-Curie heating. Power factor correction of 475 kVAr is provided by capacitors rated 730 kVAr at 400 volts, 4kHz.

### 3.6 Concluding Summary

The discussion of this and the previous chapter gives an introduction to induction heating and the theoretical principles related to coil design methods in current use. The mathematical basis of induction heating for simple billets has been examined and the derivation of magnetic flux equations developed towards a calculation method for coil design. A calculated example of a GKN production coil design shows that calculated values are in general agreement with practical results but at variance where the billet becomes non-magnetic. The method is limited in accuracy, depending on the applicability of the assumptions for a particular case. As presented in the literature, no calculation method adequately accounts for multi-sectioned coil design for through-heating of steel billets with relevance to the physical nature of the heating process and changing material properties. Further consideration to this problem is given in Chapters 6 and 7 for induction heating of both solid and sintered billets. This follows after an introduction to powder-forging in Chapter 4 and discussion of the properties of sintered parts (Chapter 5).



CHAPTER FOUR

AN INTRODUCTION TO POWDER FORGING

## CHAPTER 4 : AN INTRODUCTION TO POWDER FORGING

### 4.1 Introduction

The behaviour of the metal workload in induction heating has been described in Chapter 2. To recapitulate, when alternating current is passed through the electrical circuit of the induction coil a magnetic field is established in the coil vicinity. An induction field  $B$  is induced in a workload placed within the coil, such that

$$B = \mu H \quad (4.1)$$

where the permeability  $\mu$  describes the concentration effect of the workload. This constant of the workload material is often related to that of free space  $\mu_0$  by the relative magnetic permeability  $\mu_r$ ,  $\mu = \mu_r \mu_0$ . Where different magnitudes of  $B$  are present in nearby areas of the workload, voltage differences occur. The form of Ohm's law,  $E = \rho J$ , describes the subsequent current density distribution in the material, subject to the natural resistance to current flow, the electrical resistivity  $\rho$ . The energy loss density  $\bar{W} (W/m^3)$  in overcoming this flow,

$$\bar{W} = J^2 \rho \quad (4.2)$$

appears as heat in the workload.

Conduction of heat energy from the surface through the medium is governed by the temperature gradient present, and the thermal conductivity  $k$  of the material. The quantity  $1/k = \sigma_k$ , i.e. the thermal resistivity, is the heating analogy for  $\rho$ . To avoid any



possible confusion with  $\rho$  , throughout this work 'conductivity' always refers to thermal, and 'resistivity' to electrical quantities.

Thus, three physical properties of the material control the induction heating process, the relative magnetic permeability,  $\mu_r$ , electrical resistivity  $\rho$  and thermal conductivity  $k$  . For induction heating calculations it is important to define these properties, their dependence on temperature and their relationship with the physical structure of the heated material. Chapter 3 has shown how this information is used at present for solid material heating where these properties are well known in the literature.

The production process itself alters both the chemical composition of powders and their physical structure. The purpose of this chapter is threefold. First, section 4.2 presents an introductory outline of the major methods of powder manufacture and powder compact production [32,33]. Next, Section 4.3 considers each stage in detail with specific reference to its influence on the named properties. Finally, section 4.4 defines the range of GKN (steel) powder types and compacts, and the physical variables that may be expected to govern their properties.

In conclusion, it is clear that the vital information on properties depends on a wide variety of factors related specifically to powder materials.

Values of  $\rho$  ,  $k$  and  $\mu$  are greatly influenced by the size, shape and composition of the particles forming the structure. The production route is instrumental in determining these characteristics.



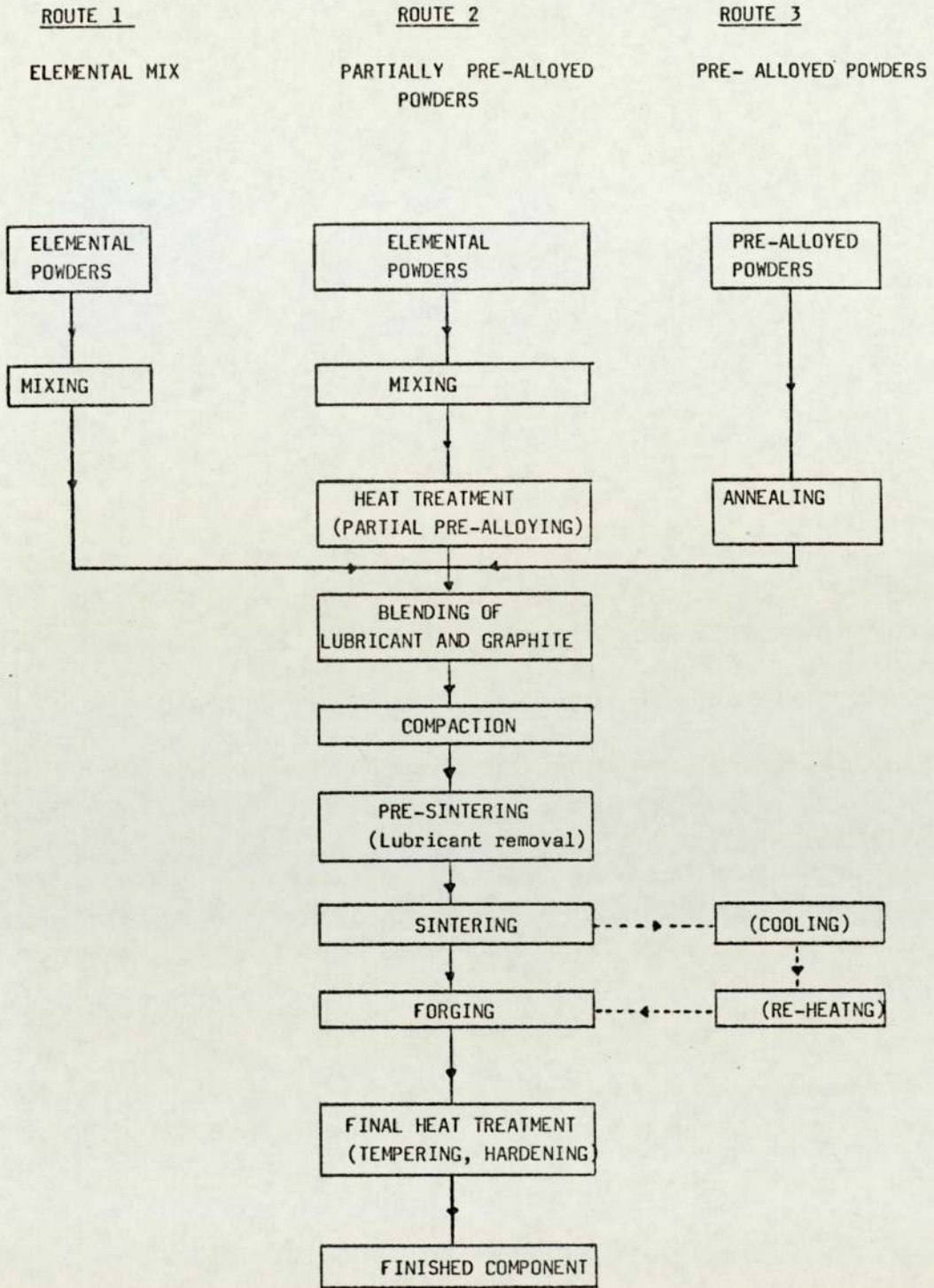


Figure 4.1 : Production routes for powder-forging steel parts. See p 65.

## 4.2 Powder and Compact Production

Manufacture of powder metal components may be summarized by the flow chart of figure 4.1. Three routes (sections 4.2.1 - 4.2.3) exist for producing the metal powder alloy, depending on the initial degree of homogeneity of constituents desired.

### 4.2.1 Elemental Mix

The simplest method consists of blending powders of different elements and sizes in large double-cone or 'Y' mixers. Mixing times are varied, depending on the range of particle sizes present, to ensure a powder with uniformly distributed constituents.

### 4.2.2 Partially Pre-alloyed Powders

In this route, the elemental mix is further treated by heating in a reducing atmosphere, to allow limited diffusion of the constituent elements between adjacent powder particles.

### 4.2.3 Fully Pre-alloyed Powders

Steel powders are produced by water atomization. Metal of the required chemical composition is melted and fed at controlled speed through a nozzle of precise size. Water jets aimed below the nozzle break the molten metal stream into droplets (atomization), which solidify into particles as they fall. Control of the nozzle size, metal temperature



and water jet flow rate gives powder particles of the required size. Fully pre-alloyed powders offer complete chemical homogeneity of each particle, but suffer from poor compressibility\* due to powder hardness. Poor compactability results due to oxidation from the water jets. A subsequent annealing stage softens the powder to improve compressibility, and if performed in an oxide reducing atmosphere, improves compactability. After powder manufacture, the production stages are common to all three powder routes shown above.

The powder is blended with carbon in the form of graphite, to give the required final carbon content, allowing for some decarburization that may take place during sintering. A lubricant, usually Zinc Stearate powder, is ad-mixed # to reduce inter-particle and die-wall friction. This improves powder flow into the die and eases ejection of the compact.

Conventional die compaction generally utilizes a double action method by "floating" the die on springs. Thus, a portion of the downward force on the top punch is re-directed upwards through the bottom punch to give a

\* For a given compaction pressure, the higher the final density the greater is the compressibility.

# For high compressibility powders, or where higher pressure may be used, lubricant is also sprayed directly onto the die walls rather than blended with the powder.

more uniform density distribution within the compact. The process consolidates the powder into a compact of the desired shape and approximate dimensions, with sufficient strength to facilitate handling.

De-waxing, i.e. heating at low temperature, follows to evaporate the stearate compaction lubricant from the compact. The main sintering stage occurs at high temperature, generally at about two thirds of the alloy melting temperature, in a protective atmosphere.

Sintering [34] is often the final stage of component production, where sufficient mechanical properties are developed, or for applications, where the residual porosity of 10-15% is acceptable, and accuracy of dimensions and surface finish are adequate.

Mechanical strength is significantly improved by a forging operation [35,36]. Forging may follow directly after sintering, or after cooling and reheating, and imparts the final shape and density to the part. This ensures that mechanical strength and tolerances of the component are met.

The final heat treatments, involving quenching, tempering or hardening of components are performed in protective atmospheres.





### 4.3 Influence of Production Stages on Properties

The physical changes occurring during each stage are summarized in the following sub-sections 4.3.1 - 4.3.5 under appropriate headings. Included in each is an indication of the influence on the electromagnetic and thermal properties  $\mu$ ,  $\rho$  and  $k$ .

#### 4.3.1 Powder Production

Some heterogeneity will be present in the composition of elemental mix and partially pre-alloyed powders, but thorough mixing minimizes any variations in properties caused by this. Fully pre-alloyed powders are chemically homogeneous and isotropic. No variation in properties will occur as there are no differences in the distribution of alloying constituents.

Initial values of  $\mu$ ,  $\rho$  and  $k$  are controlled by particle shape and size distribution. Mixing may alter this distribution by fracturing, rounding and smoothing and agglomeration of particle surfaces. Electrical and thermal continuity is provided by areas where adjacent particles touch. Both electrical resistivity and thermal conductivity will be determined by the size, nature and number of inter-particle contacts allowed by the packing structure within the powder.

The number of interparticle contacts depends on the range of particle sizes present and the shape of these particles.

A small range of rounded particles will not cohere as well as a more irregular arrangement with a large size range, where small particles may fill the spaces between large ones.

Non-spherical shapes increase the size of the particle contact areas, especially if the shapes have irregular surfaces. Thermal and electrical contact, through the contact areas, may be degraded by oxide film created on the particle surfaces on exposure to air. Magnetic permeability is a more macroscopic phenomenon which depends on the shape and orientation of the particles, and also the overall density of the material.

#### 4.3.2 Lubricant and Graphite Blending

The addition of lubricant further reduces particle-to-particle contact by effectively coating each particle with a non-conductor. Added carbon may alter the packing density, and particle contact depending on the size and shape of the graphite particles.

#### 4.3.3 Compaction

Consolidation of the powder enlarges areas of particle contact bonding, as prominent lobes are fractured. The surface oxide films rupture and the particles deform and interlock. The bulk movement and interlocking results in a denser, more efficient powder packing. The number of contact areas is increased



as the average particle co-ordination number\* rises with densification.

The compaction process increases the bulk density of the powder towards that of the solid material. Porosity reduction therefore alters  $\rho$ ,  $\mu$  and  $k$  closer to the solid material properties. The degree and distribution of porosity after compaction is related to the powder characteristics of particle size and shape, compressibility and friction coefficient. Other factors include variable-compaction pressure, press design and finally die shape. Surface oxide film is removed by interparticle abrasion and plastic deformation during pressing. Clean metal areas produced by plastic deformation will be protected from further oxidation. The electrical resistivity of the 'green' unsintered compact will be significantly reduced, and the thermal conductivity increased, by the removal of the high-resistance oxide coating.

#### 4.3.4 Sintering

Sintering influences the electrical and thermal properties through a) the variation of  $\rho$  and  $k$  with temperature and sintering temperature, and b) the change in character of the interparticle bonds previously established. Graphs of

\*This is defined as the average number of particles that are in contact with any selected individual particle.

thermal conductivity and electrical resistivity with temperature are well known for solid materials (figure 3.7).

Atomic diffusion between particles occurs, increasing bonding of adjacent particles, to give a higher degree of integrity to the material. Atomized carbon diffuses rapidly into the steel during the early stages of heating, so producing the chemical composition required.

The newly-formed bond areas between particles, necks, grow as material is transported to the neck growth sites. However, no change in the porosity distribution, or continuity, occurs until this process reaches the stage where pores become closed and the nature of the porosity is discontinuous and more rounded. As sintering continues, pore shrinkage results in the elimination of small isolated pores. The rate of increase in volume of large pores diminishes. This changes the pore distribution and therefore the electrical and thermal paths, but may not be sufficient to make a major contribution to bulk material properties.

Densification occurs as large pores shrink, decreasing the powder air-gaps, thus altering  $\rho$ ,  $\mu$  and  $k$  towards the values for solid metal.



Powder Type No.	CHEMICAL ANALYSIS OF ELEMENTAL COMPOSITION (Wt%) + IRON to 100%									
	CARBON	SILICON	PHOSPHORUS	SULPHUR	CHROMIUM	MOLYBDENUM	NICKEL	MANGANESE		
W4	Specification	0.35-0.45	0.01-0.015	0.01-0.02	0.025-0.035	0.1-0.26	0.25-0.35	0.2-0.3	0.3-0.4	
	Typical		0.01	0.013	0.025	0.19	0.28	0.25	0.36	
W135	Specification	0.17-0.23								
	Typical	0.2 or 0.26	0.02 max	0.02 max	0.01-0.02	0.15 max	0.55-0.65	0.4-0.5	0.25-0.35	
W32	Specification	0.18-0.24								
	Typical	or 0.22-0.3	0.01	0.012	0.014	0.12	0.6	0.5	0.26	
W78	Specification	0.17-0.23	0.02 max	0.02 max	0.02-0.03	0.25-0.35	0.25-0.35	0.2-0.3	0.4-0.5	
	Typical	or 0.2-0.26	0.01	0.015	0.018	0.35	0.27	0.25	0.44	
			0.015 max	0.02 max	0.01-0.015	0.1 max	0.45-0.55	1.8-2.2	0.25-0.35	
			0.01	0.012	0.014	0.08	0.53	1.9	0.29	

SCREEN ANALYSIS	MESH NO.	MESH SIZE ( $\mu\text{m}$ )	WEIGHT (%)
(Typical results for W4 material)	+65	+208	0.01
	+80	+175	0.1
	+100	+147	2.4
	+150	+104	27.6
	+200	+74	22.9
	+325	+43	24.3
	-325	<43	22.7

Table 4.1 : G.K.N. powder chemical compositions and typical particle size distribution [35].

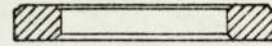
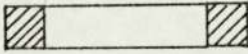
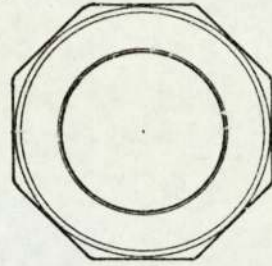
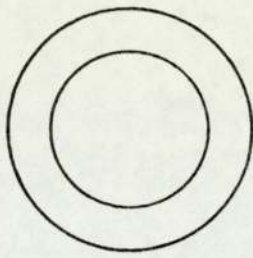
#### 4.3.5 Forging

Further densification to approximately 99% of theoretical density may occur at this stage. The forging process is used to achieve optimum mechanical properties.

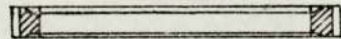
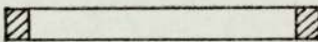
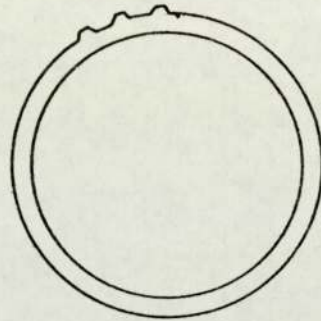
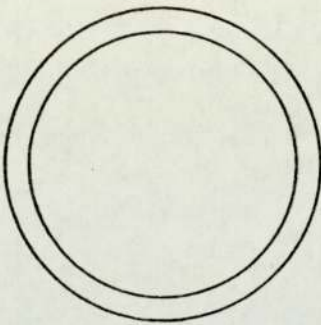
#### 4.4 G.K.N. Powders and Powder Compacts

The Powder-Forging division uses low carbon, fully pre-alloyed powder steels (route 3, fig 4.1) with varying proportions of additional elements - manganese, sulphur, phosphorus etc. Four major powder compositions may be identified with typical particle size distribution as shown in table 4.1. Each trace element is incorporated to improve mechanical or physical properties of the compact [37,38].

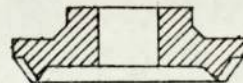
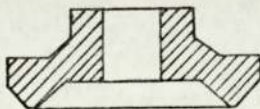
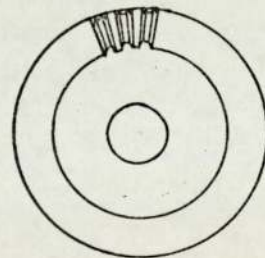
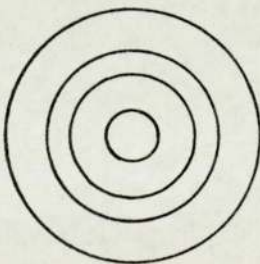




F325



F396



F350

Horizontal and Vertical Scale  
0 25 50 75 100 mm  
10 20

FIGURE 4.2: Typical range of G.K.N. preform shapes with the corresponding finished part.

Before compaction, varying additions of carbon are added to these four powders, together with 1% by weight lubricant. Compacted green compacts, preforms, are made in various forms depending on the final component. For most gear parts the preform is of the same approximate shape but without gear teeth and over-size in thickness. Other parts, rings and discs are about 10% oversize. Figure 4.2 indicates the range of preform shapes in production. Density measurements of compacted 'green' preforms appear in figure 4.3. Density variation within the preform is approximately 15%, and the average density is 75% of solid metal (Details in Appendix 1). Measured density after sintering shows a 5% - 10% change under typical sintering conditions e.g. heating in a controlled atmosphere at 1150<sup>0</sup>C, using an endogas mix, for 300 seconds.

Figure 4.4. shows a scanning electron microscope photograph of a typical powder batch. Note the irregular shape, size range and lobed surfaces present.

Compaction in the forging press results in parts of over 99% of theoretical density with the typical mechanical properties of Table 4.2.



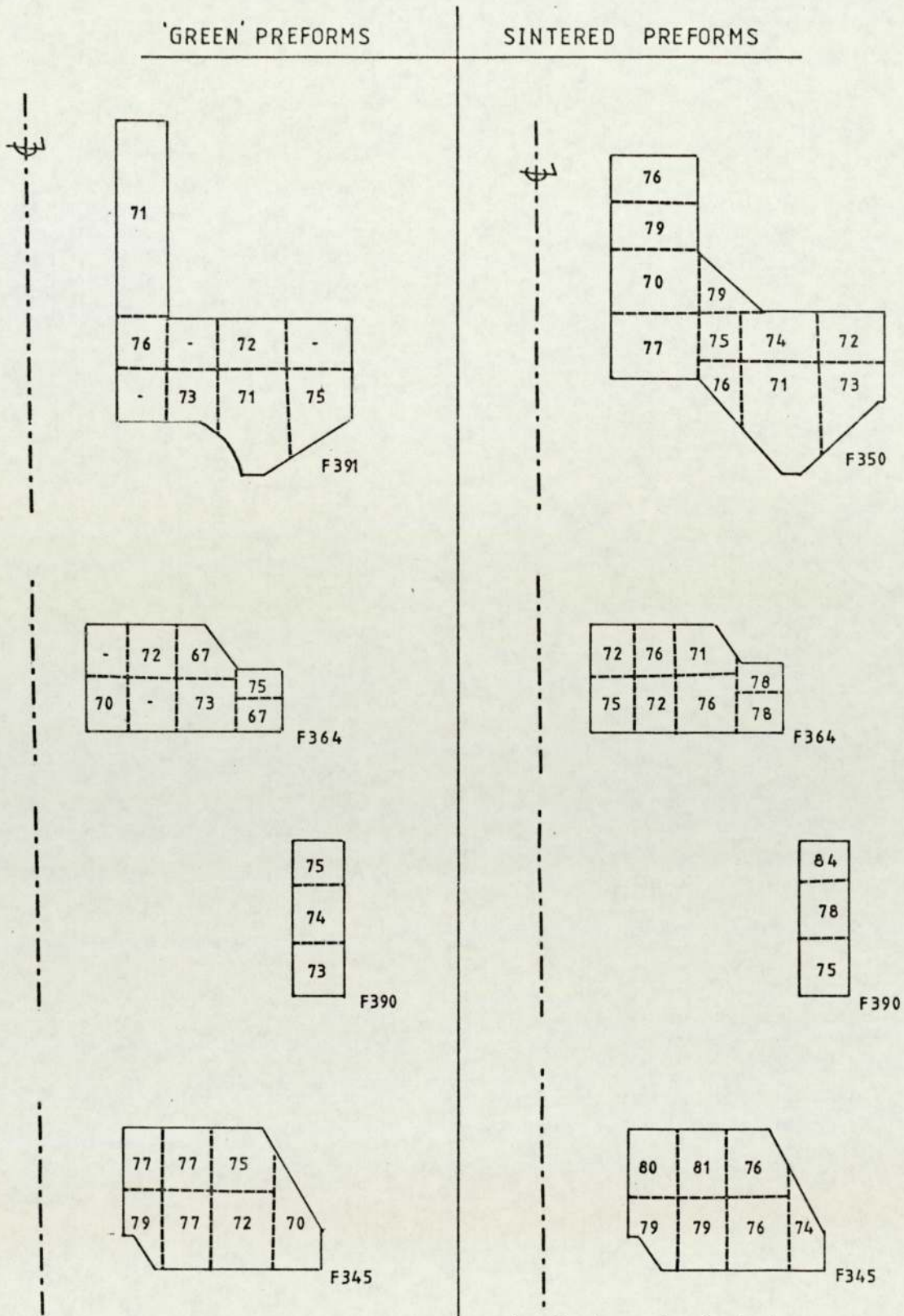


FIGURE 4.3: Measured approximate density distribution of selected unsintered ('green') and sintered G.K.N. preforms. The measurement method is described in Appendix 1. All preforms are rotationally symmetrical about the centre line indicated. Dashed lines define the block specimens cut for density analysis, and enclose the relative density of the block %.

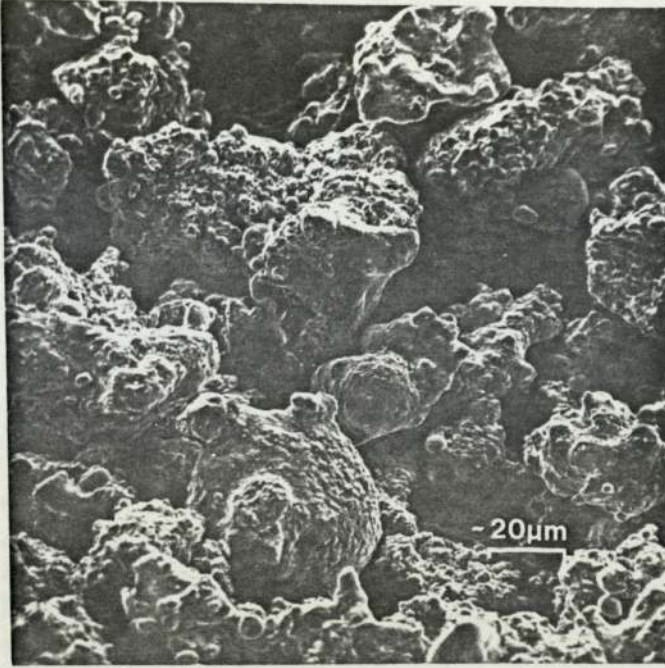


FIGURE 4.4: Scanning electron microscope photograph of compacted 'W4' powder of table 4.1.



PROPERTIES OF POWDERS

POWDER TYPE	APPARENT DENSITY (Mg/m <sup>3</sup> )	DENSITY <sup>3</sup> (Mg/m <sup>3</sup> )	'GREEN STRENGTH' (MN/m <sup>2</sup> )
W4	2.98	6.23	2.30
W78	3.03	6.06	1.8

after compaction  
of 300MN/m<sup>2</sup>

FINAL MECHANICAL PROPERTIES:

(after Sintering, forging  
oil quenching between  
830°C and 860°C and  
tempering at 525-650°C)

Powder Type	ULTIMATE TENSILE STRENGTH(MN/m <sup>2</sup> )	ELASTIC LIMIT <sup>2</sup> (MN/m <sup>2</sup> )	ELONGATION %	REDUCTION OF AREA %	IMPACT ENERGY (Joules)
W4	Minimum 725 Typical 740	550 600	10 15	22 35	10 16
0.17% to 0.23% carbon W78	Minimum 750 Typical 830	500 680	8 14	- -	12 22
with 0.2% to 0.26% carbon	Minimum 900 Typical 830	750 680	6 14	- -	9 22

Table 4.2 : Properties of compacted G.K.N. 'W4' and 'W78' powders and typical mechanical properties after forging [37].

#### 4.5 Concluding Summary

The major powder-forged metal production routes have been outlined in this chapter. The effect of each stage upon the powder density and particle size and shape has been shown. The physical properties  $\rho$ ,  $k$  and  $\mu$  have been linked to the changes imposed by each process, namely macroscopic density and contact area changes of a material. It may be concluded that these compact properties are highly sensitive to the production methods used. The importance of metal properties demands that these properties be known when considering induction heating. The primary relationship between component density distribution and mechanical properties has been recognised by G.K.N.[36]. However, its influence on the electrical, magnetic and thermal properties has been unexplored.

Values for electrical resistivity, thermal conductivity and magnetic permeability are considered in further detail in the next chapter.



CHAPTER FIVE

POWDER COMPACT PROPERTIES

## CHAPTER 5 : POWDER COMPACT PROPERTIES

### 5.1 Introduction

The previous chapter describes the major methods of powder and compact manufacture and defines qualitatively the influence of various production stages on the properties of the powder compact material. To determine how powder compacts react to induction heating, a more quantitative definition of the thermal, electrical and magnetic properties is required.

This chapter identifies the extent of the literature on this subject, in section 5.2, and describes experiments to measure electrical resistivity, thermal conductivity and magnetic permeability in section 5.3. The results of section 5.4 show that  $\rho$  and  $k$  are related to values  $\rho_0$  and  $k_0$  for the solid material by the semi-empirical equation,

$$\frac{\rho_0}{\rho} = \frac{k}{k_0} = \frac{1 - \xi}{1 + n\xi^2} \quad (5.4)$$

The constant  $n$  varies for different powders, depending on the manufacturing route and degree of contamination during the sintering process; for the powders used by G.K.N, this constant was found to be  $n = 9$ . The relative magnetic permeability is also shown in section 5.4, to be related to the ratio of powder density to that of the solid by the equation



$$\mu = \{\mu_s\}^{1/\nu_0} \quad (5.12)$$

The measurements in this section are significant in providing G.K.N. with hitherto unrecorded information on the physical properties of their powders, to complement previously measured mechanical performance [38].

## 5.2 Review of the Literature

### 5.2.1 Theoretical Predictions - Packing Models

The electrical, thermal and magnetic properties of a powder will be largely influenced by the number and nature of inter-particle bonds. The packing arrangement will determine the character and distribution of the contact areas. Theoretical attempts to predict the type of packing of particles have been based on two approaches.[39]

- i. The construction of a hypothetical ordered assembly of particles has been used to produce a number of ideal packing arrangements with which powders are often compared. This method does not consider the influence of the powder sizes or compaction method on the packing arrangement.
- ii. Qualitative discussions have been made of the statistical probabilities of particles adopting positions corresponding to a stable, systematic structure when poured into a container. This has been compared with empirical measurements of the co-ordination number and local density of large scale packed spheres in containers under various pouring conditions.

Both approaches have been limited to spherical particles of very restricted size range.

The basis for any mathematical definition of packing must consider the possible positions adopted by particles as they



are deposited. It is possible to calculate the number of final positions of a single sphere, when dropped on an ordered or disordered horizontal layer. However, other orientations of the original layer would have to be considered and, in practice, the influence of the other falling spheres must be taken into account. Powders are composed of a range of sizes: a simple model could not therefore describe the packing of normal powder.

The resilience and departures from sphericity of powder particles also increases the complexity of the real situation. It is, therefore, unlikely that a mathematical description would result in a full solution to packing and compressing problems [40]. The only approach likely to be fruitful is an experimental one, based on the relative significance of all variables. Comparisons between the properties of the powders and solid metals may then be made in relation to the packing structure.

### 5.2.2 Empirical Results

The influence of the powder structure on thermal and electrical conductivities of powder compacts has been considered in the literature.

A general introduction to Powder Metallurgy may be found in the literature, and current developments are reported in regular review publications [41]. Many references are cited

to support general conclusions of the influence of all powder production variables on the properties of compacts. The results of previous experiments differ, however, due to the inherent variations in powder types, number and quantity of alloying additions, mixing methods, compacting pressures, die shapes, sintering and heat treatment, temperatures, atmospheres, process times and experimental conditions. General trends found may be reported; Jones [42,43] and Hausner [44] conclude that electrical and thermal resistivities are greater for sintered metals than corresponding cast metals and that coarser particle size, greater compaction pressures, cycles and process times reduce these resistivities.

The properties of the compact are highly sensitive to the production methods however, and comparisons of the results of various workers may often be difficult if insufficient information is given.

Although considerable effort has been expended by G.K.N. to develop alloys for powder-forging, the emphasis has been placed on mechanical and chemical property measurements for strength comparisons with wrought materials [45-48]. Similar articles exist of results for other powder-forging case studies [49]. The primary relation between powder compact density and mechanical



properties has been recognised but its influence on the electrical and magnetic properties of preforms has been largely unexplored.

Three factors affecting the value of electrical resistivity, and the thermal conductivity may be identified, viz. the basic material resistivity, the particle concentration i.e. density and thirdly, the number and nature of interparticle "junctions". Properties of the basic material in solid form are well documented. Powell [50] and Griffiths [51,52] give details of  $\rho$  and  $k$  measurements on a number of steels of varying compositions. From these, En3 and En8 steels closely approximate to the elemental constituents of W4 and W78 powders (Figure 3.7).

The influence of the compact density has been discussed by various authors.

Guidelines [53,54] have been given to determine the density distribution within various preform shapes, in the form of density contour maps of the preform cross-section. Density redistributions during sintering [55,56] have also been studied, relations between the physical and micro-structural changes were derived [57], and the resulting macroscopic distortion of preforms indicated.

Grootenhuis, Powell and Tye [58] give experimental results of  $k$  and  $1/\rho$  for sintered porous bronze, of 60% to 100% theoretical density, for temperatures between 20°C and 200°C. They demonstrate by plotting  $k/k_0$  with density that the ratios of conductivities of porous to solid bronze are approximately directly proportional to the density of the material by the equation for a straight line,

$$\frac{\rho_0}{\rho} = \frac{k}{k_0} = (1 - 2.1\xi) \quad (5.1)$$

where the porosity  $\xi$  of the powder is related to the density  $\rho$  of the powder by

$$\xi = 1 - \frac{\rho}{\rho_0} \quad (5.2)$$

The zero subscripts in equations 5.1 and 5.2 refer to the solid material. Previous work on porous copper, nickel and iron properties is also reported and confirms equation (5.1) for metals above 60% theoretical density.

Since the powders used in previous accounts had been manufactured by widely differing methods, the constituent particles were likely to be dissimilar. Thus particle size distribution and shape are of only secondary importance to the dependence of  $\rho$  and  $k$  on porosity. However, Grootenhuis et al. observe that results for some specimens used in earlier accounts diverge from the expected relation in equation (5.1).



This was explained by referring to the non-standard conditions of compaction pressure and sintering times by which they were made, giving incomplete sintering.

Extrapolation of the straight line graph of equation (5.1) results in the prediction that zero conductivities occur at 52.4% theoretical density. Grootenhuis, Powell and Tye equate this density with the minimum that may be obtained when spheres are packed in a cubic lattice of co-ordination number 6. Grootenhuis et al. claim that their atomized bronze powder particles are substantially spherical and will conform to this packing structure at densities near 52.4% of theoretical. No experimental evidence of particle packing is given to support these claims, but previous discussion above indicates that the approximation of particle sphericity may be made for theoretical comparison. The cubic lattice may not be considered universal. For example, results reported by Adlassig and Fogler [59] on porous copper may be represented better by a straight line giving zero conductivities at approx 40% of theoretical density. This may correspond to a systematic assemblage of spheres of co-ordination number 5, as shown by Manegold and others [60].

More recent studies by Koh and Fortini [61,62] of the electrical and thermal conductivities of stainless steel and copper powders extend the range of results to densities between 25% and 100% of theoretical density, and to a temperature of 900°C. Graphs of  $\rho$  and  $k$  with density show that all results are confined within the straight line boundaries defined by

$$\frac{\rho_0}{\rho} = \frac{k}{k_0} = (1 - x\xi) \quad (5.3)$$

where  $x$  varies from 1, resulting from a parallel cylinder model where cylindrical pores are considered, to 2.3 (Grootenhuis et al.). Koh and Fortini's results follow those of Grootenhuis but diverge below 70% of theoretical density, (figures 5.1 and 5.2)\*.

Although, for the density range of interest here, there is only a 10% maximum difference, it is best to consider the more fundamental and accurate results of Koh and Fortini, for the future possibility of preforms below 70% relative density. These results may be approximated by a generalized semi-empirical equation

$$\frac{\rho_0}{\rho} = \frac{k}{k_0} = \frac{1 - \xi}{1 + n\xi^2} \quad (5.4)$$

\* Figures appear at the end of this chapter, from page 107 to page 134.



derived by Aivazov and Domashnev [63] where  $n = 11$  (figs 5.2 and 5.3), which was found to give the best approximation to the experimental results. Aivazov and Domashnev deduce this relation from analytical expressions by Odelevskii [64] for hypothetical cubic lattices, where cubic and cylindrical pores are arranged in a regular array. Measurement of the dependence of  $\rho$  and  $k$  for titanium-nitride agreed closely with equation 5.4, when  $n = 6$  is used. The physical significance of  $n$  is stated to be the integrity of inter-particle contacts, character of the pore distribution and the pore shape; empirical comparison of equation 5.4 with experiments gives the value of  $n$ . However, no quantitative relation exists for the dependence of  $n$  on the physical properties of the powder, since the regular lattice used in deriving equation 5.4, can only approximate to the true powder structure.

The significance of the physical nature of powders on their electrical and thermal behaviour is shown below. Endo, Kubo, Morioka & Itoh [65] record results of electrical resistivity measurements on iron powder compacts during sintering. The influence of sintered and green densities, powder type, atmosphere and oxidation treatment summarise the findings of many earlier reports.

Endo et al. show that equation 5.5 closely describes their results\*

$$\frac{\rho}{\rho_0} = \left( \frac{r}{r_c} \right) \left[ 1 + \frac{2 \rho_s a}{\pi r_c \rho_0} \right] \quad (5.5)$$

Values  $r$  and  $r_c$  are respectively, the spherical metal particle radius and radius of contact between particles,  $\rho$  is the material resistivity, and  $\rho_s$  the inter-particle boundary layer resistivity of thickness  $a$ . The second term in equation 5.5 describes the effect of inter-particle contact due to changing particle boundary composition and shape during sintering. Above 350°C, for sintered powders, a simplified form of equation 5.5, ignoring the second term, is used. The simplified equation relates the resistivity of the powder to that of the solid by direct proportion of  $r$  to  $r_c$ . The ratio  $r/r_c$  describes the effect of neck growth between particles, and given by

$$\frac{r}{r_c} = \left\{ \frac{\pi \sigma_0}{4 \sigma} \right\}^{\frac{1}{2}} \quad (5.6)$$

$\sigma$  and  $\sigma_0$  are the tensile strengths of the sintered particle system and the solid, respectively.

\* The original paper containing equation 5.5 appears without the factor  $a$ . This equation is dimensionally incorrect. The writer has corrected this error after consideration of results described in an earlier report by Endo et al.[66].



The results of Endo et al agree with equation 5.4. as shown in figure 5.3. Without complete tensile strength data or direct measurements of  $r/r_c$  at all stages during sintering, no comprehensive comparison of experimental results with equation 5.5 can be made: However, a qualitative explanation of the resistivity changes occurring whilst sintering is given below.

Equations 5.5 and 5.6 would form an adequate theoretical model for the powder/property relationship for a regular packing of uniform particles. For real powders of irregular shape and variety of size however, theoretical predictions remain on a semi-empirical level.

The third contribution to electrical resistivity and thermal conductivity lies in the nature of interparticle junction "necks". The influence of oxide layers is shown by the change in resistance with compaction pressure and negative temperature coefficients of resistivity occurring during sintering. Quantitative comparisons show that resistivity is inversely proportional to density, and inversely proportional to the square root of compaction pressure. Hausner [44] and Goetzel [67] indicate the marked importance of sintering temperature on the electrical properties of powder compacts, corroborated by Sands and Shakespeare [68].

The importance of the resistivity of particle contacts to the overall resistivity of the compact was shown by

Leheup and Moon [69,70]. They report electrical resistivities of  $0.5 \text{ m } \Omega \text{ m}$  at room temperature, falling to  $1.7 \text{ } \mu\Omega \text{ m}$  at  $375^{\circ}\text{C}$  for unsintered pure iron compacts heated in air; lower resistivities being retained on cooling to  $20^{\circ}\text{C}$ . They conclude that the electrical resistivity of unsintered compacts is controlled by interparticle contact regions and that a plausible and consistent explanation is the growth and structural modification of surface oxide films.

Similar trends of high values of resistivity ( $1.0 \text{ m } \Omega \text{ m}$ ) have been reported for unsintered steel compacts at room temperature, falling to  $0.1 \text{ m } \Omega \text{ m}$  as temperature is raised to  $250^{\circ}\text{C}$ . Conta [71] explained this as due to the loss of adsorbed gas and moisture during heating but, although this may be a contributory factor, it is unlikely to be the primary cause of the changes observed [66,70], since these are irreversible. It is more likely that this is due to changes in the nature of the surface layer of particles.

The effect of surface layers on the electrical resistivity of copper and nickel powders was investigated [72] with increasing compaction pressure. A similar dramatic drop in resistivity from  $12 \text{ } \mu\Omega \text{ m}$  to  $0.26 \text{ } \mu\Omega \text{ m}$  at  $20^{\circ}\text{C}$  was found as the oxide layers were removed from particle contacts during compression.



An empirical equation quoted relates the electrical resistance to compacting conditions. It is unlikely that the form of this equation gives an insight into the changing resistance during sintering since the mechanisms of oxide removal are different. However, agreement with the results of Leheup and Moon and Conta may be concluded.

Magnetic permeability measurements of powder compacts have been reported in the literature [73-78], using standard measurement techniques described by Berkowitz and Kneller [79]. Results show a large variation in the magnetic permeability that may be expected, depending on the number and amounts of alloying elements present. Many articles refer only to high nickel, molybdenum and cobalt alloy steels, found to give very high magnetic permeabilities and suitable for many magnet applications.

Widely differing values have been quoted for bulk solid material relative permeability  $\mu_s$  for example, ranging from 2400 to 9000 for iron, depending on purity. Bozorth [80] quotes increasing maximum permeability related to increasing carbon content in iron. For percentages of 0.23% and 0.4% carbon (approximately corresponding to 'W78' and 'W4' materials), the maximum permeability is reduced to 0.16 and 0.15 of the plain iron value, respectively.

The dependence of  $\mu_s$  with field strength H varies widely in the literature: from May's [81]

$$\mu_s = \frac{6.33 \times 10^5 B_s}{H} \quad (5.7)$$

to Baker's [23]

$$\mu_s = \frac{1.43 \times 10^6 B_s}{H} + 1 \quad (5.8)$$

Most equations have the following form

$$\mu_s = \left\{ \frac{x B_s}{H} \right\}^y + 1 \quad (5.9)$$

where  $B_s$  is the saturation flux density. Davies and Simpson [18] use  $y = 0.92$  and neglect 1 to give

$$\mu_s = \left( \frac{2.38 \times 10^6}{H} \right)^{0.92} \quad (5.10)$$

This agrees well with their experimental results.

Experimental values of  $\mu$  for powder materials are also reported. Degtyareva and Shvartzman [73] give magnetic permeability dependence on magnetic field strength H for 98% pure iron powder. They found that the relation

$$\mu = 20.19 H^{-0.22} \quad (5.11)$$

gave agreement with results, up to 250 A/m. It is questionable whether this relation may be extrapolated to orders of  $10^5$  A/m for induction heating. Other references [74-76]



give results in the form of graphs of measurements using various powders but with no corresponding data for solid material; no conclusions are drawn for predicting the magnetic permeability from the powder composition for magnetic field strength. The most reliable information on the effect of powder density on magnetic permeability is reported by Legg & Given [82] and others [83,84], and is generally represented by

$$\mu = \left\{ \mu_s \right\}^{\frac{1}{2}} \quad (5.12)$$

Typical maximum relative permeabilities are given as  $\mu_{rmax} \approx 10^4$ , and values of  $\mu_r = 700-1000$  for densities between 65% and 85% of theoretical density.

The work of Steinitz [85,86] on iron powder compacts, sintered at 1150°C, gives fair agreement with equation 5.12 (see figure 5.4), where measurements of  $\mu_{max}$  are plotted against density, with values for pure Armco iron and from equation 5.12 for comparison. Also shown is data by Lenel [87] for iron powder compacts sintered at a higher temperature, 1300°C. Reference is made [86] to theoretical studies by Polder and Santen [88] whose predictions are also shown in figure 5.4 for spherical holes and disc shaped holes in a solid substance. On the basis of the modern concepts of the sintering mechanism, the pores in the pressed compact may be somewhat flattened,

with high temperatures and longer sintering times favouring the transformation of these pores into spherical holes. The results of figure 5.4 confirm the influence of sintering temperature on  $\mu$  and are in approximate agreement with theory. Lenel's compacts are sintered more than Steinitz's, approximating to the curve for powders with spherical pores, as opposed to those where disc-shaped pores dominate.

Little information on the temperature dependence of magnetic permeability has been found, although Kir'yanov [89] reports that  $\mu_r$  declines linearly with a temperature coefficient of about  $6.3 \text{ (K}^{-1}\text{)}$  for iron powders, well below the Curie temperature. Fluereşu [90] provides the most complete graphs seen of permeability against temperature and field strength, but his source is not stated. Due to the critical dependence of  $\mu$  on the exact powder constituents, and the variability of solid material  $\mu_s$  with temperature and magnetic field, for comparison, measurements of powder magnetic permeability are required.

### 5.3 Measurement of Powder Compact Properties

#### 5.3.1 Electrical Resistivity

The measurement principle lies within the definition of resistivity  $\rho = RA/\ell$ .  $R$  is given by  $V/I$  and  $A$  is the cross-sectional area of the rod, where voltage measurements are made over length  $\ell$ . To ensure uniform current distribution (assumed in the definition) the measurement points are positioned where  $I$  is uniform.



Sintered carbon steel discs of 68mm diameter were prepared from two material compositions 'W4' and 'W78', at relative densities  $\rho/\rho_0$  of 0.74, 0.79 and 0.84. From these, six bars of 60mm x 10mm x 10mm were cut, surface ground and polished (figure 5.5a). Two similar nichrome measurement wires were spot welded 25mm apart on one face of each bar and insulated along their length. A mineral insulated chromel - alumel thermocouple was implanted 3mm into the opposite face (fig 5.5b).

A test bar was positioned in the apparatus as shown in figure 5.6, consisting of a long steel tube capped at one end, an internal rod and a device for exerting pressure on the central rod and test bar to ensure electrical continuity. The test bar sides were electrically insulated. The apparatus assembly was inserted into a thermostatically controlled tube furnace, such that the test bar was sited in uniform temperature at the furnace centre, and heated from room temperature to 1000<sup>o</sup> C at 50<sup>o</sup> C intervals, or at 20<sup>o</sup> C intervals during Curie transition between 700<sup>o</sup> C and 800<sup>o</sup> C. The potential difference between the wires was measured when a known direct current was passed longitudinally through the bar, via leads brazed to the rod and tube ends. The readings were confirmed during cooling. Similar experiments were completed for bars of the other densities and material. Also tested were standard test bars of high purity iron, 0.74% carbon steel and En8 steel to check measurement accuracy and the dependence of the Curie

temperature on material composition.

### 5.3.2 Thermal Conductivity

The principle (derived in Appendix 3) of these measurements lies in the theoretical equation

$$\sqrt{\frac{k_1}{k_2}} = \frac{\log [c_2 + \sqrt{(c_2-1)}]}{\log [c_1 + \sqrt{(c_1-1)}]} \quad (5.13)$$

relating the ratios  $c_1 = \frac{T_1 + T_3}{2 T_2}$  of the test bar to that of a standard bar for which the conductivity  $k_2$  is known. Six test bars (0.74, 0.79 and 0.84 relative density of 'W4' and 'W78' powder) were prepared according to subsection 5.3.1. A standard En8 bar was similarly made. Each bar was thermally insulated except at each end and wound with a small resistance heating element, as shown in figure 5.7 to provide a thermal gradient along the bar. Three ceramic insulated chromel-alumel thermocouples were implanted at 3mm depth at 25mm intervals on one face of each bar.

A test bar was placed in the apparatus (figure 5.8), which was then positioned in the furnace described above. The thermal gradient along the bar was enhanced by setting the test bar at a part of the furnace where a gradient exists and by forced air cooling of the opposite end of the apparatus. The thermocouple temperatures were recorded at 100°C intervals as the test bar was heated from 20°C to 1000°C, and at 20°C intervals during the Curie transition between 700°C and 800°C. This experiment was repeated for all test bars and for a bar of standard En8 material.



### 5.3.3 Magnetic Permeability

Six toroids of mean radius  $R$  and sectional area  $A$  were prepared from 'W4' and 'W78' composition sintered discs of 0.74, 0.79 and 0.84 relative density (figure 5.9) [91,92]. These were wound with approximately  $N_1=200$  primary and  $N_2=35$  secondary turns of insulation sleeved wire (the exact number being recorded) and connected to the apparatus shown in figure 5.10. A chromel-alumel ceramic insulated thermocouple was embedded 3mm into each toroid.

An alternating current was fed to the primary turns  $I_1$  from a 1 kVA amplifier with feedback, and the voltage drop across a known resistor displayed on the x axis of a cathode ray oscilloscope (C.R.O.). The voltage  $V_2$  induced in the secondary windings was integrated and displayed on the y axis of the C.R.O. Standard formulae may be used to calculate the magnetic field  $H$ ,

$$H = \frac{N_1 I_1}{2 \pi R} \quad (5.14)$$

and the magnetic induction  $B$ ,

$$B = \frac{-1}{N_2 A} \int V_2 dt \quad (5.15)$$

from these quantities.

The hysteresis loop of  $H$  vs.  $B$  was recorded, as  $I_1$  was increased, by multiple exposure photographs of the oscilloscope screen. The process was repeated at approximately  $100^\circ\text{C}$  intervals as the toroid was heated in sand from  $20^\circ\text{C}$  to  $760^\circ\text{C}$ . The experiment was repeated using the other five test toroids.

## 5.4      Results and Discussion

### 5.4.1 Electrical Resistivity

Measured values of electrical resistivity with temperature for test bars of 'W4' material appear in figure 5.11 and for 'W78' powder are given in figure 5.12. Experimental values for the standard bars of high purity iron, En8 steel and 0.74% carbon steel are presented in figure 5.13, with the expected curves from the literature. The predicted curves of figures 5.11 and 5.12 are plotted using the resistivity values of similar solid materials and the semi-empirical relationship of Koh & Fortini (equation 5.4) relating powder resistivity  $\rho$  to that of solid material  $\rho_0$ .

The constant  $n$  was found by plotting the ratio of experimental values with equation 5.4, using various  $n$  values (figures 5.15 & 5.14). For 'W4' powders  $n$  was found to be between  $n = 9$  and  $n = 10$  and for 'W78' powders  $n = 9$  approximately. Measured values for the standard bars agree closely with the predicted curves from the literature (figure 5.13). The experimental accuracy of these measurements is approximately 5%. This represents good accuracy for measurements which are difficult, especially at high temperatures without major refinement of the apparatus. Current uniformity within the test bar between the measurement wires may be assured.

Graphs of the experimental electrical resistivity ratio against temperature show that there is general agreement with



the predictions of Koh and Fortini but that their constant  $n$  lies between 9 and 10. It proved difficult to establish the dependence of the Curie temperature on material composition as the change in slope of the resistivity versus temperature curves is not sharp at the Curie point.

#### 5.4.2 Thermal Conductivity

The presentation of thermal conductivity results follow similar lines to those of the previous section. Measured thermal conductivity values with temperature for three powder densities appear in figures 5.16 and 5.17, for 'W4' and 'W78' types, respectively. The thermal conductivity of the standard bars was not low enough for reliable measurements to be made from small temperature gradients present. Again, predicted curves are shown on figures 5.18 and 5.19 from the thermal conductivity ratio part of equation 5.4 for both powder and solid metal. Here a constant value  $n = 9$  for 'W78' and  $n = 9$  for 'W4' was found to best fit the results.

These results show fair agreement with the predictions of Koh and Fortini [62]. The inherent inaccuracies of temperature measurement give a larger variation of results than the electrical resistivity measurements. The experimental error of 10% gives greater deviation of the ratio  $k/k_0$  in figures 5.18 and 5.19, from predictions.

However, the thermal conductivity results give no contradictory evidence for any other relationship. The average ratios strengthen the argument for accepting that the equations

$$\frac{\rho_0}{\rho} = \frac{k}{k_0} = \frac{1 - \xi}{1 + 9\xi^2} \quad (5.16)$$

describe the dependence of k upon density.

#### 5.4.3 Magnetic Permeability

The relationship,

$$\mu = \mu_r \mu_0 = \frac{B}{H} \quad (5.17)$$

was used to obtain relative permeability readings from measurements taken from C.R.O. photographs.  $\mu_r$  is plotted against magnetic field H, for 'W4' (figure 5.20 to 5.22) and 'W78' (figure 5.23 to 5.25) powders of  $\rho/\rho_0 = 0.74, 0.79$  and  $0.82$ , respectively, for temperatures between  $50^\circ\text{C}$  and  $760^\circ\text{C}$ .

The results for W4 powder of 0.74 relative density are taken as an example and replotted (figure 5.26) showing the dependence of relative magnetic permeability with temperature for various field strengths. Measured  $\mu_r$  values at the lowest temperatures recorded and the predicted relationships considered in sub-section 5.2.2 are given in figure 5.27 for 'W4' and 'W78' powders at  $\rho/\rho_0 = 0.74$ , in figure 5.28 for



both types at 0.79 relative density and similarly for the remaining density in figure 5.29.

The relative magnetic permeabilities of compacts in both powder types were comparable, although  $\mu_r$  was generally a little larger for 'W78' powder. Values of  $\mu_r$  appear to decline steadily with increasing temperature to about 650°C and fall sharply to unity between 650°C and 760°C for all powders.

The measured dependence of  $\mu_r$  with magnetic field strength, H (figures 5.20 to 5.25) is consistently lower than the curves drawn from inserting the dependence of permeability of the solid to H from May (equation 5.7), Baker (equation 5.8) and Davies and Simpson (equation 5.10) into the relationship for the powder,

$$\mu = \{\mu_s\}^{1/2} \quad (5.12)$$

May's equation gives closest agreement with measured values but deviates at high field strengths. A better approximation is made by taking Davies and Simpson's relation and using lower saturation flux densities  $B_s$  of 1.2 T for 'W78' and 0.7 T for 'W4' rather than the value  $B_s$  of 2.0 T for low carbon steels. The literature gives little information beyond the endorsement that  $B_s$  and  $\mu$  do fall with increasing carbon content.

## 5.5 Concluding Summary

Consideration of the literature on the sintered preforms properties, electrical resistivity, thermal conductivity and magnetic permeability has shown that various theoretical relationships have been postulated. Of these, the semi-empirical equations that have been found are the most successful in describing experimental results.

However, it is hazardous to extend conclusions due to the limited validity of these equations and the variety of powder compositions and types used in confirmatory tests. For this reason,  $\rho$ ,  $k$  and  $\mu$  were measured for the particular G.K.N. powders, using the methods reported here. The results show that both electrical resistivity and thermal conductivity are related to the values of the corresponding solid material by the equation

$$\frac{\rho_0}{\rho} = \frac{k}{k_0} = \frac{1 - \xi}{1 + 9\xi^2} \quad (5.16)$$

The powder magnetic permeability  $\mu$  was found to agree with the relationship

$$\mu = \{\mu_s\}^{\gamma/\gamma_0} \quad (5.12)$$

where  $\mu_s$  is the permeability of the solid and  $\gamma$  and  $\gamma_0$  are the densities of the powder and solid. The value for  $\mu_s$  varies in the literature and is not available for a similar alloy to 'W4' or 'W78'.



Closest agreement with experimental values was obtained using the formula

$$\mu_s = \left( \frac{1.19 \times 10^6 B_s}{H} \right)^{0.92} \quad (5.18)$$

where saturation flux  $B_s$  is equal to 1.2 Tesla for 'W78' and 0.7 Tesla for 'W4' powder.

With powder properties thus defined, it is now possible to proceed to consider the induction heating of 'W4' and 'W78' materials both theoretically, in the next chapter, and experimentally in Chapter 7.

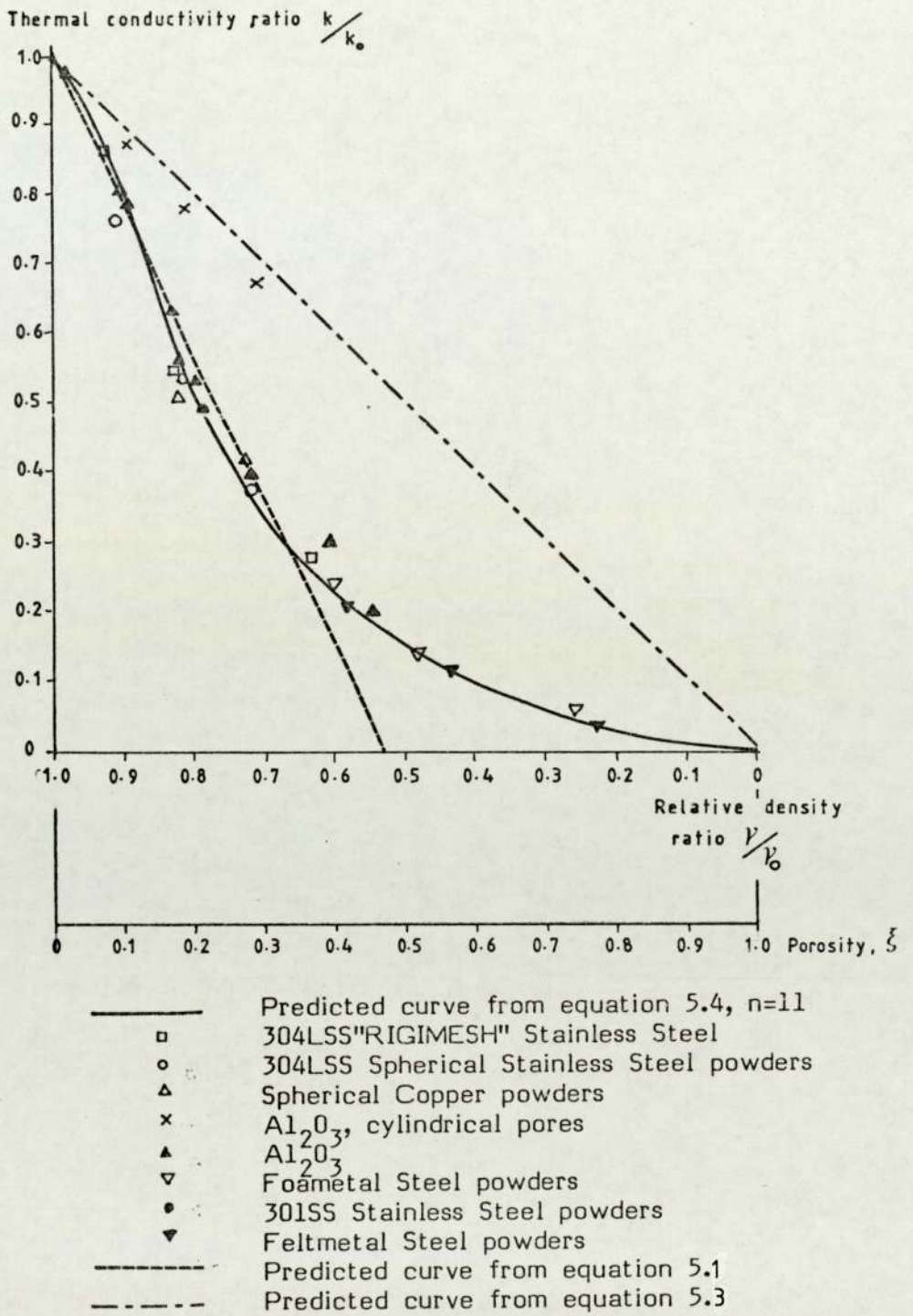
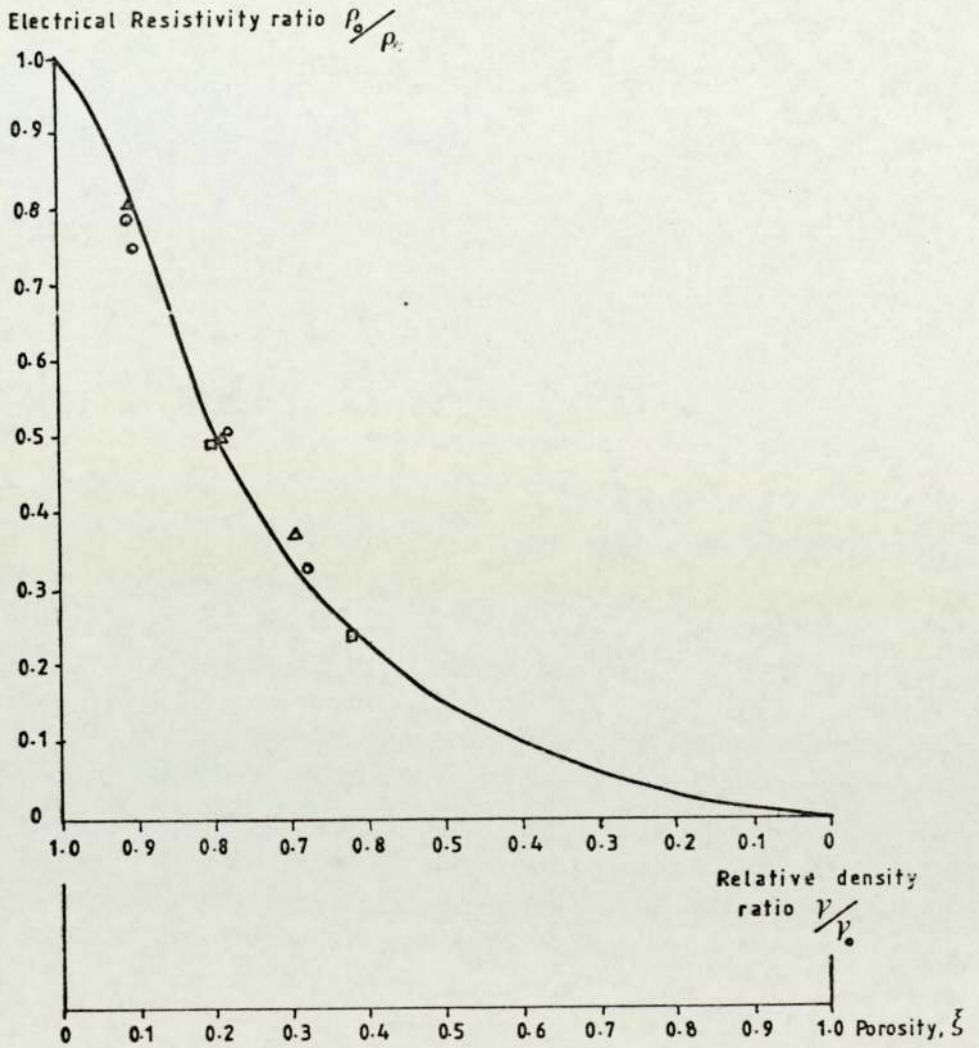


FIGURE 5.1: Thermal conductivity measurements with powder density, with the theoretical predicted curves from equations 5.1, 5.3 and 5.4 for various powder compositions and structure, as indicated.

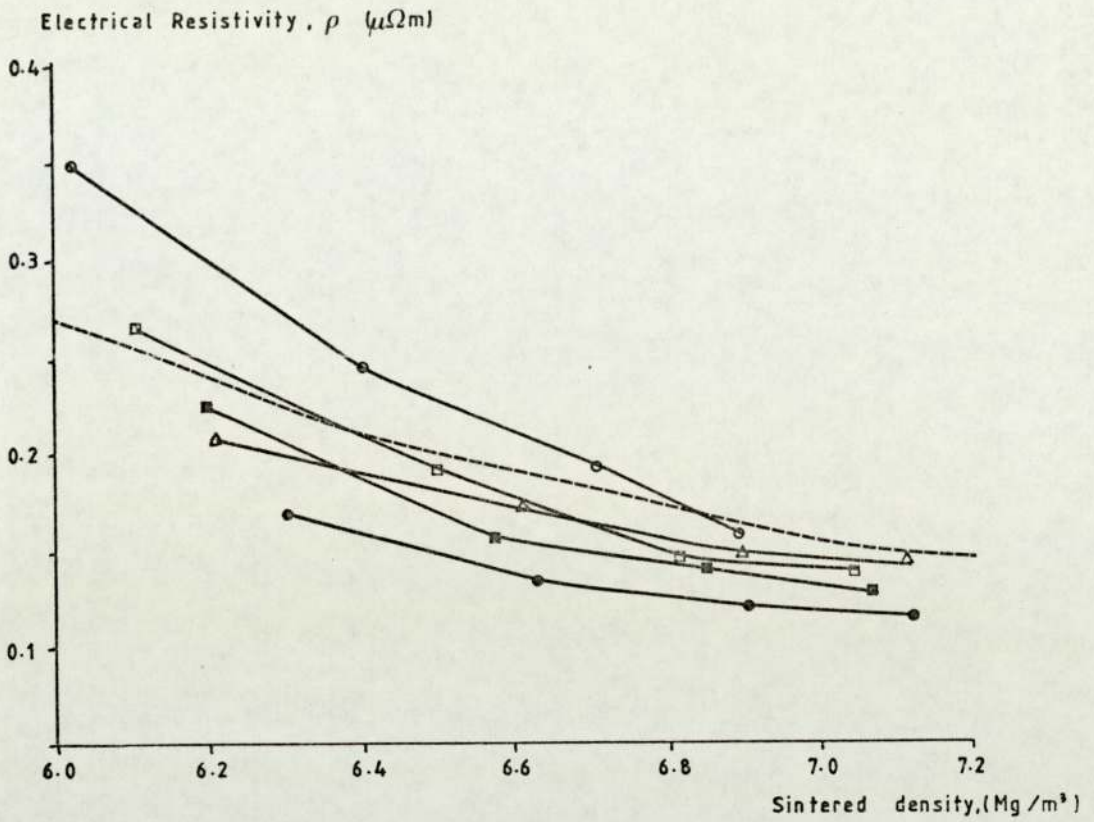




- 304 LSS Rigimesh
- 304 LSS Powders
- △ OFHC Copper Powders

— Predicted curve eqn. 5.4  $n=11$

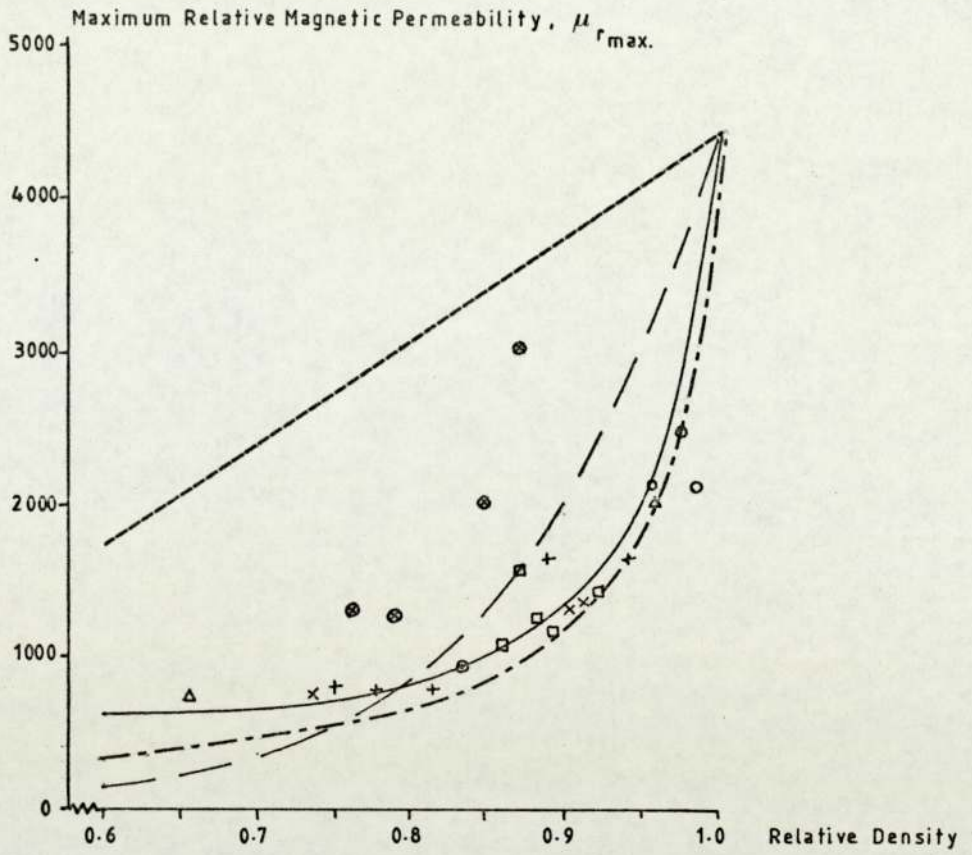
FIGURE 5.2: Electrical resistivity measurements [62] with powder density and theoretical predicted curve from equation 5.4.



- Iron Powder, reduced from millscale (low Sulphur content)
- Iron Powder, reduced from millscale (high Sulphur content)
- Iron Powder, reduced from ore
- Iron Powder, electrolytic
- △ Iron Powder, atomized
- Predicted curve

FIGURE 5.3: Electrical resistivity measurements, [65,66] with density recorded by Endo et.al. for iron powders produced by various methods. Also given is the predicted relationship of equation 5.4.,  $n = 11$ .





Iron Powders

- △ Electrolytic
  - + × Reduced
  - ⊙ Lenel's Value
  - ⊗ Lenel's Value
- } Sintered at 1150°C
- } Sintered at 1300°C
- Curve fitted to those sintered at 1150°C

Theoretical Relationships

- for spherical holes
- · - · - for disc-shaped holes
- — — from equation 5.12

FIGURE 5.4: Relative magnetic permeability measurements with [85,86] density and predicted relationship from Polder and Santen [88], Legg and Given [82], equation 5.12.

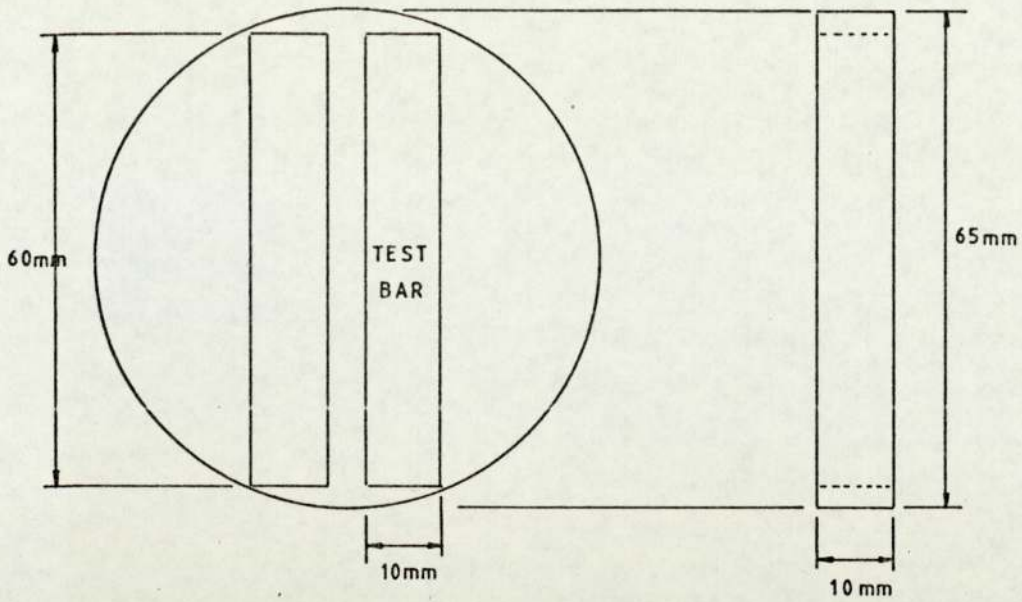


FIG. 5.5a

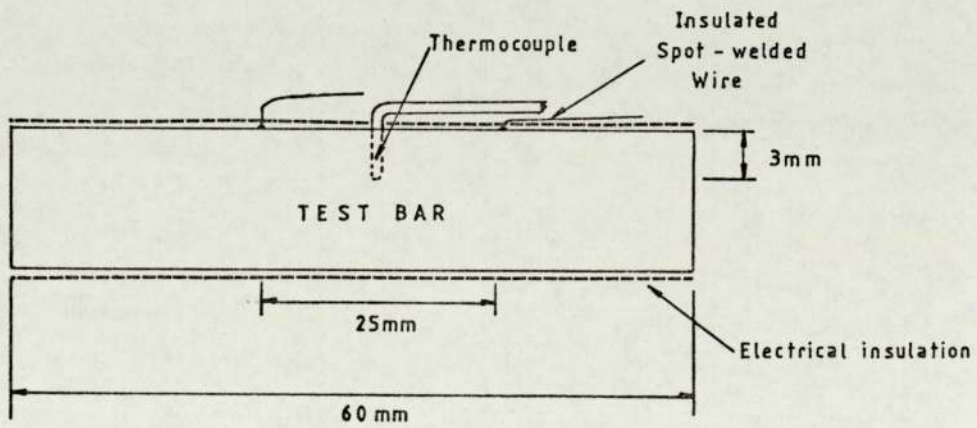


FIG. 5.5b

FIGURE 5.5: Preparation of test bar for measurement of Electrical Resistivity. a) Test bar cut from sintered disc b) Attachment of spot-welded measurement wires, thermocouple and insulation. See figure 5.6 for apparatus.



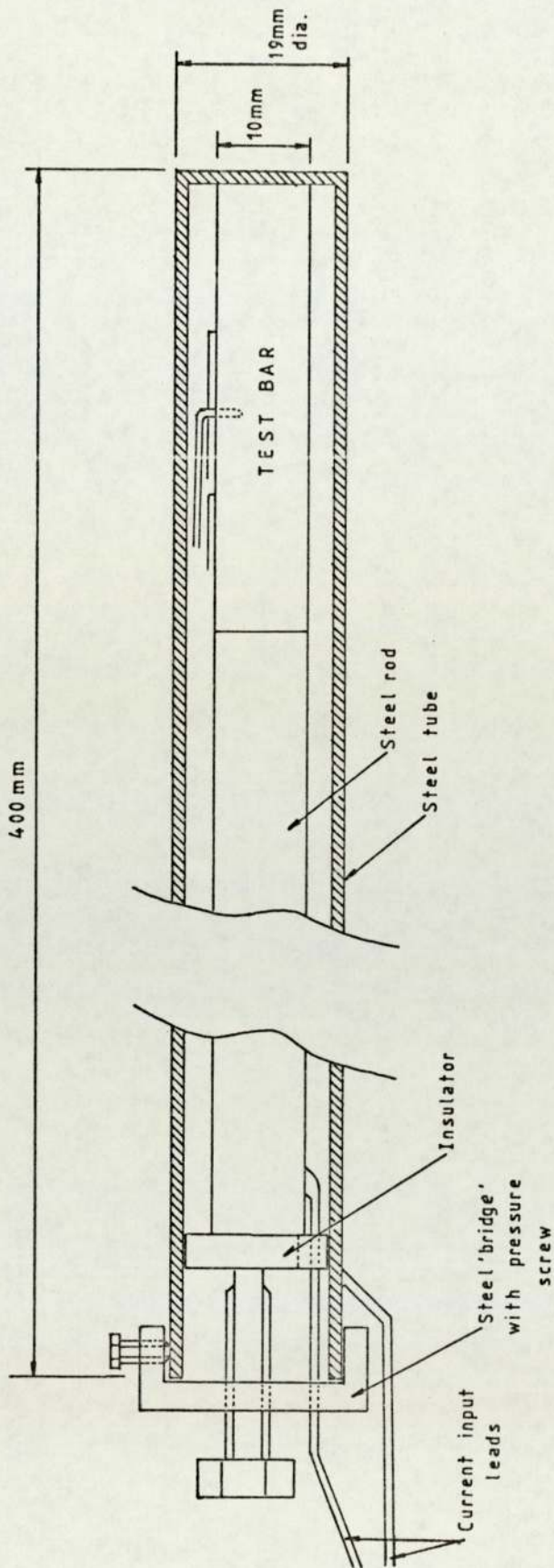


Figure 5.6 : Apparatus for  $\rho$  measurements from  $20^{\circ}\text{C}$  to  $1000^{\circ}\text{C}$ , showing position of test bar (figure 5.5b).

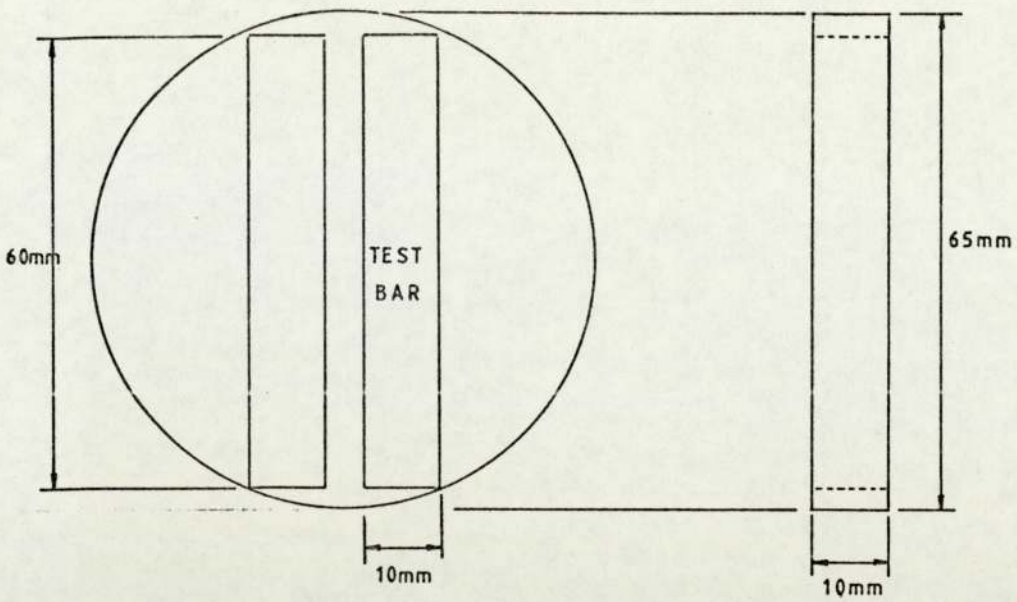


FIG. 5.7a

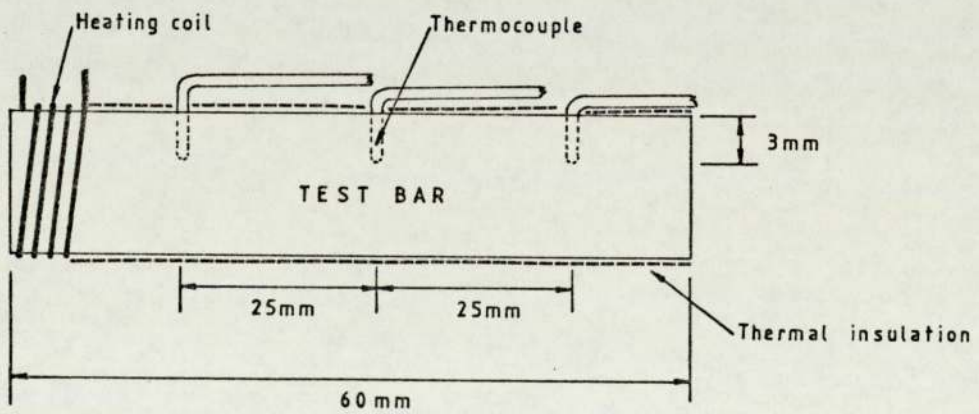


FIG. 5.7b

FIGURE 5.7: Preparation of test bar for measurement of Thermal Conductivity. a) Test bar cut from sintered disc. b) Attachment of thermocouples, heating coil and thermal insulation. See figure 5.8 for Apparatus.



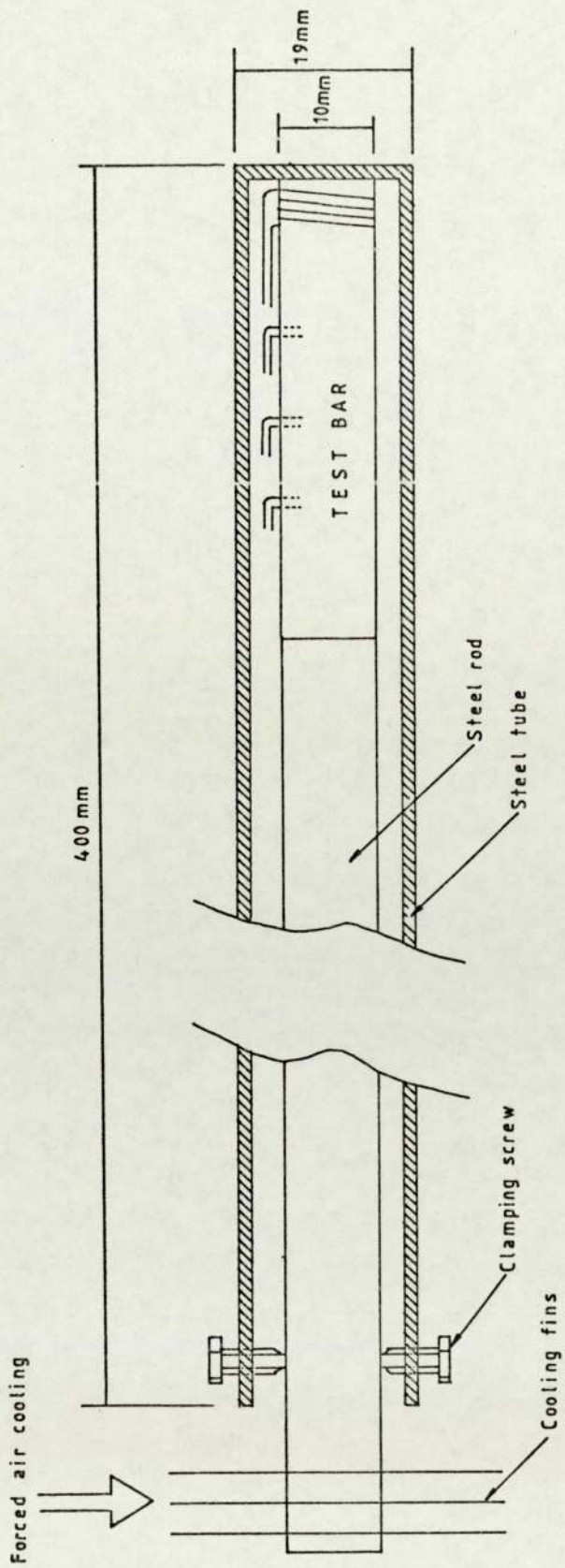


Figure 5.8 : Apparatus for  $k$  measurements from  $20^{\circ}\text{C}$  to  $1000^{\circ}\text{C}$ , showing position of test bar (figure 5.7b).

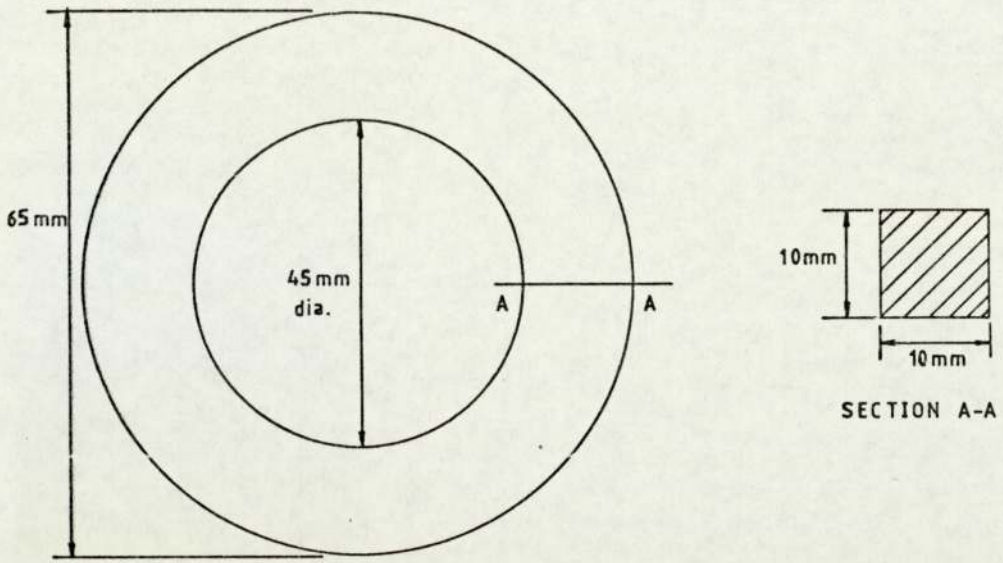


FIGURE 5.9: Test toroid cut from sintered disc for measurement of Magnetic Permeability,  $\mu$ .

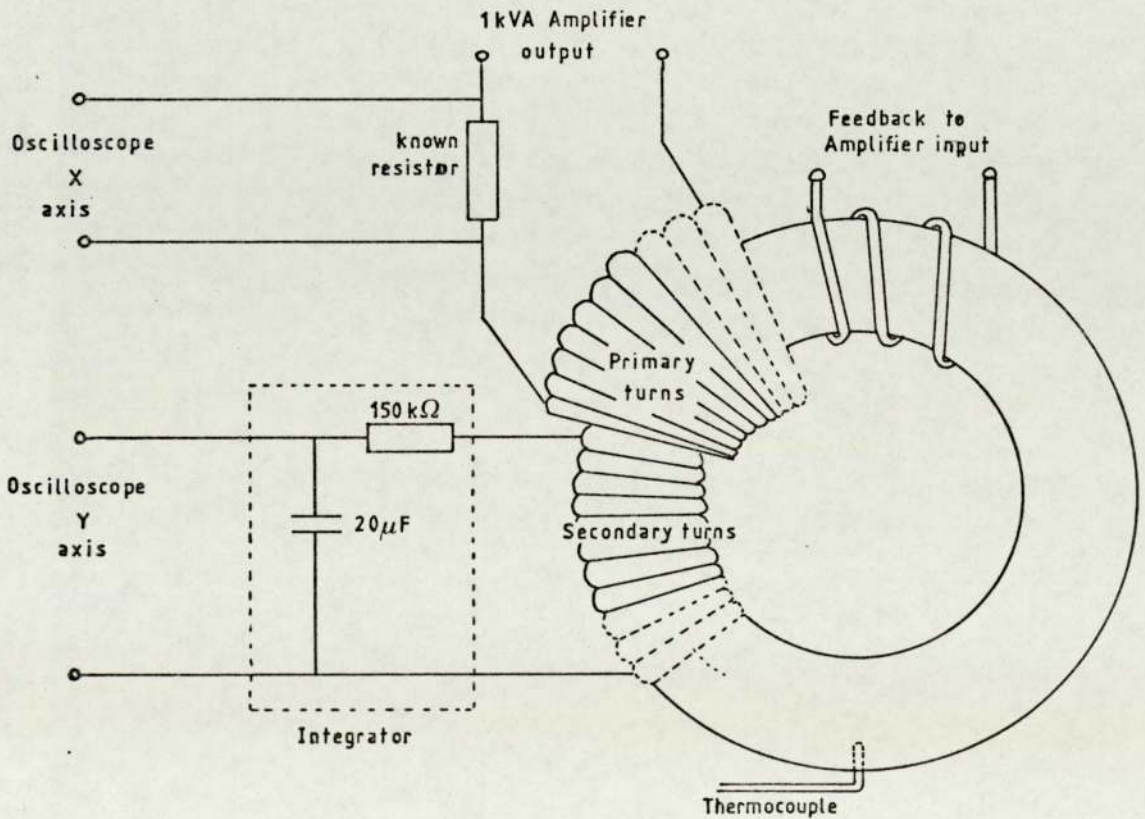


FIGURE 5.10: Apparatus for  $\mu$  measurements from 50 $^{\circ}$ C to 760 $^{\circ}$ C, showing position of insulated windings on test toroid (these extend around the complete circumference) and connections for power input and oscilloscope.



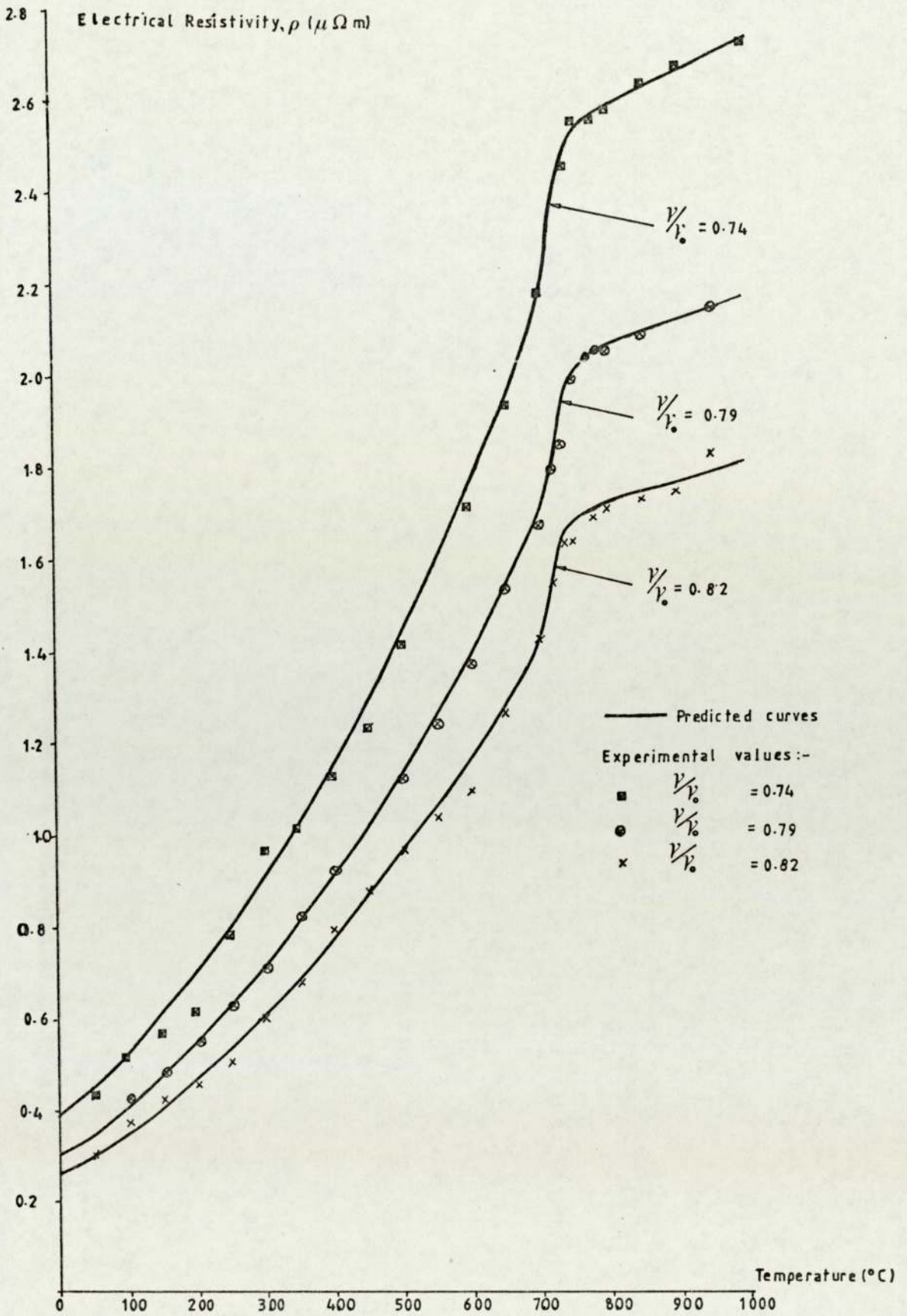


FIGURE 5.11: Measured electrical resistivity values for 'W4' powders with predicted curves from equation 5.4, where  $n=9$ .

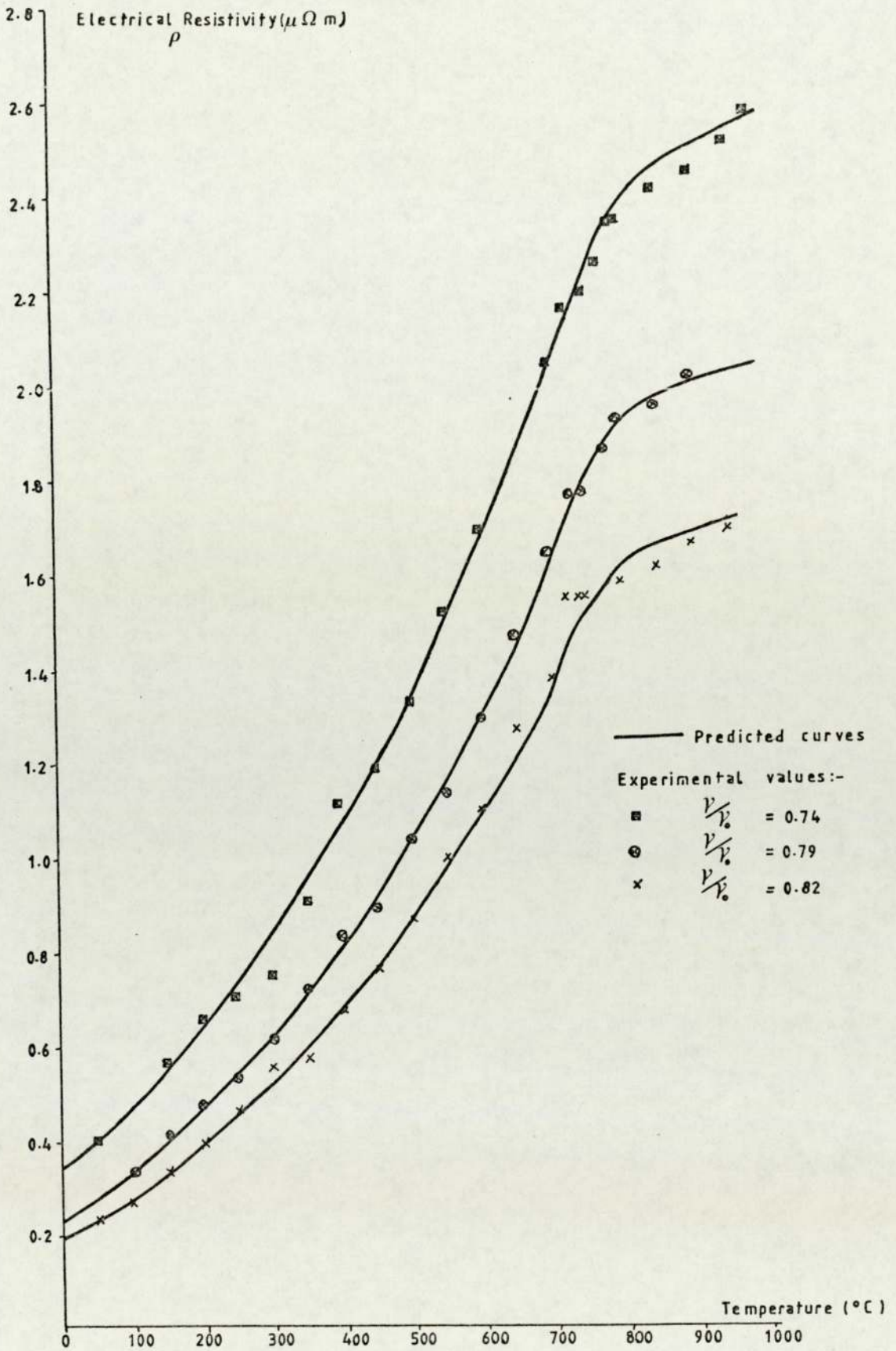


FIGURE 5.12: Measured electrical resistivity values for 'W78' powders with predicted curves from equations 5.4, where  $n=9$ .



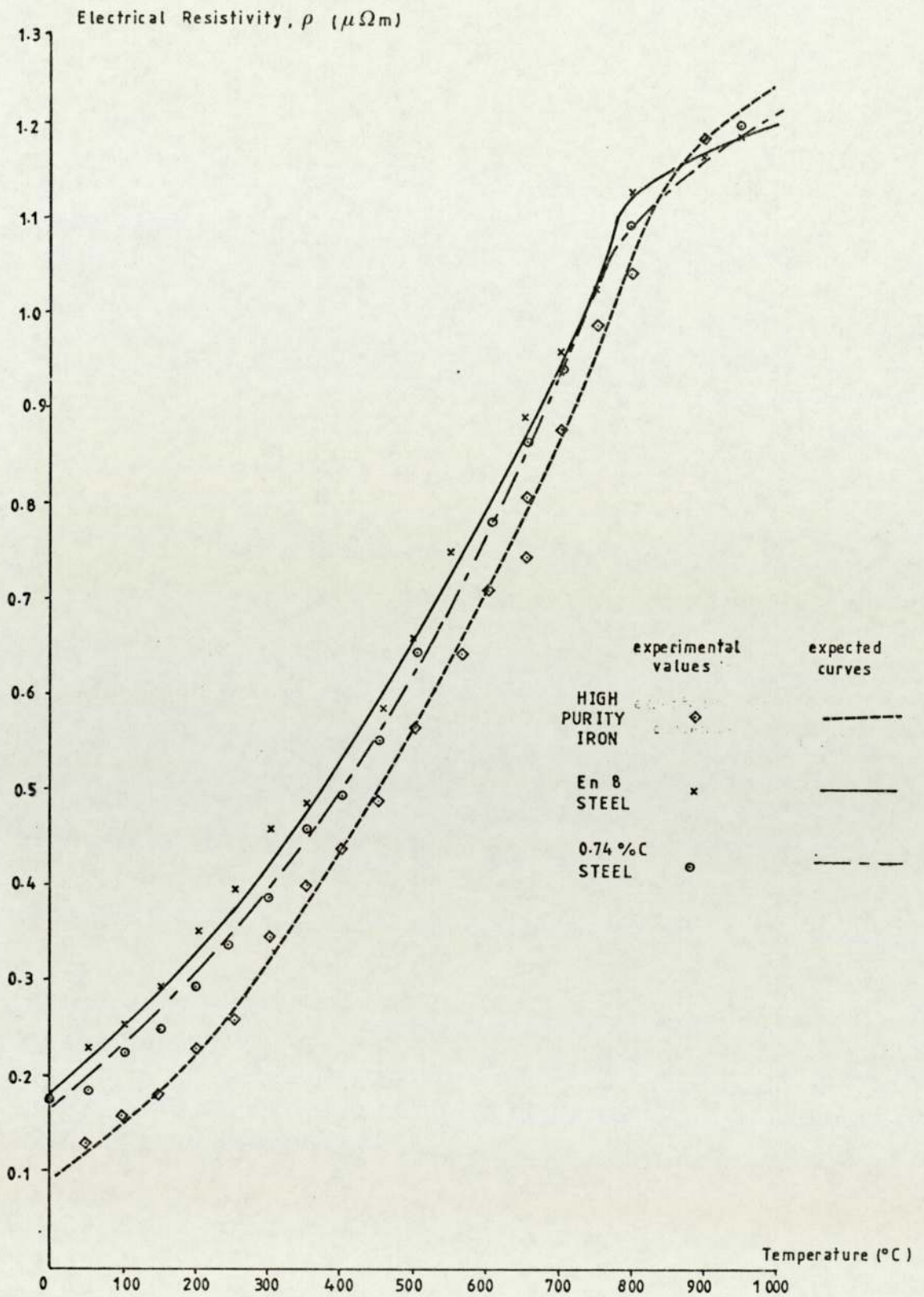


FIGURE 5.13: Measured electrical resistivity values for standard solid bars with the predicted curves from the literature [52].

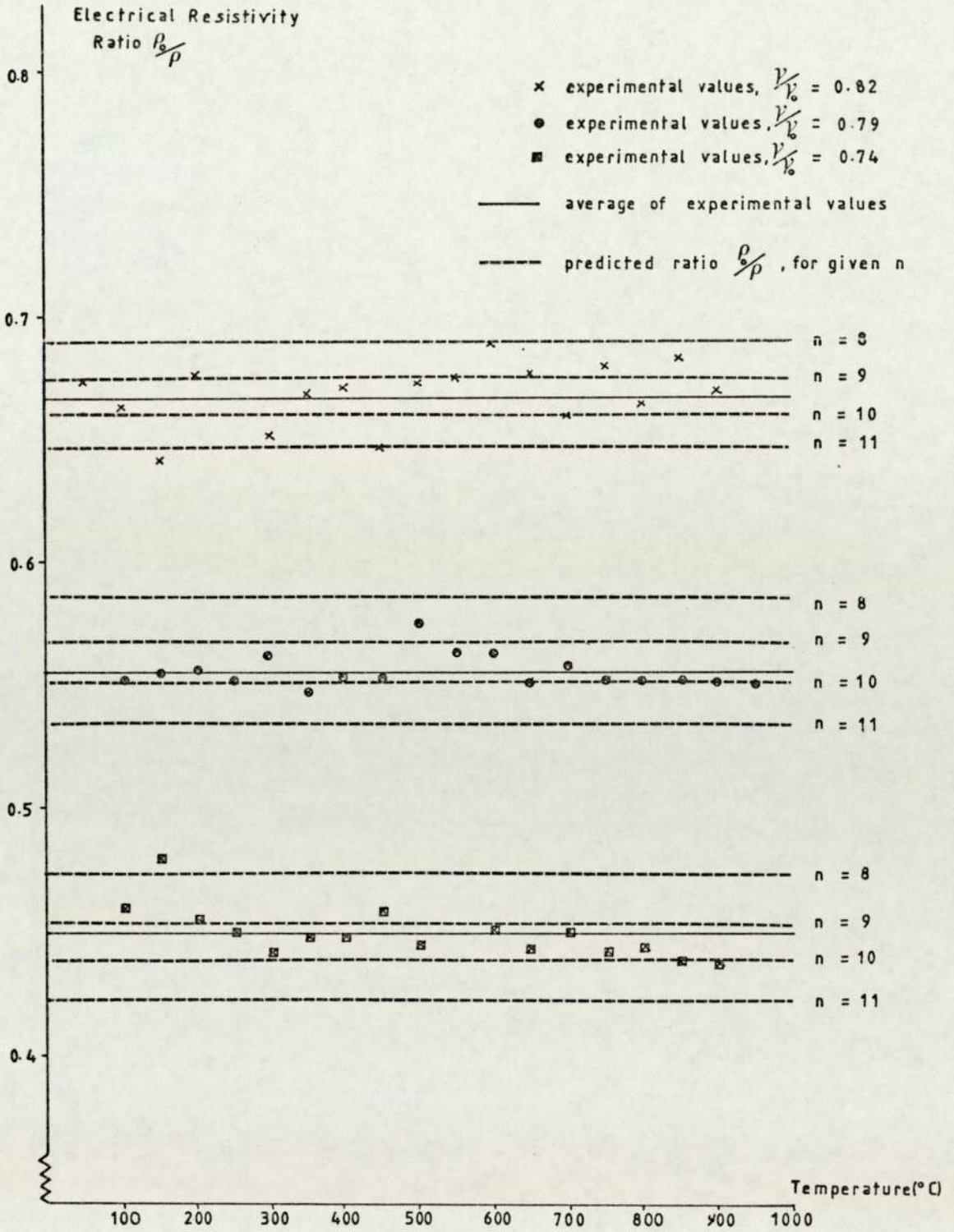


FIGURE 5.14: Measured ratio of 'W4' powder resistivity  $\rho$  to solid resistivity  $\rho_0$ , with predicted ratios (dashed lines) from equation 5.4 for various n values.



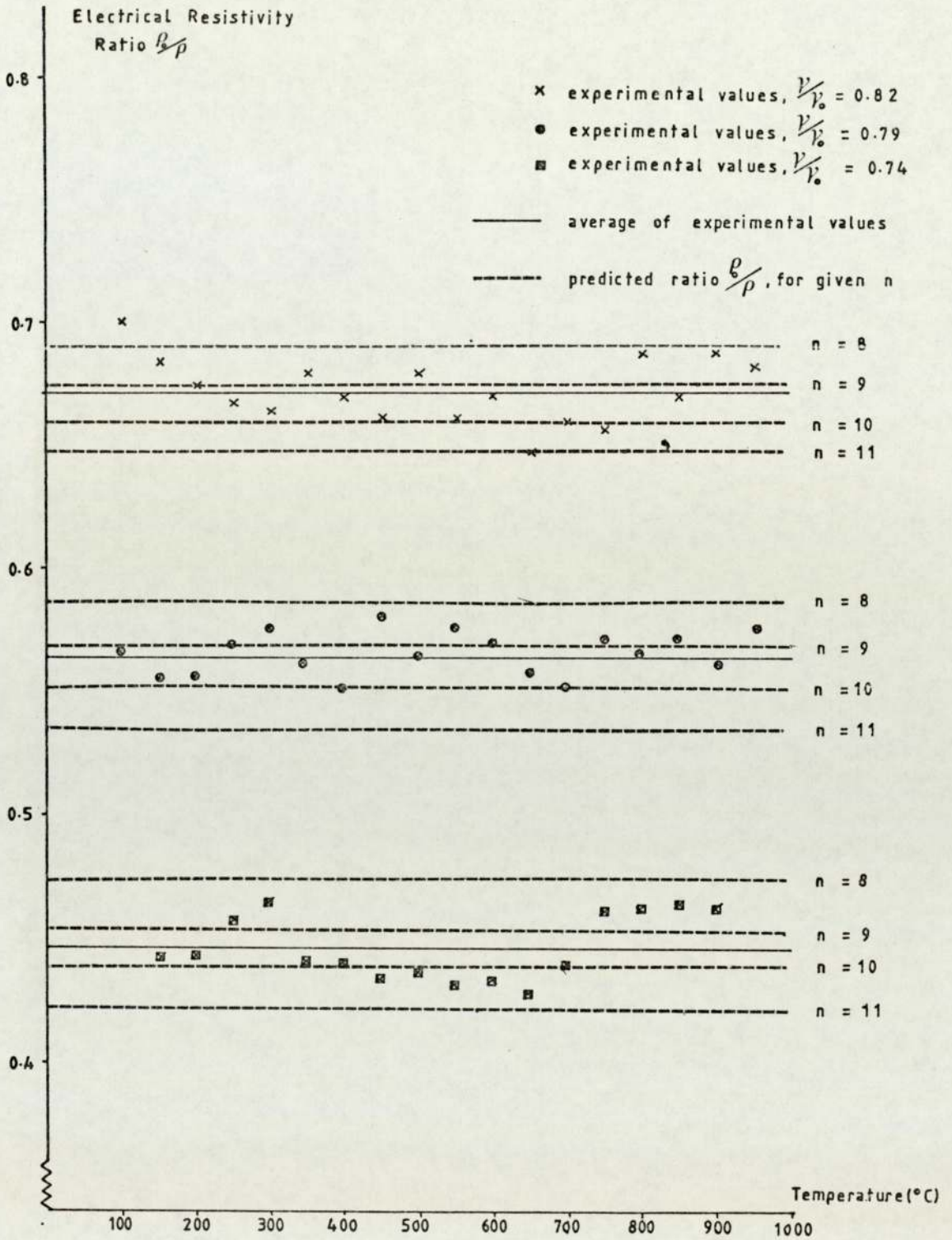


FIGURE 5.15: Measured ratio of 'W78' powder resistivity  $\rho$  to solid resistivity  $\rho_0$ , with predicted ratios (dashed lines) from equation 5.4, for various n values.

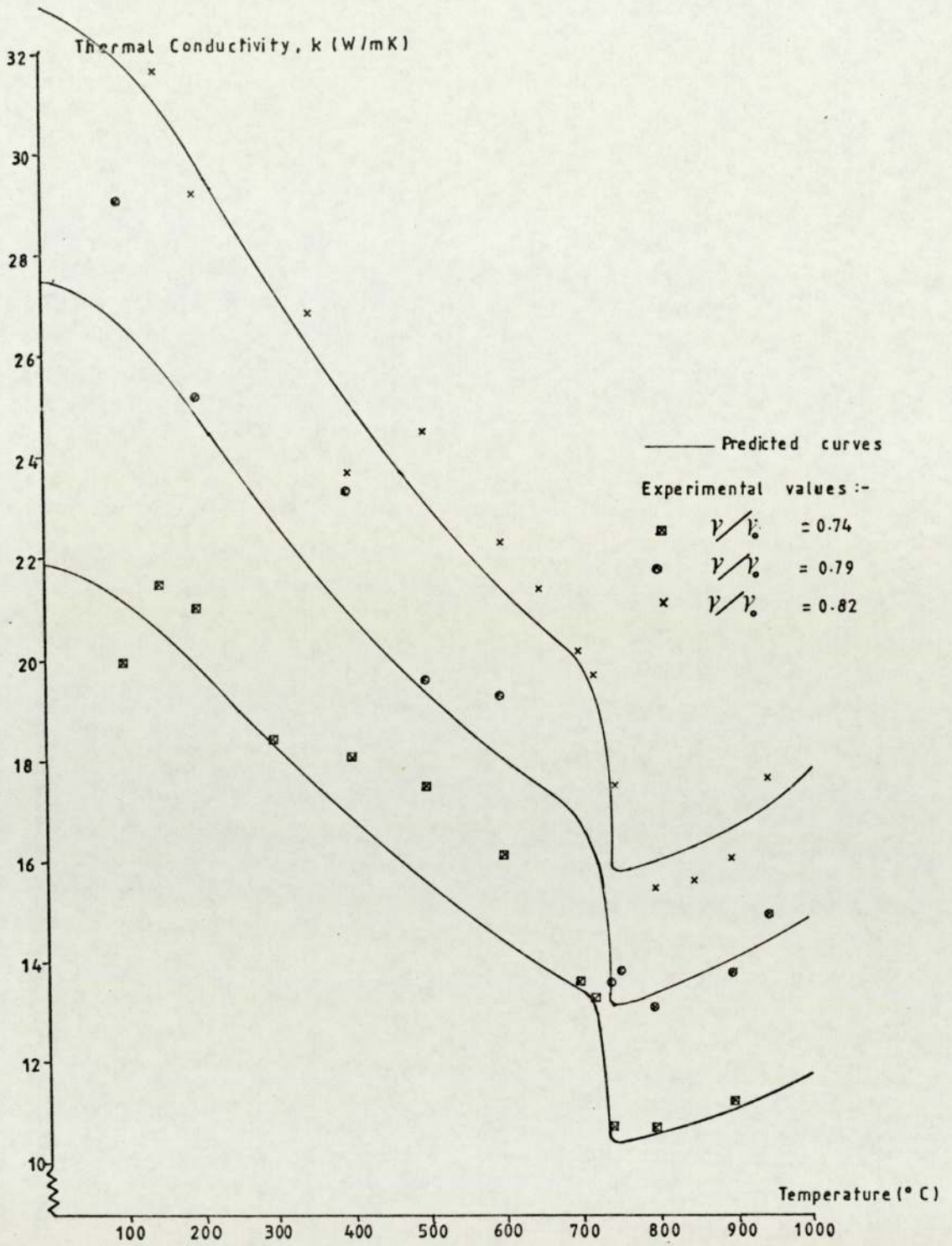


FIGURE 5.16: Measured thermal conductivity values for 'W4' powders with predicted curves from equation 5.4 where  $n = 9$ .



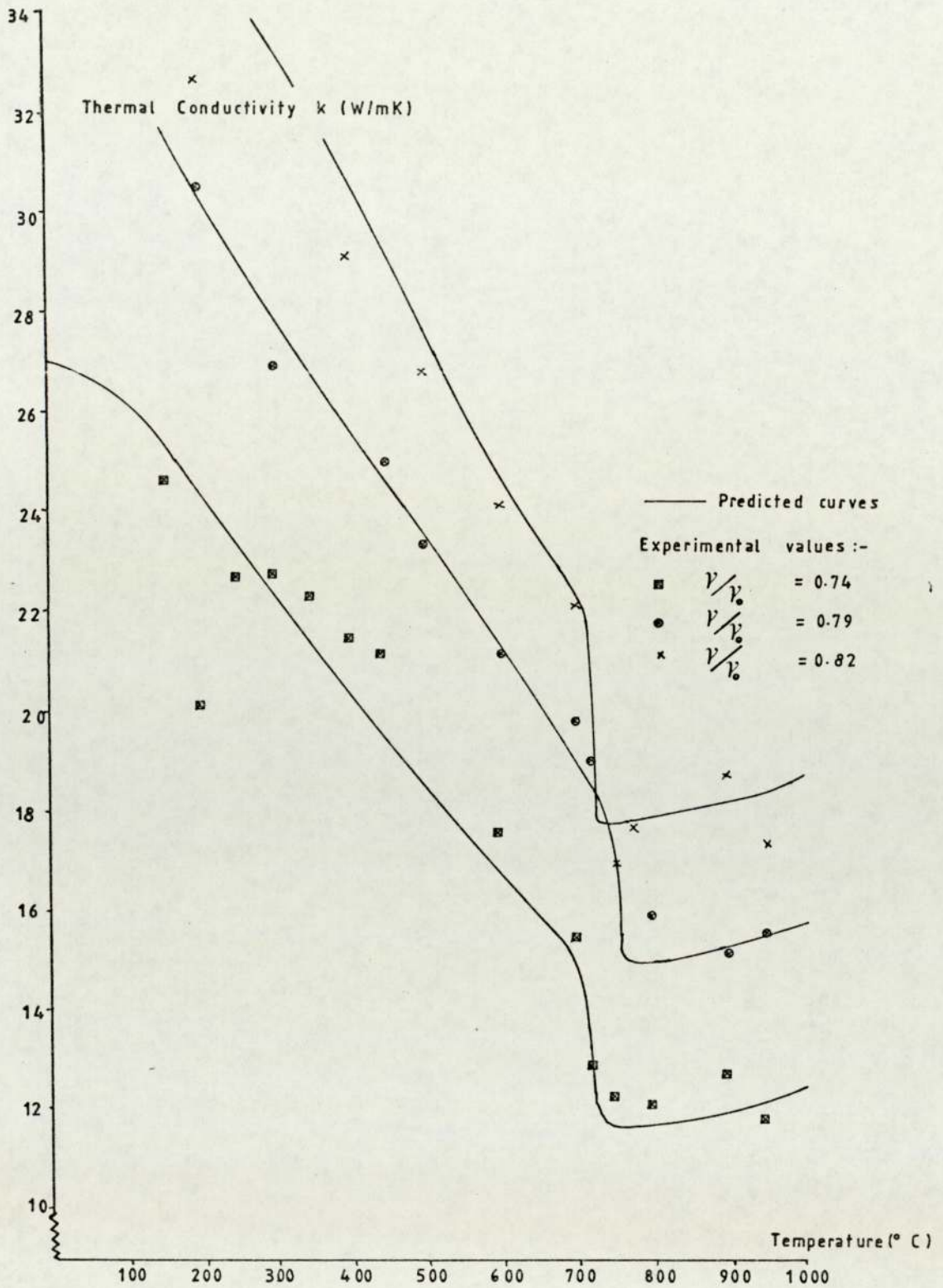


FIGURE 5.17: Measured thermal conductivity values for 'W78' powders with predicted curves from equation 5.4 where  $n=9$ .

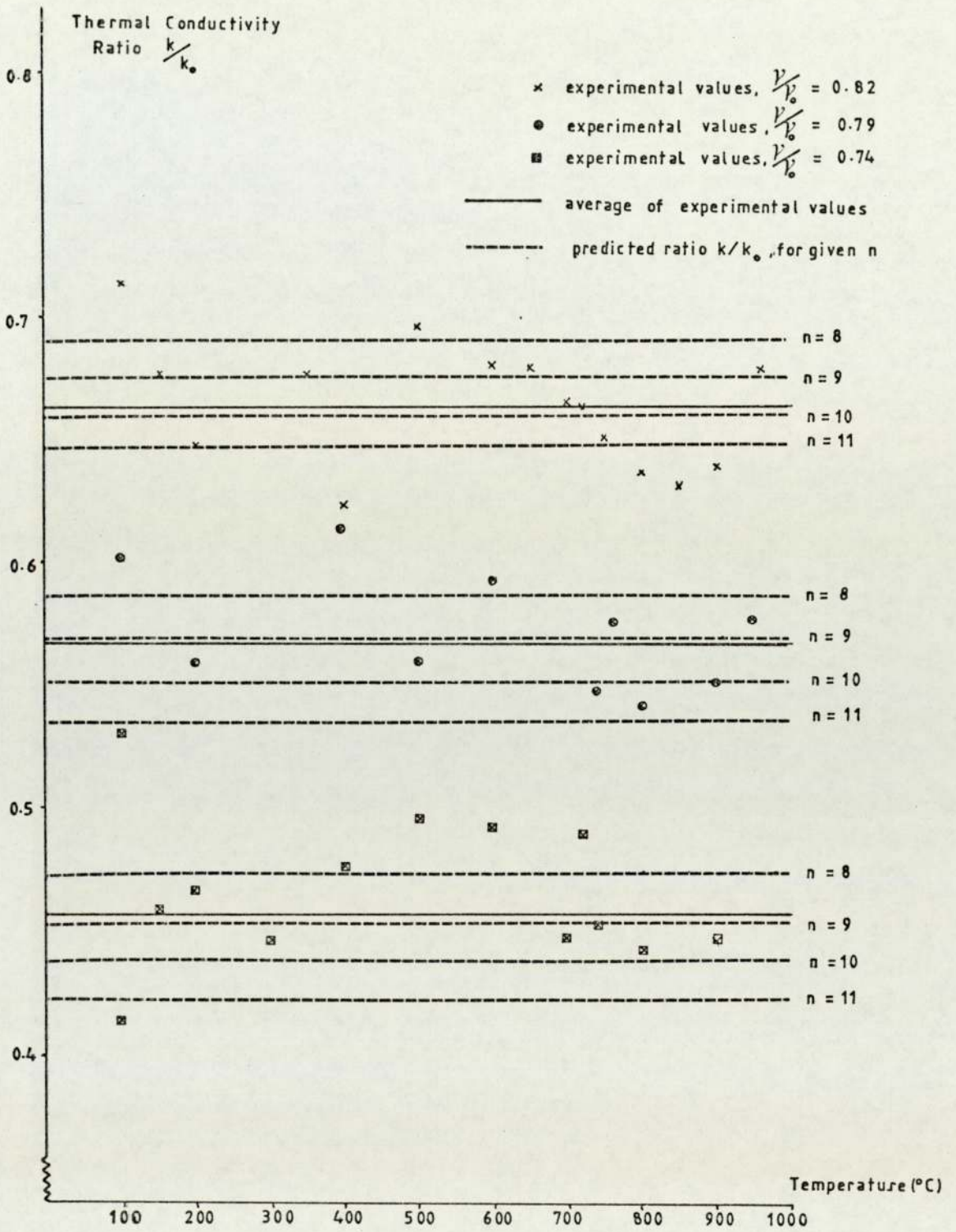


FIGURE 5.18: Measured ratio of 'W4' powder conductivity  $k$  to solid conductivity  $k_0$ , with predicted ratios (dashed lines) from equation 5.4, for various  $n$  values.



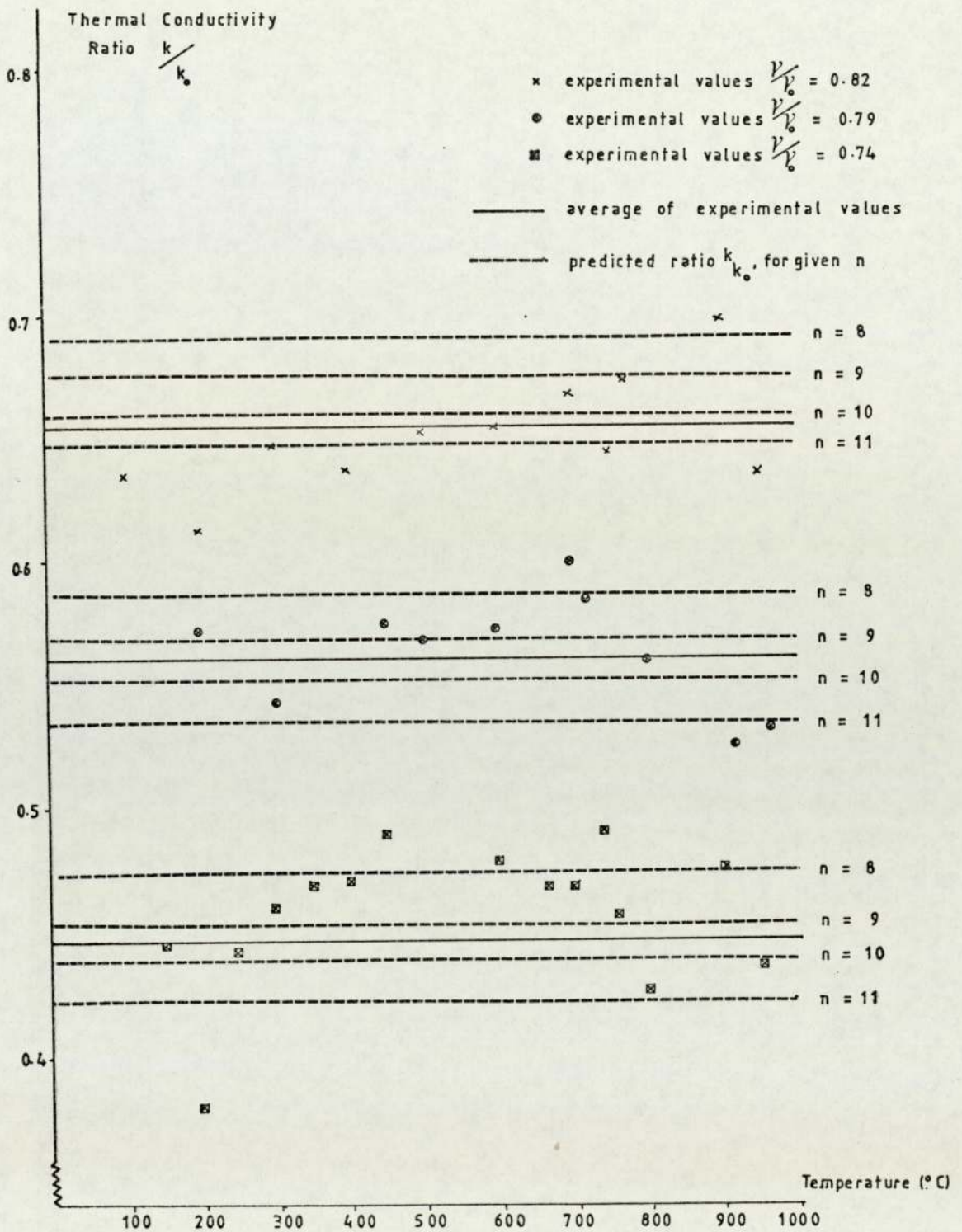


FIGURE 5.19: Measured ratio of 'W78' powder conductivity  $k$  to solid conductivity  $k_0$ , with predicted ratios (dashed lines) from equation 5.4, for various  $n$  values.

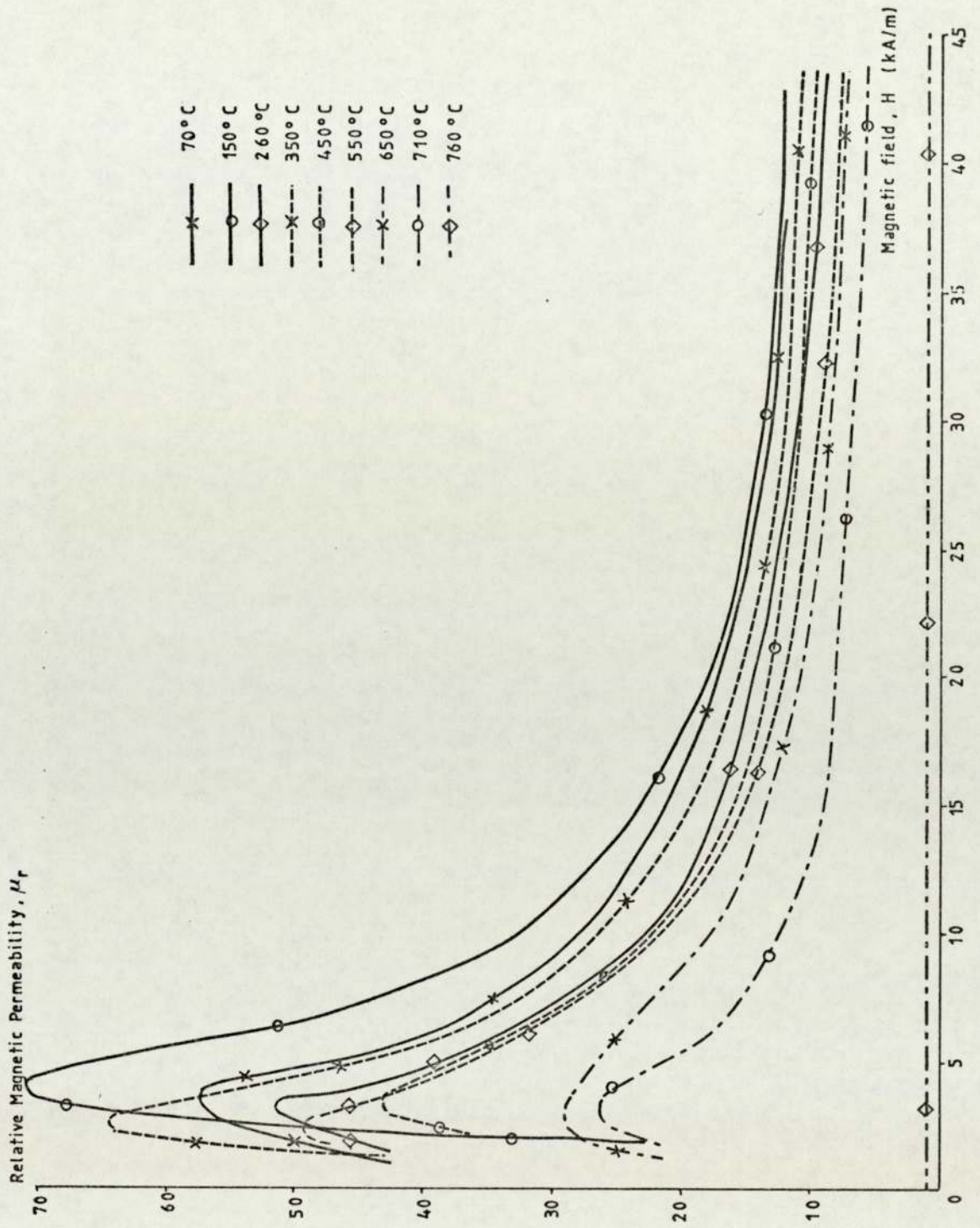


FIGURE 5.20: Measured relative magnetic permeability with magnetic field at temperatures up to 760°C for 'W4' powder of 0.74 relative density.



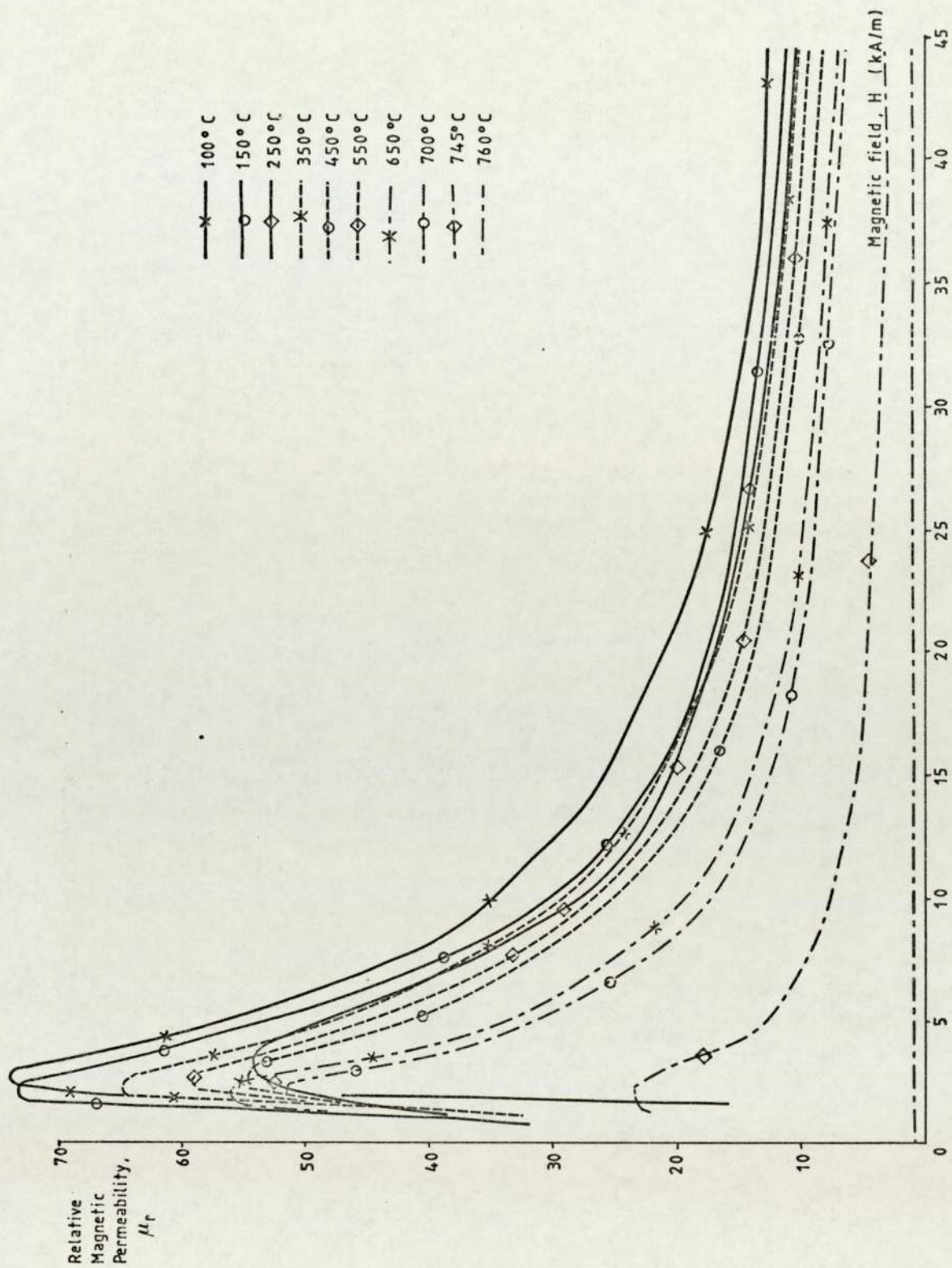


FIGURE 5.21: Measured relative magnetic permeability with magnetic field at temperatures up to 760°C for 'W4' powder of 0.79 relative density.

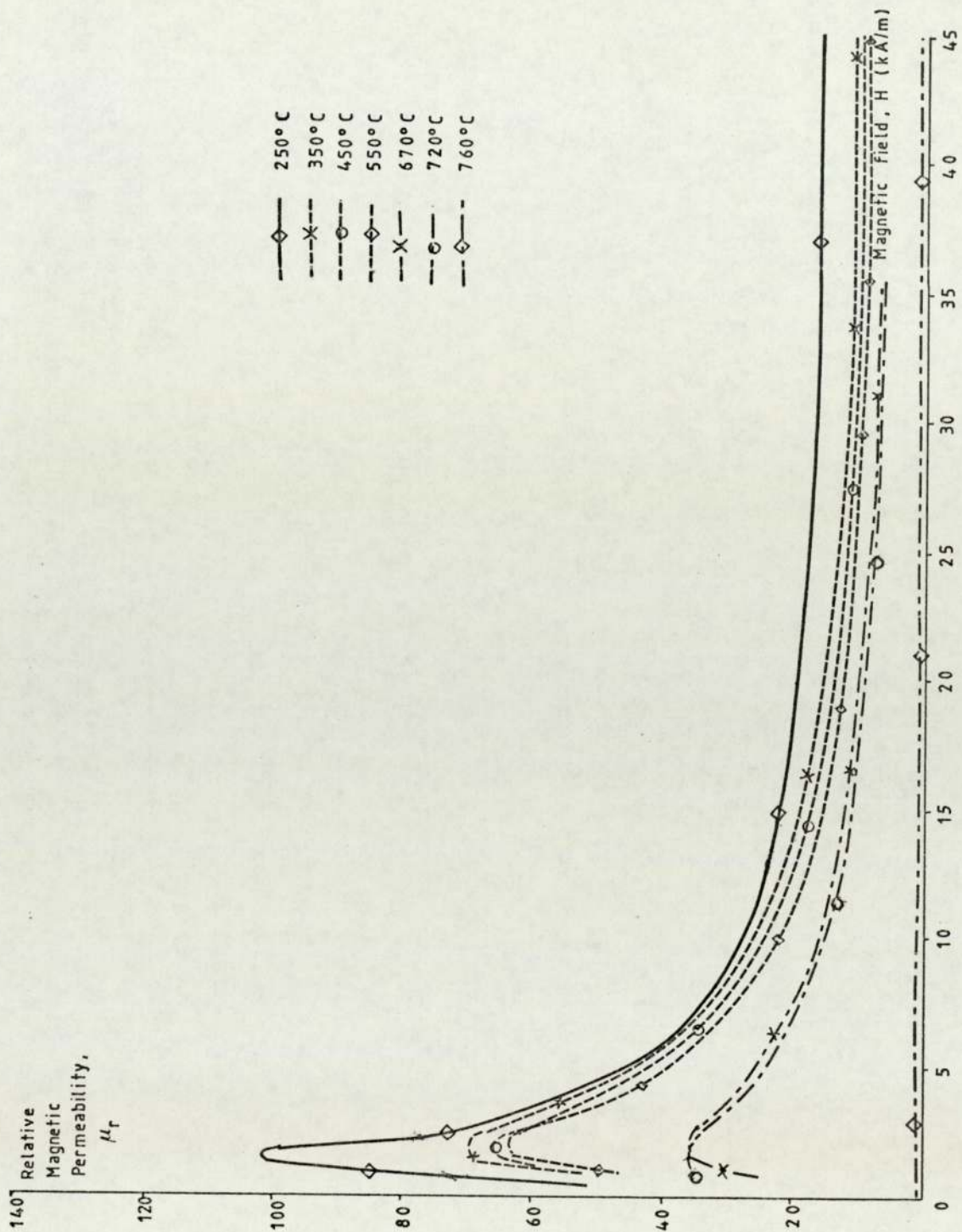


FIGURE 5.22: Measured relative magnetic permeability with magnetic field at temperatures up to 760°C for 'W4' powder of 0.82 relative density. Note change of scale from figure 5.21.



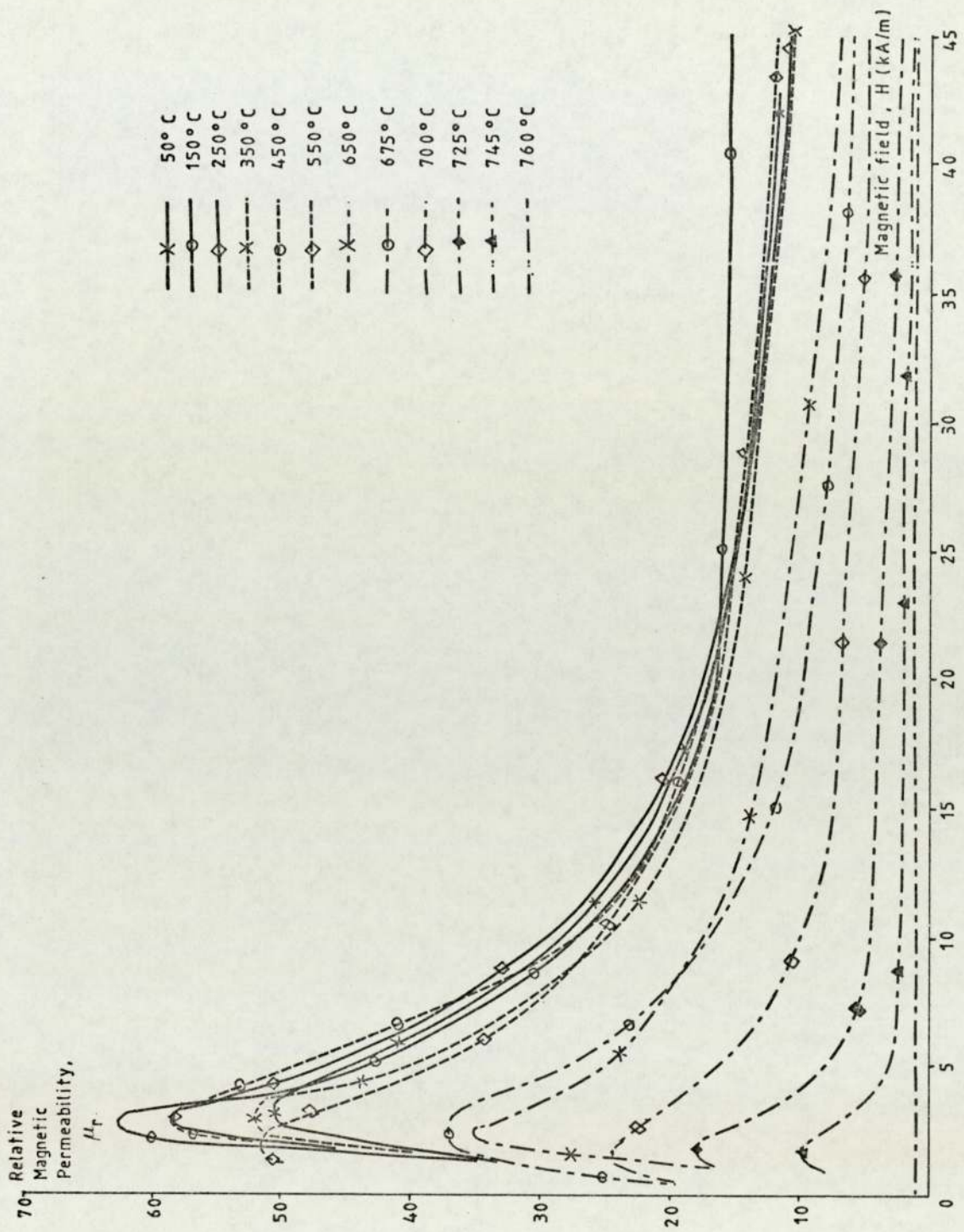


FIGURE 5.23: Measured relative magnetic permeability with magnetic field at temperatures up to 760°C for 'W78' powder of 0.74 relative density.

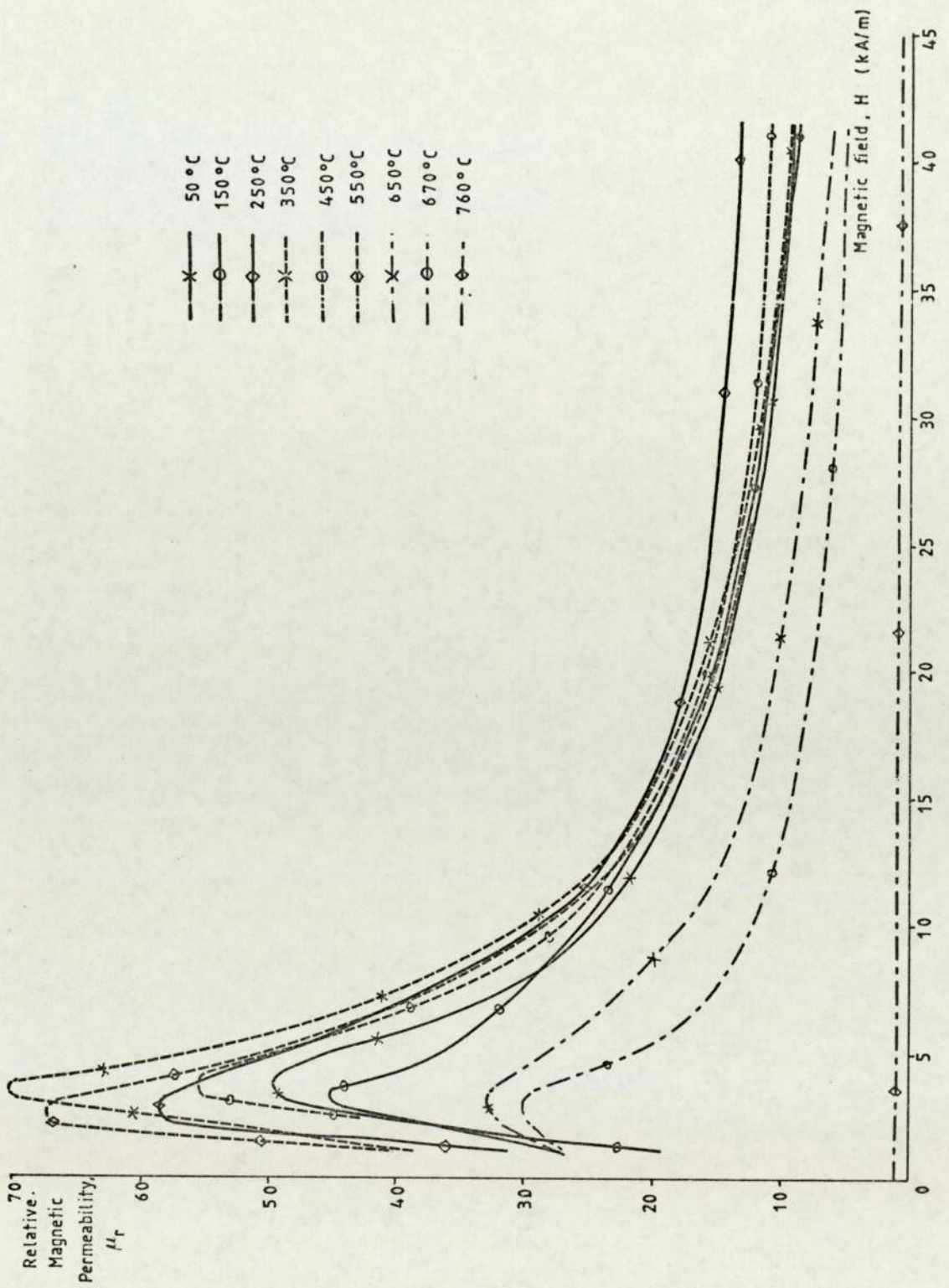


FIGURE 5.24: Measured relative magnetic permeability with magnetic field at temperatures up to 760°C for 'W78' powder of 0.79 relative density.



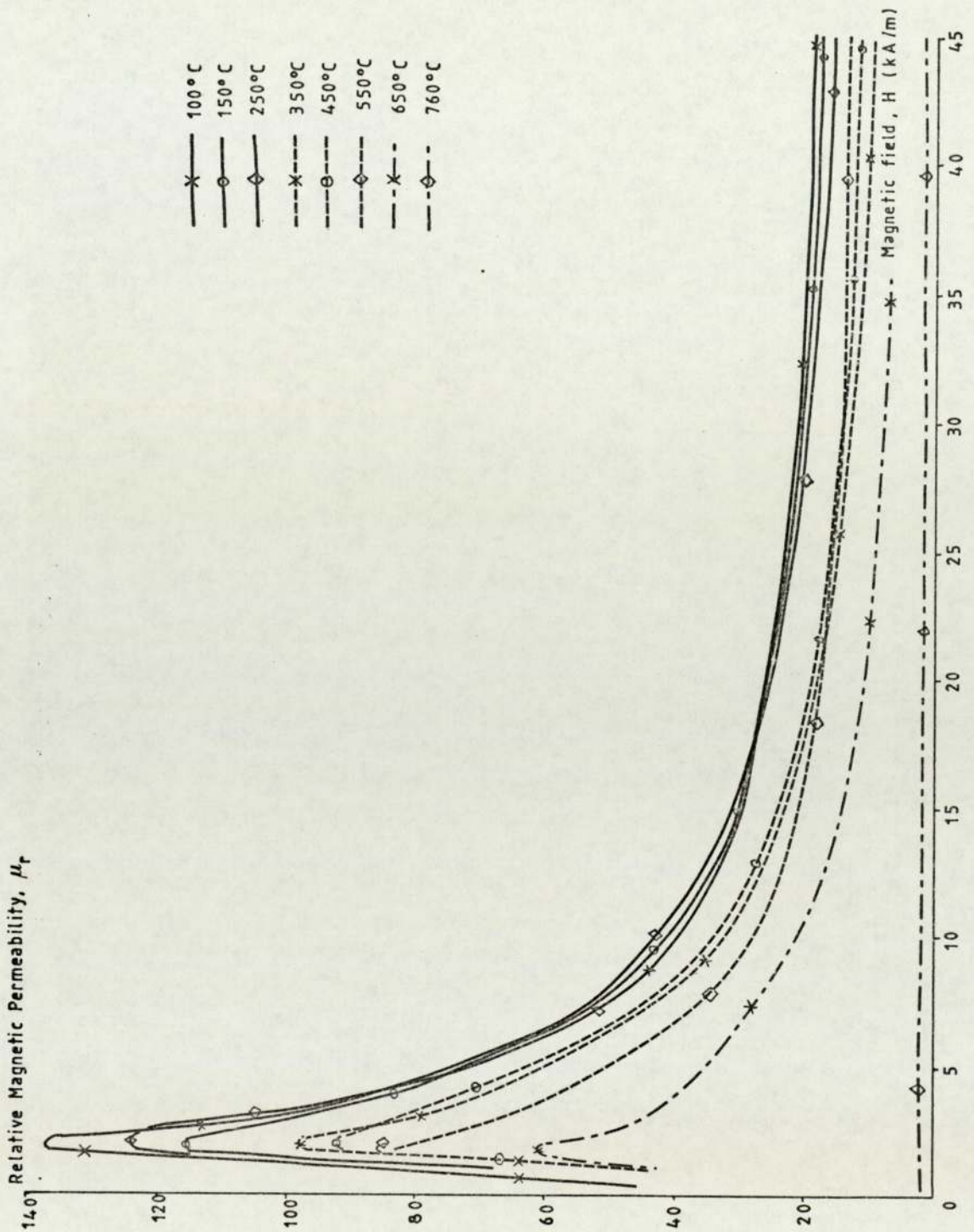


FIGURE 5.25: Measured relative magnetic permeability with magnetic field at temperatures up to 760°C for 'W78' powder of 0.82 relative density.

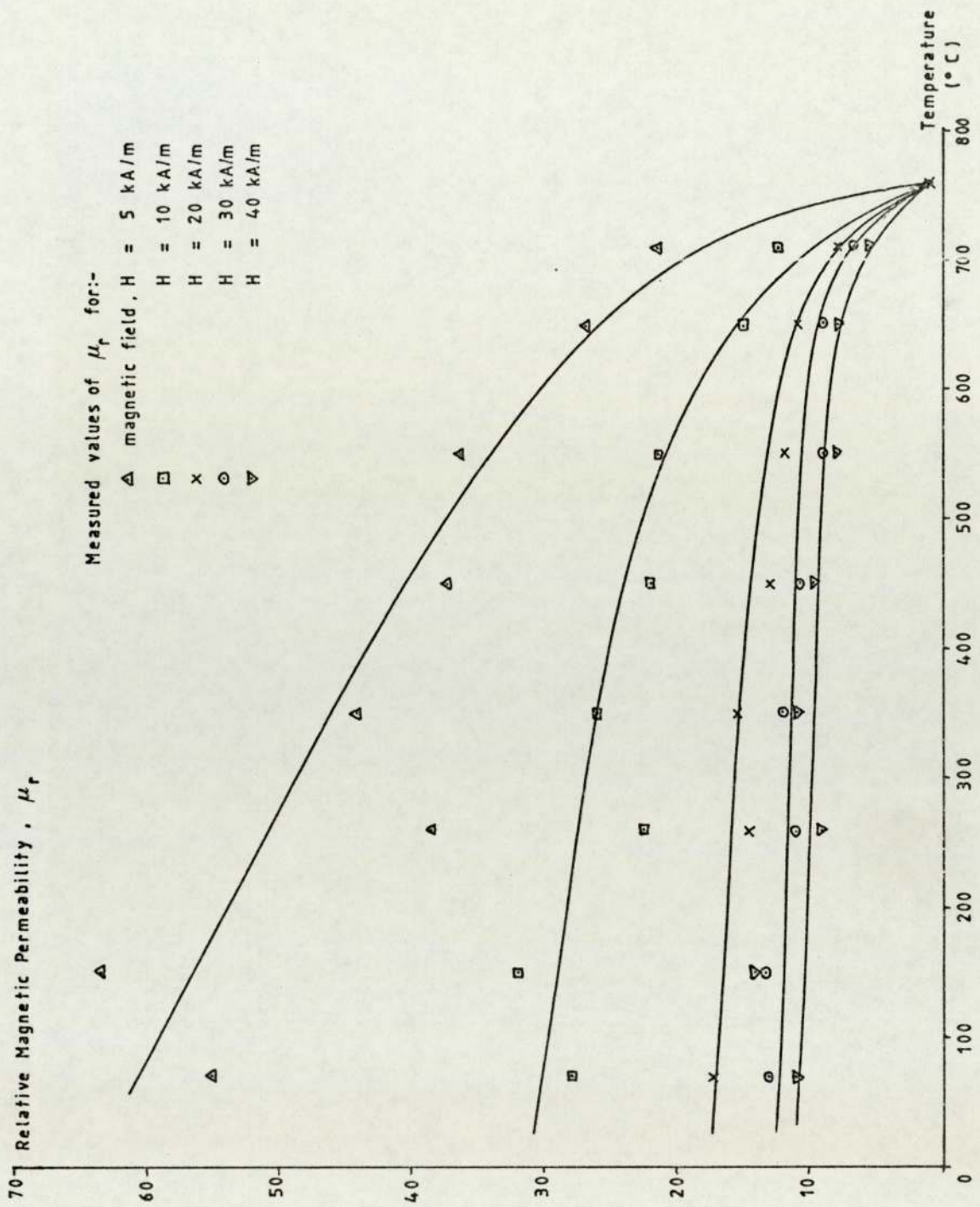


FIGURE 5.26: Measured relative magnetic permeability with temperature at various magnetic fields for 'W4' powder of 0.74 relative density.



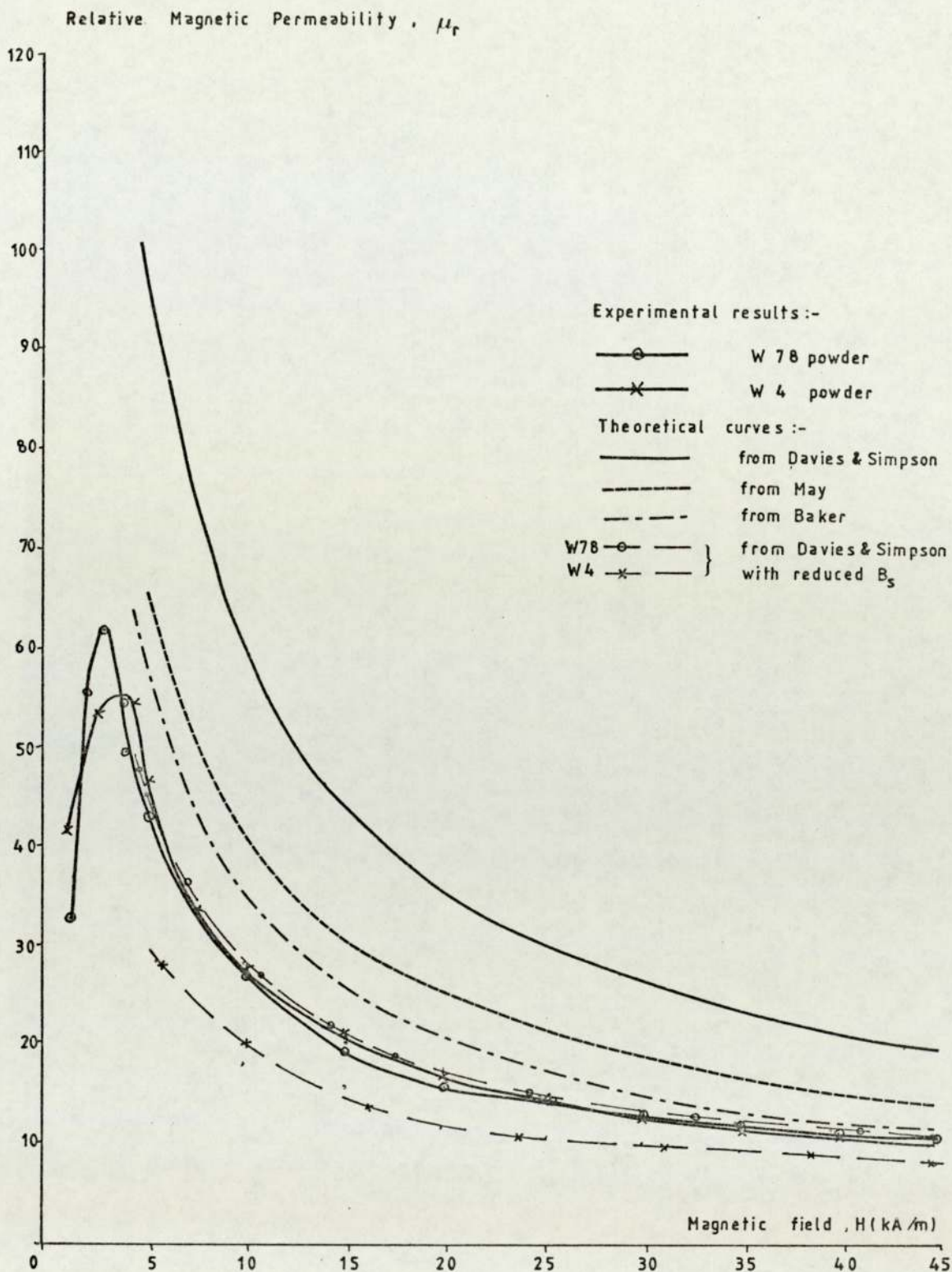


FIGURE 5.27: Measured  $\mu_r$  values for 'W4' and 'W78' powders of 0.74 relative density at the lowest temperatures recorded, with theoretical curves from equations 5.7-5.10 using the formula  $\mu = (\mu_s)^{3/2}$  of Legg & Given.

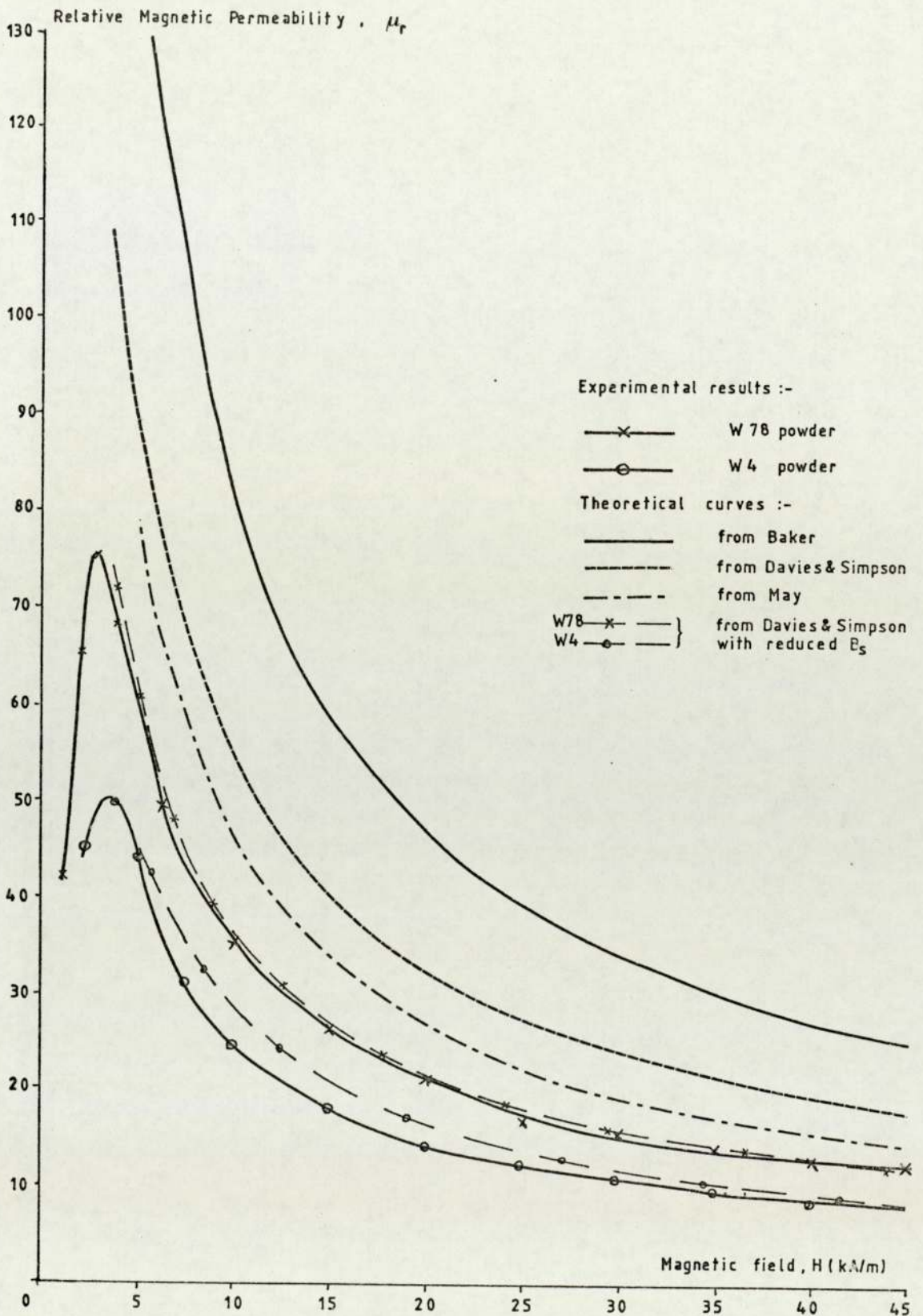


FIGURE 5.28: Measured  $\mu_r$  values for 'W4' and 'W78' of 0.79 relative density of the lowest temperatures recorded, with theoretical curves from equations 5.7-5.10 using the formula  $(\mu = (\mu_s)^{3/4})$  of Legg & Given.



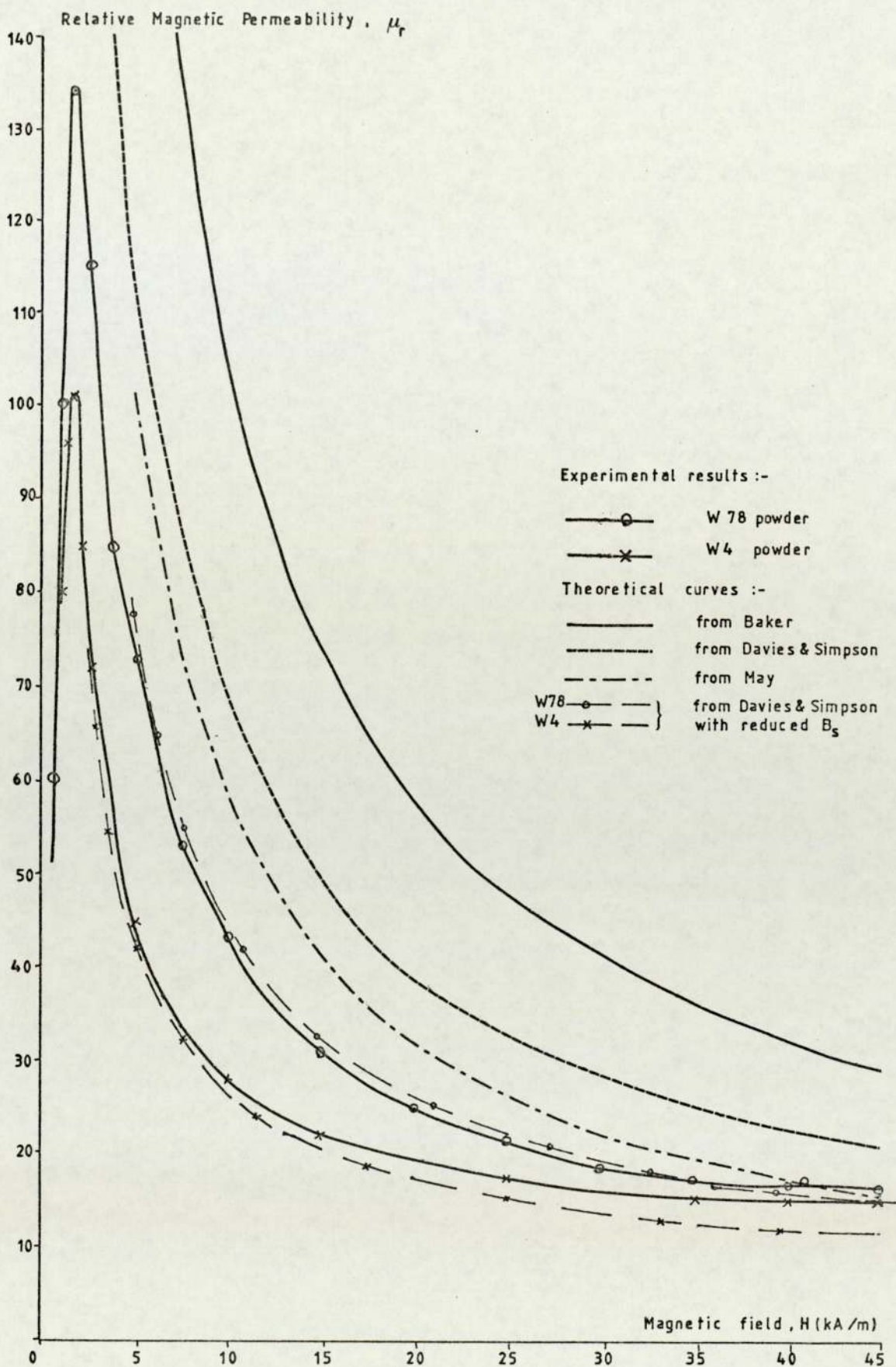


FIGURE 5.29: Measured  $\mu_r$  values for 'W4' and 'W78' powders of 0.82 relative density at the lowest temperatures recorded, with theoretical curves from equations 5.7-5.10 using the formula ( $\mu = (\mu_s)^{3/4}$ ) of Legg & Given.

CHAPTER SIX

SOLENOIDAL COIL DESIGN FOR SIMPLE SHAPES



## CHAPTER 6 : SOLENOIDAL COIL DESIGN FOR SIMPLE SHAPES

### 6.1 Introduction

In Chapter 3, the coil design theory, as presented in the literature, was shown to have limitations for the design of production coils of multiple sections. It does not help the coil designer to appreciate the influence of physical properties on the heating pattern within the workload. In this chapter, the design method is modified to overcome some of these limitations, and a simple iterative process described for plotting the temperature distribution within a billet shaped workload. The predicted temperature profile is compared with measured values for solid material to show the degree of accuracy achieved.

Section 6.2.1 describes the extensions to the equivalent circuit coil design method and derives the load power densities used for the iterative thermal solution. In section 6.3, the predicted temperature field during heating is compared with experimental values recorded using methods described in Chapter 7.

## 6.2 Revised Coil Design Calculation Method

Because the material properties vary with temperature, the workload presents a continuously altering electrical load to the coil. Ideally, the coil and load should be matched at all times to accommodate these changes, thus for continuous through-put, this corresponds to a coil infinitely 'tunable' along its length. In practice this is approximated by having a number of coil sections, each imposing a particular temperature profile on the heated part. Here the method of Chapter 3 is extended to give a better approximation for designing the solenoidal coil to give the desired heating effect, efficiently.

In the improved method, the heating is divided into sub-Curie and super-Curie phases. Each section is treated individually for equivalent circuit calculations, and the power density found for a subsequent iterative calculation of temperatures. The following detailed example relates to the same two-section coil considered in section 3.4.

### 6.2.1 Calculation of Power Density

#### 6.2.1.1 First Section (sub-Curie)

Initially, a value of  $\mu_r$  must be found. This is related to the field strength by equation 5.10.

However  $H$  is found from the coil amp-turns and coil length  $l_c$ , only after the equivalent circuit calculations



are performed. To enter this closed cycle, a magnetic permeability is assumed and then compared with  $H=I_c N_c / \ell_c$ . The assumed  $\mu_r$  is then adjusted until consistent results are obtained.

The average electrical resistivity from  $20^\circ\text{C}$  to  $760^\circ\text{C}$  is given by,

$$\begin{aligned} \rho_{20-760} &= \frac{1}{4} \left\{ \sqrt{\rho_{20}} + \sqrt{\rho_{760}} \right\}^2 \\ &= 0.57 \mu\Omega\text{m} \end{aligned} \quad (3.30)$$

Assuming a magnetic field strength  $H_{\text{om}} = 71 \text{ kA/m}$ , the relative magnetic permeability  $\mu_r$  is taken from

$$\mu_r = \frac{734\,000}{H^{0.92}} = 22$$

Penetration depth  $\delta$ , is

$$\delta_w = \sqrt{\frac{2 \rho_{20-760}}{\mu 2 \pi f}}$$

Here the workload penetration depth is

$$\delta_w = 1.3 \text{ mm}$$

Similarly, the coil penetration depth,

$$\delta_c = 1.2 \text{ mm}$$

The ratio  $d/\delta$ , workload diameter to penetration depth, is used to calculate  $p$  and  $q$ ,

$$d_w / \delta_w = 39.23$$

and

$$p = 0.049$$

$$q = 0.051$$

The equivalent circuit resistances and reactances are found to be

$$\begin{aligned} R_w/N_c^2 &= K \quad 2.17 \times 10^{-3} \quad \Omega \\ R_c/N_c^2 &= K \quad 2.59 \times 10^{-4} \quad \Omega \\ X_c/N_c^2 &= K \quad 2.59 \times 10^{-4} \quad \Omega \\ X_w/N_c^2 &= K \quad 2.24 \times 10^{-3} \quad \Omega \\ X_g/N_c^2 &= K \quad 6.23 \times 10^{-3} \quad \Omega \end{aligned}$$

where

$$\begin{aligned} K &= 103.6 \times 10^{-3} N_c^2 \quad \Omega/m^2 \\ Z &= 9.39 \times 10^{-4} \quad \Omega \end{aligned}$$

the coil efficiency  $\eta = 0.894$  relates the power generated in the coil  $P_c$  to the power absorbed by the workload  $P_w$ ,

$$P_c = P_w / \eta$$

In the first section, below Curie temperature,

$$\begin{aligned} P_w &= 33.5 \text{ kW} \\ P_c &= 37.5 \text{ kW} \\ \cos \varphi &= 0.268 \\ (VA)_c &= 139.7 \text{ kVA} \end{aligned}$$

Coil volts per turn and ampere turns are, respectively,

$$V_c/N_c = \sqrt{\{(VA)_c (Z/N_c^2)\}}$$

and

$$I_c N_c = \sqrt{\{(VA)_c / (Z/N_c^2)\}}$$

With substitution these give,

$$\text{and} \quad V_c/N_c = 11.45 \text{ V}$$

$$I_c N_c = 12.2 \text{ kA}$$

The billet surface reaches Curie temperature before the end of the first coil section. The approximate coil length,  $l_c = 170\text{mm}$ , gives

$$H = 71 \text{ kA/m}$$



### 6.2.1.2 First Section (super-Curie)

The calculations of section 6.2.1.1 are repeated for non-magnetic billets in the first coil section. These are heated from  $760^{\circ}\text{C}$  to an estimated  $850^{\circ}\text{C}$ , the surface temperature at the end of the first section. Coil parameters are relatively insensitive to a small deviation from this final temperature.

$$\begin{aligned} \rho_{760-850} &= 0.33 \mu\Omega\text{m} \\ \delta_w &= 4.57 \text{ mm} \\ d_w/\delta_w &= 11.2 \end{aligned}$$

giving

$$\begin{aligned} p &= 0.162 \\ q &= 0.179 \\ \mu_r &= 1 \end{aligned}$$

thus,

$$\begin{aligned} R_w/N_c^2 &= K \quad 3.30 \times 10^{-4} \Omega \\ R_c/N_c^2 &= K \quad 2.59 \times 10^{-4} \Omega \\ X_c/N_c^2 &= K \quad 2.59 \times 10^{-4} \Omega \\ X_w/N_c^2 &= K \quad 3.36 \times 10^{-4} \Omega \\ X_g/N_c^2 &= K \quad 6.23 \times 10^{-3} \Omega \end{aligned}$$

The efficiency,

$$\eta = 0.56$$

so

$$\begin{aligned} \cos \varphi &= 0.0845 \\ P_w &= 11.9 \text{ kW} \\ P_c &= 21.2 \text{ kW} \\ (\text{VA})_c &= 251 \text{ kVA} \\ V_c/N_c &= 13.5 \text{ V} \\ I_c N_c &= 18.7 \text{ kA} \end{aligned}$$

The remaining coil length is

$$l_c = 0.135 \text{ m}$$

thus

$$H = 134.1 \text{ kA/m}$$

### 6.2.1.3 Second Section

Super-Curie heating from 850°C to 1250°C assigns

$$\rho_{850-1250} = 1.18 \mu\Omega\text{m}$$

$$\delta_c = 1.2 \text{ mm}$$

$$\delta_w = 8.64 \text{ mm}$$

$$d_w/\delta_w = 5.9$$

giving

$$p = 0.28$$

$$q = 0.33$$

$$\mu_r = 1$$

thus

$$R_w/N_c^2 = K \quad 5.72 \times 10^{-4} \quad \Omega$$

$$R_c/N_c^2 = K \quad 2.76 \times 10^{-4} \quad \Omega$$

$$X_c/N_c^2 = K \quad 2.76 \times 10^{-4} \quad \Omega$$

$$X_w/N_c^2 = K \quad 6.74 \times 10^{-4} \quad \Omega$$

$$X_g/N_c^2 = K \quad 6.23 \times 10^{-3} \quad \Omega$$

$$K = 103.6 \times 10^{-3} N_c^2 \quad \Omega/\text{m}^2$$

The efficiency is

$$\eta = 0.675$$

and since

$$P_w = 23 \text{ kW}$$

then

$$P_c = 34.1 \text{ kW}$$

$$\cos\phi = 0.116$$

$$(VA)_c = 294.2 \text{ kVA}$$

Volts per turn

$$V_c/N_c = 14.9 \text{ V}$$

and ampere-turns

$$I_c N_c = 197 \text{ kA}$$

follow.

Therefore the magnetic field strength is

$$H = 65.1 \text{ kA/m}$$

The magnetic fields are substituted in the equation



	POWER DENSITY (MW/m <sup>2</sup> )		average k (W/mK)	dθ dt, (K/s)	TIME (s)	TEMPERATURE (°C)					
	φ	φ-φ <sub>c</sub>				INITIAL			FINAL		
						θ <sub>c</sub>	θ <sub>m</sub>	θ <sub>s</sub>	θ <sub>c</sub>	θ <sub>m</sub>	θ <sub>s</sub>
First Coil Section	1.08	1.08	46.75	-	13.8	20	20	20	147	313	413
	1.08	1.07	39.75	18.4	5.44	147	313	413	242	413	543
	1.08	1.07	36.70	17.0	5.89	242	413	543	328	513	656
	1.08	1.06	34.00	15.4	6.48	328	513	656	414	613	768
	1.08	1.06	31.60	13.5	7.41	414	613	768	481	713	800
	1.08	1.05	30.00	12.3	3.81	481	713	800	538	760	828
	0.585	0.551	30.00	-	11.5	538	760	828	646	822	868
	0.585	0.496	25.00	-	16.0	646	822	868	788	899	949
	0.585	0.496	25.00	-	10.7	788	899	949	857	958	1011
	0.585	0.496	25.00	-	7.7	857	958	1011	892	993	1033
Second Coil Section	-	-	-	-	-	-	-	-	-	-	-
	0.239	0.186	27.30	-	15.4	892	993	1033	976	1012	1024
	0.239	0.186	27.30	-	15.4	976	1012	1024	1025	1052	1064
	0.239	0.186	27.90	22.1	7.5	1025	1052	1064	1047	1074	1086
	0.239	0.186	27.90	22.1	7.5	1047	1074	1086	1069	1096	1107
	0.239	0.186	27.90	22.1	7.5	1069	1096	1107	1091	1118	1129
	0.239	0.186	27.90	22.1	7.5	1091	1118	1129	1104	1131	1142
	0.239	0.186	27.90	22.1	7.5	1091	1118	1129	1104	1131	1142
	0.239	0.186	27.90	22.1	7.5	1091	1118	1129	1104	1131	1142
	0.239	0.186	27.90	22.1	7.5	1091	1118	1129	1104	1131	1142

Table 6.1 : Summary of temperature distribution calculations for solid En8 billet. See p143.

$$\mathcal{P}_w = \frac{\mu 2 \pi f H^2 A_w p}{\pi d_w}$$

giving the workload power densities in the first section (sub-Curie),

$$\mathcal{P}_1 = 1.08 \text{ MW/m}^2$$

in the first section (super-Curie),

$$\mathcal{P}_1 = 0.59 \text{ MW/m}^2$$

and in the second section

$$\mathcal{P}_2 = 0.24 \text{ MW/m}^2$$

The equivalent circuit results may be developed further for coil turns, capacitors etc., as was discussed in Chapter 3. Here we need only the power densities for the following thermal solution.

### 6.2.2 Iterative Thermal Solution

Although calculation times and intervals between steps would be reduced by the use of a computer, for ease of presentation a manual calculation is given here. A summary of the approximate solution steps appears in table 6.1 and is described below.

From ambient temperature, the billet temperature rises in the first coil section, according to the transient stage of power input density  $\mathcal{P}_1$ . This is represented by a single step, but may be considered in detail using figure A2.2. The steady-state conditions are represented by considering mean temperature rise intervals of 100°C. During each step, the temperature at the billet surface and centre are re-calculated from the prevailing power density and the average thermal conductivity. Due regard is shown for the



effect of radiation on  $\mathcal{P}$ . The influence of finite current depth is taken into account by reducing the  $(\theta_s - \theta_m)$  difference by the amount indicated in figure 3.4 of the temperature profile with various  $d/\delta$  ratios. As soon as the surface temperature reaches approximately  $760^\circ\text{C}$ , the power density used to calculate  $(\theta_s - \theta_m)$  is reduced to the super-Curie value  $\mathcal{P}'_1$ . The temperature difference  $(\theta_m - \theta_c)$  continues to be calculated from  $\mathcal{P}'_1$ , until  $\theta_m = \theta_{\text{curie}}$ . There the temperature field imposed by  $\mathcal{P}'_1$  is allowed to 'soak' while the transient stage of  $\mathcal{P}'_1$  is superimposed for the duration of the Curie transition period.

During any remaining time in the first coil section, the super-Curie power transient temperature rise is completed and the steady-state profile is established. A similar superposition occurs as the second, and subsequent coil sections are entered. The  $\mathcal{P}'_1$  distribution equalizes with a soaking period and the new power density  $\mathcal{P}'_2$  temperatures are added.

### 6.3 Comparison of Calculated and Measured Temperatures

Figure 6.1 shows the calculated centre, surface and mean temperatures from table 6.1, plotted with measured values at  $r = 0, R/4, R/2, 3R/4$  and  $R$ , where  $R$  is the billet radius. Details of the experimental method may be found in Chapter 7.

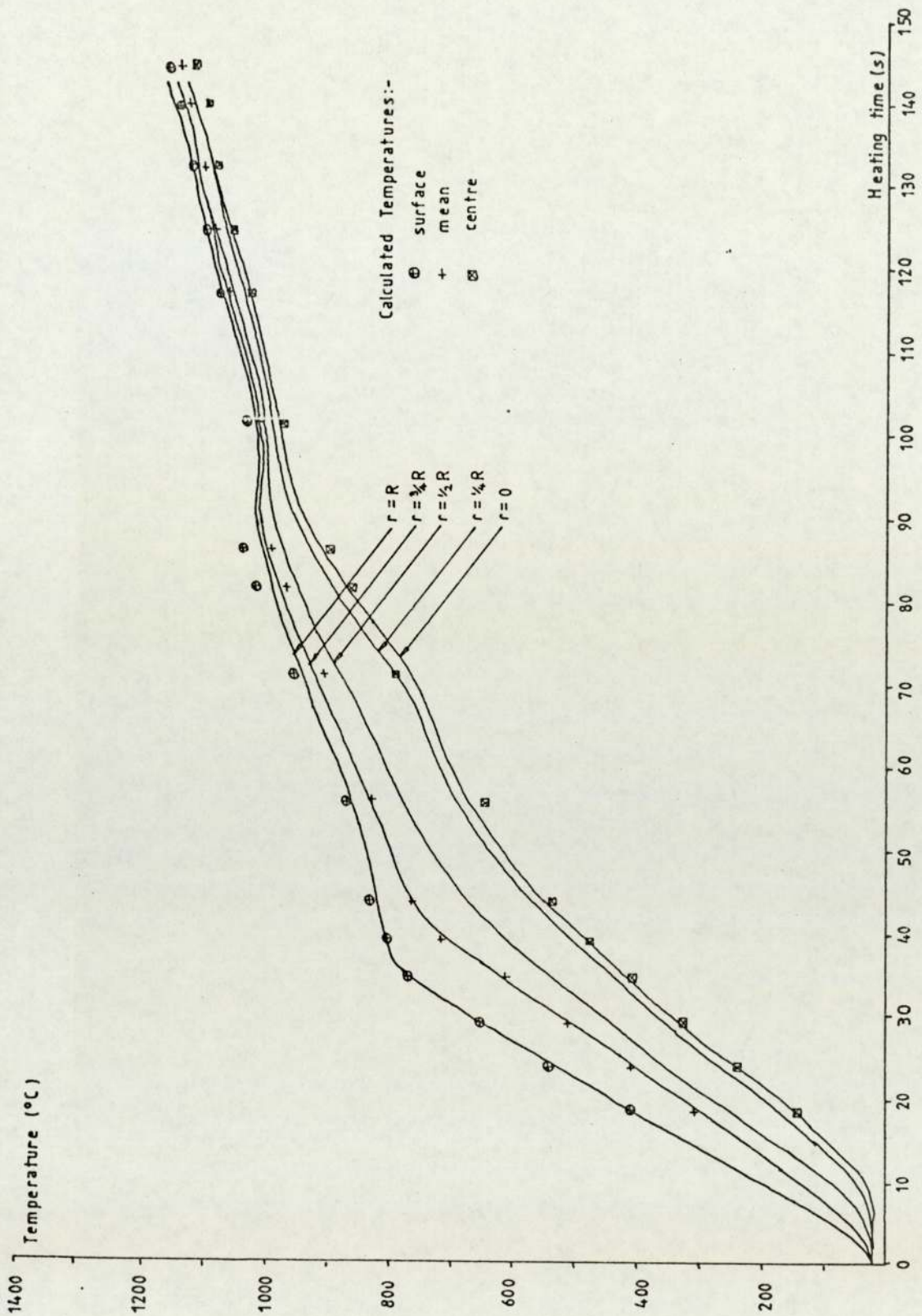


FIGURE 6.1: Measured temperature curves at various radii with induction heating time for a solid En8 Steel billet of radius  $R=25.4\text{mm}$  and  $51\text{mm}$  length. Surface, centre and mean temperatures, calculated using the method of section 6.4, are shown for comparison.



The calculated and measured temperatures with time agree well. The effect of decreasing thermal conductivity from 20°C to 760°C is reflected by a steady increase in ( $\theta_s - \theta_c$ ) temperature differential, in the steady-state of the first coil section. The initial transient takes longer to reach the predicted temperatures than expected. This is due to the reduced magnetic field occurring at the ends of the coil as flux spreads into the external regions.

Above  $\theta_{\text{curie}}$ , the calculated temperatures are slightly higher than the recorded data. This may be due to inaccuracies involved in the Curie transition approximation, and also to a larger radiated power than predicted. During measurement, the coil refractory lining was cooler than it would be under normal operating conditions, for which the calculations apply.

## 6.4 Concluding Summary

The modifications to the equivalent circuit coil design method and the iterative thermal calculations presented here, are in agreement with measured values.

It is recommended that these calculations are done for any new design so that more information is gained on the physical heating behaviour before the coil is built. The method is well suited to automatic computation, where smaller calculation intervals would improve accuracy. However, the intention here is to identify the principles involved, the relative importance of the coil and work load variables, and show that a simple manual calculation may be sufficient for coil design purposes.

Calculations for production coils should be treated with care; it was found that, in practice, small deviations in billet and coil dimensions, and billet initial temperature, could alter the work power by as much as 5%. [93].

The magnetic transition remains the area for improvements in prediction methods. The approximations used here are still quite primitive. A system for dividing the billet into layers for calculation of work power purposes would allow better representation of the radius at which greatest power is developed. This is especially important at the Curie temperature where the outer regions may be above  $\theta_{\text{curie}}$  while the inner parts are still magnetic. This is further considered in Chapter 10 with predictive methods for complex shapes.



CHAPTER SEVEN

SOLENOIDAL COIL INDUCTION HEATING  
OF SIMPLE SINTERED BILLETS

## CHAPTER 7 : SOLENOIDAL COIL INDUCTION HEATING OF SIMPLE SINTERED BILLETS

### 7.1 Introduction


In Chapter 6 the coil design method used in the literature was extended and an iterative solution developed to describe the heating of a solid steel billet within a solenoidal induction coil. The predictions were compared with the results of practical tests.

This chapter describes the experimental method used (section 7.2) and considers the results of similar heating trials on sintered billets. The results are discussed in section 7.3 by considering the comparison of measured and predicted values (section 7.3.1), the comparison of solid and sintered billet heating (section 7.3.2), and the effect of density (section 7.3.3). A summary of the calculated values is contained in Appendix 4.

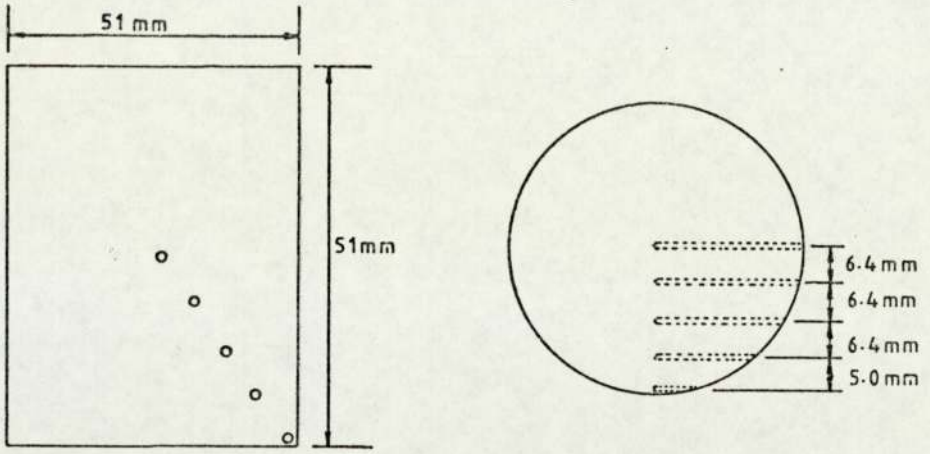


## 7.2 Method of Billet Temperature Measurement

A cylindrical test billet was prepared from each of the following materials; solid En8 steel, 'W4' sintered steel at relative densities of approximately 0.74, 0.79, and 0.82. Five holes were drilled as shown in figure 7.1a to accommodate ceramic insulated chromel-alumel thermocouples for temperature measurement at the billet surface (radius  $R$ ), centre and at radial distances of  $R/4$ ,  $R/2$  and  $3R/4$ . The positions of the thermocouples were chosen so that any disturbance of the temperature distribution due to neighbouring thermocouples was minimal.

The test billet was placed within a solenoidal coil (figure 7.1b) and the thermocouples connected to a six-input temperature chart recorder. The thermocouple leads were directed as shown because the coil unit incorporated an automatic billet feeding and extraction mechanism. This could not be made inoperative while the heating coil was in use. The  billet was positioned at the entrance to the coil, and rose towards the billet extraction claws during heating as more billets were fed in below it. The test billet was the first to travel the full length of the coil and thus experienced the normal heating cycle. (Those above and below the test billet ensure that the coil and load are matched at all times).

The temperature at each measurement position was recorded every 9 seconds as the test billet passed through the energised coil



○ ≡ drilled hole for thermocouple (1.5mm dia.)

FIG. 7.1a

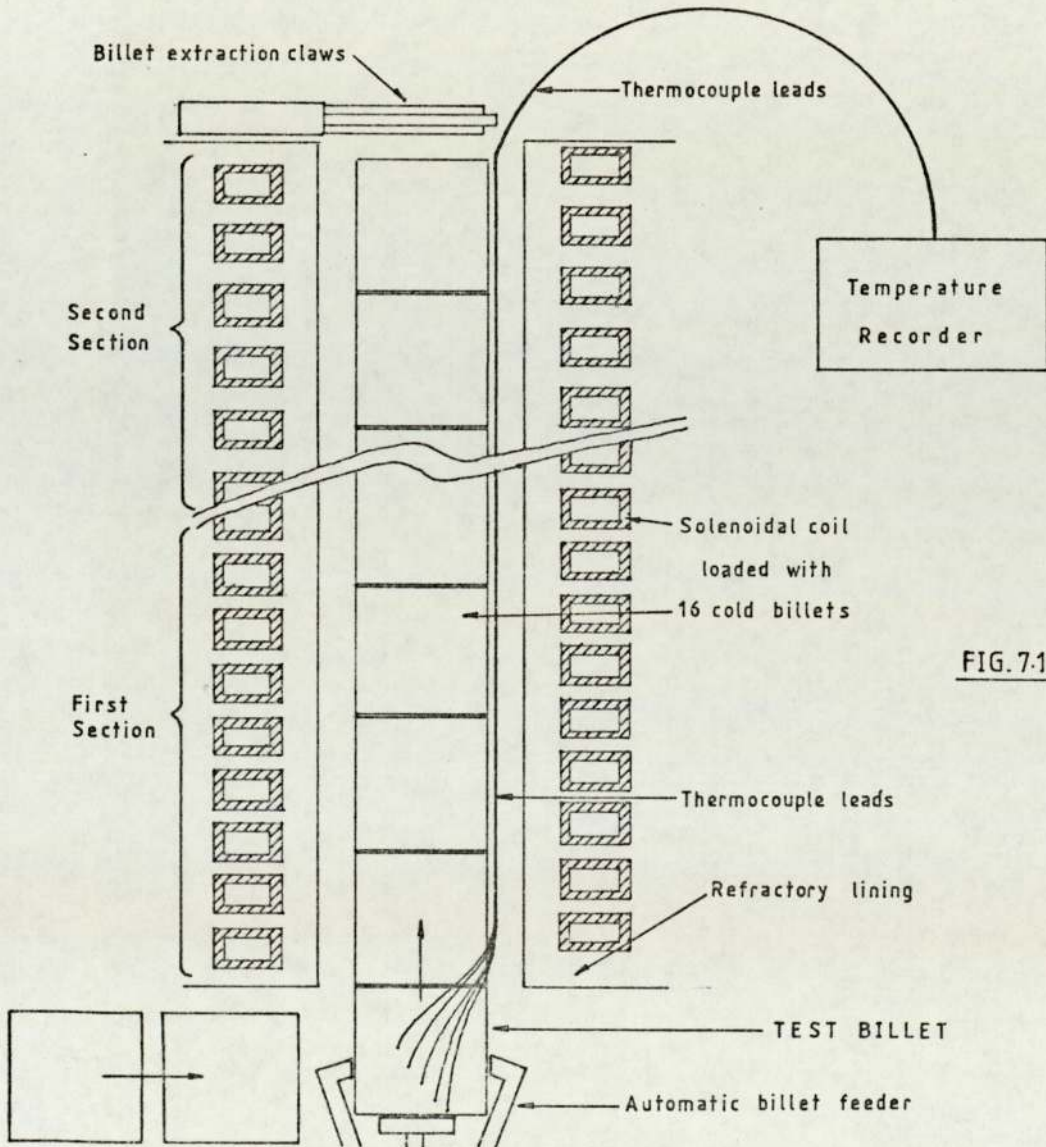


FIG. 7.1b

FIGURE 7.1: Preparation of cylindrical test billet, of radius  $R$ , for temperature measurement at  $r=0$ ,  $R/4$ ,  $R/2$ ,  $3R/4$  and  $R$  (Fig 7.1a). Position of billet within a solenoidal coil prior to testing, (Fig.7.1b).



from the starting position shown in figure 7.1 to when it was gripped by the extraction claws. This test was performed using all four test billets.

### 7.3 Results of Temperature Measurements

The temperature curves at radii  $r = 0, R/4, R/2, 3R/4$  and  $R$  for the solid En8 steel billet were plotted against heating time in figure 7.2. Also shown, at selected heating times, are the surface, centre and mean temperatures calculated by the method described in Chapter 6. Similar graphs \* appear in figures 7.3, 7.4 and 7.5 for sintered steel test billets with a relative density of 0.74, 0.79, and 0.82 respectively. A summary of calculated values for sintered billets appears in Appendix 4.

The recorded coil voltage, current, coil power and reactive power are shown with heating time in table 7.1. Power factor correction capacitors are automatically switched in to reduce reactive power. Voltage and current limiters are also in operation. This explains some anomalies, for example during heating of the powder billet of 74% relative density, the maximum number of capacitors available had switched in after 60 seconds.

\* The thermocouple at  $r = R/4$  failed during the tests on sintered billets of  $\rho/\rho_0 = 0.79$  and 0.82 and so the temperature curve was not recorded.

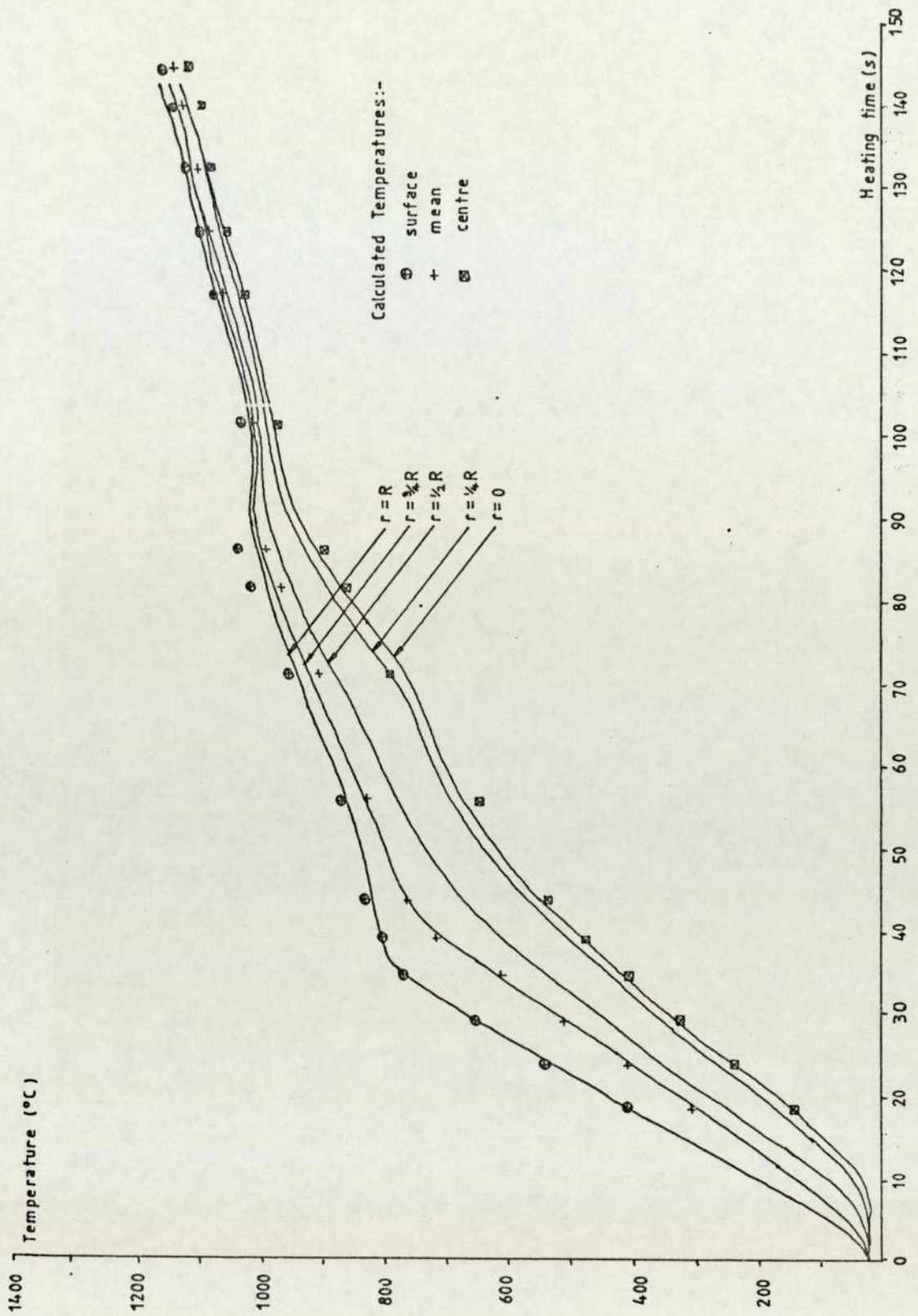


FIGURE 7.2: Measured temperature curves at various radii with induction heating time for a solid En8 steel billet of radius  $R=25.4\text{mm}$  and  $51\text{mm}$  length. Surface, centre and mean temperatures, calculated using the method of section 6.4, are shown for comparison.



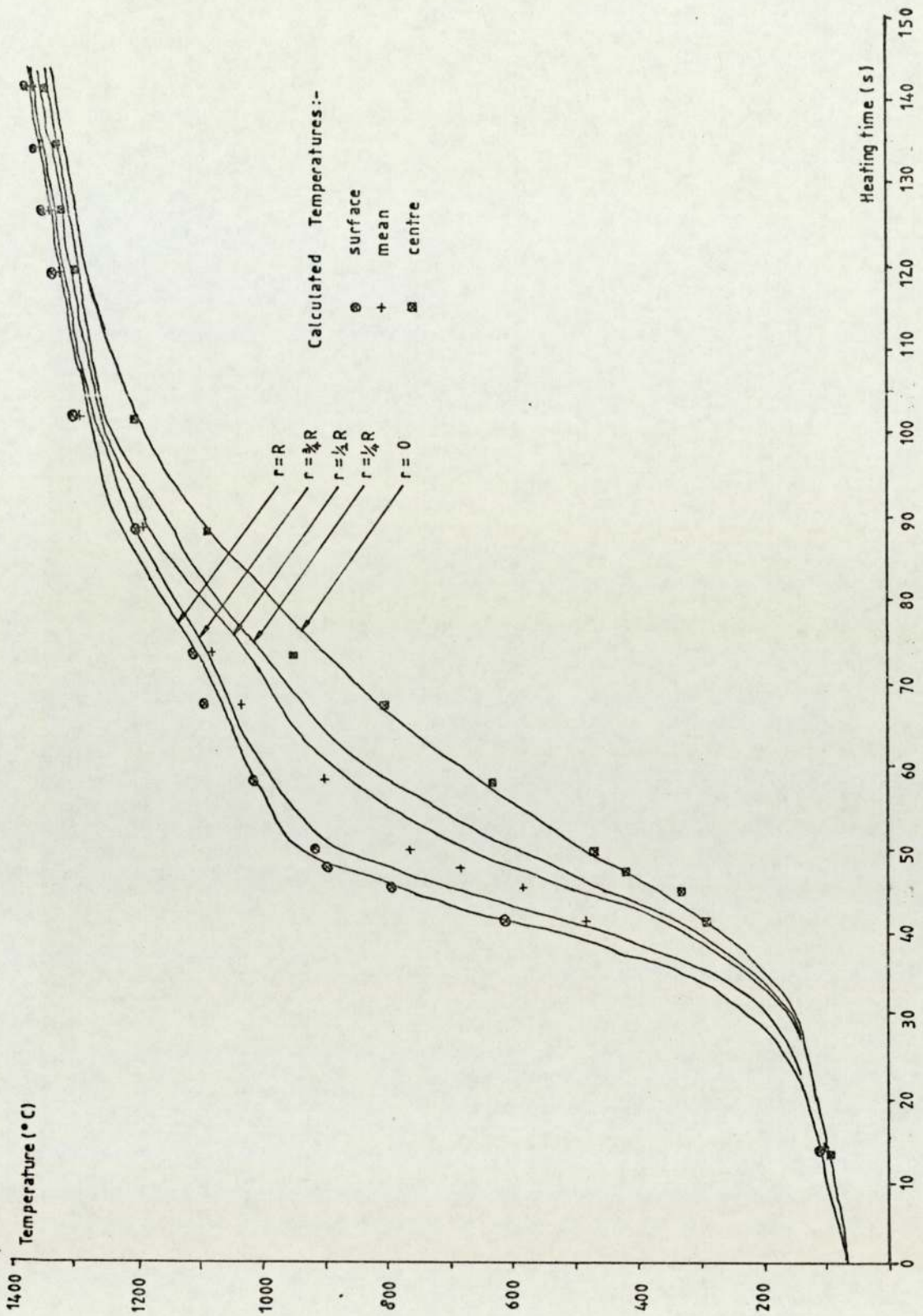


FIGURE 7.3: Measured temperature curves at various radii with induction heating time for a sintered billet,  $\nu/\nu_0=0.74$ , radius  $R=25.4\text{mm}$  and  $51\text{mm}$  length. Surface, centre and mean temperatures, calculated using the method of section 6.4, are shown for comparison.

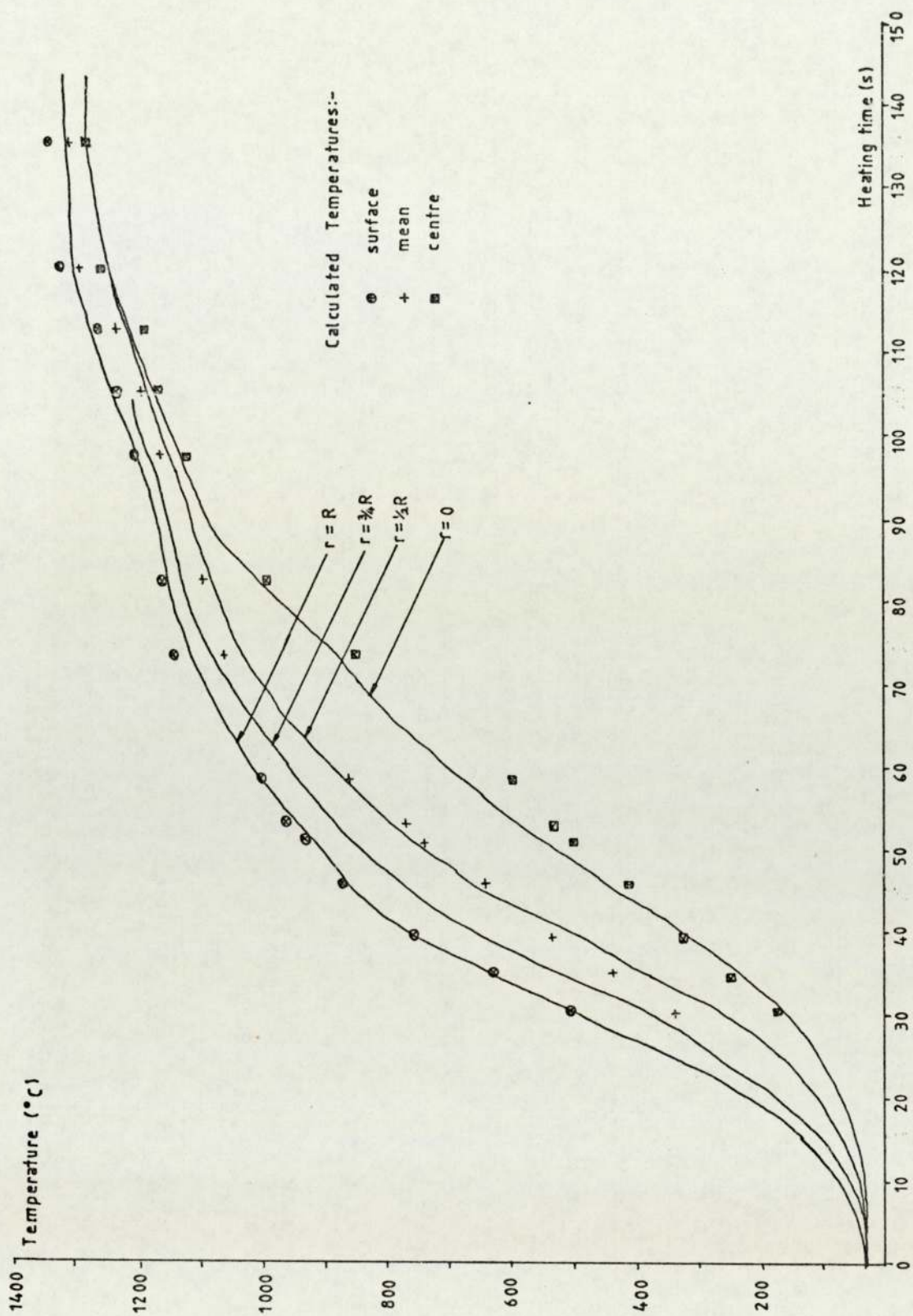


FIGURE 7.4: Measured temperature curves at various radii with induction heating time for a sintered billet,  $\nu/\nu_0 = 0.79$ , of radius  $R=25.4\text{mm}$  and  $51\text{mm}$  length. Surface, centre and mean temperatures, calculated using the method of section 6.4, are shown for comparison.



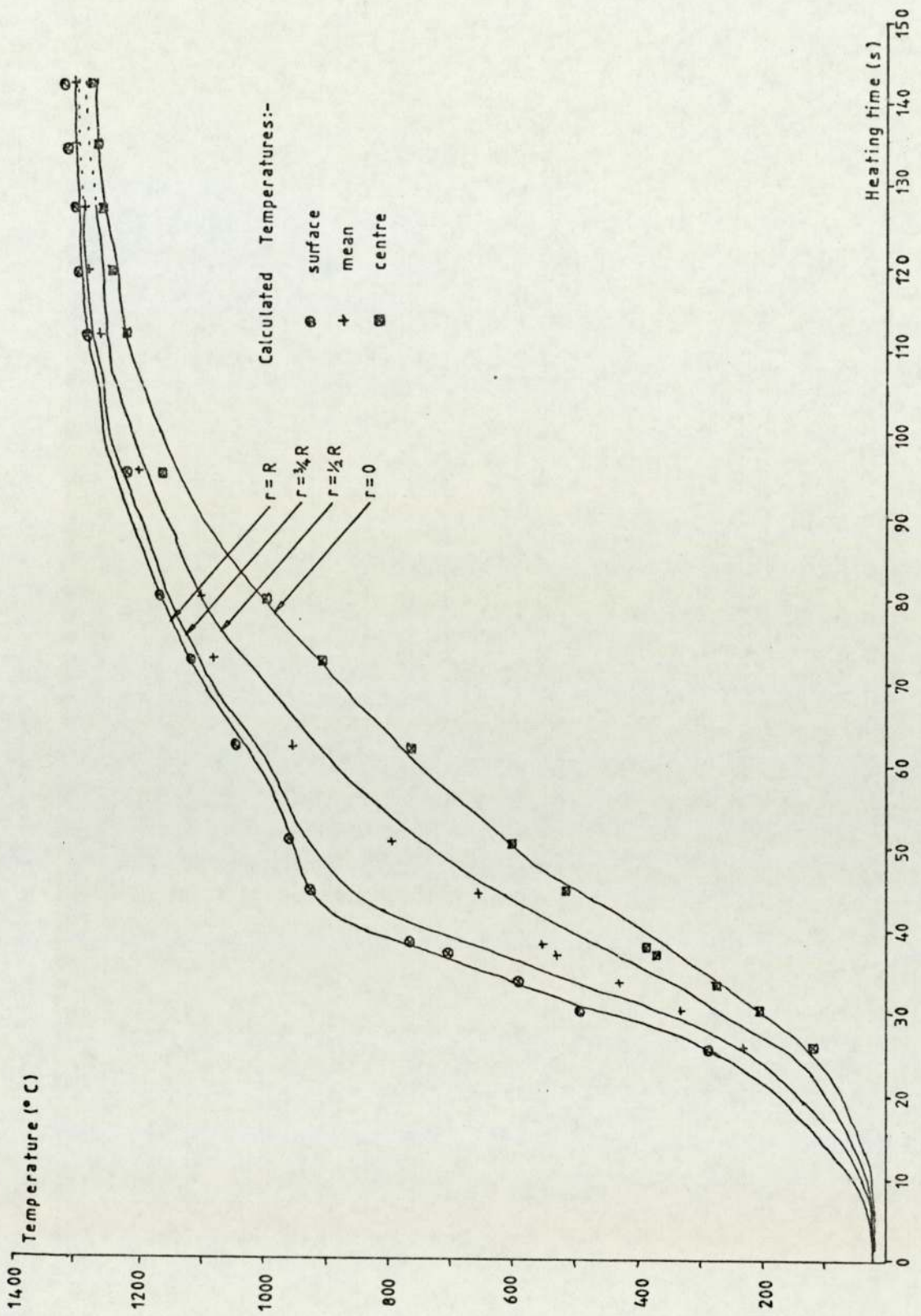


FIGURE 7.5: Measured temperature curves at various radii with induction heating time for a sintered billet,  $\nu/\nu_0=0.82$ , of radius  $R=25.4\text{mm}$  and  $51\text{mm}$  length. Surface, centre and mean temperatures, calculated using the method of section 6.4, are shown for comparison.

Solid En8  
Steel Billet

TIME (secs)	COIL VOLTAGE (V)	COIL CURRENT (A)	REACTIVE POWER (kVAr)	COIL POWER (kW)
0	550	240	20 Lag	130
15	550	205	10	112
30	550	200	8	110
45	550	200	10	109
60	550	230	25	124
75	560	190	5	106
90	560	200	7	112
105	560	200	5	112
120	560	195	3	109

Sintered  
billet  
 $V/V_0 = 0.74$

TIME (secs)	COIL VOLTAGE (V)	COIL CURRENT (A)	REACTIVE POWER (kVAr)	COIL POWER (kW)
0	560	300	30 lag	165
30	570	270	45	147
60	580	240	60	125
90	580	230	60	119
120	580	230	60	119

Sintered  
billet  
 $V/V_0 = 0.79$

TIME (secs)	COIL VOLTAGE (V)	COIL CURRENT (A)	REACTIVE POWER (kVAr)	COIL POWER (kW)
0	560	260	50 lag	137
30	560	260	49	137
60	560	250	49	131
90	560	220	25	121
120	560	220	25	120

Sintered  
billet  
 $V/V_0 = 0.82$

TIME (secs)	COIL VOLTAGE (V)	COIL CURRENT (A)	REACTIVE POWER (kVAr)	COIL POWER (kW)
0	565	240	0 lag	136
30	570	210	15 lead	119
60	570	210	16	118
90	570	210	14	118
120	570	210	15	118

Table 7.1 : Recorded voltage, current, reactive power and coil power during temperature measurement tests on solid En8 and sintered billets in the solenoidal coil of section 3.4.



The comparison of practical results and calculated values for the solid billet has already been considered in Chapter 6.

The temperature predictions from approximate iterative theoretical methods may now be compared with practical results for sintered billet heating (section 7.3.1.). The effect of changes in the thermal and electromagnetic properties, is investigated in section 7.3.2, by comparing the experimental results for the sintered billets with those for the solid material, and in section 7.3.3 by considering the effect of various densities on the heating characteristics.

### 7.3.1 Comparison of Predicted and Measured Results for Powder Materials

The calculated temperatures are generally in excellent agreement with the measured values. The calculated surface and centre temperatures are compared with the measured temperature curves at  $r = R$  and  $r = 0$ , respectively, and the measured curve at  $r = 3R/4$  is approximated by the calculated mean temperature. This mean occurs at  $r = 0.71R$  for a parabolic temperature distribution.

Steady-state heating within the first coil section (between approximately 30 and 45 seconds), and the second section (between 90 and 145 seconds), are well matched by the calculated values. The surface-to-centre temperature difference

$$\left(\theta_s - \theta_c\right) = \frac{\mathcal{P} R}{2 k} \tag{3.13}$$

rises in the first section as the thermal conductivity falls with rising temperature. A marginal increase in  $k$  during the second section reduces the final ( $\theta_s - \theta_c$ ) in all cases to below  $50^{\circ}\text{C}$ . Temperature equalization in the second section is assisted as the billet becomes hotter, as more induced power is radiated from the surface, and as the coil magnetic field decreases at the coil ends as more flux is 'lost' to the air-gap and surroundings. Towards the end of the second section, the calculated temperatures are slightly higher than the measured values. This is due to an under-estimate of the power lost to the refractory lining by radiation. The lining was cooler than it would be under normal operating conditions, for which the predicted values apply, as the tests were performed from the initial cold state.

The effect of reduced magnetic field at the coil ends also accounts, in part, for the variance between the measured and the calculated heating times for the transient temperature rise at the start of the first coil section. In practice, the time taken for the steady state temperature profile to become established is nearly twice the calculated value. For the sintered billet of 0.74 density in particular, an increase in time at the start of heating may be attributed to a delay in the operating of the billet feed (piston) mechanism.



The method of calculation for treating the Curie transition follows similar lines to the solid billet case of Chapter 6, as follows.

During steady-state heating in the first section, as the temperature rises above  $760^{\circ}\text{C}$ , the surface-to-mean temperature difference  $(\theta_s - \theta_m)$  is calculated from the reduced super-Curie power input  $\mathcal{P}'_1$  for the non-magnetic part of the billet. The effect of current depth on the temperature profile is also taken into account. The temperature rise for the magnetic part of the billet continues, using the sub-Curie power density  $\mathcal{P}'_1$ . When the mean calculated temperature reaches  $760^{\circ}\text{C}$ , the billet is subjected to the superposition of a soaking period and a transient temperature rise calculated from  $\mathcal{P}'_1$  for the duration of the Curie transition. For heating during the remainder of the first coil section above  $\theta_{\text{curie}}$ , the billet completes the transient state and enters the steady-state.

Figures 7.3-7.5 show that the magnetic transition is well approximated by the above method. Computed surface and centre temperatures are within 5% of measured values but calculated mean temperatures are lower than expected. The mean temperature is calculated from the equivalent steady-state temperature parabola: In practice however, the profile is altered for the effect of finite current depth, thus more of the billet is above the  $(\theta_s + \theta_c)/2$  mean for the parabolic case.

The temperature profiles of sintered billets of various densities are well predicted by the approximate method of Chapter 6, using the measured dependence of the billet density on the thermal and electromagnetic properties.

### 7.3.2 Comparison of Solid with Sintered Billet Heating

The measured temperature distributions with time for sintered billets (figures 7.3-7.5) may be considered with the results for the solid billet (shown in figure 7.2). However, table 7.1 shows that, although the coil power is not identical for each test, especially at the the start of heating, the powers vary nominally only by 8%, and the following trends may be identified. In general the coil power falls from about 130kW initially to a steady 120kW. The  $\rho/\rho_0 = 0.74$  powder billet has an abnormally high coil power (165kW) at the start but falls to the typical value of 126kW after 60 seconds.

The solid material reaches the Curie transition temperature before the powder billets, since the sub-Curie work power density is larger for En8 solid by virtue of higher  $\mu_r$ , giving increased surface power density. Above  $\theta_{\text{curie}}$  however, the sintered steel power densities  $\mathcal{P}_1$  are larger than for the solid, since the higher resistivity gives deeper skin depth and



reduces  $d/\delta$  for a larger  $p$  factor (figure 3.2). Higher temperatures, therefore, exist in a sintered billet at the end of the first section, the surface temperature being approximately  $1100^{\circ}\text{C}$ , compared with  $960^{\circ}\text{C}$  for a solid billet. This difference is maintained in the second coil section where, despite lower magnetic field strength, the higher resistivity of the sintered material ensures higher efficiency and thus more heat generated within the billet. The final surface temperatures are  $200^{\circ}\text{C}$  higher for the porous material.

In general the surface-to-centre temperature differential is greater for sintered metal, since lower thermal conductivity slows heat conduction from the billet surface.

### 7.3.3 Effect of Density on Sintered Billet Induction

#### Heating

Throughout periods of steady-state heating, in the first and second coil sections, the surface-to-centre temperature differential follows the expected trend of larger  $(\theta_s - \theta_c)$  with decreasing density. This occurs due to the reduced conduction of the generated heat from the surface to the billet centre, with reduction of the number of powder particle bonds at lower densities.

An increase in electrical resistivity with porosity gives higher final temperatures for the 0.74 relative density

sinter ( $\theta_s = 1367^\circ\text{C}$ ) compared with  $\gamma/\gamma_0 = 0.79$  and  $0.82$ ,  
 $\theta_s = 1328^\circ\text{C}$  and  $1312^\circ\text{C}$ , respectively.

During sub-Curie conditions, the heating rate falls with declining relative permeability  $\mu_r$  at reduced densities; heating times to  $\theta_s = 760^\circ\text{C}$  are 38, 40 and 44 seconds for  $\gamma/\gamma_0 = 0.82, 0.79$ , and  $0.74$  respectively.



#### 7.4 Concluding Summary

The evidence described in this chapter shows that excellent agreement may be achieved between the measured temperature profile of powder-metal billet induction heating with time and the predicted values, as calculated from Chapter 6. In particular, the treatment of the steady-state temperature rise, including the effect of current within the skin depth, the influence of radiation, and the complex magnetic transition at the Curie temperature  $\theta_{\text{curie}}$ , concur with experimental values.

Comparison of sintered and solid billet heating reveals that reduced power input occurs below  $\theta_{\text{curie}}$  for the former. This is because of the lower magnetic permeability of powder materials. However, above the Curie temperature, powder billets achieve higher temperatures as larger electrical resistivity dissipates greater quantities of heat within the body.

As expected, the effect of density on the physical properties of the material may be seen from the powdercompact results. The heating rate below  $\theta_{\text{curie}}$  falls with decreasing density and therefore lower  $\mu_r$ . The surface-to-centre temperature difference increases with falling thermal conductivity at low density. Higher final temperatures are recorded for the least dense billets, with largest  $\rho$  values and consequently greater power density.

These results provide additional confirmation that the calculation methods of Chapter 6, extended from the procedure in current use (Chapter 3), give an accurate description of induction heating with time for simple shapes in a multi-sectioned production coil. In this chapter a further variable, that of powder material, is considered. The results of Chapter 5 are used to give  $\rho$ ,  $k$  and  $\mu$  for each powder billets. These approximate calculations are equally applicable to the heating of powder compact billets in solenoidal coils.



CHAPTER EIGHT

PRODUCTION COIL OPTIONS -  
QUALITATIVE CONSIDERATIONS

## CHAPTER 8: PRODUCTION COIL OPTIONS - Qualitative

### Considerations for sintered preforms of complex shape

#### 8.1 Introduction

An introduction to induction heating for forging, including established theory and present induction coil design methods, was presented in Chapters 2 and 3. The application of these ideas to the induction heating of simple shaped sintered billets in solenoidal coils was described in Chapter 6 (with extensions of the present theory) and compared with practical tests (Chapter 7).

Previous discussion and the economic considerations of Appendix 5 indicate that the advantages of using the powder metallurgy route are greatest where machining costs are substantially reduced, i.e. for more complex shaped parts (eg. bossed gear wheels). The use of induction heating would reduce the costs of heating these complex shaped preforms prior to forging. However, long straight-sided solenoidal coils produce unacceptable non-uniformity of heating at high power and large production through-puts.

This chapter introduces the latter part of the study on coil design, directed towards the induction heating of complex sintered shapes. Initially, the advantages and limitations of solenoidal coils in current use are discussed. The general requirements and production demands of the induction coil follow, with regard to foreseeable shape complexity. The range of induction coil types is then briefly



evaluated and the relative merits of the more viable options considered.

Later chapters report theoretical and practical studies on the most promising solenoidal and linear coil systems, and the development of coil design guidelines for heating powder compact parts of complex shape (for which no present method completely describes the heating behaviour for all coil conditions).

## 8.2 Solenoidal Coils

### 8.2.1 Advantages

The theory of induction heating of simple shapes is well known. Approximate analytical solutions for solid and hollow non-magnetic billets exist, where temperature-invariant properties are assumed. These solutions have been successfully modified to take account of "end-effect" corrections for short coils and short billets, and also used for calculating the electrical parameters of sectionalised inductor coils. Refinements may be introduced for varying the power input to the billet during production standby periods [94] and to allow for temperature equalization within the billet.

The close coupling of the coil to a heated billet for simple cylindrical shapes reduces flux leakage and ensures a high overall efficiency (approaching 50%) to give uniform heating.

Much production experience has been gained over many years, resulting in adequate billet-heating coil design for most industrial applications. Ease of fabrication, electrical insulation and water cooling makes the solenoidal coil cheap and reliable. These coils may be easily adapted for automatic in-feed, transport and handling of parts.



### 8.2.2 Disadvantages

Present analytical solutions do not accommodate metal properties which vary with temperature and cannot completely describe the behaviour of magnetic materials. Although numerical iterative techniques have been evolved to overcome this, the literature considers only billet heating, since the complex problem then reduces to a simpler one-dimensional solution. The heating of parts of complex shape in solenoidal coils has not yet been completely described.

In practical tests, non-uniformity of heating complex axi-symmetric shapes has been found, since parts of the shape are closer coupled to the coil than others. Experimenters at G.K.N. [3] have previously had difficulties maintaining close control on the induction furnace atmosphere during continuous powder-metal part production.

Alignment of complex-shaped parts during automated operation may not be easy using the "pusher feed/grab withdrawal" system favoured for use with solenoidal coils.

### 8.3 Coil Requirements

The following list indicates the general attributes required for an ideal induction heating coil for this forging application.

COIL, REQUIREMENTS	COIL TYPE				
	Straight- Sided Solenoidal Coil	Shaped Solenoidal Coil	Multiple Shaped Solenoidal Carousel	Trans former type, internal flux	Linear 'Skate' Coil
1 Heats full range of G.K.N. Parts.	?	*	*	*	?
2 Temperature distribution control	see section 8.2.2	*	*	see section 8.4.4	*
3 High efficiency	*	*	?	*	?
4 High Through-put	?	discontinuous 'single-shot coil'	*	discontinuous 'single-shot coil'	*
5 Adjustable or interchangeable for many parts	?	*	*	*	*
6 Simplicity of construction, maintenance etc	*	*	?	*	*
7 Resistant to mechanical and thermal shock.	*	*	*	*	*
8 Sufficient flow of water for cooling	*	*	*	see section 8.4.4	*
9 Ability to heat parts at Press rates.	*	?	*	?	*
10 Automation.	*	*	*	*	*
11 Maintenance of Protective atmosphere.	?	*	*	*	*
12 Power Input control	*	?	*	power concentrated on inner portions	*

Table 8.1 : Ability of various coil types to meet desired coil attributes. An asterisk (\*) indicates that a particular requirement is met by the coil type, in general, and a question mark shows that the desired attribute is met in part or in some cases.



These points have been used when considering the possible coil options to construct the check list of Table 8.1.

The coil(s) should;-

- 1) heat the full range of component preforms produced at G.K.N. Powder-Forgings Division (figure 8.6),
- 2) heat parts to a controllable final temperature (to within  $25^{\circ}\text{C}$ ) and with a surface-to-centre temperature difference less than  $50^{\circ}\text{C}$ ,
- 3) be efficient, with small air-gap between part and coil for close coupling, consistent with the practicalities of part transport through the heating stages,
- 4) be capable of heating parts at high through-put rates,
- 5) be either adjustable, interchangeable or capable of accommodating all part sizes and shapes. Each component of the range should achieve an acceptable temperature by whichever method is used,
- 6) be simple to construct, install and maintain,
- 7) be adequately robust to withstand mechanical and thermal shocks,
- 8) allow sufficient water flow for coil cooling.

The system should;-

- 9) deliver parts at the approximate rate of 1 every 7 seconds, for full utilization of the forging press,
- 10) be automated to reduce handling costs and to ensure repeatability of the heating cycle for each part,

- 11) allow the maintenance of a protective atmosphere in all stages of heating and permit removal of undesirable combustion products,
- 12) provide for changes in the operating conditions, e.g. power factor correction and control of input power.

#### 8.4 Coil Options

The range of practicable coil types considered for production systems is given below. Reference to table 8.1 allows comparison of each method and an indication of the coil requirements fulfilled; only the major advantages and disadvantages are stated below.

##### 8.4.1 Conventional Straight-sided Solenoidal Coil (Figure 8.1)

This coil will heat some simple G.K.N. parts (figure 8.6 part a) in the form of rings and discs. Other more complex shaped parts will be heated non-uniformly and therefore require long temperature equalization time, inconsistent with high through-puts. This type has a proven record for meeting requirements 6 to 10, but not all parts may be heated by simple coil adjustment or change.

##### 8.4.2. Shaped Solenoidal coil (figure 8.2)

This extension of the solenoidal coil type allows a suitable temperature distribution to be developed, dependant on the



coil position and power [95]. Since the part is stationary, the coil may be shaped closer to the part to heat all those shown in figure 8.6.

It is doubtful however, whether power input could be controlled and directed to the desired areas of the shape (at different stages of heating) with the few coil turns permissible in the space available. One coil would be inadequate for the high through-puts demanded.

#### 8.4.3 Multiple Shaped Solenoidal Coil Carousel (figure 8.3)

The drawbacks of low through-put and semi-fixed power input for a single shaped coil are removed by using multiple stages; one coil may be used for heating to Curie temperature, another for heating to forging temperature at the surface and yet another for equilization of temperature. These distinct advantages must be weighed against reduced efficiency caused by thermal losses during transfer from coil to coil and increased complexity of the mechanical apparatus.

#### 8.4.4 Transformer-type, Internal Flux Concentration (figure 8.4)

The part to be heated forms the secondary "winding" of a transformer. All G.K.N. components may be heated by this method. However, since current is induced on the inner

surface and is conducted to the outer regions of the shape, variable radiation losses may cause uneven heating. The addition of insulation around the preform would reduce the heat loss and improve temperature uniformity.

A more controllable temperature distribution could be achieved by combining this method with an outer shaped solenoidal coil. This system is not readily adaptable for automated high-throughput production as the need to insert and remove the component hinders good flux linkage in the magnetic core and the provision of adequate cooling.

#### 8.4.5. Linear ("skate") Coil (Figure 8.5)

Long straight conductor pairs in series are used to induce current to heat the parts travelling through the coil. This coil satisfies most of the coil requirements having easy atmosphere maintenance, part transport and coil change.

The linear coil suffers from the disadvantages of low efficiency (since flux leakage is high) and possible localised heating near the coil bars. A transport system that allows for rotation of the parts would reduce non-uniformities of heating.



Flux concentrators [96] may be used with any of the coil options above to modify the magnetic flux linked with the heated part to improve efficiency or to modify the heating pattern by shielding areas of low thermal capacity. The concentrators would be either located on the parts before entering the coil, contained within the coil assembly or attached to the part transport mechanism.

### 8.5 Concluding Summary

Choice of coil type for a production system for heating the range of powder-metal parts produced by G.K.N. is by no means straight forward. Table 8.1 show that each option fails to meet all the requirements for an ideal system. The most promising arrangements are multiple shaped solenoidal coils and the linear coil.

At present, no theory has been developed nor tests conducted on the performance of the linear coil to heat metal parts for forging. Chapter 9 describes the initial trials of this study on heating simple shaped parts in the linear coil and developments of the theoretical aspects for linear coil design of simple shapes.

Coil design for complex shaped parts is considered in Chapter 10. Extensions of present solenoidal coil design methods for billets (Chapter 6) are developed for predictions of shaped solenoidal coil design, and results of the study on linear coils are projected towards linear coil design for G.K.N. component preforms.

Application of these ideas to G.K.N. operations will be discussed in Chapter 11, including an economic and technical appraisal of the relevance of the project to the Company with the implications for the choice of coil type.



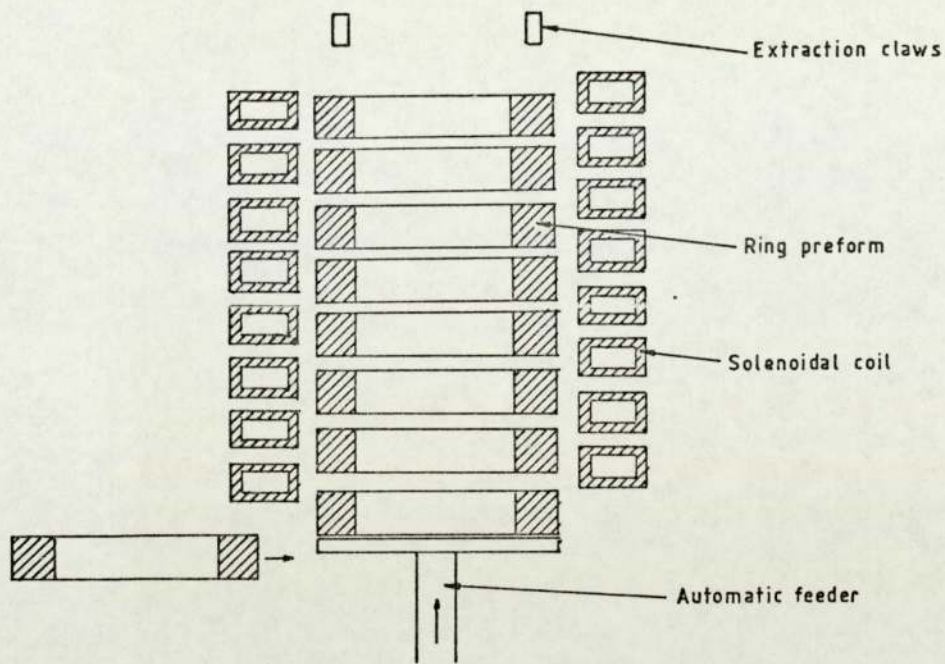


FIGURE 8.1: Conventional straight-sided solenoidal coil.

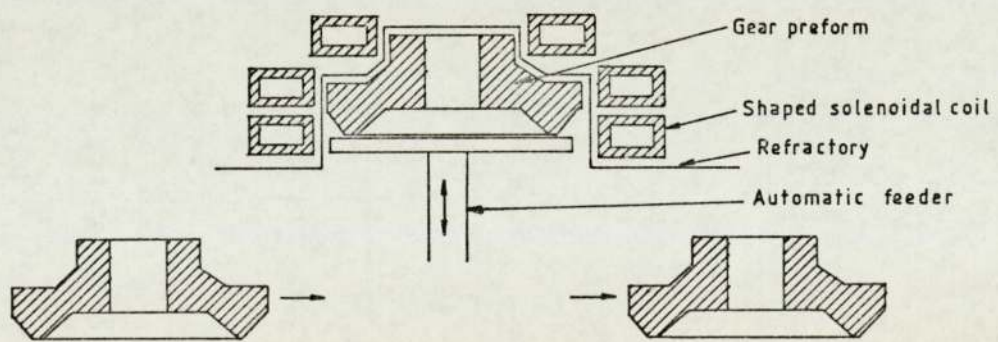


FIGURE 8.2: Shaped solenoidal coil.

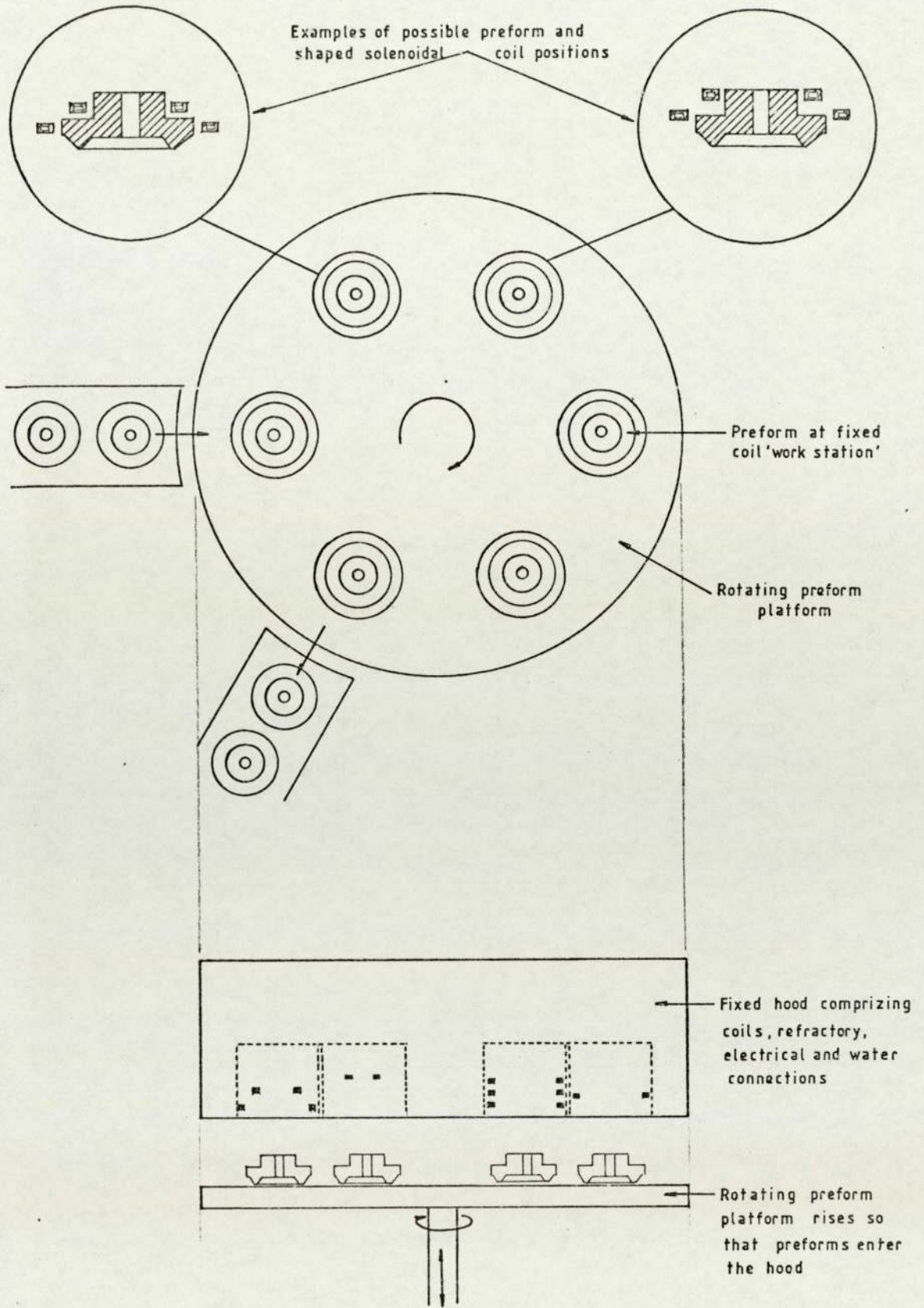


FIGURE 8.3: Multiple shaped solenoidal coil carousel.



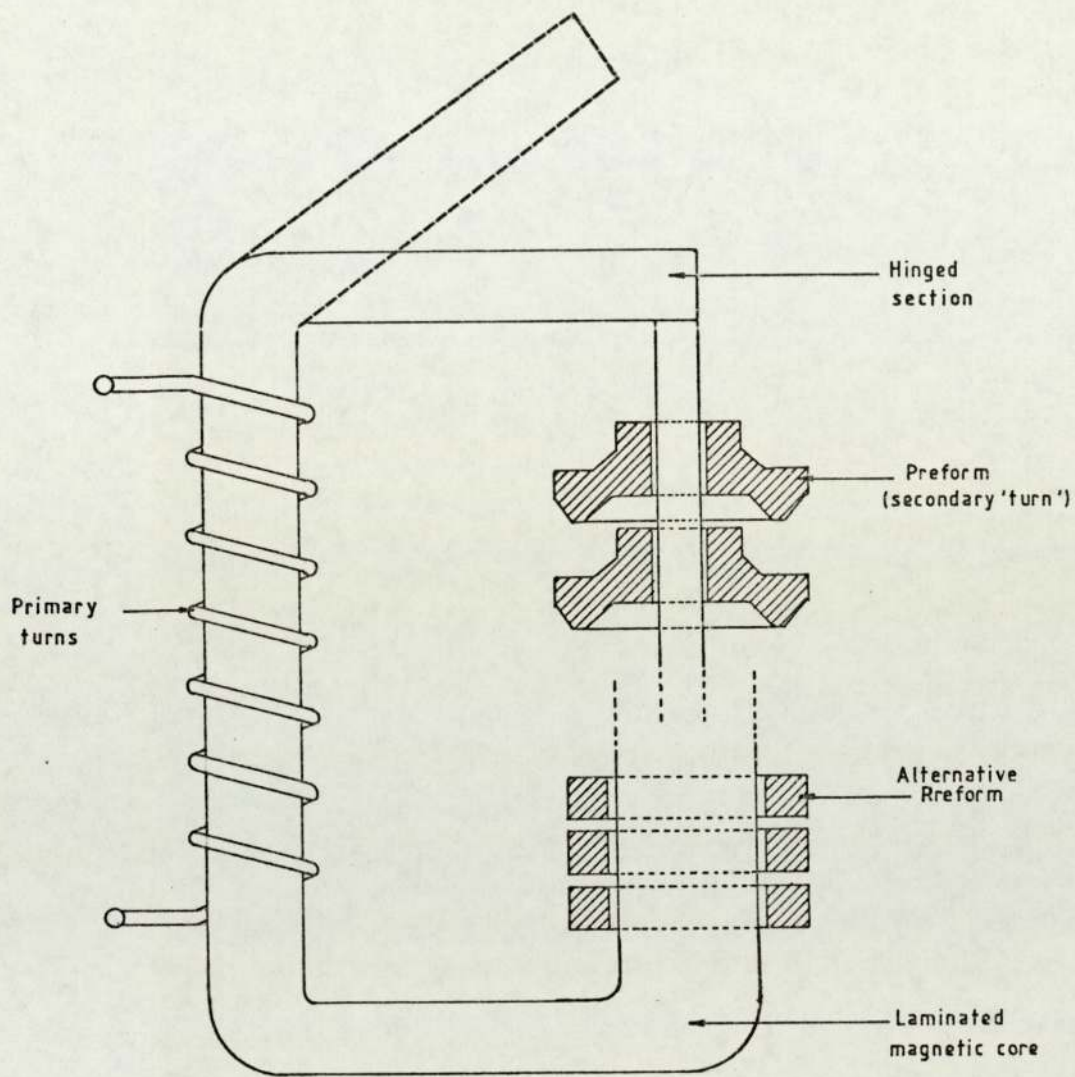


FIGURE 8.4: Transformer-type coil, with internal flux concentration.

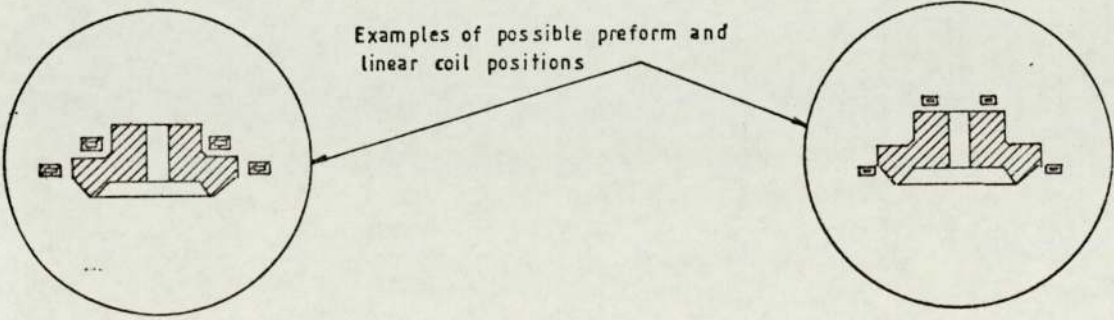
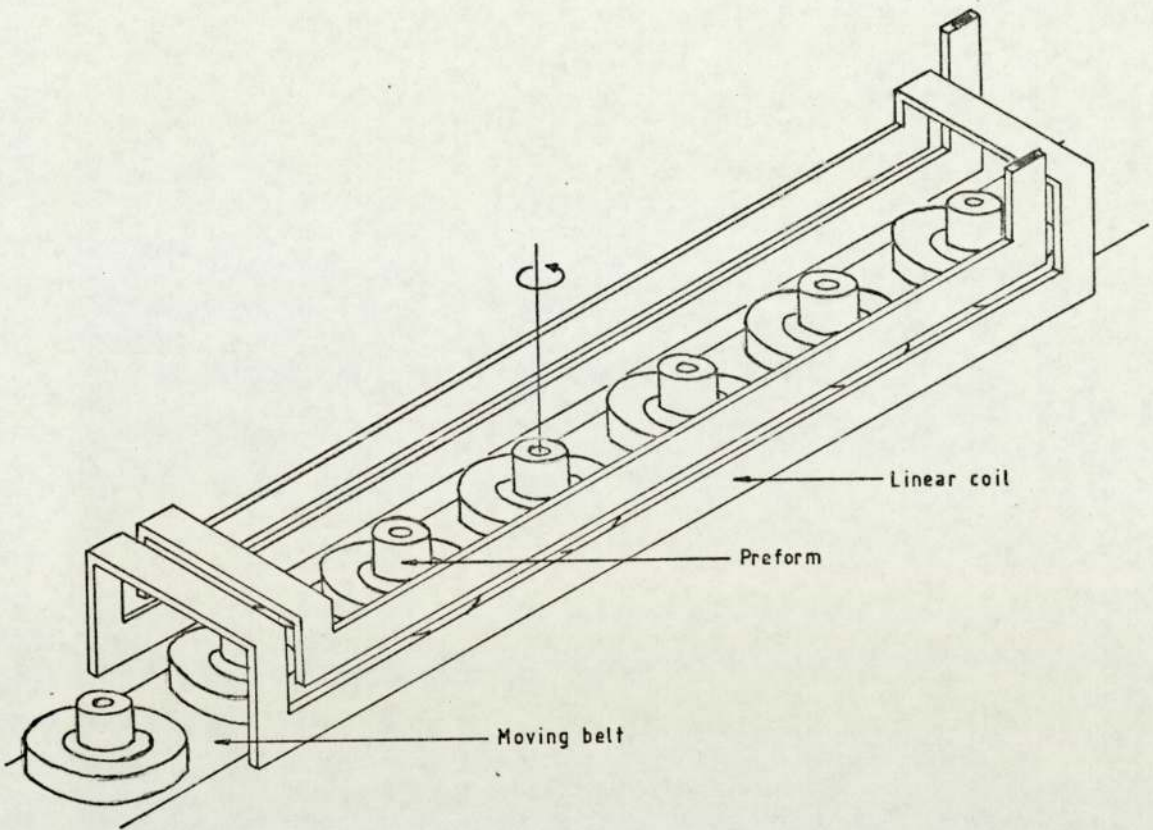


FIGURE 8.5: Linear 'skate' coil.



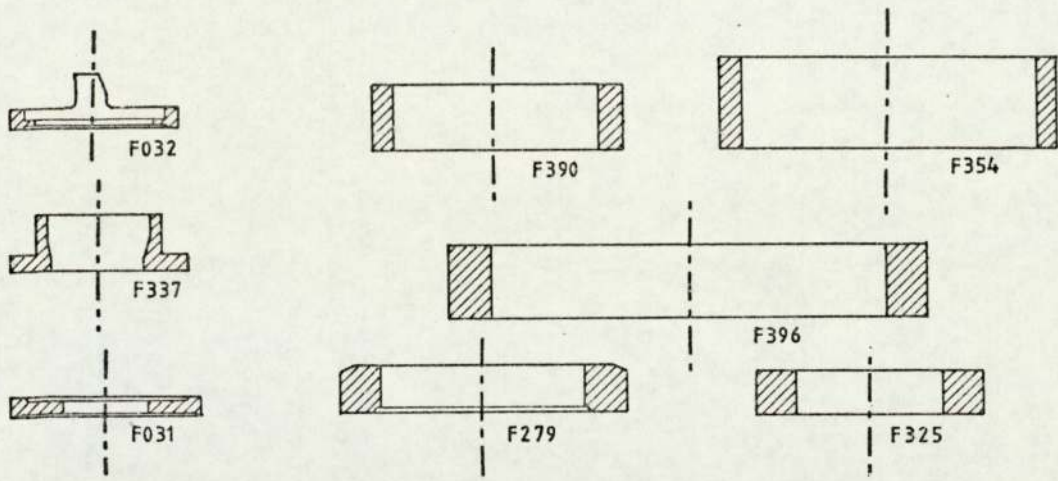


Fig. 8.6a

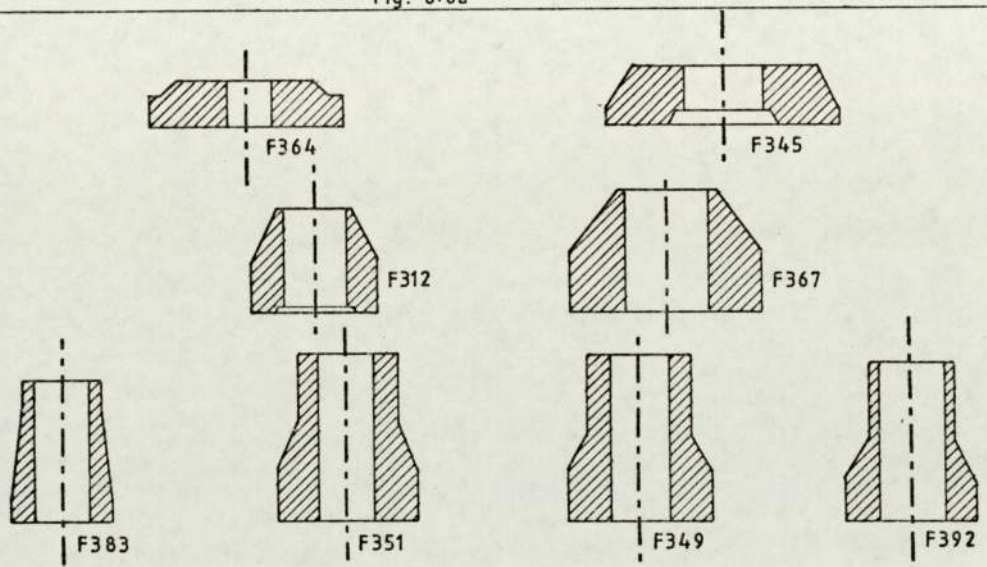


Fig. 8.6b

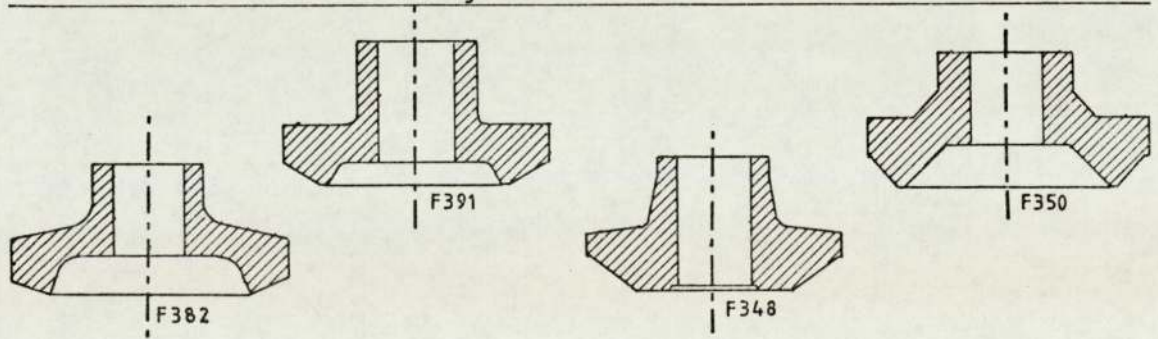


Fig. 8.6c

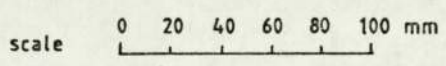


FIGURE 8.6: sections of the range of G.K.N. preforms for powder-forging; a) Simple rings and discs, b) stepped billet shapes, and c) gear preforms. G.K.N. identifying codes are given [97].

CHAPTER NINE

LINEAR COIL INDUCTION HEATING OF  
SIMPLE SHAPES



## CHAPTER 9 : LINEAR COIL INDUCTION HEATING OF SIMPLE SHAPES

### 9.1 Introduction

Chapters 2 and 3, and Chapters 6 and 7, considered the induction heating of simple shaped solid and powder compact workloads in straight-sided solenoidal coils. The equivalent circuit design method has been presented, with its derivation from theory. Solution of the mathematical equations relies upon a knowledge of the distribution of induced current streamlines and a reduction in the complexity for a problem with axial symmetry. After solution, it is possible to calculate the efficiency of the coil, and the effect of increasing the air-gap and coil magnetic field on the workload heating behaviour.

The latter part of this thesis focuses on electroheating of more complex shapes. Chapter 8 outlines the types of coil suitable for induction heating of shaped parts for forged part production. Of these coils, the shaped solenoidal coil (and carousel) and the linear coil are the most promising categories for heating G.K.N. axi-symmetric powder preforms. Chapter 10 considers the development of equivalent circuit solenoid coil design theory, for application to rotationally-symmetric coil and workload arrangements.

However, the linear coil configuration does not conform to a simplified two-dimensional symmetry that facilitates solution of axi-symmetric preform heating. Unlike the solenoidal coil, the current distribution for the linear configuration is unknown, even for simple shaped workloads.

For heating axi-symmetric shapes in solenoidal coils, all parts of the workload are closely coupled to the coil, since the air-gap is minimized around the workload circumference. However, where shaped workloads are heated in the linear coil only the portions nearest to the coil conductors are closely coupled. This is analogous to proximity heating, where the magnetic field produced by current in a straight conductor is coupled only with a flat workload surface adjacent to it. In the linear induction coil case, the power induced in the remainder of the workload is small and therefore these areas are largely heated passively by conduction from the active areas of heat generation near the coil bars.

In attempting to define the expected temperature distribution from linear coil heating of steel workloads, it is of fundamental importance to determine the induced heat distribution. In practical terms, the only method available is to measure the accessible induced current density distribution at the surface.

The aims of this chapter are to define the current density  $J$  field experimentally for simple shapes and derive relationships for the influence of increased air-gap and magnetic field on the induced power density  $\bar{W} = \rho J^2$  ( $W/m^3$ ) and its distribution. The significance of  $\bar{W}$  on the workload average heating rate is defined by ([18], p 341),

$$\mathcal{P} = \frac{\theta_m}{t} c \gamma \frac{V_w}{A_w}$$

where  $V_w$  is the workload volume and  $A_w$  is the total surface area heated. In terms of the average volume density of induced power  $\bar{W}$  the equation above becomes

$$\bar{W} = \frac{\theta_m}{t} c \gamma \frac{V_w}{\delta_w A_w} \quad (9.1)$$



For ferromagnetic materials the average power induced is not easy to derive from the surface values of  $\bar{W}$  measured here, since the current density does not fall exponentially with depth into the workload, because of the nonlinear variation of  $\mu$ . For a first approximation to the efficiency of various coil configurations used in this chapter, exponential attenuation of current density is assumed.

With the benefit of results gained here, Chapter 11 and Appendix 5 evaluate the relative merits of linear and solenoidal coils for heating G.K.N. preforms on an industrial scale. Chapter 10 considers methods for developing theoretical techniques for induction heating problems, with particular emphasis on solutions for treating ferromagnetic workloads and complex shapes.

Section 9.2 describes the principle of the current density measurements, preparation of the test billets, experimental method and apparatus. Previous discussion of the results of Chapter 7 has shown that sintered powder compacts heat in a way that is easily related to that of solid metal: For ease of preparation, therefore, solid billets are used for these tests. Section 9.3 gives the results of  $J$  measurements on the surface of a cube and cylinder test billet and these are discussed in section 9.4. A concluding summary is given in section 9.5.

## 9.2      Measurement of Current Density

### 9.2.1   Principle of Current Density Measurements

Surface current flows, due to potential differences induced in the workload by the coil magnetic field. The temperature distribution is then determined by the heat flux density  $\bar{W}$ , generated by  $J^2\rho$  power loss, and by heat transfer. Measurement of the voltage differences, over a representative measurement area of the workload surface, provides an indirect means of assessing workload heating.

In these tests, the measurement area was divided into small 5mm x 5mm square regions. Two orthogonal voltage measurements are required to measure the average current density magnitude and direction within each small square. A voltage measurement utilizes two lacquer-insulated fine wires, spot-welded at the mid-point of opposite sides of the 5mm x 5mm square (figure 9.2a<sup>\*</sup>) [99]. However, voltage induced in the wires themselves, by the presence of the coil magnetic field, must be minimized by ensuring that no area is enclosed by any pair of measurement wires. The wires are glued close to the billet surface so that negligible area is enclosed by the loop comprising the wires and the return electrical circuit through the metal. Similar precaution is taken, for the lengths of wire between the measurement area and the voltage recorder, by machine-twisting each pair.

\*      Figures and tables for this chapter appear between p 202      and  
p 222      .



The necessity for two potential difference measurements means that two wires would cross at the centre of each small square (figure 9.2a). This arrangement introduces an undesirable area beneath one wire. To overcome this problem, two identical measurement areas are used: On one area, only wires in a vertical direction are spot-welded, and on the other, only those positioned horizontally are affixed. Vector addition of the measurements taken for corresponding squares in the two areas, gives the desired orthogonal measurement of potential differences over each 5mm x 5mm square.

### 9.2.2 Preparation of Test Billets

Two test billets, figures 9.2b and 9.3b, were machined and surface ground in preparation for J measurements. The first billet was a cube with side length of 50mm, the second was a solid cylinder of 50mm diameter and 50mm height.

Measurement of the current density distribution over the complete surface was unnecessary, because of the symmetries existing in both shapes. The minimum measurement areas were defined as one quadrant of one cube face and a quarter of the circumference of half of the cylinder surface\*. Each measurement area was prepared as described in section 9.2.1. A datalogger was used for voltage measurement, consisting of a D.C. digital voltmeter and high-speed switches (10/second) for connecting each input to the meter in turn.

\* The flat surfaces of the cylindrical billet were excluded due to a restricted total number of voltage measurements possible.

Potential difference measurements were recorded on punched paper tape for subsequent analysis. Each pair of measurement wires was connected to an input channel, with a diode at each pair to rectify the signal.

High speed recording reduced the labour involved in taking readings and minimized the effect of any change in J distribution (with time or temperature) during experiments.

### 9.2.3 Experimental Method

Figure 9.1 shows the linear coil and a photograph of the apparatus. The coil consists of three supported brackets of adjustable height and width: To these are bolted hollow rectangular-sectioned conductor bars 2.4 m long, of high conductivity copper, via long, threaded shafts brazed normal to the bar in the middle and at either end of the bar. The conductors are mounted in pairs and connected by hollow copper U - tubes via hydraulic compression fittings to give a single water cooling circuit and electrical continuity through the coil. The linear coil is connected to a 400V, 400A, 4kHz motor-alternator induction heater by low-loss co-axial cable. The induction heater set incorporates automatic power factor correction by switchable capacitors and provides meters for kV, A and kVAr monitoring.

A test billet was positioned between the bars of the linear coil, with nine other billets to ensure that the coil impedance matched that of the heater. The test billet was air-cooled to prevent over-heating, with possible damage to the measurement wires or change in the current density field.



Measurement area voltages were recorded at room temperature for both test billets in a linear coil, consisting of one, two or three conductor bar pairs, adjusted so that the minimum spacing  $d$  between a coil bar and billet was 5, 10 or 15mm. Each test consisted of two measurements without energising the coil, and two recordings with coil current flowing. The test was performed three times on the cube billet: Between each test the billet was rotated so that faces A, B and C (figure 9.2 b) were recorded in succession. A single test was necessary for the cylindrical billet. Readings from duplicate measurements were averaged. Induction heater voltage, current and reactive power were similarly recorded.

### 9.3 Results of Current Density Measurements

The current density  $J$  is found from the vertical  $V_v$  and horizontal  $V_h$  voltage differences recorded, at each small measurement square, using the formulae,

$$\begin{aligned} J_v &= \frac{V_v}{\ell} \frac{1}{\rho} \\ J_h &= \frac{V_h}{\ell} \frac{1}{\rho} \end{aligned} \quad (9.2)$$

where  $\ell$  is the distance between spot welds of each pair (here  $\ell = 5\text{mm}$ ).  $J_v$  and  $J_h$  are added vectorially to give the resultant magnitude of the current density. Since diodes are used to rectify the datalogger inputs, the direction of  $J$  is deduced from the physical nature of the problem. The surface power loss density,

$$\bar{W} = \rho J^2 \quad (9.3)$$

may then be calculated.  $\bar{W}$  results are considered for the cube and cylinder test billets in sub-sections 9.3.1 and 9.3.2, respectively.

Table 9.1 gives details of the measured induction heater voltage, current and reactive power during the tests. These readings are taken from meters with few scale markings and must be regarded as approximate only. For the purposes of comparison between tests, the coil currents used for linear coils comprising one, two and three conductor bar pairs were scaled to 45A, 90A and 135A, respectively.

### 9.3.1 Cube Test Billet

Figures 9.4, 9.5 and 9.6 show the current density distribution for one, two and three coil conductor bars, where coil currents are 45A, 90A and 135A, for spacing  $d$  of 5, 10 and 15 mm. These distributions are summarised in figure 9.7, where the arrow line width indicates the approximate strength of the induced current. The isometric projection of figure 9.8 shows this information, in relation to the position of the coil bars, and extended over the upper half of the cube.

The induced surface power density  $\bar{W}$  is plotted at selected positions over the measurement face (on logarithmic scale) against the coil spacing  $d$ , for measurement area faces A (figure 9.9), B (figure 9.10) and C (figure 9.11). The dependence of  $\bar{W}$  on the number of conductor bars, and hence coil current, appears in figure 9.12 for face A, and figures 9.13 and 9.14 for faces B and C; a logarithmic scale is used.



### 9.3.2 Cylinder Test Billet

The current density field is plotted for the single, double and triple conductor pair coil, where  $I_c = 45A, 90A$  and  $135A$ , in figures 9.15, 9.16 and 9.17 with the summarized version appearing in figure 9.18. Figure 9.19 shows the position of the cylinder, measurement area and  $J$  distribution with respect to the coil bars. In a similar way to the cube billet, figure 9.20 shows the measured power density for increasing coil spacing. The relationship between  $\bar{W}$  and the number of conductors, and hence coil current, is given in figure 9.21.

## 9.4 Discussion of Results

### 9.4.1 Cube Test Billet

The current flow distribution may be best considered by referring to figures 9.4 to 9.6, with reference to the generalized pattern (figure 9.7) and its relation to the coil position indicated in figure 9.8.

High current is concentrated around the mid-plane of the cube, parallel to the coil bars, on the lower parts of faces A and B (path a on figure 9.7). This horizontal flow reduces in intensity as the distance from the mid-plane increases. On face B, current flows divide (path b on figure 9.7); one path continues in the horizontal plane around the cube while the

other proceeds vertically onto face C, parallel to the longitudinal axis of the coil (path c on figure 9.7). On the cube top face, nearest to the longitudinal mid-plane of the coil, the current decreases to near zero. Also evident, on faces adjacent to the coil bars, are circulating flows indicated by path d, extending onto the top face (path e on face C, figure 9.7.).

Examination of the recorded current densities of figures 9.4 to 9.6 reveals that departures of the current flow from the circumferential path a decline with the addition of conductor bars; particularly noticeable is reduced circulation on face A (path d, figure 9.7). Horizontal current flow around the circumference is favoured by the more uniform magnetic field, produced by a larger number of linear coil bars.

The relationship between induced power density and the number of conductor pairs, and increasing coil current, was found to be

$$\bar{W} (= \rho J^2) \propto N_c^2 \propto I_c^2 \quad (9.4)$$

This is represented by a straight line slope on log-log scales (figures 9.12 to 9.14), with the index s shown, where s=2.0. Measurement inaccuracies appear as bends in some lines on these figures. The closely coupled face A positions conform to the expected square law relationship,  $\bar{W} \propto (\text{conductor pairs})^2$ , with an index s=2.0.



Lesser slopes on figures 9.13 and 9.14, for faces B and C, illustrate the reduction of current flow on non-circumferential paths (along paths c and e of figure 9.7) as a) a more uniform field develops for a greater number of coil bars, giving J flow less restriction to the circumference, or b) as the (weaker) coupling between coil and workload decreases for larger coil spacing d.

The graphs of power loss density (on logarithmic scale) against coil spacing d (figures 9.9 to 9.11) are not as consistent. The average index  $s = -0.07$  suggests that the governing equation is approximately

$$\bar{W} = \bar{W}_0 \exp \{-0.07 d\} \quad (9.5)$$

This reflects the dependence of the magnetic potential  $A'$  on coil spacing,

$$A' \propto \exp \{-kd\}$$

This assumption is used by Reichert [106] and Renner [115], who set up the differential equations in terms of the magnetic vector potential, for numerical solution of a solenoidal coil surrounding a cylindrical workload. They state that this exponential equation approximates to the dependence of  $A'$ , in free space, with radial distance between the workload and coil, and is valid at close coupling near the plane of the coil. Therefore, the power density  $\bar{W}$  is given by

$$\bar{W} = \rho J^2 = \frac{\omega^2}{\rho} A'^2$$

and equation 9.5 follows. Provided that the coil and workload are closely coupled, as for face A of the cube billet and regions of the cylinder close to the conductors, a similar relationship exists for the linear coil case.

#### 9.4.2 Cylindrical Test Billet

Analysis of the current density distributions follow along similar lines to the cube, with reference to figure 9.15 to 9.17 for one, two and three conductor bar pairs and coil currents of 45A, 90A and 135A, respectively. Generalized current flow appears in figure 9.18, and its relationship to coil bar position is shown in figure 9.19. For the cylindrical test billet, the currents are more constrained to lie on circumferential paths. Some deviation may be noted, however, as the distance from the coil bar nearest to the cylinder transverse mid-plane increases. There is no evidence of significant circulating flows in the immediate proximity of the coil bars, but current flow in a vertical plane, to cross the top surface, is apparent. An increasing predominance of circumferential flow occurs for larger  $N_c$  and coil current, especially where the coil spacing  $d$  is small, as the magnetic field becomes more uniform.

Somewhat surprisingly, the  $J$  distribution is confined to flow approximately parallel to the coil bars at all spacings, especially in the centre part of measurement area ABCD. Greater evidence of circulating paths was expected for weaker magnetic fields; no explanation has been found for this anomaly.



Conformity to the expected relationships between power density and coil current, and between  $\bar{W}$  and coil spacing, is fair. The relationship  $\bar{W} \propto (\text{conductor pairs})^2$ , confirming equation 9.4. Figure 9.20 contains the greatest variability of slope for the dependence of  $\bar{W}$  on d spacing.

#### 9.4.3 Cube and Cylinder Results Comparison

Quantitative comparisons between current density distributions on the cube and the cylindrical test billet are difficult to make, with the limited amount of data presented here. Few measurement points on both test billets are in equivalent positions, with respect to the linear coil. The distribution of current flow is also largely influenced by the billet shape: Circumferential flow around the cylinder was greater than similar flow around the cube, with a corresponding reduction in current towards the upper and lower faces of the billet. In general, current density flow around the cylinder mid-plane was approximately 40-50% greater than measured values at equivalent positions on the cube face A. If the current distributions were comparable, and therefore proportional to the circumferential path length, only a 28% improvement would be expected. On areas not adjacent to the coil bars, non-circumferential flow around the cylinder reduces to approximately 12% more than the corresponding J results on the cube; circumferential flow on these areas is increased to between 1.6 and 2.0 times the flow around the cube.

Power density at each measurement square, averaged for both shapes at each test condition of spacing and  $N_c$ , indicates that the induced power is comparable for cube and cylinder test billets. The first approximation to overall efficiency (table 9.1) indicates that the cylinder is slightly more efficient than the cube, in general. These figures may be misleadingly high, since current density on the flat portions of the cylinder was not measured. On these faces, significantly lower J values may be expected. A more representative estimate of  $\eta$  (contained within brackets in table 9.1) is found by assuming that the average power density on the cylinder flat faces is reduced, in relation to the measured average on the curved faces, by a similar ratio to the averages found on the cube face C to that on face A. Within the accuracy of these tests, the efficiencies of cube and cylinder billets are comparable. Without further data, notably on the cylinder flat faces, further comparison must be inconclusive.

#### 9.4.4 Efficiency

Overall efficiencies, between 4% and 26%, are low. By comparison, solenoidal induction coils for heating solid cylindrical billets of equivalent dimensions and air-gap may be expected to show efficiencies between 88% and 91%, below Curie temperature [93].

#### 9.4.5 Uniformity of Heating

Figures 9.4 to 9.6 and figures 9.15 to 9.17 show that, on the cube and cylinder faces with greatest current concentration, the induced power density decreases with distance from the coil bars to



approximately one half of its maximum value. The rate of temperature rise, calculated from equation 9.1, will not exceed  $0.4^{\circ}\text{C/s}$  for the largest power densities of table 9.1. The power for these experiments was kept low to avoid damage to the insulation on the fine measurement wires. For a production linear coil heater, higher power densities must be used to raise the through-put of the coil. Assuming that production power densities will be commensurate with heating similar shaped parts in solenoidal coils, power densities below and above the Curie temperature will be approximately  $\mathcal{P}_1=1\text{MW/m}^2$  and  $\mathcal{P}_2=0.25\text{MW/m}^2$ , respectively from table 6.1. Taking the worst case of heating for the cube, where the induced power is confined to the active faces of the billet closest to the coil bars, analogy may be drawn with the heating of a small slab from both sides. Following [18] p391, the time to heat a slab of thickness  $b$  to  $1250^{\circ}\text{C}$  is given by,

$$t_{1250^{\circ}\text{C}} = b(c\gamma) \left[ \frac{\theta_1}{\mathcal{P}_1} + \frac{\theta_2}{\mathcal{P}_2} \right]$$

where suffices 1 and 2 refer to temperatures below and above  $\theta_{\text{curie}}$ .

Substituting the relevant values into this equation gives

$$t_{1250^{\circ}\text{C}} = t_1 + t_2 = 181 + 447 = 635 \text{ s} = 10\frac{1}{2}\text{min.}$$

The normalized time at the end of sub-Curie heating,

$$\tau_1 = \frac{k t_1}{(c\gamma) b^2} = 0.44$$

is greater than 0.25, so the temperature distribution will be parabolic.

In a similar manner to the method of Chapter 6, superposition of a soaking period of the sub-Curie temperature distribution, and the temperature distribution established by the  $\mathcal{P}_2$  induced power density, gives the final temperatures.

At the Curie temperature the surface and centre temperatures may be found [18]:-

$$\theta_{s1} - \theta_{c1} = \frac{P_2 b}{4k} = 423^\circ\text{C}$$

$$\theta_{s1} = \theta_{m1} + \frac{P_2 b}{6k} = 760 + 282 = 1042^\circ\text{C}$$

$$\therefore \theta_{c1} = 619^\circ\text{C}$$

The  $(\theta_{s1} - \theta_{c1})$  difference is reduced during the soaking period of  $t_2$ , after which  $\tau_2 = 1.04$ . A similar graph to figure 3.6, but for a slab [18], figure A2.3, shows that at  $t_2 = 447\text{s}$ ,  $\theta_{s1} = \theta_{c1} = \theta_{m1} = 760^\circ\text{C}$ . The temperature distribution created by the super-Curie  $P_2$  component is derived similarly,

$$\theta_{s2} = \theta_{m2} + \frac{P_2 b}{6k} + \frac{2P_2 b \tau}{k} + \frac{P_2 b}{6k} = 449 + 71 = 520^\circ\text{C}$$

$$\theta_{s2} - \theta_{c2} = \frac{P_2 b}{4k} = 106^\circ\text{C}$$

$$\therefore \theta_{c2} = 414^\circ\text{C}$$

Thus the total temperatures are

$$\theta_s = 760 + 520 = 1280^\circ\text{C}$$

$$\theta_c = 760 + 414 = 1174^\circ\text{C}$$

$$\Delta\theta = 106^\circ\text{C}$$

From [18], figure A2.3 this temperature difference will be reduced to an acceptable  $\pm 25^\circ\text{C}$  for forging after a minimal soaking time ( $\tau = 0.057$ ) of ~25 seconds.



## 9.5 Concluding Summary

Measurements of the induced current density distributions, on the surfaces of simple cubic and cylindrical test billets, within a linear coil are reported in this study. Described here are apparatus and techniques necessary to minimize anomalous results, caused by induced voltage from stray magnetic fields. The current density is difficult to measure accurately and experimental error of 10% may be expected from the results; no similar measurements of this kind are known for comparison.

The relationship between the power density  $\bar{W}$  induced in the workload and the coil current  $I_c$  was found to be

$$\bar{W} (= \rho J^2) \propto I_c^2 \quad (9.4)$$

and the effect of coil bar spacing  $d$  mm, given by

$$\bar{W} = \bar{W}_0 \exp \{-0.07d\} \quad (9.5)$$

Overall efficiency of the linear coil in these tests varied between 4% and 26%, comparable efficiencies were estimated for the cube and cylinder billets under similar conditions. For the most uniform and efficient heating of simple shaped parts within the linear coil, the conductor bars should be positioned with the minimum spacing consistent with mechanical clearances, and a large number of bar pairs used to give the most uniform field possible. The low efficiency of the linear coil, in comparison to solenoidal arrangements, suggests that its use can only be justified where the advantages of simplicity and flexibility for production are paramount.

Qualitative assessment of the J distribution revealed that deviations of the flow, from that expected for a solenoidal coil, were reduced where a more uniform magnetic field was established by the linear coil (at close coil spacing and with a large number of conductor bars). Power density magnitudes were found to vary by a factor of two over faces of the test billets. It is estimated that temperature differences produced by this variation are unlikely to produce large differences in the final temperature, over a typical heating cycle, for induced power magnitudes of production heaters.

The next chapter considers the heating of more complex shaped parts. The results of these tests, for parts of uniform cross-section, may be used to provide preferential heating effects in parts of more complex shapes.



Number of Induction coil bar pairs	Coil spacing			Voltage (V)	Current (A)	Reactive Power (kVAr)	Current Scaled to	Coil Power Scaled (kW)
	5 mm	10 mm	15 mm					
1	*			200	315	40 lag	45A	7
1		*		200	310	40 lag	45A	6.9
1			*	200	315	40 lag	45A	6.9
2	*			240	190	30 lag	90A	16
2		*		240	190	28 lag	90A	17
2			*	240	170	29 lag	90A	15
3	*			220	120	17 lag	135A	23
3		*		210	130	17 lag	135A	22
3			*	230	150	10 lag	135A	30
				INDUCED POWER DENSITY (MW/m <sup>3</sup> ) averaged over surface and within skin depth.		Overall Efficiency		
				Cube	Cylinder	CUBE	CYLINDER	
1	*			5.1	6.5	11%	12% (10%)	
1		*		2.8	3.4	6%	6% (5%)	
1			*	1.8	2.2	4%	4% (3%)	
2	*			16.6	27.1	14%	20% (17%)	
2		*		10.2	20.1	9%	15% (13%)	
2			*	7.3	13.1	6%	10% (8%)	
3	*			36.7	52.7	21%	26% (22%)	
3		*		24.2	22.2	14%	11% (9%)	
3			*	19.6	21.8	11%	11% (9%)	

Table 9.1 : Calculation of coil power, average induced power density and overall efficiency during current density measurements on cube and cylinder test billets.

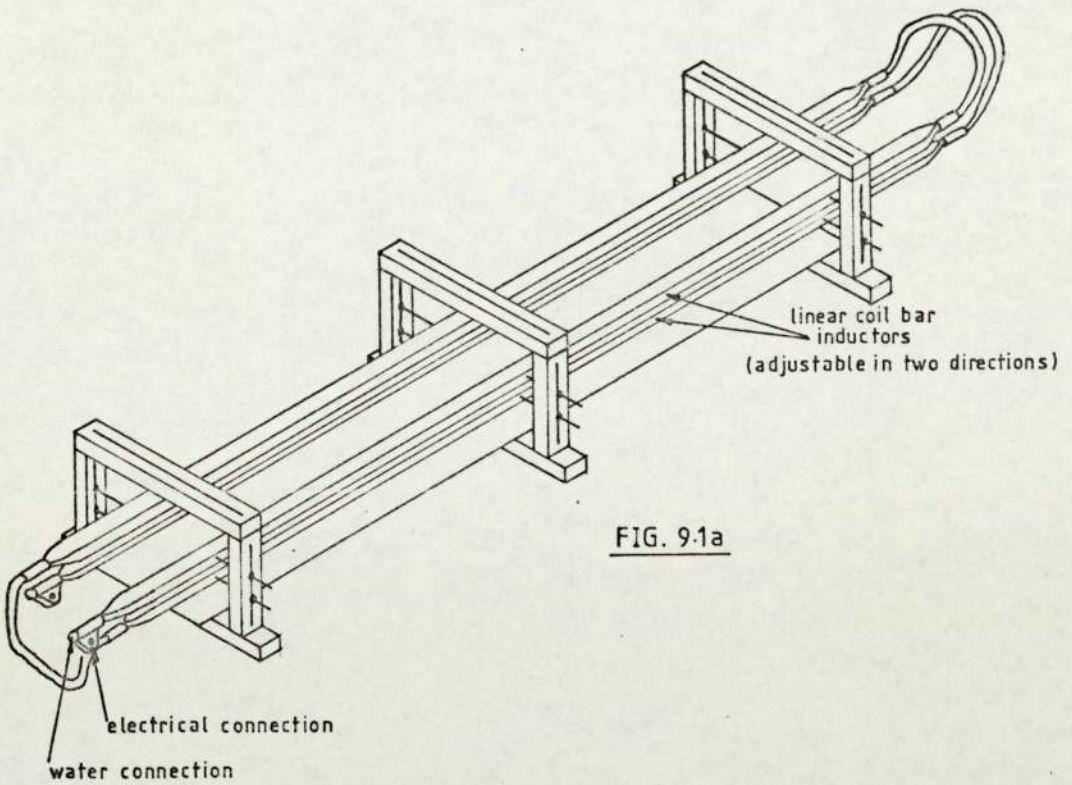


FIG. 9.1a

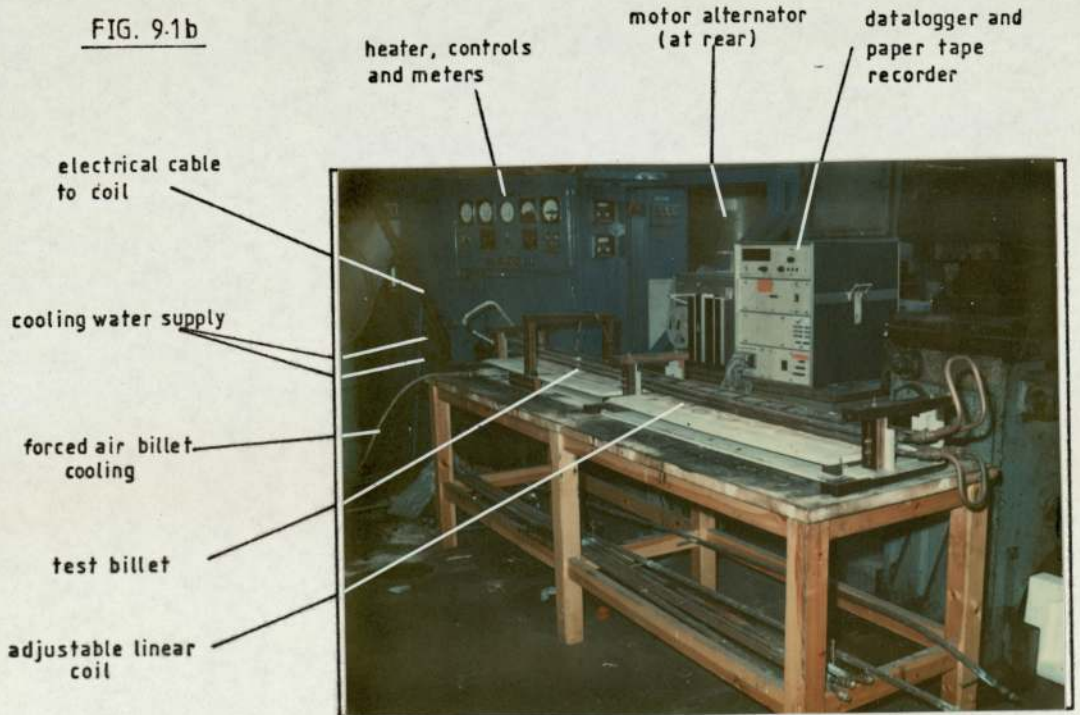


FIGURE 9.1: Apparatus for linear coil experiments showing a) the adjustable coil and b) connections to the induction heater, (photograph).



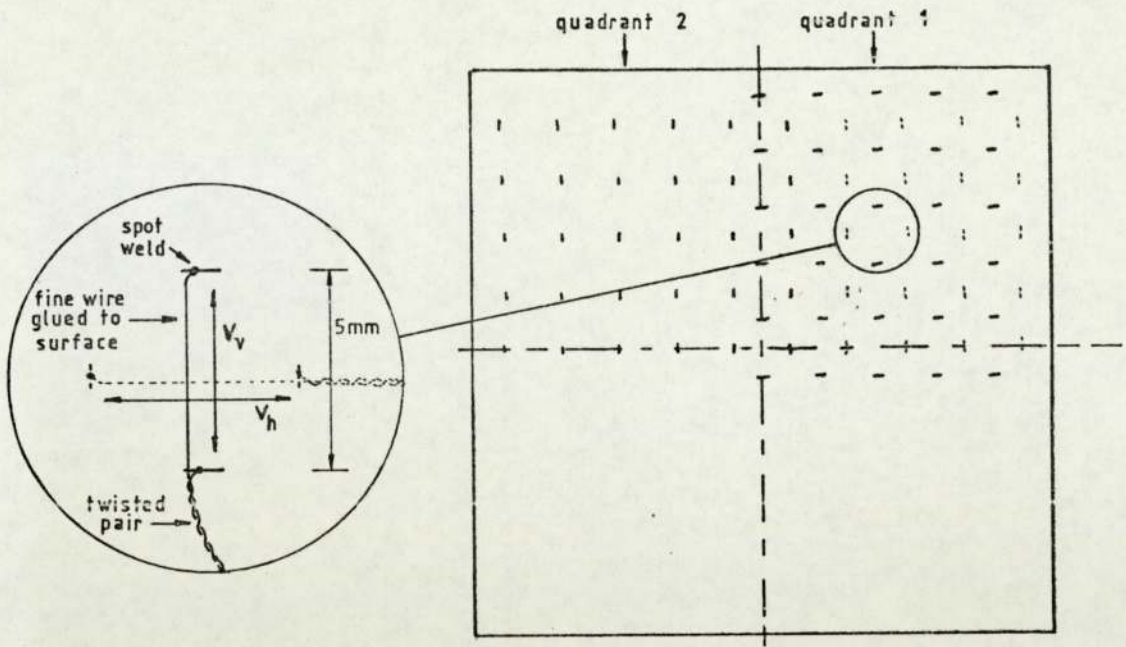


FIG 9.2a

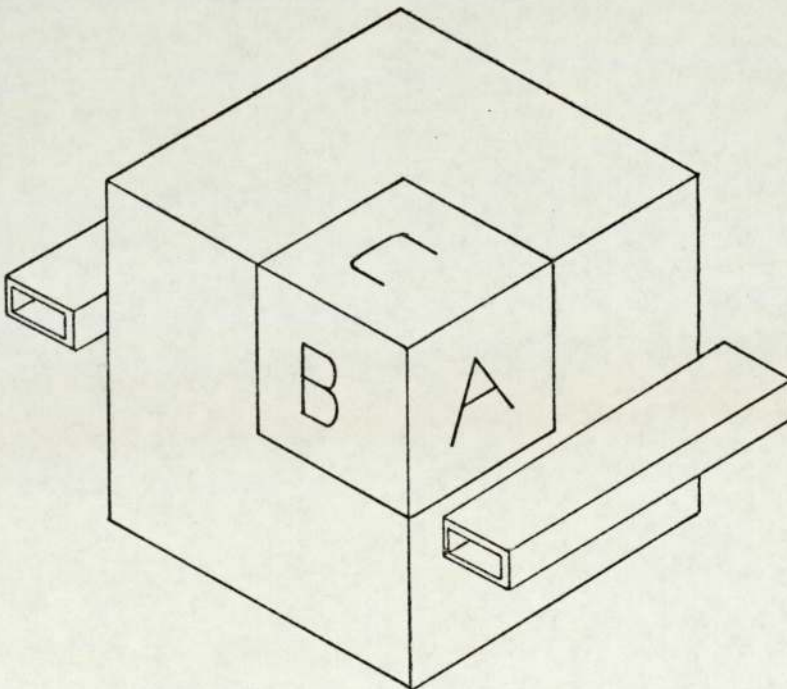


FIG.9.2b

FIGURE 9.2: Preparation of cube test billet for current density measurements, showing a) division of the measurement quadrants 1 & 2 and positioning of spot-welded wires (dashed lines on quadrant 1 indicate corresponding measurement positions on quadrant 2) and b) position of cube with respect to linear coil bars (one pair shown) for measurement of faces A, B and C.

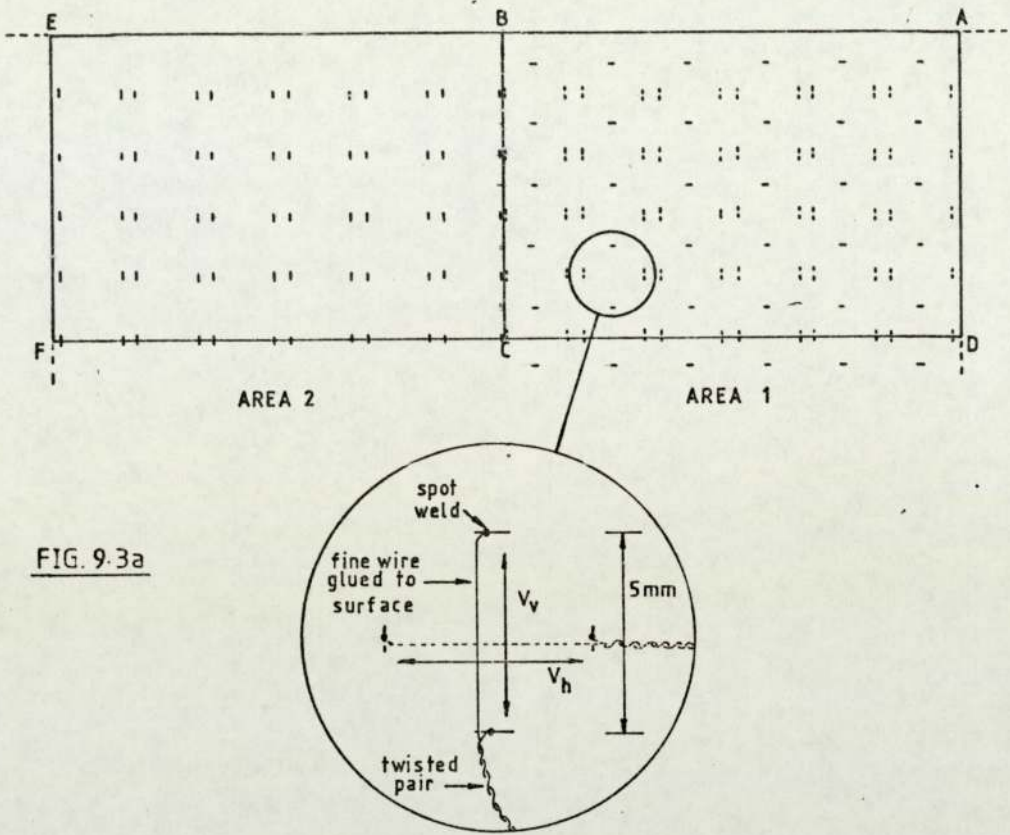


FIG. 9.3a

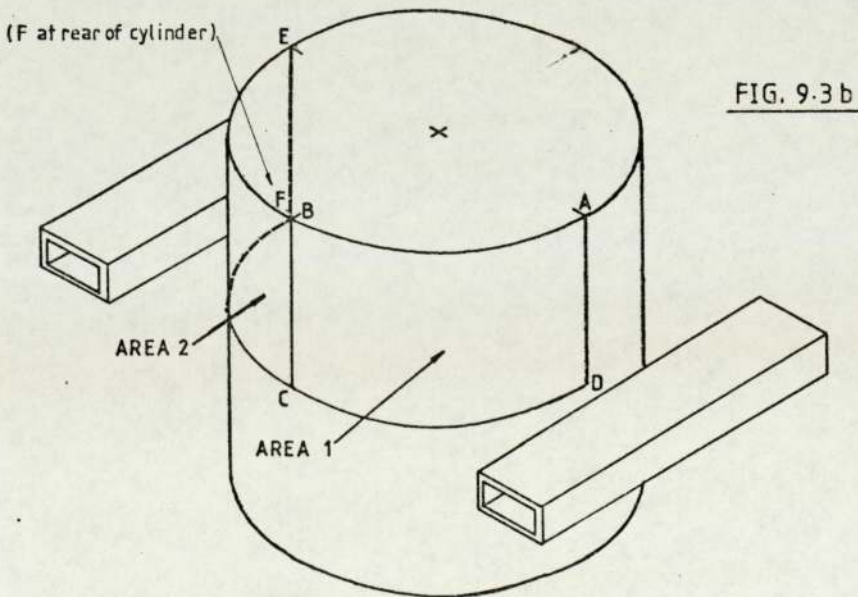


FIG. 9.3b

FIGURE 9.3: Preparation of cylinder test billet for current density measurements a) division of measurement areas ABCD and BEFC and positioning of spot-welded wires (dashed lines on ABCD indicate corresponding measurement positions of BEFC) b) position of cylinder with respect to linear coil bars (one pair shown).



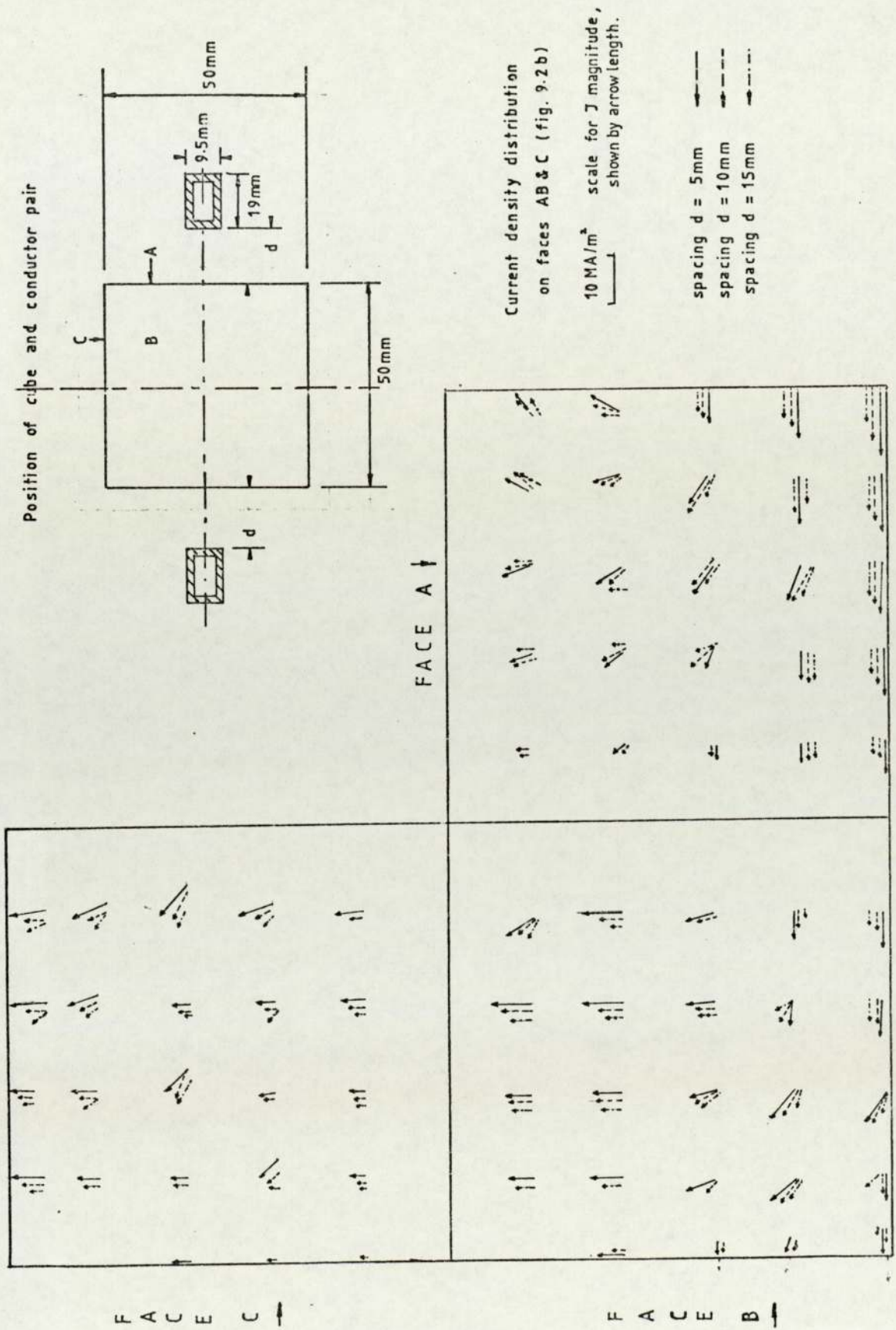


FIGURE 9.4: Measured current density distribution with spacing  $d$  on cube test billet surfaces A, B and C in a single conductor pair linear coil.

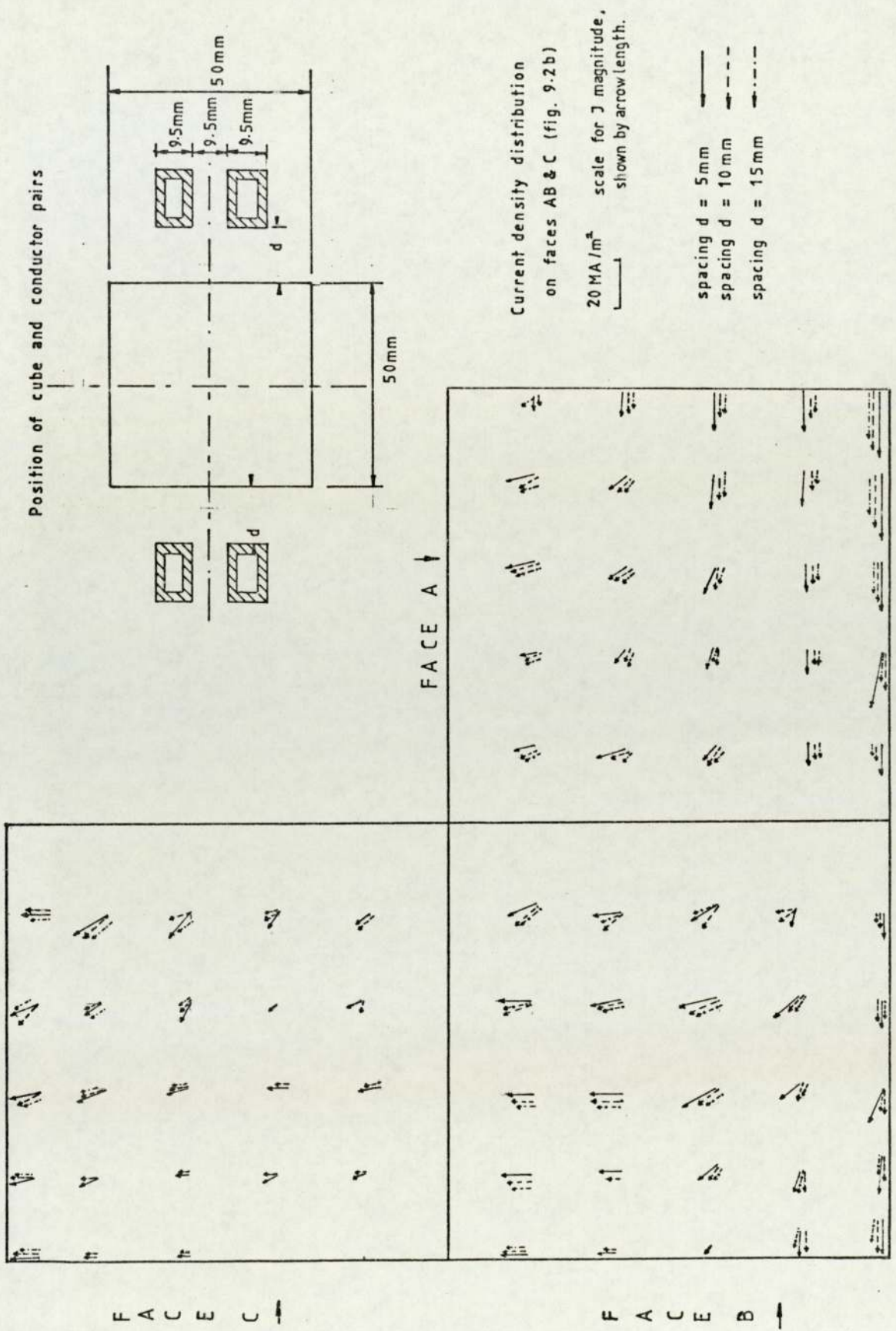


FIGURE 9.5: Measured current density distribution with spacing  $d$  on cube test billet surfaces A,B and C in a two conductor pair linear coil. Note change of current scale from figure 9.4.



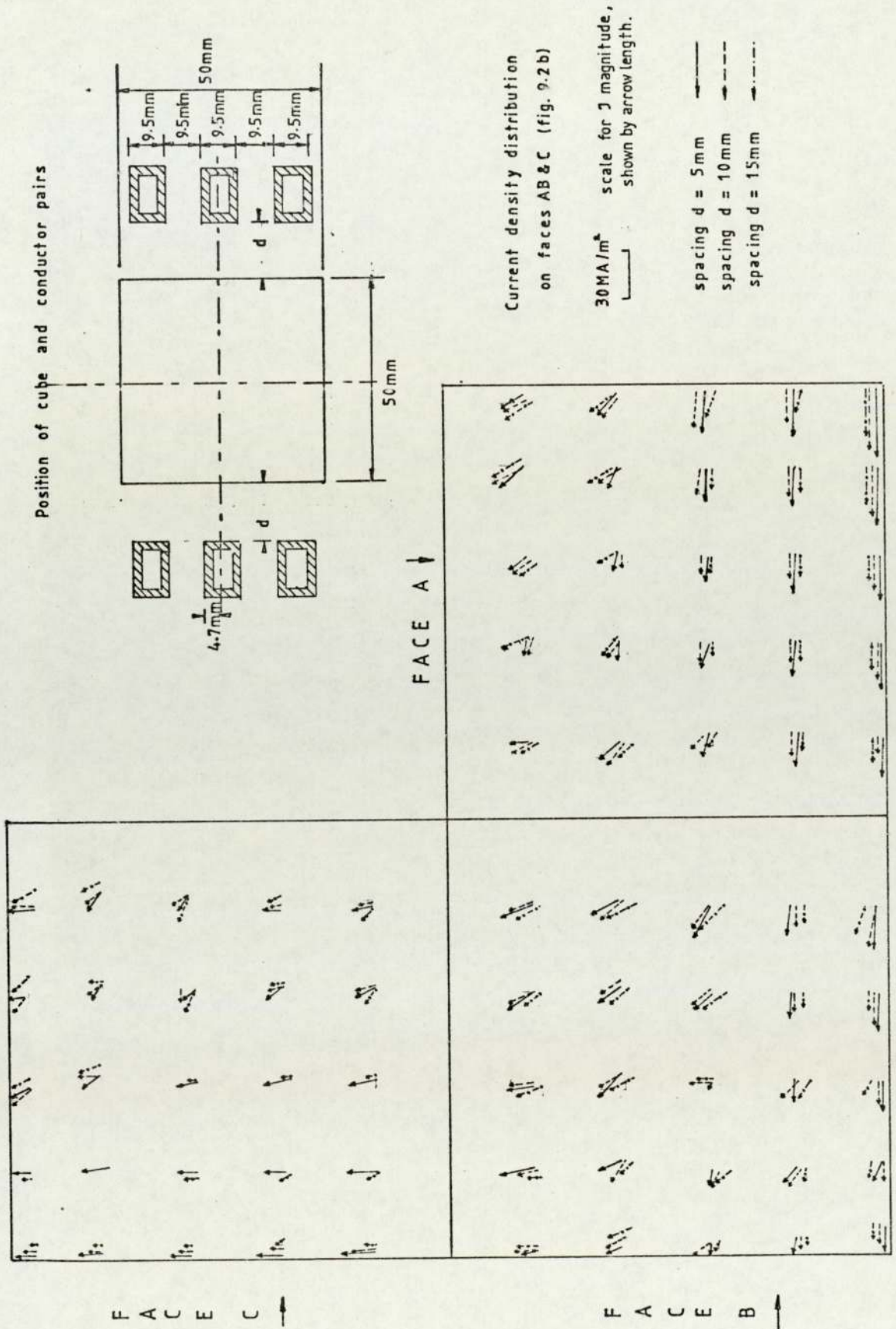


FIGURE 9.6: Measured current density distribution with spacing  $d$  on cube test billet surface A, B and C in a three conductor pair linear coil. Note change of current scale from figures 9.4 and 9.6.

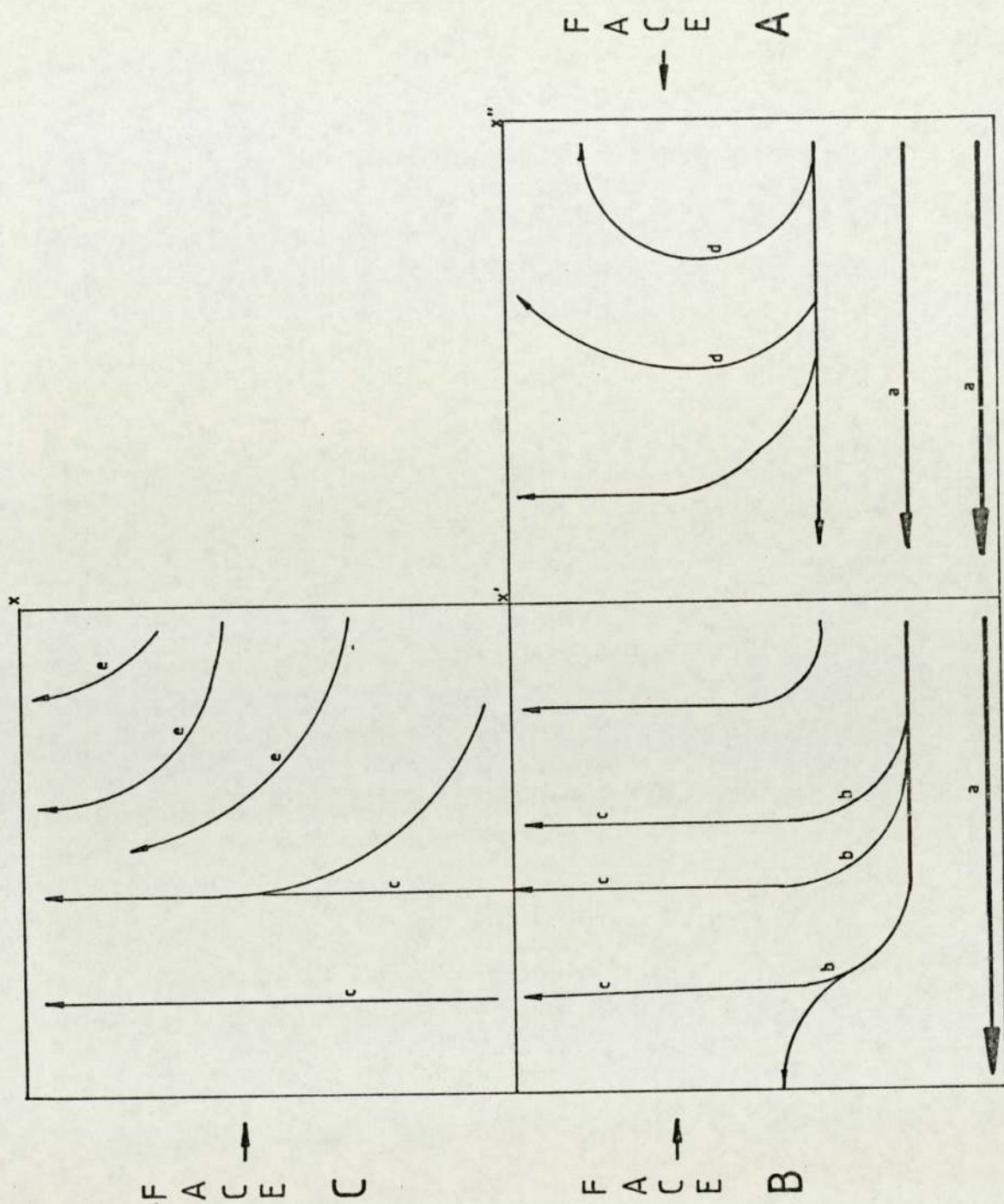


FIGURE 9.7: Generalized current density distribution on cube faces A, B and C of figures 9.4 to 9.6. Arrow line width indicated induced current magnitude. Lower case lettered flows are discussed in section 9.4.1. Note that edge  $xx'$  is the same as edge  $x'x''$ .



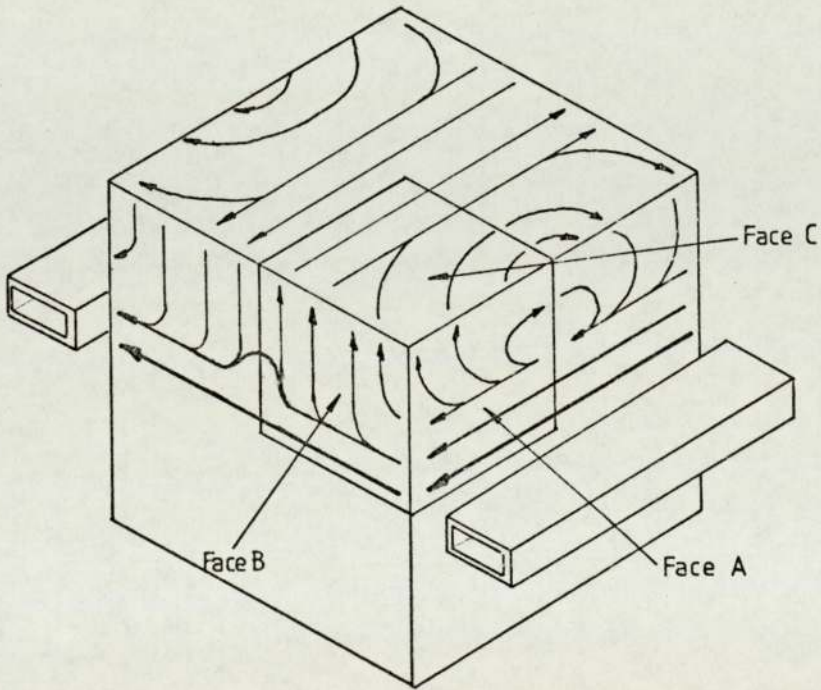


FIGURE 9.8: Generalized current density distribution on the cube billet of figure 9.7 shown in relation to the linear coil conductor position (single pair shown).

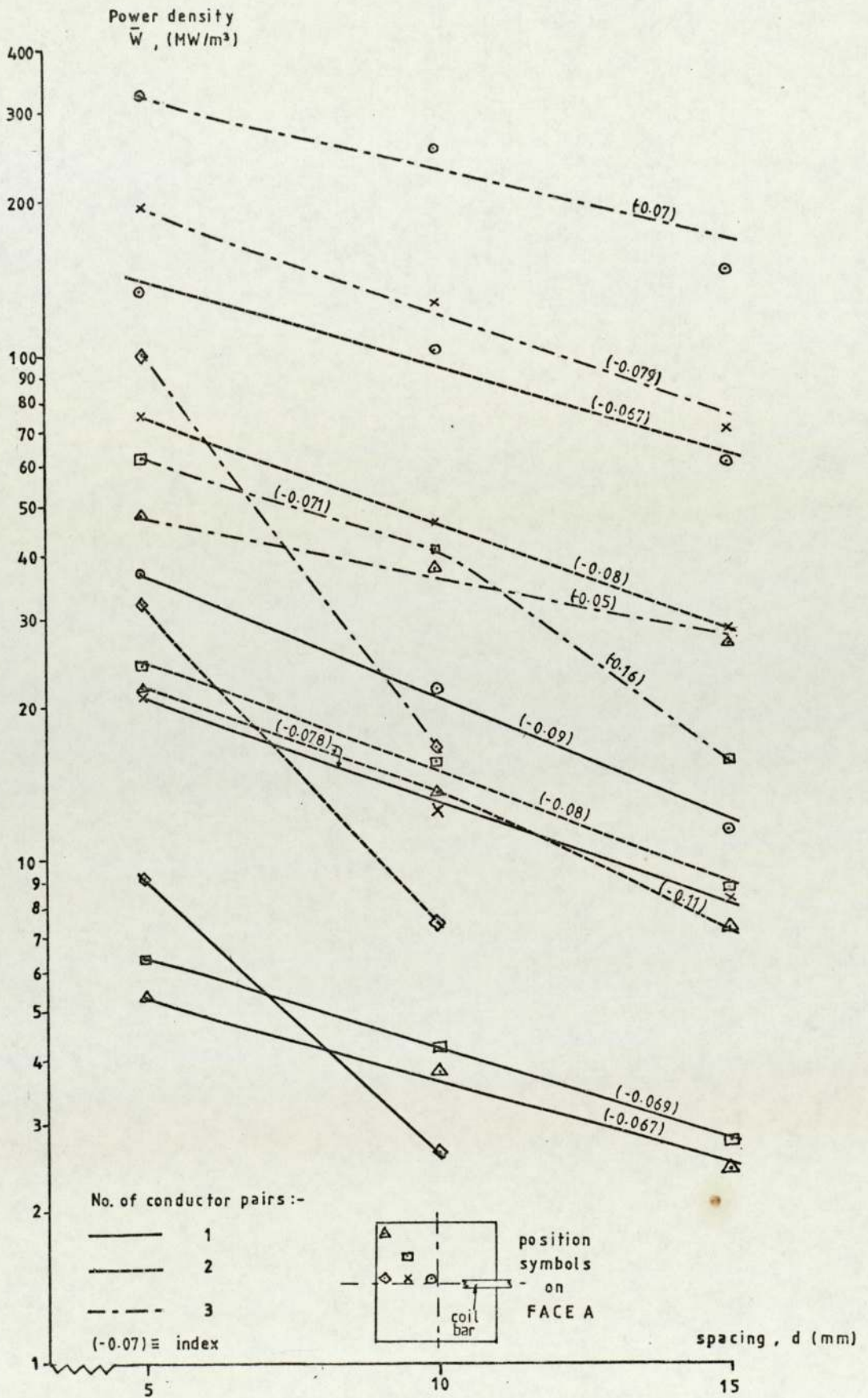


FIGURE 9.9: Power density  $\bar{W}$  induced at selected positions of cube billet face A with linear coil spacing d. The value of  $\bar{W}$  is calculated from current density measurements.



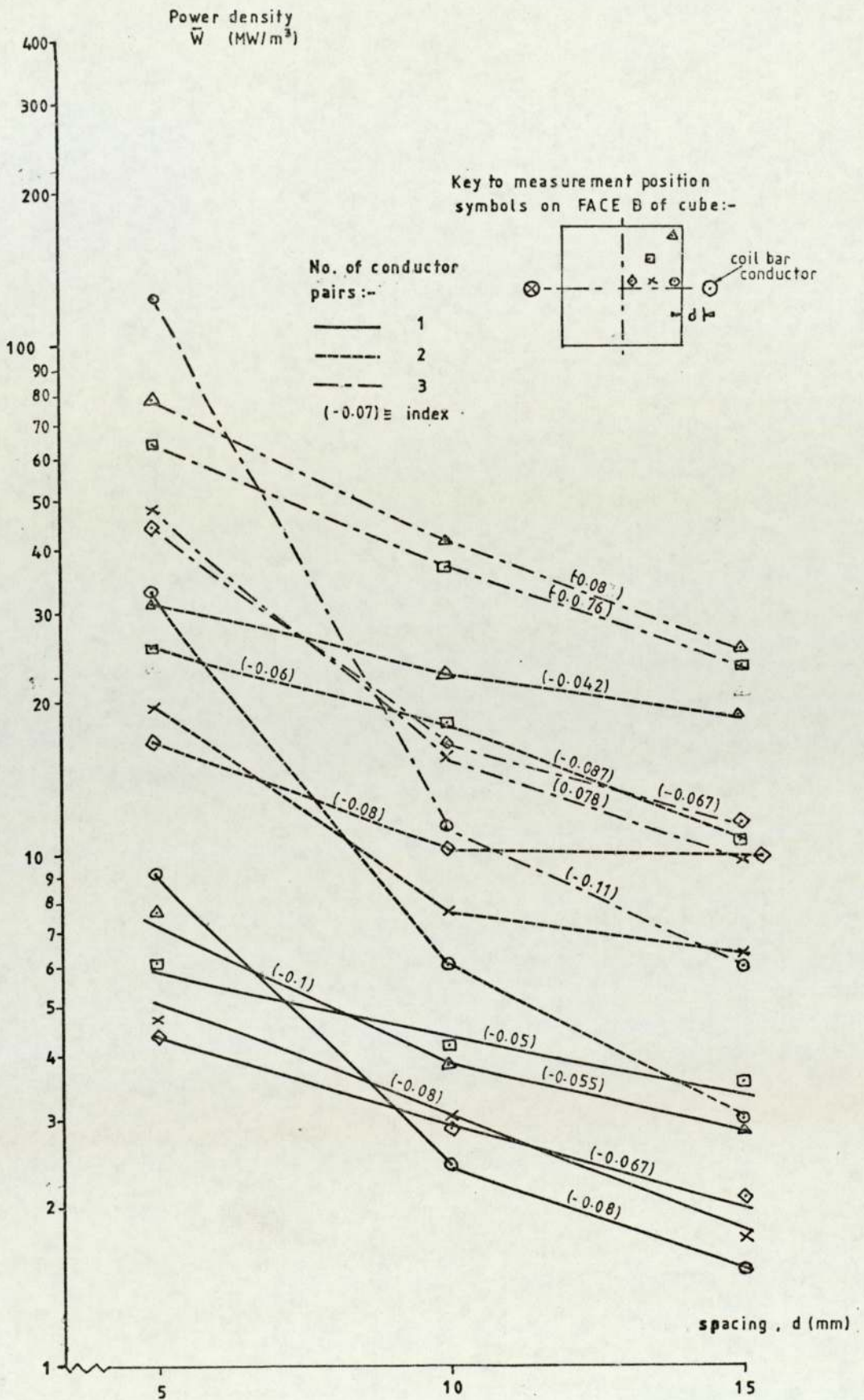


FIGURE 9.10: Power density  $\bar{W}$  induced at selected positions of cube billet face B, with linear coil spacing  $d$ . The value of  $\bar{W}$  is calculated from current density measurements.

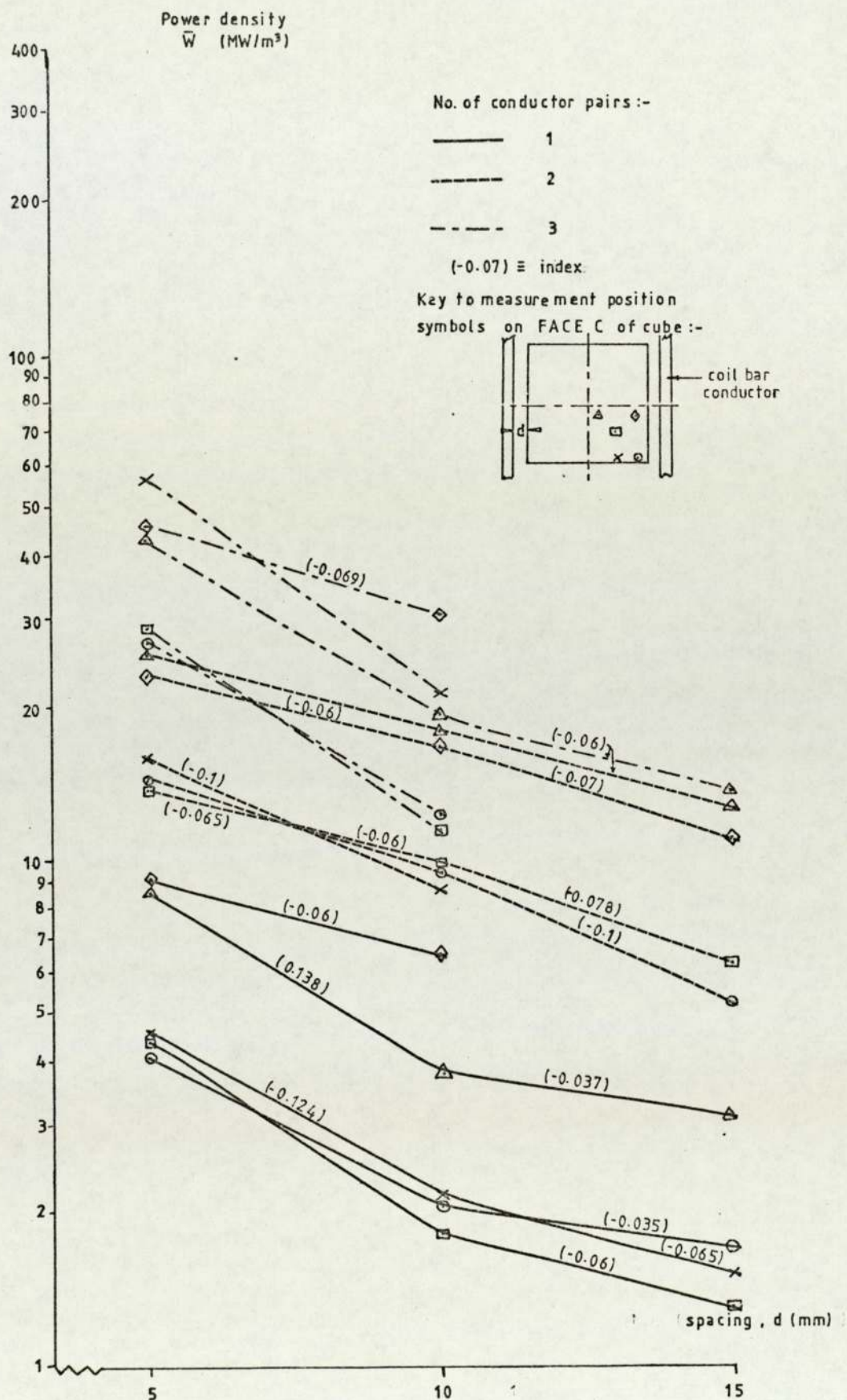


FIGURE 9.11: Power density  $\bar{W}$  induced at selected positions of cube billet face C with linear coil spacing  $d$ . The value of  $\bar{W}$  is calculated from current density measurements.



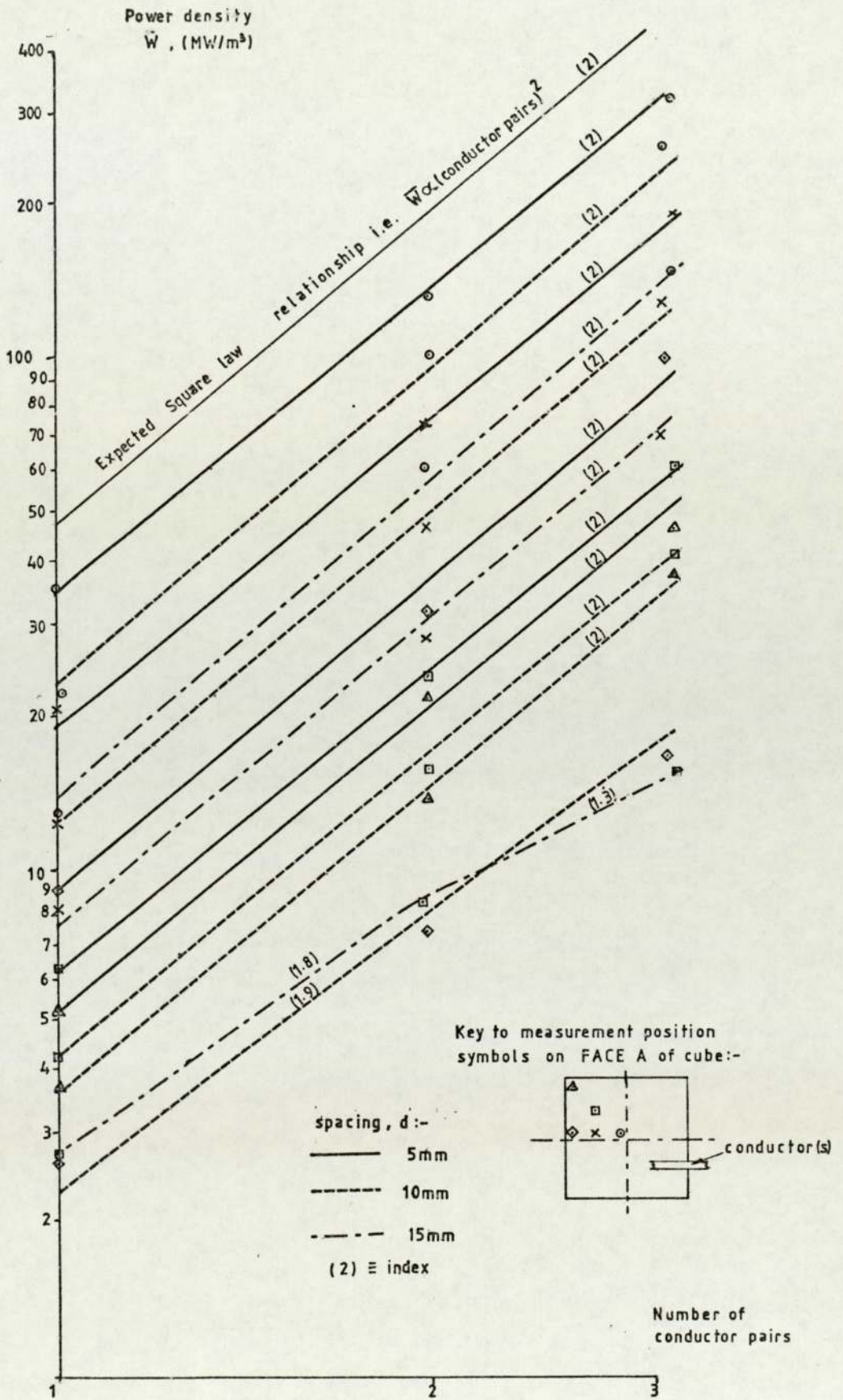


FIGURE 9.12: Power density  $\bar{W}$  (calculated from current density measurements) at selected positions of cube billet face A, with number of linear coil conductor pairs.

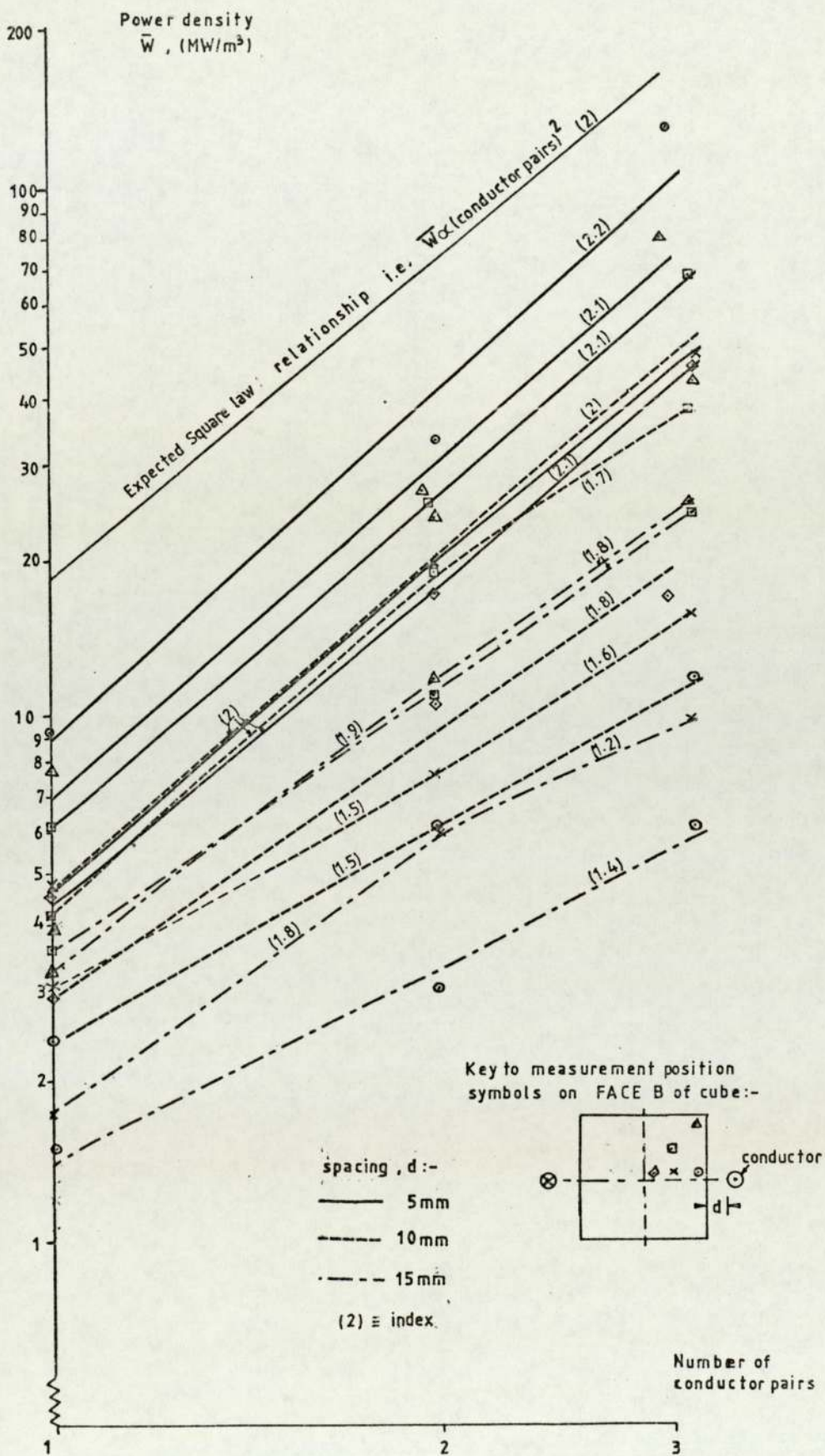


FIGURE 9.13: Power density  $\bar{W}$  (calculated from current density measurements) at selected positions of cube billet face B with number of linear coil conductor pairs.



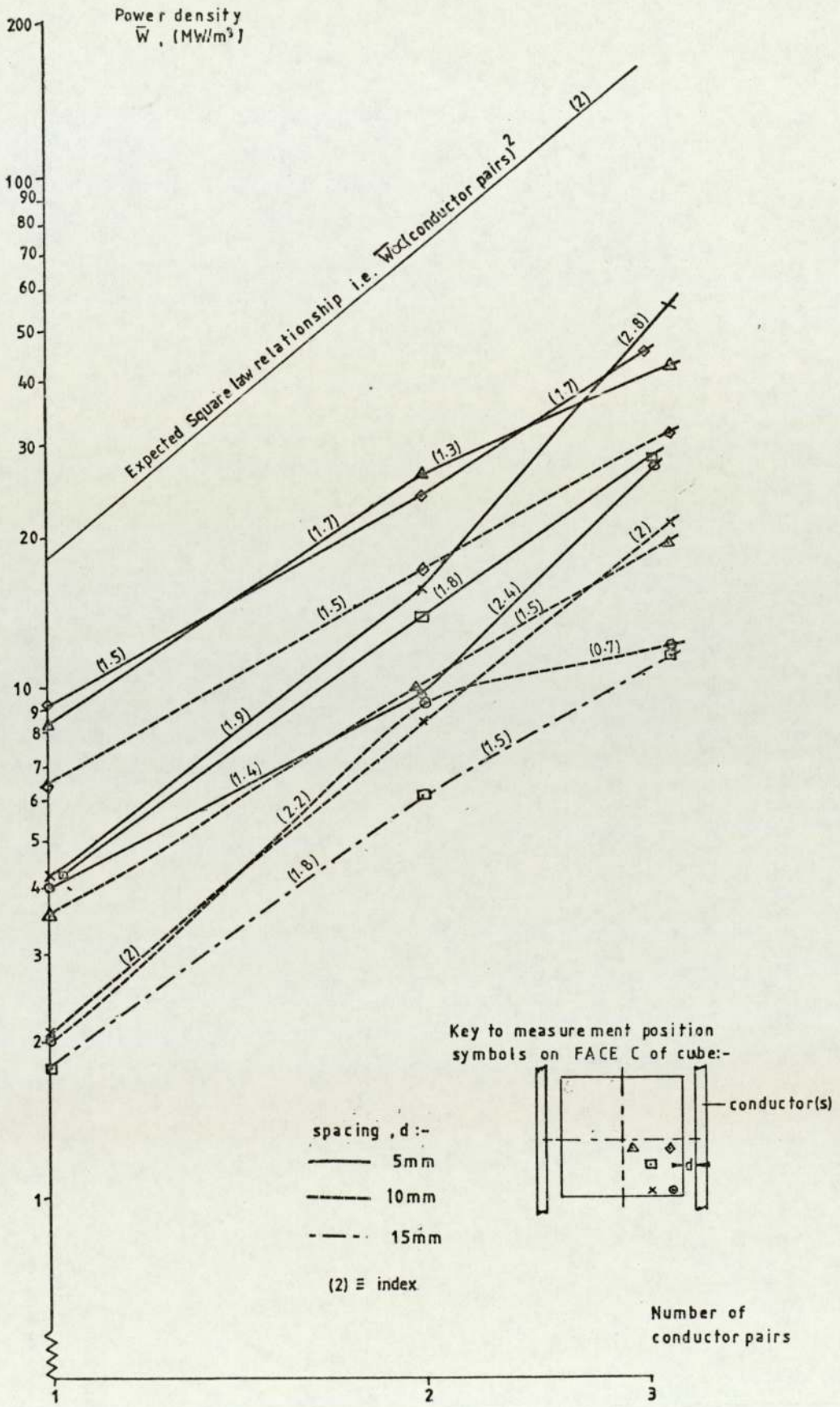


FIGURE 9.14: Power density  $\bar{W}$  (calculated from current density measurements) at selected positions of cube billet face C with number of linear coil conductor pairs.

Position of cylinder and conductor pair

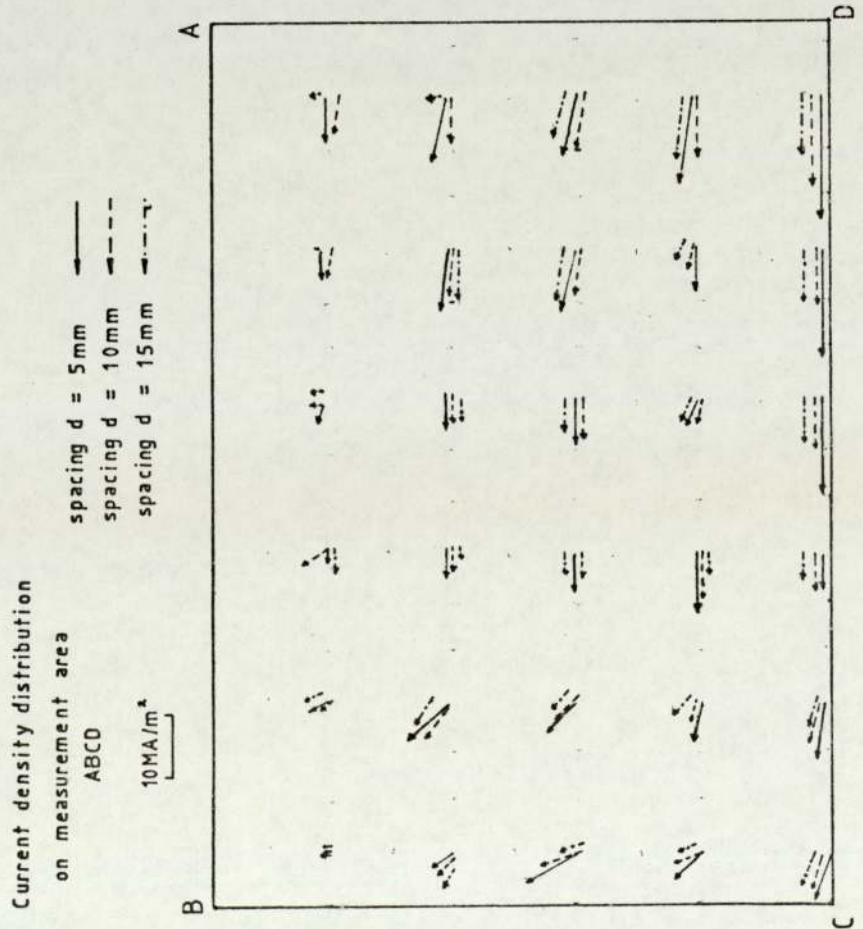
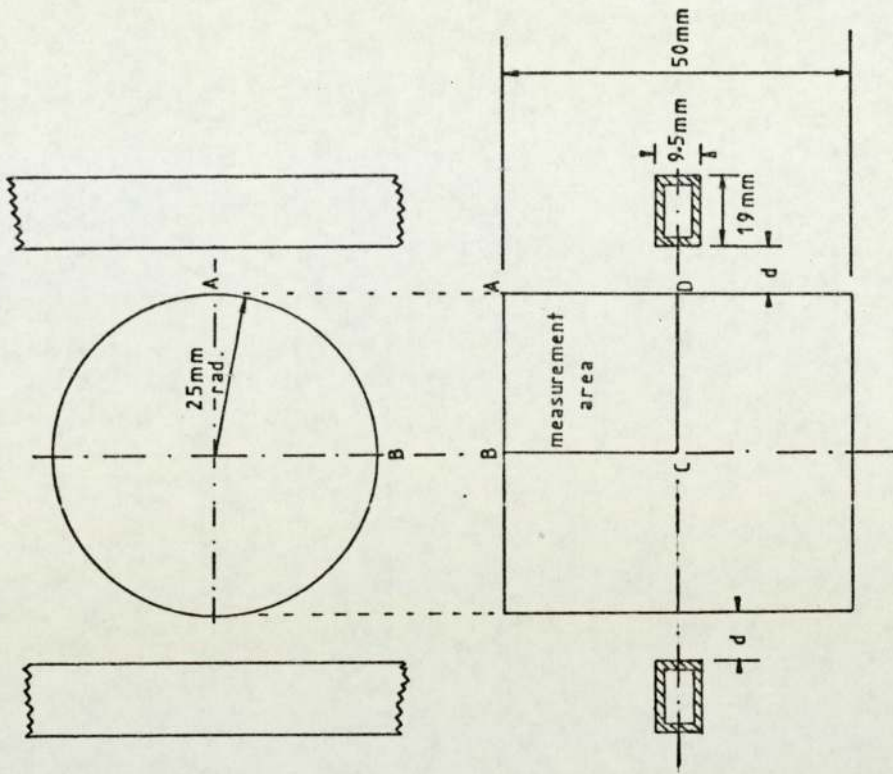


FIGURE 9.15: Measured current density distribution with spacing  $d$  on cylindrical test billet surface in a single conductor pair linear coil.



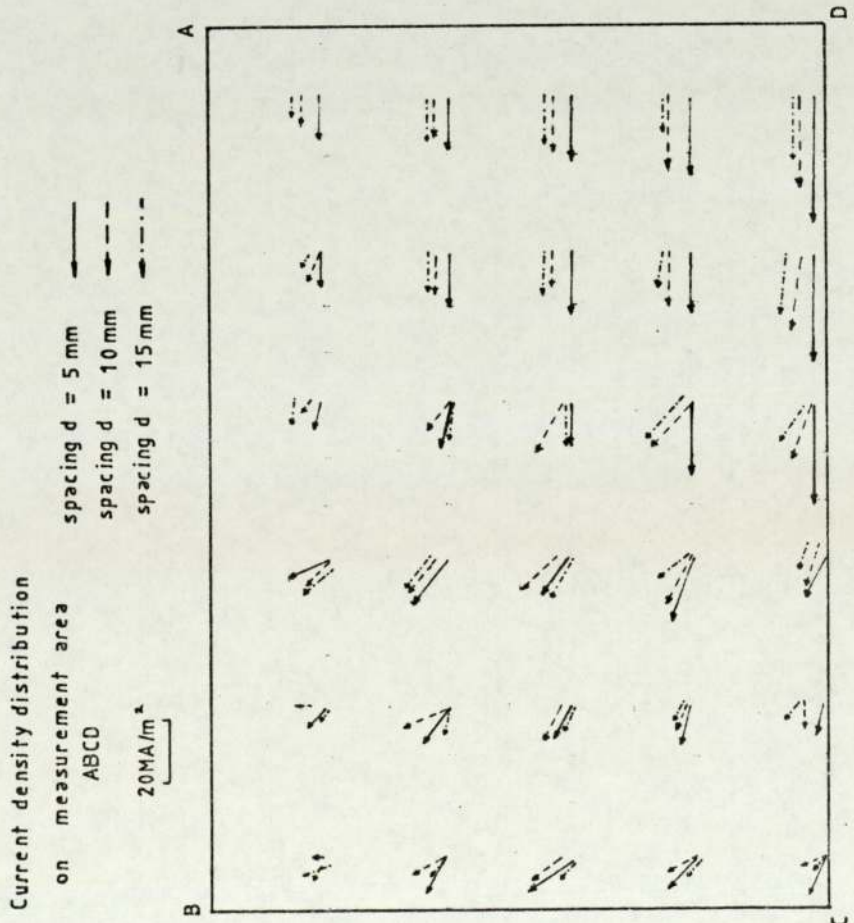
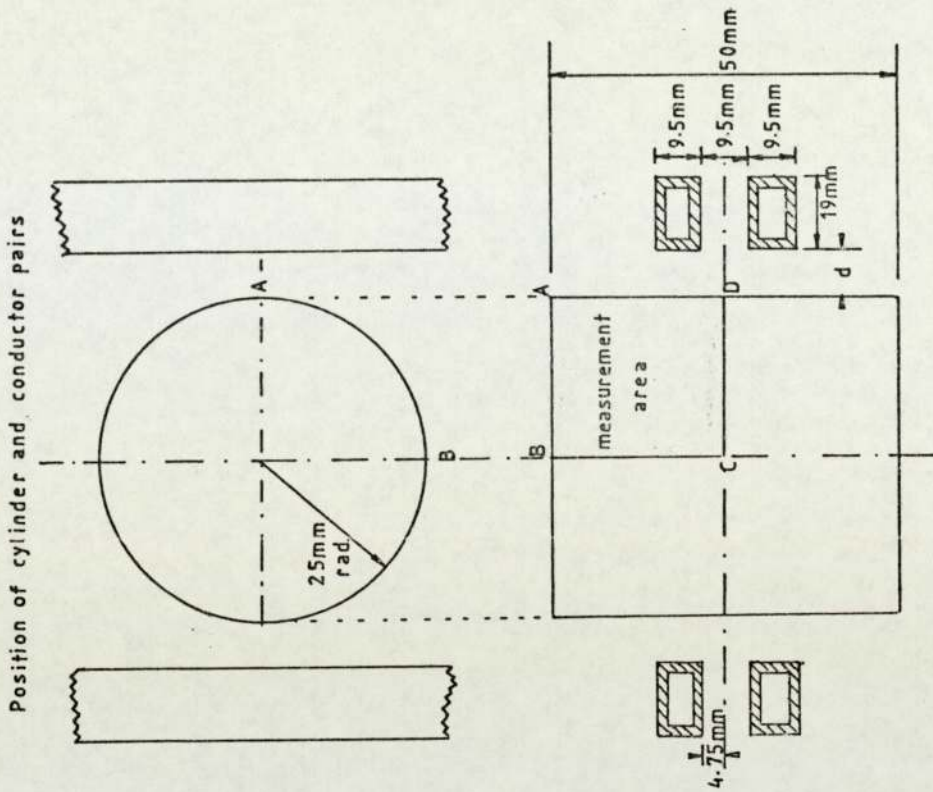


FIGURE 9.16: Measured current density distribution with spacing  $d$  on cylindrical test billet surface in a two conductor pair linear coil. Note change of current scale from figure 9.15.

Position of cylinder and conductor pairs

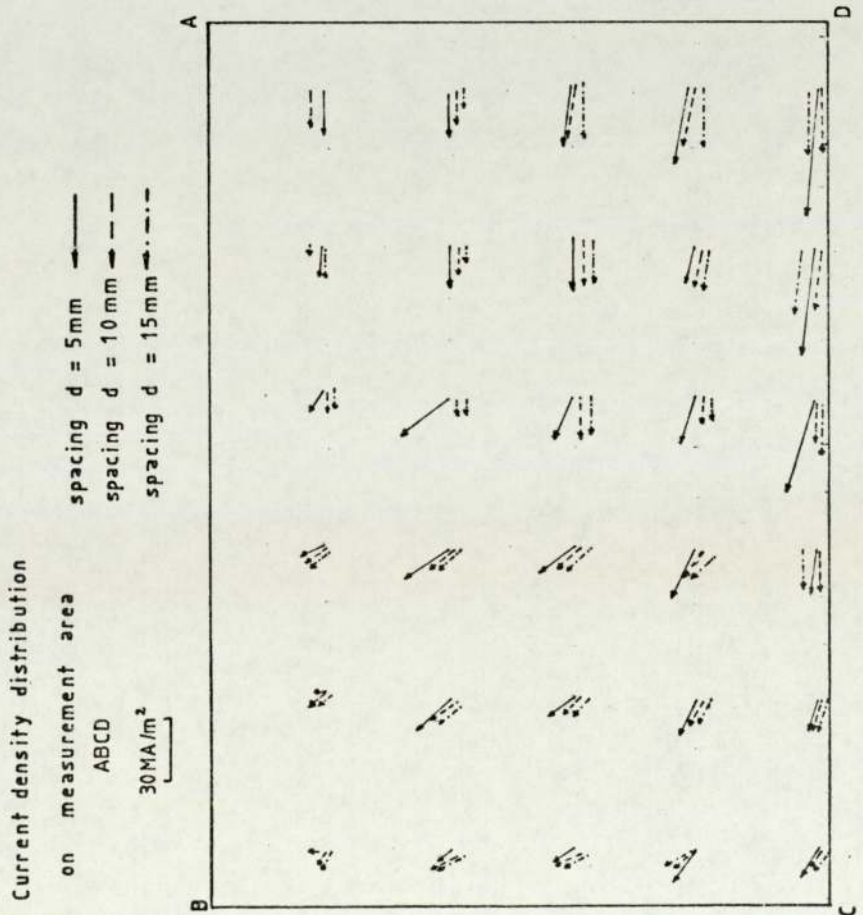
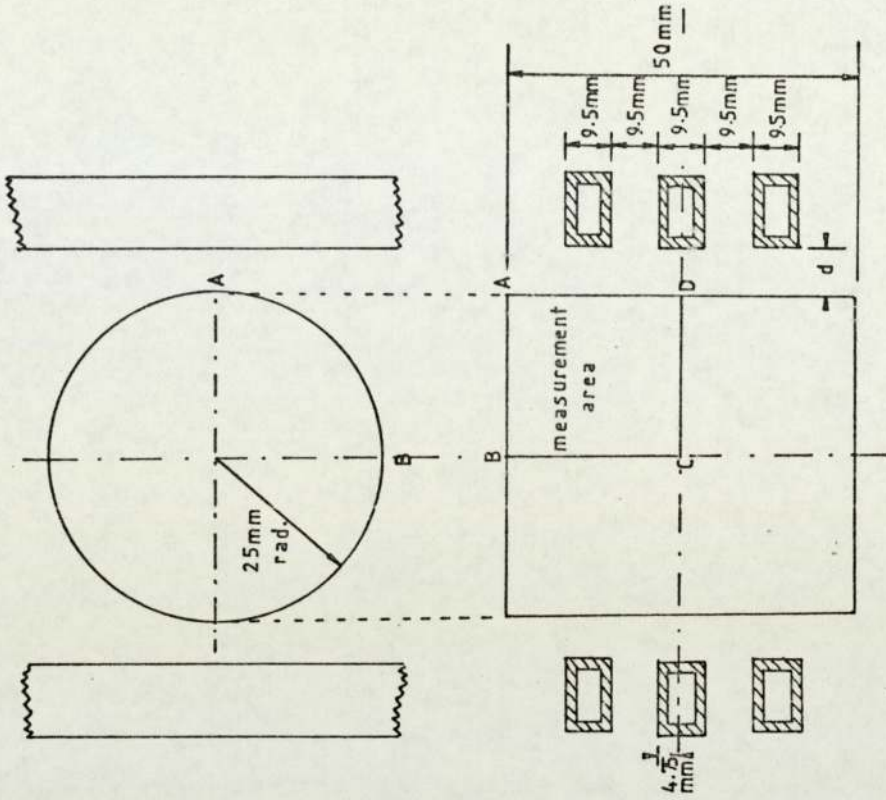


FIGURE 9.17: Measured current density distribution with spacing  $d$  on cylindrical test billet surface in a three conductor pair linear coil. Note change of current scale from figures 9.15 and 9.16.



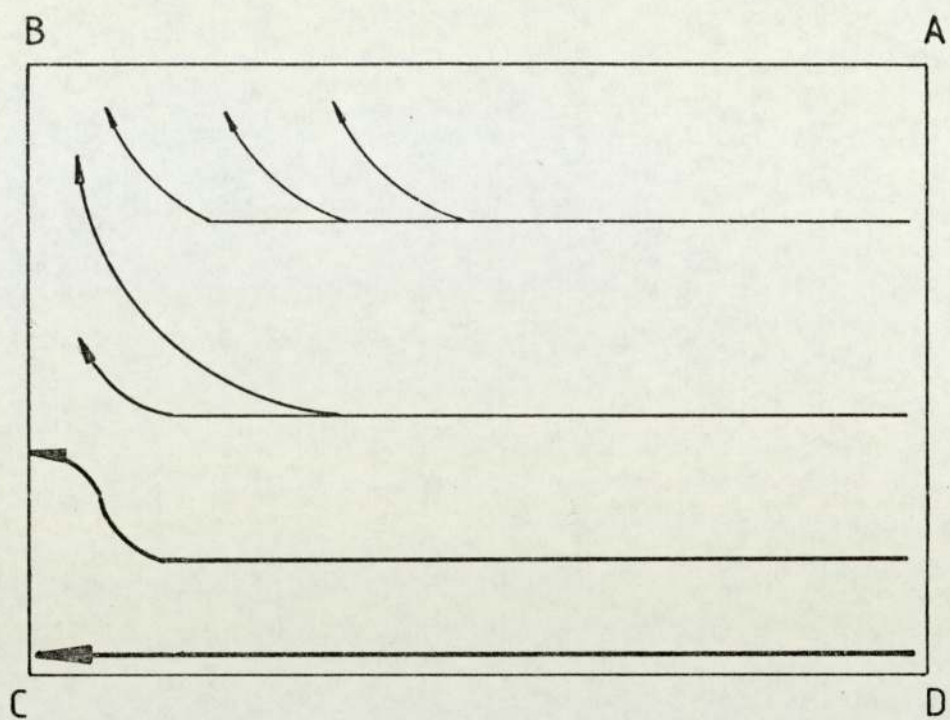


FIGURE 9.18: Generalized current density distribution of figures 9.15 to 9.17 on cylinder surface. Arrow line width indicates induced current magnitude.

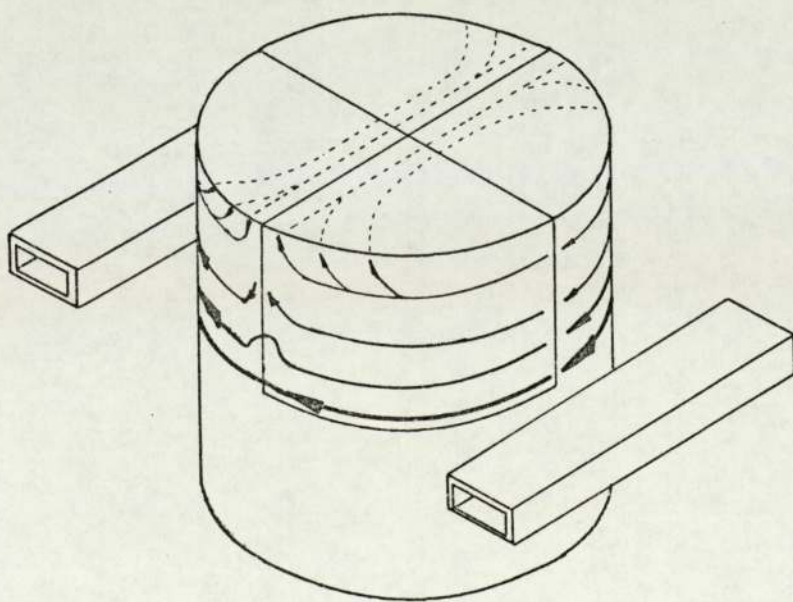


FIGURE 9.19: Generalized current density distribution on cylindrical billet of figure 9.18 shown in relation to the linear coil conductor position (single pair shown). Dashed lines show the extrapolated distribution on the top face.

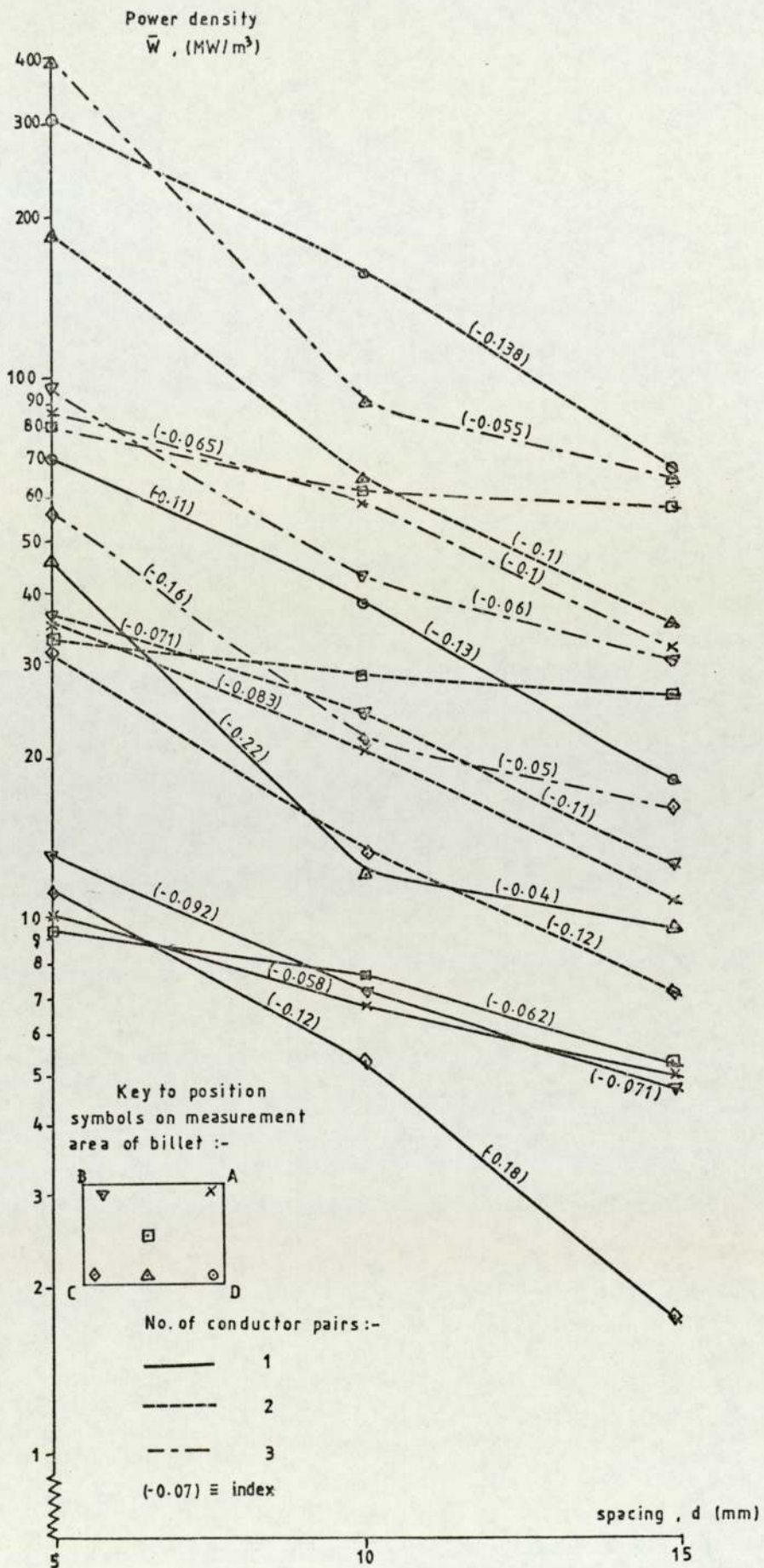


FIGURE 9.20: Power density  $\bar{W}$  induced at selected positions on cylindrical test billet, with linear coil spacing  $d$ . The value of  $\bar{W}$  is calculated from current density measurements.



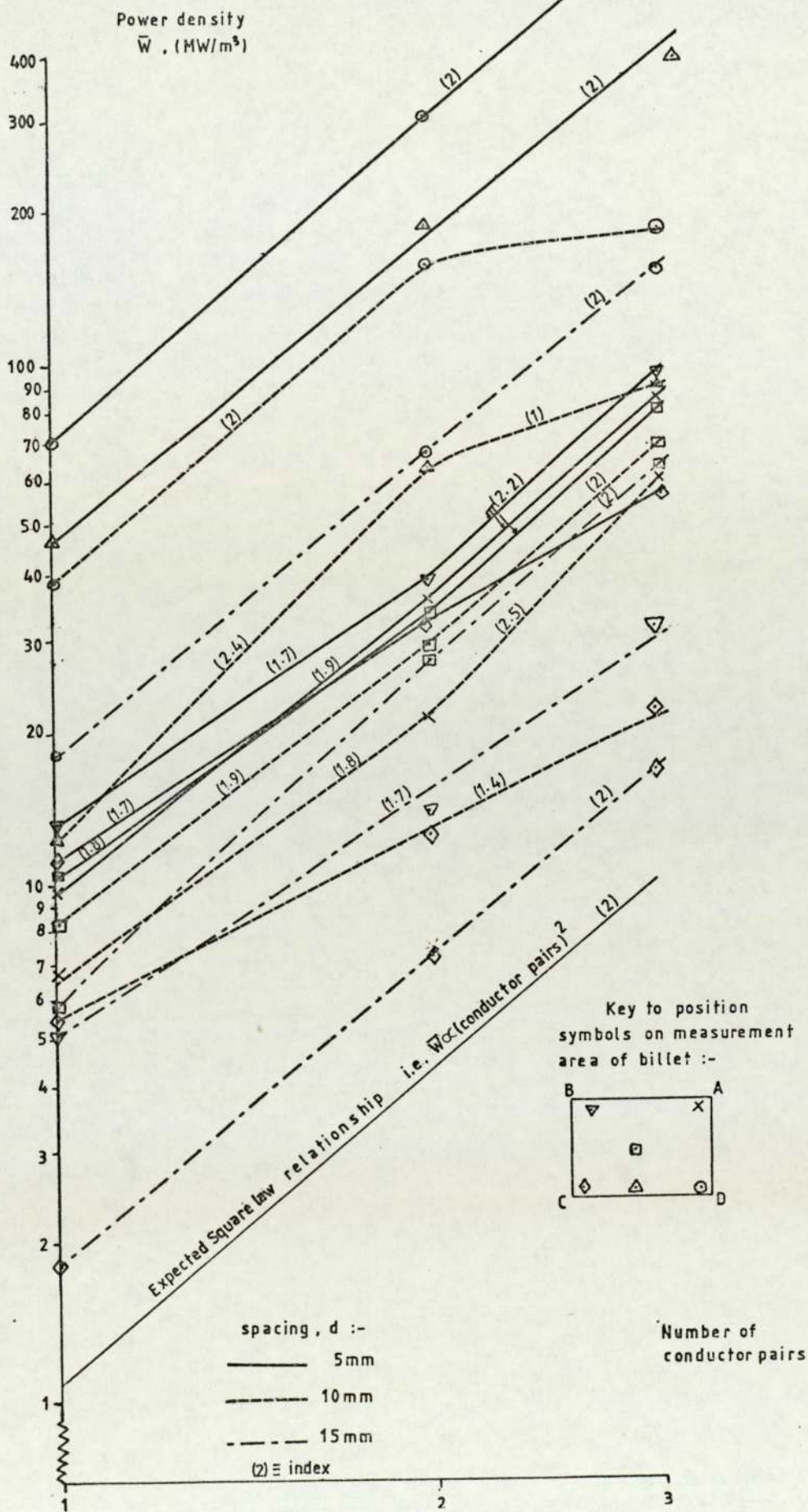


FIGURE 9.21: Power density  $\bar{W}$  (calculated from current density measurements) at selected positions on cylindrical test billet, with number of linear coil conductor pairs.

CHAPTER TEN

INDUCTION HEATING OF COMPLEX SHAPES



## CHAPTER 10 : INDUCTION HEATING OF COMPLEX SHAPES

### 10.1 Introduction

The post-heating forging operation is dependant on the temperature distribution in the heated preform. Temperature uniformity is required for prolonged die life, assumption of the final shape and acceptable metallurgical response. The heating coil must be designed to induce maximum power consistent with high production rates, without surface overheating, and yet conform to requirements for a low final surface-to-centre temperature difference.

For complex shaped preforms, the qualitative discussion of Chapter 8 showed that the shaped solenoidal coil, and the linear coil, offer the most promising solutions for the industrial production of axi-symmetric G.K.N. powder preforms. Similar to the heating of simple shapes, as discussed in previous chapters, the solution of practical induction heating problems may be separated into two distinct but interrelated stages. First, the characteristics of the electromagnetic field have to be resolved to give the power distribution generated in the workload. Secondly, analysis of the flow of heat by conduction and radiation leads to the temperature distribution.

In this chapter the major methods of developing the solenoid electromagnetic theory will be considered, (section 10.2). No solutions are presented here; this chapter is intended as a review of existing techniques with particular emphasis on methods for their extension for application to heating rotationally-symmetric complex shapes.

The extent to which similar solutions may be used for complex shape heating in linear coils is discussed in section 10.3 with reference to the results of Chapter 9. Solution methods for the thermal problem appear in section 10.4. Section 10.5 considers the combination of calculations of power and heat distribution for a full solution. Further work is necessary on the implementation of the recommendations of this chapter before these techniques may be ratified.



## 10.2 Electromagnetic Solution for Solenoidal Induction Coils

For efficient heating, an inductor of solenoidal shape is best suited for close coupling with cylindrical or axi-symmetric loads.

The design treatment of simple shaped billets, rings and discs has been considered in Chapters 3 and 6. In the basic theory it has shown that optimum efficiency occurred when the  $p$  function for a particular shape was maximized. In extending the theory in Chapter 6 for closer predictions of billet heating, the remaining disparities were concluded to be:- the extended time taken for heating at the ends of the coil and the poor approximations of values during the Curie magnetic transition. Drawing on previous work described in the literature, solutions to each of these problems are considered in this section. Sub-section 10.2.1 describes methods for solenoidal coils of constant radius (straight-sided), and sub-section 10.2.2 examines more complex coil and workload geometries.

### 10.2.1 Straight-sided Solenoidal Coils

As shown in Chapter 3, Baker [23], Vaughan and Williamson [29,30] have presented equations, developed from Birch and Davis's treatment, for calculating the equivalent electrical circuit of a long solenoidal coil when heating a long cylindrical billet. The close analogy between induction heating and the transformer permits the calculation of the effective resistances and reactances of circuit components. From this, the major coil properties of efficiency, power factor, and voltage and current in each coil turn are determined.

The simplest approximation to practical coils of finite length is to modify this solution to represent the short coil and load configuration. Baker's empirical modification factor  $k_e$  is included to account for external leakage flux at the coil ends in short coils. This factor may be replaced by a correction coefficient taken from graphs derived analytically by Lavers and Biringer [100,101]. This modifies the  $p$  factor in the induced power equation to give 50% improvement in accuracy for a limited range of cylinder and straight-sided solenoid configurations.

Other shapes may be considered by defining the  $p$  and  $q$  shape coefficient functions for the example. This is not simple, but Horoszko [102] gives an elegant approximation for the workload heating power of a sphere within a straight-sided solenoidal coil, by replacing it with an equivalent cylinder of mean  $p$  and  $q$  values. By dividing the sphere into 'slices' on planes perpendicular to the coil axis, and calculating values for cylinders of equivalent cross-section, mean  $p$  and  $q$  coefficients may be calculated from the averaging formulae

$$\begin{aligned} p(x) &= \frac{1}{n} \sum_{x=1}^n p(x) \cos^2 \psi \\ \text{and} \quad q(x) &= \frac{1}{n} \sum_{x=1}^n q(x) \cos^2 \psi \end{aligned} \tag{10.1}$$

Experimental values quoted for the power input to non-magnetic spheres are between 80% and 85% of calculated values. Although very approximate, the method may be applied generally to arbitrary workload shapes. However, this does not give the detailed information on the distribution of power within the work.



The implications have been largely ignored in the literature in favour of developments of the equivalent circuit design method, where the power input distribution may be more closely defined.

The equivalent circuit method is well suited for the coil designer's first approximation for rapid solutions to simple cases, but as the results and calculations of Chapters 6 and 7 show, it is inadequate for accurate appraisal of high throughput production systems. The material thermal and electrical properties ( $\rho$  and  $k$ ) are assumed to have mean values throughout the heating cycle, which can lead to errors as large as 10% in the surface-to-centre temperature difference. The primitive treatment of the magnetic permeability ( $\mu$ ) variation with temperature, severely restricts the use of an equivalent circuit method for magnetic loads. In discussion of Baker's paper [23] Weed asserts that "the greatest single error in this (Baker's) approach is the assumption of constant permeability, particularly when working with ferrous materials", and Biringer states that large errors may be expected when the surface layers of the part assume a relative permeability of unity at the Curie temperature, whilst the core remains magnetic. It is clear that detailed analysis of a particular coil and load configuration requires the use of more accurate theoretical models, especially for ferromagnetic materials, to reflect the effect of non-linear  $\mu$ ,  $\rho$  and  $k$  for high output coils and to predict for a wider variety of geometries.

Most of the recent attempts at achieving better solutions involve sub-division of the coil and/or workload into a round- or rectangular-sectioned sub-conductor mesh, as shown in figure 10.1.

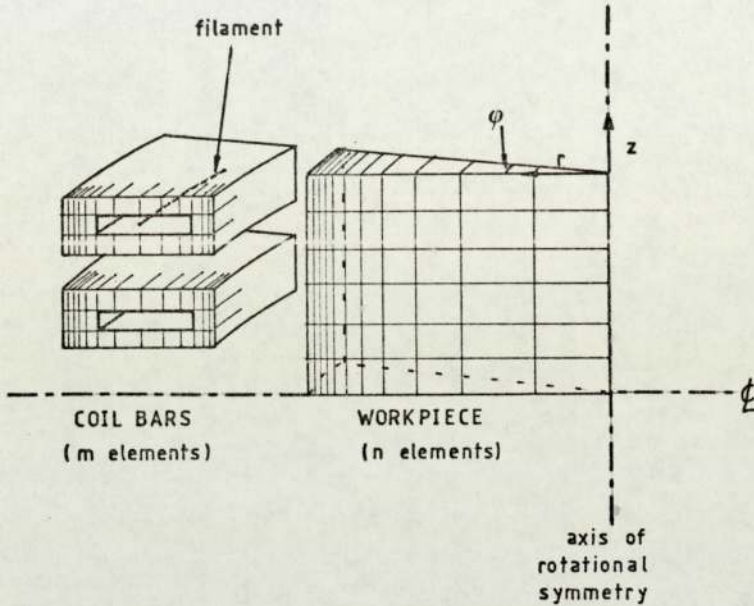


Figure 10.1 : Division of coil and workload into mesh elements for finite difference solutions of the electromagnetic and thermal equations.

The mesh elements must follow current stream-lines, giving toroidal sub-conductors for rotationally-symmetric arrangements. The mesh is more finely divided within the current penetration depth, where flux changes are greatest. A series of simultaneous equations is developed, equating the known coil element voltages or currents to the resistance of each element and the mutual inductances with every other element in the mesh. A numerical procedure, usually accomplished by computer, solves the resulting matrix equation, subject to the boundary conditions or physical constraints of the arrangement.



Ryff, Biringer and Burke [103] compare three methods for calculating the current distribution in non-magnetic single-turn coils of arbitrary cross-section. It is of value to discuss these here for comparison with the methods of other workers.

The mathematical treatment of the current distribution in a conductor is governed by the diffusion equation

$$\nabla^2 J = \frac{\mu}{\rho} \frac{\partial J}{\partial t} \quad (10.2)$$

with similar relationships for H and E.

For a solution using classical techniques, the boundary conditions (namely surface current densities) are required. In general these are unknown and vary during heating. The first method is based on the solution of a first boundary value problem for the diffusion equation of the form,

$$\nabla^2 H = \frac{\mu}{\rho} \frac{\partial H}{\partial t} \quad (10.3)$$

Approximate boundary values of the magnetic field H are found from an equivalent filament, carrying the total coil current, at the centre of the coil mesh ( figure 10.1).

Rewriting equation 10.3 into the following form,

$$\nabla^2 H - K H = 0 \quad (10.4)$$

Numerical integration of the equation proceeds over the whole mesh of n regions. The matrix system

$$\underline{A} \underline{H} = \underline{b} \quad (10.5)$$

results, where  $\underline{b}$  is a column vector of the initial boundary values and  $\underline{A}$  is an  $n \times n$  matrix, relating  $\underline{b}$  to the unknown matrix  $\underline{H}$  of magnetic field values at the interior points, from which the current density  $J$  may be calculated. The new current density is used to improve the accuracy of the boundary values of  $H$  and the process is repeated until convergence is established.

The second approach concerns the solution of the integral equation, derived from the vector potential:

$$D_2 J_2 = \frac{-j\omega\mu}{\rho} \sum_{l=1}^n \iint J_l \sqrt{R_1 R_2} \kappa \left[ \frac{(2-\kappa^2)K(\kappa) - 2E(\kappa)}{\kappa^2} \right] d\ell \quad (10.6)$$

where

$$\kappa^2 = \frac{4R_1 r \sin \phi}{R_1^2 + r^2 + 2R_1 r \sin \phi}$$

and  $K(\kappa)$  and  $E(\kappa)$  are the complete elliptic integrals of the first and second kind [104]. Equation 10.6 may be written as

$$D_k^* J_k = \frac{-j\omega\mu}{\rho} \sum_{l=1}^n J_l A_l \kappa \Delta_{kl} \quad (10.7)$$

a system of simultaneous linear equations with complex coefficients, where  $\Delta_{kl}$  is a measure of the mutual induction between segments  $k$  and  $l$ . As in the first method, this may be solved in the form,

$$\underline{A} \underline{x} = \underline{b} \quad (10.8)$$

The final method appears more closely related to the equivalent circuit approach. Each subconductor is replaced by its corresponding electrical circuit representation as shown in figure 10.2.

$$D_k^* = \frac{\Delta y_k - \Delta y_{k+1}}{2\Delta x_k} + \frac{\Delta y_{k+1} - \Delta y_k}{2\Delta x_{k+1}} + \frac{\Delta x_k - \Delta x_{k+1}}{2\Delta y_{k+1}} + \frac{\Delta x_{k+1} - \Delta x_k}{2\Delta y_k} + K A_k \quad \text{where } \Delta x_k = x_{k+1} - x_k, \Delta y_k = y_{k+1} - y_k$$



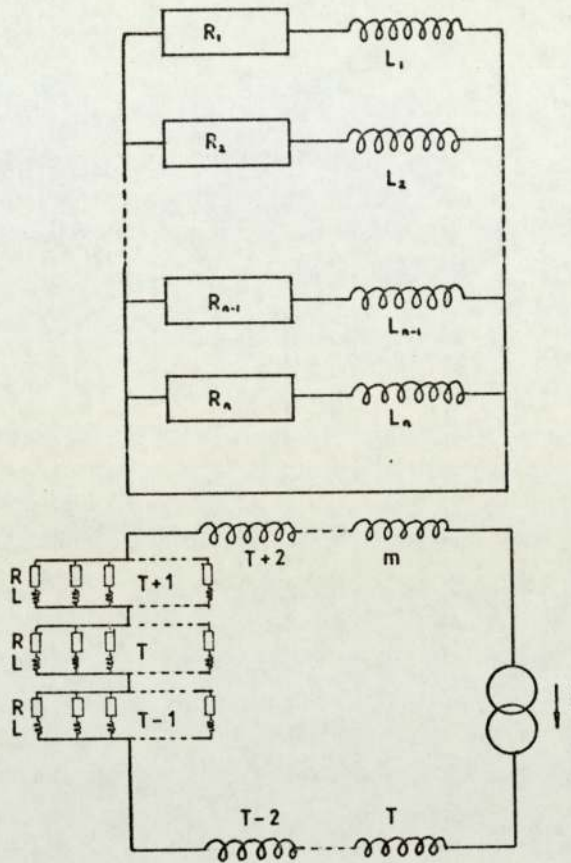


Figure 10.2 : Equivalent electrical circuit representation of a solenoidal coil and billet workload.

Again, this results in a matrix system of equation 10.8, where  $\underline{b}$  is a column matrix of the known coil voltage,  $\underline{x}$  are the unknown mesh element currents and  $\underline{A}$  contains the resistances of each element and the approximate mutual inductance of a filament at each element centre.

The solution of the complex matrix equation for each method is found using the numerical technique of Gaussian elimination [105] with partial pivoting, i.e. re-ordering of the matrix rows.

This is the most commonly used direct method of solving systems of simultaneous equations, e.g. equation 10.9,

$$\begin{array}{r} a_{11}T_1 + a_{12}T_2 + \dots + a_{1N}T_N = b_1 \\ a_{21}T_1 + a_{22}T_2 + \dots + a_{2N}T_N = b_2 \\ \vdots \\ a_{N1}T_1 + a_{N2}T_2 + \dots + a_{NN}T_N = b_N \end{array} \quad (10.9)$$

and avoids instability in the solution. The first equation is divided by  $a_{11}$  to obtain an expression for  $T_1$  and the result used to eliminate  $T_1$  from all other equations. The second is divided by the new coefficient of  $T_2$  and the corresponding expression for  $T_2$  is eliminated in a similar way. After the whole matrix is so treated, the upper triangular matrix,

$$\begin{array}{c} \left[ \begin{array}{cccc} a_{11} & a_{12} & a_{13} & \dots & a_{1N} \\ 0 & a'_{22} & a'_{23} & \dots & a'_{2N} \\ 0 & 0 & a'_{33} & \dots & a'_{3N} \\ \vdots & \vdots & \vdots & \ddots & \vdots \\ 0 & 0 & 0 & \dots & a'_{NN} \end{array} \right] \left[ \begin{array}{c} T_1 \\ T_2 \\ T_3 \\ \vdots \\ T_N \end{array} \right] = \left[ \begin{array}{c} b_1 \\ b'_2 \\ b'_3 \\ \vdots \\ b'_N \end{array} \right] \end{array} \quad (10.10)$$

is formed. The last unknown is given by

$$T_N = \frac{b'_N}{a'_{NN}}$$

and the rest may be found by back-substitution,

$$T_k = \frac{1}{a'_{kk}} \left\{ b'_k - \sum_{i=k+1}^N a'_{ki} T_i \right\} \quad (10.11)$$

Ryff et al. state that the three methods are comparable in terms of required computer storage and calculation times. However, the first method suffers from the disadvantage of uncertainty when to terminate the iteration process, and the third uses a rather approximate method of calculating mutual inductances.



Various authors have extended the methods of Ryff et al. to tackle the non-magnetic billet in finite solenoidal coil problems. Coil and billet mesh sub-division allows the variation of  $\rho$  and  $k$  with temperature to be accounted for, using local values for each segment at different temperatures. Riechert [106] uses the differential equation approach of method 1, but no experimental comparison with his results is given, and long computer calculation times of approximately 20 minutes are involved, to reach convergence. Kolbe and Reiss [107,108] followed method 2 of Ryff et al., but considerable error was introduced by using an inadequate representation for the mutual inductance between mesh elements. Burke et al. [109] solved the coupled equivalent circuit (method 3) but were restricted to solutions for hollow billets due to the limited validity of their inductance formulae and <sup>the</sup> use of a uniformly segmented mesh. Dudley and Burke [110] appear to have resolved many of these problems in their paper describing the coupled equivalent circuit approach for three-dimensional axi-symmetric cases. The range of validity of inductance formulae is discussed and the more refined formulae of Weinstein [111], Lyle [112] and Rosa [113] used. Much needed experimental verification is given [110] for the current distributions in a solid billet within a wound coil, a billet and sheet coil arrangement, and in the turns of a coil: Measured and calculated data agree well.

Few articles which consider the mathematical problem of magnetic materials appear in the literature.

Since the dependence of the induced flux upon the magnetic field  $H$  is non-linear (the ratio  $B/H = \mu$ ), it is necessary to assume an initial  $H$  value boundary condition at the air-gap and proceed with a magnetic solution (similar to Ryff's method 1). Current densities are calculated using local  $\mu$  values and the initial boundary estimate compared with the calculated value at that point. The matrix solution is repeated until convergence is achieved, when the calculated current densities are consistent with the effects of penetration depth and known surface field strength. Lavers [114] describes a simple, efficient method of solving the magnetic problem in one-dimension in a way which dispenses with the need for large amounts of computer storage. Although his technique is limited to long, solid or hollow billets in long coils, it provides valuable insight into using this method for larger mesh systems and more complex geometries. A similar one-dimensional solution is provided by Renner [115], and Fluereşu [90] for a flat slab. Gibson [116,117] reports on computer programs, known as SLEDDY and BIEDDY, which apply the method to flat slabs and long cylindrical billets in one-dimension and to long rectangular slabs and billets in two-dimensions, respectively. The programs cater well for a wide range of industrial applications and include the ability to impose constant or variable induction furnace power and constant coil current during heating. This exemplary work provides the user with quick and more accurate solutions to real problems of slab and billet within straight-sided solenoidal coils.



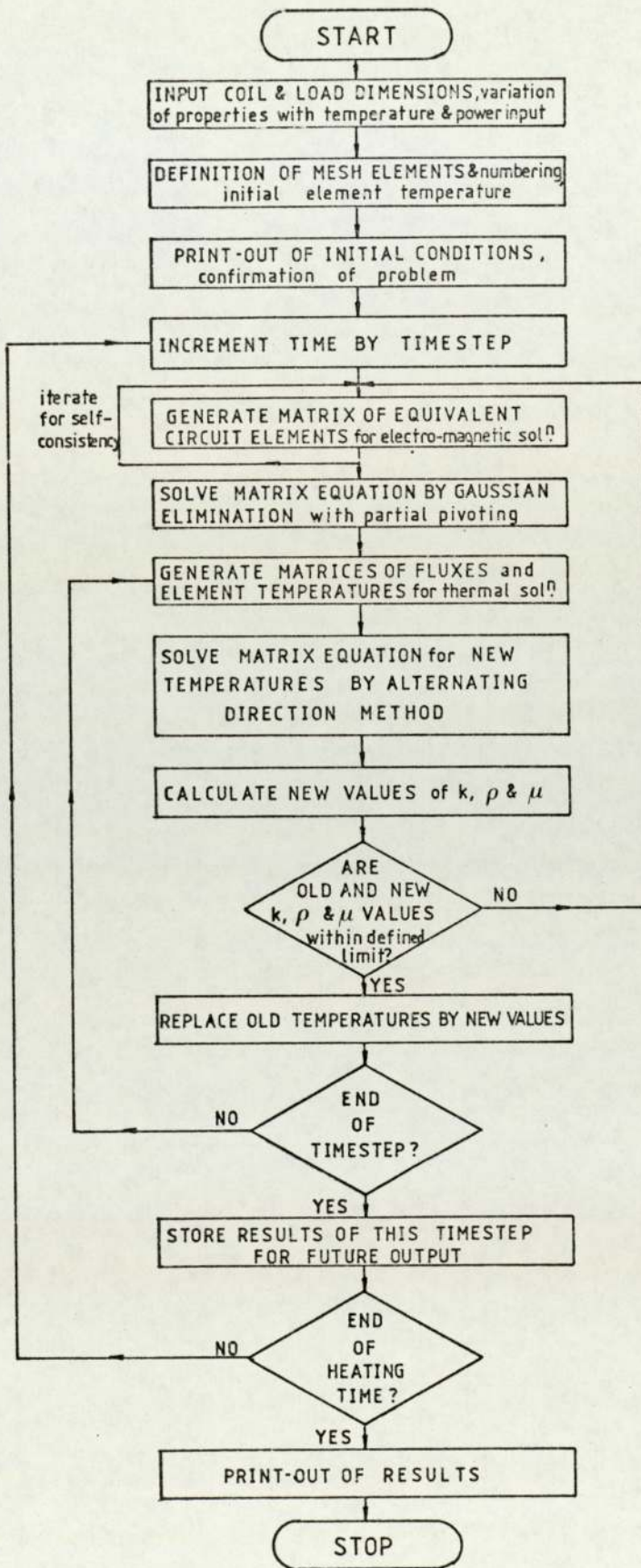


Figure 10.3 : General flow diagram for the computer solution of the electromagnetic and thermal equations by finite differences.

### 10.2.2 Complex Geometries

Although only simple shaped workloads of non-magnetic metals are considered in the literature, the mesh sub-division method shows promise for applications where complex axi-symmetric coil and workload shapes are used. The shaped coil and load may be approximated by setting to zero all currents in mesh elements not corresponding to the conductor area, as shown in figure 10.1. In matrix terms, the modification simply eliminates the impedances of the appropriate elements before solution. The full solution may be computed according to the flow diagram of figure 10.3, discussed in section 10.5. In principle, it should be possible to predict for any axi-symmetric load, co-axial with a solenoidal coil of arbitrary configuration using this method, provided that adequate information, similar to the results of Chapter 5, is available on the changes of material properties with temperature. In the past, inadequate attention has been given to this factor, especially for magnetic materials where the crude assumption of a "step" approximation for the magnetic permeability is used

$$\begin{aligned} \mu_r &= \text{constant} & 0 < \theta < 760^\circ\text{C} \\ \mu_r &= 1 & \theta \geq 760^\circ\text{C} \end{aligned} \quad (10.12)$$

### 10.3 Electromagnetic Solution for Linear Coils

The results of Chapter 9 show that the current distribution induced in simple shapes within linear coils is not rotationally-symmetric. It is not possible to reduce the problem to two-dimensions by considering current stream-lines, as with solenoidal arrangements. The coil designer must therefore employ one of the following methods.



A first approximation to the power induced in a complex-shaped workload may be estimated from a superposition of the empirical relationships for simple shapes found in Chapter 9. For example, where a gear preform boss requires only one third of the power necessary to raise the lower portion to forging temperature, the spacings  $d_u$  and  $d_l$  may be related by

$$\frac{\bar{W}_u}{\bar{W}_l} = \frac{\exp(-0.07 d_u)}{\exp(-0.07 d_l)} \Rightarrow \frac{1}{0.07} \ln\left(\frac{\bar{W}_u}{\bar{W}_l}\right) = d_l - d_u \quad (10.13)$$

or the number of bars adjacent to upper and lower parts,  $N_u$  and  $N_l$  respectively, in the ratio

$$\frac{N_u \left\{ \frac{I_u}{I_l} \right\}}{N_l} = \sqrt{\frac{\bar{W}_u}{\bar{W}_l}} = \sqrt{\frac{1}{3}} \quad (10.14)$$

Conduction across the boundary between upper and lower parts has been ignored here.

An alternative approach may be considered if there is a facility for rotating the preforms about an axis normal to the linear coil plane. If part rotation is rapid, compared with heat conduction within the metal, then the coil arrangement approximates to that of a shaped solenoid with respect to the workload. Since the magnetic field at the centre of the coil is less than that near the conductor bars, an oscillating field strength, or a mean H value, should be used in the equivalent circuit calculations, which now apply.

For a better approximation to the temperature distribution established by a particular coil arrangement, it is necessary to resort to a complete three-dimensional solution in space.

Some computer programs [118-120] exist for multi-dimensional axi-symmetric electromagnetic field analysis, but these are extremely costly in calculation time, for parts of complex geometry. Michaels and Streifer [121] and Muñoz-Yagüe and Leturcq [122] show that long linear coil conductors may be considered to be composed of simple sections and the electromagnetic field, in the plane normal to the coil bars, is then easily calculated by superposition of each contribution. This is a considerable aid to reducing the solution time required, but the induced power and heat fluxes within the load must still be calculated explicitly for a three-dimensional thermal solution.

#### 10.4 Thermal Solution

Analytical solutions to the temperature distribution of an induction heated load exist only for some simple cases. Carslaw and Jæger [24] consider these in detail. Heisler [123] and others [124,125] have plotted the results for cylinders with surface heat flux in graph form, to ease calculation. In practice however, power cannot be assumed to be concentrated at the surface, especially for magnetic materials heated through the Curie temperature. Radiation and material properties varying with temperature also influence the distribution. Again it is necessary to use finite difference methods for a reliable solution. For axi-symmetric shapes, the governing Poisson equation may be written

$$\frac{\partial^2 T}{\partial r^2} + \frac{1}{r} \frac{\partial T}{\partial r} + \frac{1}{r^2} \frac{\partial^2 T}{\partial \theta^2} + \frac{\partial^2 T}{\partial z^2} + \frac{F_v}{k} = \frac{c \rho}{k} \frac{\partial T}{\partial t} \quad (10.15)$$

in cylindrical polar co-ordinates, where  $F_v$  is the heat flux density.



For solid and hollow billets with power input depending only on radius, a one-dimensional solution is required. Heat flow within more complex axi-symmetric shapes, where the shape varies with the z co-ordinate, needs solving in two-dimensions (r,z) (figure 10.1). As for the electromagnetic solution, the load is divided into small rectangular elements in a one- or two-dimensional mesh. Each derivative of the partial differential (Poisson) equation may then be replaced by an algebraic approximation for each element in the region. The resulting difference equation system approximates to the energy balance in each element, where heat is lost and gained by conduction, lost by radiation and gained by eddy-current heat generation. The use of Taylor expansions provides a brief and simple way of representing these derivatives. As an example, the generalized equation in one-dimension may be written

$$\frac{T_{i,j+1} - T_{i,j}}{\delta t} = \frac{1}{\delta x^2} \left[ (a) \left( T_{i+1,j+1} - 2 T_{i,j+1} + T_{i-1,j+1} \right) + (1-a) \left( T_{i+1,j} - 2 T_{i,j} + T_{i-1,j} \right) \right] + \frac{F_v}{k} \quad (10.16)$$

where  $T_{i,j}$  is the temperature of the  $i$ th mesh element at the  $j$ th time-step.

Finite difference transient heat conduction problems may be solved explicitly or implicitly [126]. An explicit method of solution is one in which the temperature of an unknown mesh position is expressed directly in terms of the known temperatures at a previous time, ( $a = 0$  in equation 10.16). This method is straightforward and is easily solved from initial temperature values or power generation histories by computer, without large amounts of storage space. However, the solution becomes unstable if the time-step  $\delta t > \frac{\delta x^2}{2\alpha}$  (s), where  $\delta x$  (m) is the mesh element width. This limitation becomes more restrictive as the mesh is refined to improve accuracy.

Alternatively, an implicit solution method may be used, whereby the expression for the unknown temperature at a point includes other unknown temperature terms, ( $a = 1$  in equation 10.16). For the implicit case, at each time-step of the transient state, a system of algebraic equations has to be solved for the element temperatures. This approximation is unconditionally stable and convergent where  $a = 1/2$  in equation 10.16, - the Crank-Nicolson [127] approximation. The resultant tri-diagonal matrix system may be solved in one-dimension by Gaussian elimination with partial pivoting, [104] as in the electromagnetic case. For solution in two dimensions, it is necessary to solve in each dimension individually at each time-step. For the full implicit Crank-Nicolson method, the solution of  $n \times m$  simultaneous equations is required, where  $n$  and  $m$  are the number of mesh positions in direction  $r$  and  $z$  respectively. For large meshes the computing time becomes prohibitive, and an 'alternating direction' implicit method is most efficient. This method advances by solving the temperatures in one direction explicitly and in the other direction, implicitly. As the name suggests, at the next time-step, the mesh temperatures in the first direction are found implicitly, and in the other explicitly. This alternating procedure involves only  $m$  sets of  $n$  unknowns or  $n$  sets of  $m$  unknowns, so using less computing time, and is stable for constant time-step. By suitably adjusting the mesh by eliminating unwanted elements, the methods above may be adapted for any axi-symmetric part. Computer programs exist for the solution of large meshes and problems in three-dimensions [128]. Here the temperatures are solved by an iterative process which sequentially up-dates the value at each mesh point, with regard to the temperatures at neighbouring points, until convergence is achieved.



## 10.5 Combination of Electromagnetic and Thermal Solutions

Initially, the material properties and starting temperatures are defined and the time-step set. The electromagnetic problem is then solved, using a fine mesh to cope with large changes in  $H$  over small distances. This is followed by the transient thermal calculations over the time-step where a coarser mesh is adequate. The choice of mesh requires careful consideration so that the magnetic and thermal fields are sufficiently defined, but computing time does not become excessive with over-fine divisions. The shaped coil and the complex shape may be approximated by setting the currents equal to zero in those elements of the mesh not corresponding to the conductor area, as shown in figure 10.2. The mesh matrix is adjusted before solution to include zeros at appropriate places. The solution then proceeds according to the flow-diagram in figure 10.3. For each time-step the following procedure is adopted. The matrix of equivalent circuit impedances is generated and iterated until the boundary conditions of the problem concur with their respective mesh representation. The matrix is then solved by Gaussian elimination with partial pivoting, to give the mesh element current densities. From these, the heat fluxes generated in each element are found and solved to give temperatures by the method described in section 10.4 in two-dimensions. Updated material properties are found at the new temperatures and checked against the old values. If too large a difference is found, the properties have changed too much, giving a crude approximation. The solution reverts to the equivalent circuit component stage for a re-calculation of the fluxes developed within each mesh element based on the new properties.

If old and new properties are within the defined limits, the old mesh temperatures are superseded by the new values, and the thermal solution repeated until the end of the time-step. At the end of each calculation time-step, the program returns to the first stage of equivalent circuit calculation and electromagnetic solution. Any change in coil power input or position of coil bars may be included for the next time, so that change in part position in the coil, expansion of the part and soaking period may be taken into account.

At the end of each time-step the results are stored for later output and also to facilitate the partial running of a previous solution where, for example, only the second stage is repeated. At the end of the heating time the relationship between temperature and time may be displayed. With this method it should be possible to predict for any axi-symmetric shape part within any solenoidal coil arrangement. Adequate attention may be given to the changes in properties with temperature in various parts of the workload.

Few authors consider the full solutions of both the electromagnetic and the thermal problem together, and fewer give comparison between their predictions and experimental results. Fluereşu [90], Holmdahl and Sundberg [118] and Gibson [116,117] give flow diagrams for their respective computer programs which, in general form, are similar to figure 10.3. Fluereşu's predicted results, at 50Hz, 500 Hz and 5000 Hz, for steel heating show the effect of current depth on the surface-to-centre temperature differential and highlight the pronounced change in power input as the material becomes non-magnetic at the Curie temperature. Gibson [129] gives comparisons between the anticipated temperature distribution and measured values within a solid steel billet.



Agreement was within 15%, which may be adequate for predicting overall furnace performance. Gibson states that the discrepancies were due to an inaccurate value for the Curie temperature, but the author suspects that the disparity is caused by inaccurate assumptions when calculating the magnetic permeability, (equation 10.12) and the use of explicit rather than implicit methods for the thermal solution.

## 10.6 Concluding Summary

A survey of the literature related to predictions of temperature distribution for complex part induction heating shows that, in the past, emphasis has been placed on the solution of solenoidal arrangements. Of these studies, two solution systems have been identified; those based on extensions of the overall equivalent circuit form, and more fundamental methods of sectioning the shape and performing incremental equivalent circuit calculations, approximating to the electromagnetic and thermal conditions at all depths in the workload. Although many of the latter solution types claim to be able to incorporate variable material properties  $\rho$ ,  $k$  and  $\mu$ , lack of experimental data, especially for  $\mu$ , where a crude step approximation

$$\mu_r = \text{constant}, \quad 0 < \theta < 760^\circ\text{C}$$

$$\mu_r = 1, \quad \theta \geq 760^\circ\text{C}$$

is often used, has limited the accuracy of predictions. It may be apparent from this chapter that sophisticated techniques may be generally employed to solve induction heating problems by computer.

Methods by which these may be adapted for special consideration of complex shape heating in both shaped solenoid and linear coils have been presented here. Care must be exercised in using these methods to avoid excessive computing times by using an over-fine mesh, whilst retaining the required degree of accuracy. A flow chart of calculation steps has been developed which, with reliable property information on sintered parts of Chapter 5, will enable definitive programs to be written, giving a better approximation to the solution and for comparison with measured data of Chapters 7 and 9.



CHAPTER ELEVEN

IMPLICATIONS FOR G.K.N.

## CHAPTER 11 : IMPLICATIONS FOR G.K.N.

### 11.1 Introduction

Until now, this thesis has concentrated upon the theoretical aspects of induction heating, related to coil design. The equivalent circuit has been modified and compared with practical trials on billet heating. With the results of property measurements on sintered powder compacts, it has been shown that sintered metal behaves in a similar way to solid metal under induction heating.

In Chapter 8, the qualitative aspects of coil design for the heating of shaped preforms were introduced and the shaped solenoidal coil and linear coil were identified as the most feasible coil types. The commitment of G.K.N to the use of the linear induction coil, directed further experimental work to the study of this coil type for heating simple shapes as seen in Chapter 9, and some preliminary relationships relevant to induction heating were defined. Consideration of the theoretical aspects of adapting coil design prediction techniques for shaped part heating has been presented in Chapter 10. It is now appropriate to consider the implications of this study for the sponsoring Company, in terms of the economic and technical viability of induction heating for powder-forging. How this affects the choice of coil-type for production systems, is also examined in more detail.

Appendix 5 contains details of cost analyses prepared for this thesis comparing a) induction heating with conventional fuel furnaces b) the powder-forging route with conventional forging of solid material and



c) the merits of induction heating for full scale powder-forging production. The main findings are summarized in section 11.2 under appropriate sub-headings. Section 11.3 discusses the influence on cost analyses of production requirements and the heating coil chosen. The constraints briefly presented in Chapter 8, are now considered with particular reference to their effect on manufacturing costs. It is now possible to put forward guide-lines on the choice of coil system to suit the complexity of sintered preform shape (section 11.4). In particular, the efficiency necessary for a coil system is shown, with due regard to the effect on capital and running costs, and the implications these have on the viability of a production system. In many cases, where only financial factors are considered, the more general advantages of induction furnaces are over-looked. It is frequently difficult to quantify the less obvious attractions of induction heating for a meaningful comparison in projected feasibility studies. Section 11.5 raises some of these environmental and utility issues, so that a balanced view of all implications for the production system under consideration may be formulated.

## 11.2 Cost Analyses

### 11.2.1 Induction Heating versus Conventional Heating

For similar production schedules, induction heating for forging is generally cheaper than using conventionally fuelled furnaces. The examples given in section A5.2.2 show that the most important factors affecting profitability of heating for forging are metal loss in heating and forging (scale, scrap and flash), and costs during down-times.

Considering the capital and running costs of heater and forging press alone, the cost per tonne of forged material is reduced by about one quarter, using induction methods. This economy is typical of many installations of other manufacturers. The overall profitability of the complete forging installation is increased by 50% to 16% of the forged part price, which may be wholly accounted for by reduced scale and scrap loss. The cost advantages of the other factors, listed above, offset the higher cost of energy for the induction route.

### 11.2.2 Powder-Forging versus Conventional Forging

By comparing the total energy consumed in material and part production, section A5.3 shows that, at present, the powder-forging route offers considerable cost savings over conventional forging methods. On changing to powder-forging, consumption is reduced by at least 30% of the previous requirement. The savings are achieved by improving material utilization due to a large reduction in machining necessary.



Similar results have been reported in the literature for many diverse applications, where powder metallurgy methods have replaced existing technologies. Within the foreseeable future, the more widespread adoption of automation, for which powder-forging is well suited, will result in cheaper parts and powder through increased demand, and accentuate the advantages of powder-forging.

### 11.2.3 Induction Heating of Sintered Preforms for Forging

It is not easy to compare the combined findings from sections 11.2.1 and 11.2.2, i.e. the induction heating of preforms for forging, with its most costly counterpart, since no equivalent production plants have been found that produce similar forgings using the entirely conventional methods of fossil fuel-fired heating of solid metals. However, an energy cost reduction of 30% for powder compacts may be expected to reduce the overall cost per tonne for heating in a solenoidal coil by approximately 40% compared with gas heated solid parts. Profitability rises by 60% or more to 17% of the sale price. Projected cost estimates for simple-shaped ring preforms and gear preforms show that running costs are reduced by 45%-50%, using induction heating, compared with single shift operation using gas. This is reduced to 35%-40% if the gas furnace is used at its optimum level of continuous, three shift operation. For this estimate, the induction and gas heaters were assumed to be 35% and 19% efficient, respectively. Gas furnaces are frequently of lower efficiency than this. The induction heater efficiency depends largely on the coil type:

It has been shown that solenoidal coils assume an overall efficiency of about 65%; Table A5.11 shows that the measured efficiency of a linear coil for heating simple ring shapes lies between 26% and 33%. Section 11.4 considers the implications of this for coil design in detail.

### 11.3 Production Requirements

It is essential that the best possible coil system is chosen by rigidly adhering to the constraints of production. In the following assessment of the individual attributes desired of the coil in relation to the cost analyses of Appendix 5, it is difficult to isolate each factor since they are closely inter-related. The major contributions to the processing costs are;

- metal loss in heating and forging (scale, flash and scrap),
- costs during down-times,
- die life,
- labour costs,
- forging rates.

The reduced amounts of scale and scrap are an intrinsic feature of induction heating. Provided that a protective atmosphere can be maintained in all stages of heating, and that a controllable final temperature with limited surface-to-centre difference can be assured, each induction coil type will perform better than its fuel-fired counterpart. Tests at G.K.N., on vertical straight-sided solenoidal coils [3], showed that decarburization and oxidation occurred during heating, caused by an ingress of air that could not be completely prevented, even when using an 'air-lock' system for preform insertion and extraction.



Reports of other examples, however, do not mention this problem for production systems. A static arrangement of coil and workload facilitates the maintenance of an atmosphere, in the shaped solenoid, multiple solenoid carousel and transformer-type coils. The method used for the linear coil is less efficient, where the gas is kept at a slight positive pressure inside the coil and is burned-off at the entrance and exit. The cost of the extra gas is negligible compared with the total energy requirement.

Temperature distribution and efficiency control are improved for shape preforms by using coils where the coil is closely coupled to the workload, i.e. shaped solenoid, multiple solenoid carousel and linear coil. Coil efficiencies are discussed in section 11.4. Die life is closely linked to preform temperature. Up to 30% improvement in die life is credited to induction heating systems due to lower die temperature, resulting in less severe thermal cycling, and accounting for half of the cost advantage for heating solid material, table A5.6.

The second major contribution to costs concerns expense during down-times. Again induction heaters have an intrinsic advantage over conventional furnaces, where the costs of maintaining temperature during standby periods exceed normal heating charges by 25% - 30% for single shift operation, (table A5.12). For two shift use, standby energy costs 40% of the total gas heating bill; only when continuous operation is considered, are the heating charges for induction and gas furnaces comparable (for 35% and 19% furnace efficiencies, respectively.)

Indirect factors are also important. During production stoppages, steel may be scrapped due to overheating from the gas furnace, since the temperature cannot be reduced to a standby state, where heated material is maintained at temperature, until full throughput is resumed. While the absolute cost is small, profit is reduced by 4%, the delay after breaks is detrimental to forging press rate and hence output.

Maintenance is closely linked to down-time costs. Constituting between 15% and 24% of the running costs of projected powder preform induction heating, maintenance costs represent a sizeable contribution. Simplicity of coil construction and installation will minimize expenditure on maintenance, favouring shaped solenoidal and linear coils, which will cost about the same as the straight-sided solenoid. It is not easy to estimate the increase in cost of maintaining a complex system such as the multiple shaped solenoidal coil without first-hand experience. At worst, however a linear relationship between number of coils and repair costs may be assumed. Thus, for only 35% induction coil efficiency for heating the preforms of table A5.12, when more than four shaped coils are used, running costs between induction and gas heating are equal.

Labour costs generally account for 40-50% of the cost of processing, approximately 10% of the total works cost. A reduction of labour costs by half, with automation, would increase gross profit for billet heating by 8% of the sale price. Similar figures may be expected for preform heating.



Such automated systems are invariably expensive and longer payback time must be allowed for, to offset the additional capital expenditure. An individual assessment of a particular proposed installation is essential. Nevertheless, depreciation of capital cost accounts for only 4% of the total costs per hour for billet heating. (table A5.6). For example, at the expense of a reduction in profit from 16% to 13% of sale price, and accounting for increased profit from labour reduction, an automated equipment or a more complex coil system of six times the value of the billet heater may be installed.

Section 11.4 considers the design of efficient induction coils, best suited to complement the cost advantages of induction heating for powder-forging, within the production constraints outlined above.

#### 11.4   Coil Design

It has always been the policy of G.K.N. to develop specialised plant and equipment which would be flexible in operation, and capable of meeting the fluctuating needs of automotive and general manufacturing industries. With this tenet in mind, the Company has been committed to the linear coil principle. However, in Appendix 5 and Chapter 9, the linear coil is shown to be rather inefficient for heating simple shaped parts. At the lowest value, using a single return electrical circuit of one coil bar, the efficiency is 4%, rising to a maximum of 33% with three bars. Lower efficiencies may be anticipated for larger, more complex shapes, where a greater amount of flux is distributed in the coil surroundings.

The arguments for selecting which coil type is best suited to heat a particular preform shape are complex. It has already been shown in section 11.3 that much depends on the effects of all costs, pin-pointed by a full cost analysis of an individual system.

The influence of the type of coil chosen, on the major factors identified in the cost analyses of Appendix 5, are coil efficiency and throughput. Calculation of coil efficiency for heating G.K.N. preform shapes is not advanced enough for prediction, until the computer methods of Chapter 10 are implemented. However, the limits of efficiency for solenoidal and linear coils, found in this study, may be compared with the costings in Appendix 5 to derive general trends for G.K.N. preforms (figure 8.6). They may be treated separately by grouping similar preforms; rings and discs figure (8.6a) are considered in section 11.4.1; stepped billet preforms of figure 8.6b in section 11.4.2; and the heating of gear preforms, of figure 8.6c, in section 11.4.3.

#### 11.4.1 Heating of Ring and Disc Preforms

Ring and disc shaped preforms, figure 8.6a, may be heated in a straight-sided solenoidal coil, or a linear coil. The minimum induction coil efficiency is 9% for comparable running costs with the most efficient continuous use of a gas furnace (table A5.12). The linear coil (figure A5.3) at G.K.N. Powder-Forgings Division has a uniform magnetic field and heats ring preforms with an efficiency of 32%, giving a reduction in running cost of 48% over continuous gas furnace operation. However, unless specific production reasons dictate the use of a linear coil, the solenoidal type should be used.



The overall efficiency of a straight-sided solenoidal coil for heating preform rings will be approximately 70%, provided that the air-gap is no greater than for billet heating and the ratio of diameter to penetration depth gives a similar value of the p function. In practice, provided that the ring diameter is not greater than twenty times the ring thickness, the graphs of p functions, for hollow and solid cylinders yield similar values. Running costs for powder preform heating are reduced by 57% of the costs for continuous operation of the gas furnace.

For both coil types, a separate coil will be required for each ring or disc, since the efficiency falls as the air-gap increases. For linear coils especially, the air-gap must be reduced to the minimum clearance allowed by coil insulation and variability in preform positioning, otherwise the coil will fall below the minimum requirement of 9% efficiency. It is curious that the efficiency in heating preform F390 in the Powder-Forge linear coil (figure A5.3) where the air-gap is 17mm, is approximately the same as heating solid cylinder in the adjustable linear coil (figure 9.1a) with an air-gap of 5mm. The powder part will certainly be more efficient due to higher resistivity, but if solid billet tests are similar, an efficiency difference of only 5% would be noted between powder compact and solid samples: This is worthy of further investigation.

#### 11.4.2 Heating of "Stepped Billet" Shaped Preforms

The preforms of figure 8.6b are shapes of intermediate complexity, consisting of a combination of hollow billets of various radii.

For those parts where radius does not vary greatly over the preform length, a straight-sided solenoidal coil may still be considered. Lower efficiency is to be expected since the air-gap is increased at the portion of the preform of smaller radius.

This fact may be beneficial in limiting the power input to the thinner walled section of the preform, where less heat energy is required to raise the metal mass to temperature than for the thicker section. For example, preform F351 (figure 8.6b) consists of a thick lower section with a radius of 29mm, and thin walled portion of approximately the same length with a radius of 20mm. As before, a straight-sided solenoidal coil of 50mm radius will heat the larger radius at approximately 70% efficiency. For the thinner walled section, the efficiency reduces to 48%,(after taking the new values of  $p$  and  $A_w$  in the equivalent circuit approximation.) For a given coil power  $P_c$ , the equal lengths of thick and thin walled parts will absorb about  $0.35 P_c$  and  $0.24 P_c$  respectively. Even with a reduced power input, 68% of the power to the thick walled section, the thin walled portion may still overheat, since the mass ratio of the two halves are only 0.4. However, the surface area per unit of mass is larger, so that radiation may reduce the net power input to the thin-walled portion to a more acceptable value. The use of a straight-sided solenoidal coil, for heating a stepped billet shape, can only be justified where the ratio of efficiencies happens to coincide approximately with the ratio of energies required to raise both thin and thick walled parts of the preform to temperature.



It would be better to use a shaped solenoid arrangement for shapes that do not conform to this requirement.

Although efficiency averaged within the shaped coil will be comparable with the straight-sided type for billet heating, no more than 60% may be expected for the most efficient case where there is little spacing between preforms. The use of coil turns of various radii will give better control of induced power, and hence temperature, within different parts of the preforms. Some parts, for example, numbers F351, F349 and F392 (figure 8.6b), may be heated within the same shaped solenoid, but a reduction in efficiency must be expected if this entails a larger air-gap for some preforms of the group. The only advantage of using the linear coil for heating this range, to the detriment of efficiency, would be if the temperature at some parts of the preform could not be controlled sufficiently. The preforms may be spaced along the linear furnace mesh belt to prevent overheating above about 1300<sup>0</sup>c, when the preforms would otherwise tend to stick together.

#### 11.4.3 Heating of Gear Preforms

Preforms F382, F348, F350 and F391, figure 8.6c are best suited to the shaped solenoidal and linear coil types. Preform mass for gear parts is high compared with others in figure 8.6. To maintain forging rates it is essential to increase the efficiency of heating, so the power input must be raised, or to increase the number of preforms heated at one time. Heating time should be reduced to minimise radiation energy loss from the large surface area.

For the shaped solenoidal coil, an increase in heating efficiency is unlikely because adequate mechanical clearances must be preserved. The use of a shaped coil carousel allows relatively slow heating while keeping forging output high. The effects of increased capital and maintenance expenditure on running costs have been discussed previously. Nevertheless, it may be noted that the gear preforms are of approximately similar shape and size. At least one shaped coil in the carousel may give a suitable temperature distribution in all gear preforms, in the initial stages of heating. For heating different gear shapes in the same carousel, only one coil may need to be inter-changeable. Savings in down-time and maintenance costs will result.

The linear coil presents similar problems for more efficient heating of gear preforms. However, heating time would be reduced if more coil power were to be applied and the air-gap kept to a minimum. To avoid localized overheating in close proximity to the coil as a result of this, it will be necessary to rotate the preforms as they are heated. Therefore, the capital and maintenance costs will be increased. It is unlikely that the extra cost of preform rotation machinery will be as expensive as the construction of a coil carousel. Also, maintenance charges will be less for this simpler system. It may be argued that the efficiency will approach 30%, since the air-gap can be reduced as a result of precise preform positioning on the rotating supports. Individual linear coils for each part shape may be required to take advantage of this closer coupling.



The factors affecting the choice between the carousel and linear coil types are complex. A thorough cost analysis is needed for each proposed production system, but is hampered by lack of reliable information on the capital cost of each coil type, and its reliability. These guide-lines indicate the major constraints to be considered for future applications of induction heating on preform shapes. All things considered, with experience of the G.K.N. production workshop environment, the simpler linear coil is to be preferred.

#### 11.5 Other Factors

For a production system, flexibility and adaptability are important factors. For heating a small number of parts especially, induction heating systems must be designed to aid quick coil removal, for replacement and maintenance, or coil exchange for the heating of another preform type. The system is then competitive with conventional muffle furnaces, which accept a wider range of part sizes without alteration.

The possibilities for automation of the heating and forging processes are similar for induction and conventional heating methods. However, the consistency of induction heating produces fewer reject parts with unacceptable temperature distributions. Also, faster heating times improve forging rhythm and increase output by as much as 20%. Higher quality is ensured by automatic control of furnace power, and lower price is achieved with reduced inspection and supervision costs.

Fixed costs of furnace operation are usually accounted by shop floor space occupied. Induction heaters occupy considerably less floor area than conventional units of comparable power. Running costs are reduced since automated equipment requires only semi- or non-skilled workers. Induction heaters are lighter and more compact than conventional types and can be optimally positioned in the forging suite. G.K.N. Garringtons Ltd. found that by raising their heaters, hot billets could be chuted into the forging press, improving press rates by 20% [130]. Environmental and working conditions are improved using induction heating, with the advantages of less radiated heat, fewer combustion fumes and reduced noise levels. Noise emanates from the heater power supply, which may be conveniently located away from the forging area, and also from the automatic handling equipment.

Efficient though induction heating is, it is worthwhile commenting briefly on some methods of improvement. Coil efficiency is improved using a static inverter rather than a motor-alternator. The inverter frequency continuously alters to match the coil and work impedance. Closer coupling of the coil to heated metal will improve efficiency by minimizing air-gap flux. The flux may be further utilised by incorporating flux concentrators or intensifiers. These carbonyl-iron powder materials, of high magnetic permeability, are shaped around the coil to modify and concentrate the flux distribution into the preforms.

The flexibility of the coil arrangement affects its efficiency. It may be more cost-effective to heat more than one shape of part in a single coil arrangement rather than incur the cost of building and installing more coils.



This is at the expense of the most efficient energy use, and will depend on the variety and numbers of preforms to be heated, in relation to production volumes.

Apart from energy saved by powder recycling (section A5.3.3) much can be done to conserve heat energy, and thus reduce costs when induction heating powder compacts for forging. Better coil insulation will result in less radiation losses, lowering the overall heating time and power input. Heat produced by the burning-off of protective atmosphere at the furnace ends may be used, possibly as a preform or atmosphere pre-heat. Heat exchangers could be incorporated in the coil cooling system to use heat from circulating water, at approximately 30°C, for office and workshop heating. Savings of £2 500 per annum, with a £10 000 system [147] may be expected, and are worthwhile considering for new installations. Heated air from cooling forgings may be used for a similar purpose if heat pumps are installed.

## 11.6 Concluding Remarks

The discussion of economic aspects for induction heating of powder preforms, presented in this chapter, with regard to production systems or applications on an industrial scale, illustrate the complexity of resolving the technical problems in the most cost-efficient manner. Cost analyses for induction heating and powder-forging, given in detail in Appendix 5, show that major advantages may be gained by considering this route. The effects of the major constraints imposed by production are considered with respect to the financial evaluation of the installation. Guide-lines on choice of coil type are also given. Inevitably, generalised statements fall short of a more rigorous analysis of an operating design. Greater precision must await the realization of these ideas, and the implementation of the computer prediction methods of Chapter 10, for complex shapes.



CHAPTER TWELVE

SUMMARY, CONCLUSIONS AND RECOMMENDATIONS

## CHAPTER 12: SUMMARY, CONCLUSIONS AND RECOMMENDATIONS

### 12.1 Introduction

In this chapter, the knowledge gained by this study is reviewed, and the extent to which the initial questions posed on the problem topics considered, have been answered. A general overall view of the results in relation to the industrial context of the sponsoring Company follows, with recommendations for further work to complement future developments in G.K.N.

A brief summary of the academic results of experiments is described in section 12.2, and conclusions drawn from these findings (section 12.3). The implications of the project results for industry are summarized in section 12.4. Finally section 12.5, recommendations for further studies, discusses the logical progression of this study.



## 12.2 Summary of Results

### 12.2.1 Induction Coil Design

The first priority of all induction coil design studies is to define the desired heating pattern within a metal workload, of known properties and dimensions. Chapter 2 has shown how this information may be combined with required coil throughput and workload heating depth, so that the optimum coil frequency is chosen and a suitable power input and heating time selected.

The current theory of induction heating coil design was derived from the fundamental equations, in Chapter 3. By analogy with the transformer, it was shown that the induction coil and workload may be represented by an equivalent electrical circuit. This standard, but approximate method was used to calculate the design of a single section production coil of low throughput, for heating solid metal billets of circular section. The design results are in agreement with practical trials with the built coil. However, the assumptions of the present method lead to discrepancies when applied to more efficient, high production-rate coils. The equivalent circuit method is inadequate to describe solenoidal coils of varied sections, and gives little information of the thermal history of various parts of the billet, especially during the Curie magnetic transition.

An improved version of the equivalent circuit design method was proposed in Chapter 6.

The equivalent circuit method is used for each coil section individually, and the sub-Curie and super-Curie heating are separately treated. Once the power inputs at all stages of heating are derived from the electrical analogue an iterative routine, simple enough for manual solution, is used to calculate the temperature at strategic positions within the billet. Corrections for radiation loss and the effect of finite depth of induced current are accounted for, and the iteration does not suffer from the assumption of uniform initial temperature for calculation purposes. Better appreciation of the Curie transition is possible and closer approximation to the actual heating pattern shown by comparative calculations and experimental results.

However, the method still has limitations. The equivalent circuit may be used only where the paths of induced currents are known, effectively limiting solution to co-axially symmetric cases of constant radius.

The heating of shaped metal workloads requires more advanced techniques. Because of the complexity of the problem and the number of calculation steps necessary, a solution by computer is required.

Chapter 10 discusses iterative techniques involving finite difference segmentation of two-dimensional cases. The calculations of Chapter 6 show the relative importance of material properties and the critical factors for accurate prediction.



These concepts have been considered when constructing a possible flow chart for computer solution. In this manner, knowledge accumulated at G.K.N of the induction heating of axially-symmetric workloads in solenoidal coils has been extended.

The linear coil favoured at G.K.N., presents a very different problem. It is shown that no theory has been developed to explain the behaviour of this shape, since the induced current paths are unknown. Chapter 9 gives experimental information on the current distributions to be expected in simple shapes, and postulates approximate relationships between the coil bar spacing and number of coil turns, in relation to the coil power and efficiency that may be expected of this type of coil. It will also provide an experimental example for comparison, when 3-D computer prediction programs are developed to derive explicitly an electromagnetic field and subsequent thermal analysis.

### 12.2.2 Induction Heating of Powder Compacts

The suitability of induction heating for powder-forging applications depends largely on knowing how compacted powder workloads behave in the coil. Chapter 4 introduces powder-forging, and shows the importance of material physical properties.

A shortage of information available on the relevant compacted powders used by G.K.N was identified in Chapter 5.

Here, experiments to measure electrical resistivity, thermal conductivity and relative magnetic permeability are described. These results are used in Chapter 7, where experimental trials, the use of the improved equivalent circuit and the iterative thermal calculation, with the measured values of  $\rho$ ,  $k$  and  $\mu$ , show that sintered powder billets heat in the same way as solids, and good correlation between the predicted temperature profile with measured values is found. The results showed that a faster temperature rise could be achieved with sintered preforms because the larger electrical resistivity gave more Joule heating.

### 12.2.3 Industrial Application of Induction Heating for Powder-Forging

This project has been conducted with the collaboration of G.K.N. and, as such, the aims are for industrially orientated interdisciplinary research. Beyond the improved theoretical understanding and new experimental evidence provided by this study, the industrial viability and applicability of the results have been considered. The industrial constraints of ease of operation, maintenance and automation have to be considered with regard to G.K.N. production and the coil options available.

Chapter 8 introduces various coil possibilities and outlines some advantages of each. It is as much a result of the commitment to the linear coil at G.K.N., as for fundamental academic reasons, that this option is pursued in later chapters.



G.K.N.'s enthusiasm for the linear coil must be tempered with the strictly economic consideration of the advantages of various coil types, with respect to a full cost analysis of the induction heating of powder preform route. Chapter 11 considers the economic aspects, with reference to the cost analyses of Appendix 5. This chapter highlights the complexity of calculating the influence of production factors on the coil analysis and the importance of conducting an economic assessment for each production installation considered. The recommended coil types for particular part shapes are shown in the next section, with the other conclusions of this study.

### 12.3 Conclusions

#### 12.3.1 On Current Methods used in Coil Designs

- a) The current equivalent circuit methods are limited to considering the heating of cylindrical shaped solid metal workloads in solenoidal coils of constant radius.
- b) Present methods fail to take account of the variations in properties with temperature and the effect of the Curie transition with sufficient accuracy, and cannot cope easily with multi-sectioned production coils.
- c) Modifications are presented for improving the current methods, and a simple iterative solution presented to provide more information to the coil designer, and give more physical significance to the variables and their effect on the temperature distribution.
- d) Comparison of the improved method, with experimental results of temperature distribution with time, showed excellent agreement within the accuracy required for coil design.

### 12.3.2 On Powder Compact Properties

- a) An absence of reliable information on the physical properties of sintered steels i.e. electrical resistivity, thermal conductivity and magnetic permeability, was identified.
- b) Using apparatus specifically designed and built for the purpose, the required powder properties were determined.
- c) Relationships between the powder properties and density were established and compared with those reported in the literature.  $k$  and  $\rho$  are related to the properties of the solid metal by the relation

$$\frac{\rho_0}{\rho} = \frac{k}{k_0} = \frac{1 - \xi}{1 + 9\xi^2}$$

and magnetic permeability similarly related to  $\mu_s$  by

$$\mu = \left\{ \mu_s \right\}^{\frac{\rho_0}{\rho}}$$

where

$$\mu_s = \left( \frac{1.19 \times 10^6 B_s}{H} \right)^{0.92}$$

Here,  $B_s$  is 0.7 T and 1.2 T for 'W4' and 'W78' powder, respectively.

### 12.3.3 On Induction Heating of Cylindrical Powder Compacts

- a) Temperature measurements made during the heating of simple preforms in a production solenoidal coil, and comparisons between predicted performance and experimental results, showed that similar heating characteristics of solid and powder compacts occurred during induction heating.



#### 12.3.4 On Induction Heating of Shaped Metal Parts

- a) The limitations of the range of theoretical models for shaped part heating to the solution of two-dimensional cases was shown.
- b) The shaped solenoidal coil and linear coil were identified as the most suitable coil options for shaped part heating for production systems.
- c) Further theoretical modelling for the solenoid and linear coil is proposed, with attention to varying material properties and ferro-magnetic materials.
- d) Preliminary tests on linear coil heating of simple shaped parts culminated in the relationships

$$\bar{W} = (\rho J^2) \alpha I_c^2 \quad , \quad \bar{W} = \bar{W}_0 \exp(-0.07d)$$

for describing the influence of power input with coil bar number and spacing.

#### 12.3.5 On the Implications for G.K.N.

- a) An economic assessment of induction heating for powder-forging indicates that costs are reduced by 27% over conventional processes.
- b) The likely efficiencies of the suggested coil types in heating parts of various complexity show that:-
  - For ring parts, straight-sided solenoidal coils are applicable;
  - For shaped billets, shaped solenoidal coils are suitable;
  - For gear preforms, shaped solenoidal or, preferably, linear coils are desirable.

c) The relative influence of changing factors in the economic analysis may be seen, and extensions of this analysis may easily be made when more information is available on powder part future demand and untried coils.

#### 12.4 Industrial Implications of This Study

The author views this work as a case study of the application of induction heating to powder-forging that will ultimately lead to a computer-aided preform and coil design facility. This project has concentrated on the experimental aspects which identify the major variables acting, and shows in which directions future studies should be aimed.

In relation to G.K.N., it has identified the areas of most importance when considering induction heating for powder-forging, and will help the Company to choose the best coil arrangement for further study. It is often difficult to make firm recommendations, especially in the present economic climate, where it is uncertain whether money or orders will be forthcoming. It is known that G.K.N. favour the linear coil and a continuous heat route comprising pre-heat, sinter and heat for forging [148].

The methods for property measurements, as described in Chapter 5, may be used for green compacts to determine their  $\rho$ ,  $k$  and  $\mu$  values. Only small modifications to the apparatus will be necessary for measuring the physical properties during the sintering process.



The whole apparatus may be inserted in a sintering furnace, with a suitable atmosphere, and subjected to the normal sintering cycle, to give dynamic  $\rho$ ,  $k$  and  $\mu$  measurements during sintering. From this stage, the application of green preforms to induction heating may be treated in the same way as sintered material. Provided that an over-concentration of power input, with localized melting [149,150,151,152] in the compact is avoided, the current flow paths will be the same. To minimize the chances of localized melting, shaped solenoidal or rotated linear coils may be used to produce more even heating. Rotation in the linear coil will be essential to equalise the flux distribution within the preform. Complex shaped parts show more promise for increasing profitability by minimizing the higher cost of machining and it is to these shapes that attention should be focused.

This study has shown the need for a critical economic assessment of a particular application. There must be proven financial advantages in addition to the desire to try new production routes, such as the linear coil.

The use of induction heating for non axi-symmetrical preform shapes, such as connecting rods and crankshafts, cannot be ruled out. The intricacies of coil design, and the low efficiencies to be expected from the heating coils, must relegate the priority of these applications. Furthermore, general use of induction heating may be considered for other areas of metal heating and re-heating. Post-forging forming operations on parts of forged components may well benefit from the close control offered by using induction coils.

The coil design methods considered in this study will aid the construction of suitable workload/inductor arrangements.

In future research and development work within G.K.N. the following observations should be noted. At the start of this project a Powder-Forgings Development committee was established with members from each of the interested G.K.N. companies; Powder-Forging Division, the Group Technological Centre and Forgings Product and Process Development Department. Frequent meetings provided an invaluable opportunity for discussion of individual research topics, sharing of facilities, disseminating information and constructing realistic schedules, budgets and dead-lines. Since this committee was dissolved, inter-company communications on developments has substantially reduced. Without such co-operation, further development work will be hindered, especially in topics where previous investigations within the Company have been inadequately documented.



## 12.5 Recommendations for Further Study

The results of this thesis suggest the following topics for further study:-

- 1 Experiments to measure the current density distribution during induction heating of complex shapes in a shaped solenoidal coil and in a linear coil. Investigation into whether heating of rotated parts within a linear coil approximates to the shaped solenoid case;
- 2 Fundamental investigation on the relationship between preform temperature distribution and quality of forging, including the influence on die life;
- 3 An examination of preform design is necessary to minimize the complexity of preform shape, with possible improvements in density uniformity;
- 4 Further developments and implementation of computer-based predictions is necessary to describe shaped solenoidal and linear coil configurations. A computer-aided simulation of the approximate heating pattern to be expected from a particular arrangement will facilitate coil and preform design.

For the single "sinter-forge" route, combining pre-heating, sintering and heating for forging in a single continuous operation, additional information will be required on:-

- 5 The physical properties of unsintered powders; electrical resistivity  $\rho$ , thermal conductivity  $k$  and magnetic permeability  $\mu$  ;

- 6 The changes to  $\rho$ ,  $k$  and  $\mu$  occurring during the sintering process, including any lubricant burn-off stage;
- 7 The maximum power density must be determined, above which localized melting occurs in unsintered preforms. Induction heating predictions may then be modified to treat unsintered material;
- 8 Specific economic assessment of the "sinter-forge" route will be required, following the format of Chapter 11 and Appendix 5. It will then be possible to ascertain whether increasing green density is the most effective way of optimizing costs[153].



APPENDICES

## APPENDIX 1 : METHOD OF DENSITY DETERMINATION

A selection of green and sintered gear preforms, made by G.K.N. Powder-Forgings Limited, were cut into small blocks. Density measurements were made using Archimedes' principle described below. Test blocks were cut from preforms as indicated in figure 4.3 and weighed in air and water to determine the density. It was found that the specimen absorbed water due to its porosity. Three weighings were therefore necessary to give true mass in air  $m_a$ , mass in water  $m_w$ , and mass in air with absorbed water,  $m'_a$ .

The density may be found from

$$\gamma = \frac{m_a \gamma_w}{m_d} \quad (A1.1)$$

where  $\gamma$  and  $\gamma_w$  are the specimen and water densities respectively,  $m_a$  is the true mass in air and  $m_d$  is the mass difference given by

$$m_d = (m'_a - m_w) \quad (A1.2)$$

The results shown in figure 2.3 show that the density throughout the preform is variable. Green preforms F391, F364 and sintered preform F364 exhibit lower density in the centre, but sintered preform F350 shows greater density at the centre. The results are inaccurate as it proved difficult to exclude adhered air bubbles from the small blocks during weighing in water, especially for green preforms. This problem may be overcome in the future by coating each block with a light impervious layer



to eliminate water absorption. However, as measurements on adjacent blocks gave densities consistent with the trend in each preform, the variation must therefore be due to differences in the filling of each gear shape as the powder is poured into the die. Note that green preform F391 and sintered preform F350 are slightly dissimilar as no green preform of the same shape as F350 was available.

The results provide sufficient information on the range of densities present in typical G.K.N. preforms.

APPENDIX 2 : DERIVATION OF TEMPERATURE DISTRIBUTION during  
change of INPUT POWER DENSITY

A2.1 The Problem

After a solid, cylindrical billet of radius  $R$  has been heated for some time with a constant power density,  $\mathcal{P}_1^*$  at the surface, the cross-sectional temperature profile is parabolic. The solution below derives the new temperature distribution reached when the power input changes to assume a different value,  $\mathcal{P}_2$ .

In effect, the new temperature distribution is a superposition of a 'soak' period of the initial temperature distribution  $f_1(r)$  (section A2.2.1), according to equation 3.18 and given in section A2.2.2, with the temperature profile established from a uniform mean temperature  $\theta_{m1}$  by  $\mathcal{P}_2$  (section A2.2.3).

A2.2 The Solution

A2.2.1 Initial Power Input

The temperature distribution is assumed to have passed the transient stage, so that the normalised time  $\tau_1$ ,

$$\tau = \frac{k t}{\gamma c R^2} \quad (3.12)$$

is greater than 0.25 and the temperature at radius  $r$  is given by

$$\theta_1(r) = \frac{\mathcal{P}_1 R}{k} \left\{ 2\tau_1 + \frac{r^2}{2R^2} - \frac{1}{4} \right\} \quad (3.14)$$

\*The subscript 1 refers to the variables before the change in power input and subscript 2 to those after the transition.



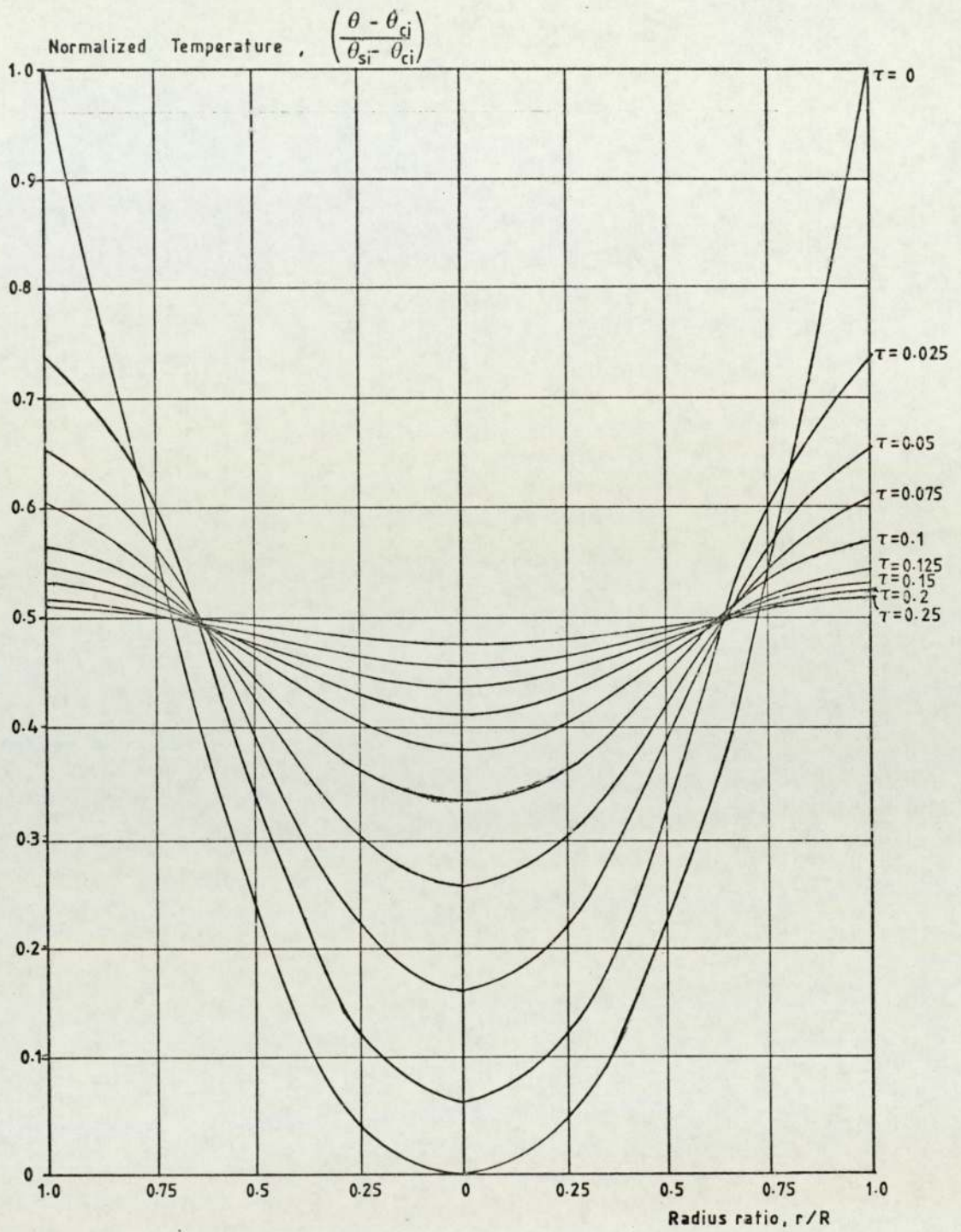


FIGURE A2.1: Variation of parabolic temperature profile during soaking.  $\theta_{si}$  and  $\theta_{ci}$  are the initial surface and centre temperatures at the start of the soaking period.

This may be re-written in terms of the mean temperature  $\theta_{m1}$

$$\theta_1(r) = \theta_{m1} + \frac{\mathcal{P}_1}{2kR} [r^2 - R^2/2] \quad (\text{A2.1})$$

### A2.2.2 Soak of Power Input $\mathcal{P}_1$

On passing to the new power input  $\mathcal{P}_2$ , the initial distribution  $f_1(r)$  equalises to

$$\theta = \frac{2}{R^2} \int_0^R r f(r) dr + \frac{2}{R^2} \sum_{n=1}^{\infty} \exp\{-\beta_n^2 \tau_2\} \frac{J_0(\beta_n r/R)}{J_0^2(\beta_n)} \int_0^R r f(r) J_0(\beta_n r/R) dr \quad (\text{3.18})$$

The normalised surface and centre temperature with time have previously been plotted in figure 3.6. Figure A2.1 gives a more detailed description by plotting the complete temperature profile of equation 3.18 with time.

Substituting equation A2.1 into equation 3.18 gives

$$\begin{aligned} \theta &= \frac{2}{R^2} \int_0^R r \left\{ \theta_{m1} + \frac{\mathcal{P}_1}{2kR} (r^2 - R^2/2) \right\} dr \\ &+ \frac{2}{R^2} \sum_{n=1}^{\infty} \exp\{-\beta_n^2 \tau_2\} \frac{J_0(\beta_n r/R)}{J_0^2(\beta_n)} \int_0^R r \left\{ \theta_{m1} + \frac{\mathcal{P}_1}{2kR} [r^2 - R^2/2] \right\} J_0(\beta_n r/R) dr \\ &= A + B \end{aligned} \quad (\text{A2.2})$$



Integration of A, equation A2.2 gives

$$A = \frac{2}{R^2} \left( \theta_{m1} + \frac{\mathcal{P}_1}{2kR} \left[ \frac{R^4}{4} - \frac{R^4}{4} \right] \right) = \theta_{m1} \quad (\text{A2.3})$$

As expected, the ultimate temperature after soaking is  $\theta_{m1}$ .

The integral part of B, B' may be written

$$B' = \int_0^R r \left\{ \theta_{m1} + \frac{\mathcal{P}_1 R}{4k} \right\} J_0(\beta_n \frac{r}{R}) + \int_0^R \frac{\mathcal{P}_1}{2kR} r^3 J_0(\beta_n \frac{r}{R}) dr = C + D \quad (\text{A2.4})$$

Carslaw and Jaeger [24] on page 198 show that

$$\int r J_0(\alpha r) dr = \frac{1}{\alpha} r J_1(\alpha r) \quad (\text{A2.5})$$

Thus term C, equation A2.4 becomes

$$C = \left\{ \theta_{m1} + \frac{\mathcal{P}_1 R}{4k} \right\} \left[ \frac{1}{\alpha} r J_1(\beta_n \frac{r}{R}) \right]_0^R \quad (\text{A2.6})$$

which is zero from the definition of  $J_1(\beta_n)$ .

Term D, equation A2.4 when integrated by parts gives

$$D = -\frac{\mathcal{P}_1}{k} \frac{R^3}{\beta_n^2} J_2(\beta_n) \quad (\text{A2.7})$$

Substituting equations A2.3, A2.4, A2.6 and A2.7 into equation A2.2 gives

$$\theta = \theta_{m1} - \frac{2\mathcal{P}_1 R}{k} \sum_{n=1}^{\infty} \frac{\exp\{-\beta_n^2 \tau\}}{\beta_n^2} \frac{J_0(\beta_n \frac{r}{R})}{J_0^2(\beta_n)} J_2(\beta_n) \quad (\text{A2.8})$$

### A2.2.3 Power Input Density $\mathcal{P}_2$

The second contribution to the modified temperature distribution is the profile created by  $\mathcal{P}_2$ . Carslaw and Jaeger's equation

$$\theta_2 = \frac{\mathcal{P}_2 R}{k} \left[ \left\{ 2\tau_2 + \frac{r^2}{2R^2} - \frac{1}{4} \right\} - 2 \sum_{n=1}^{\infty} \exp\{-\beta_n^2 \tau_2\} \frac{J_0(\beta_n r/R)}{\beta_n^2 J_0(\beta_n R)} \right] \quad (3.11)$$

may be re-written in terms of the average mean temperature (steady-state)

$$\theta_{m2} = \frac{\mathcal{P}_2 R}{k} 2\tau_2$$

of the new power input and given by

$$\theta_2 = \theta_{m2} + \frac{\mathcal{P}_2 R}{k} \left[ \left\{ \frac{r^2}{2R^2} - \frac{1}{4} \right\} - 2 \sum_{n=1}^{\infty} \exp\{-\beta_n^2 \tau_2\} \frac{J_0(\beta_n r/R)}{\beta_n^2 J_0(\beta_n R)} \right] \quad (A2.9)$$

### A2.2.4 Superposition of Temperature Distribution

The complete solution is given by adding equations A2.8 and A2.9 and rearranging to give

$$\theta_2 = (\theta_{m1} + \theta_{m2}) + \frac{\mathcal{P}_2 R}{k} \left\{ \frac{r^2}{2R^2} - \frac{1}{4} \right\} - \frac{2R\mathcal{P}_1}{k} \sum_{n=1}^{\infty} \left( \frac{J_2(\beta_n r)}{J_0(\beta_n r)} + \frac{\mathcal{P}_2}{\mathcal{P}_1} \right) \left( \frac{\exp\{-\beta_n^2 \tau_2\}}{\beta_n^2} \frac{J_0(\beta_n r/R)}{J_0(\beta_n R)} \right) \quad (A2.10)$$

The first term is the final mean temperature after the soak of  $\mathcal{P}_1$  and after steady-state conditions have been reached for  $\mathcal{P}_2$ . The second defines the steady-state parabola of temperature associated with the new power input. The transient development of the  $\mathcal{P}_2$  profile is represented by the third term, with the transient reduction of the  $\mathcal{P}_1$  distribution during soaking.



Two graphical examples appear in figures A2.2 and A2.3. The first plots the changes in temperature profile during the power input change commensurate with the Curie transition. The second shows a similar change as the billet passes from one coil section to another.

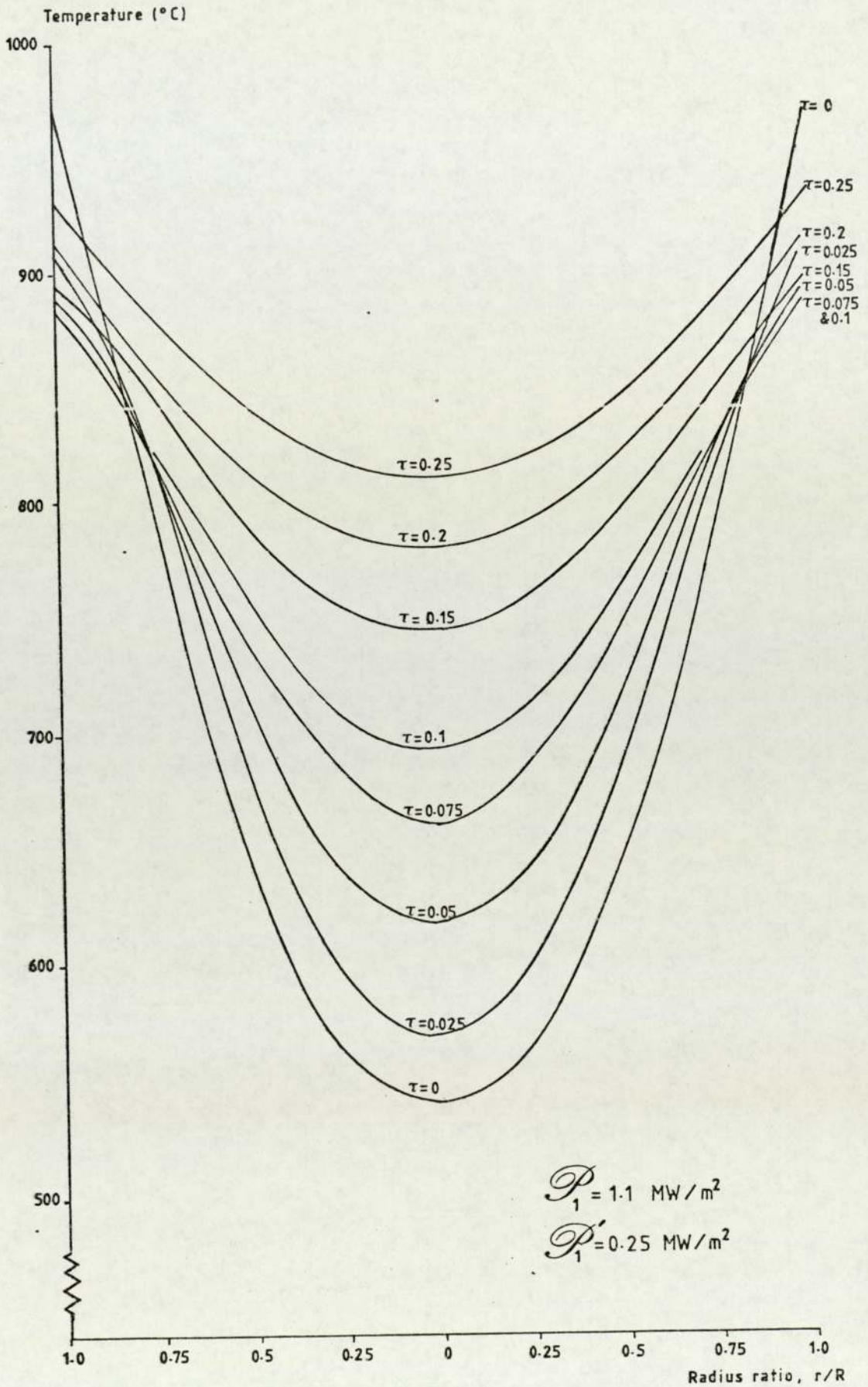


FIGURE A2.2: Example of the change in temperature profile during power input change at the Curie transition, not corrected for the effect of finite current depth.



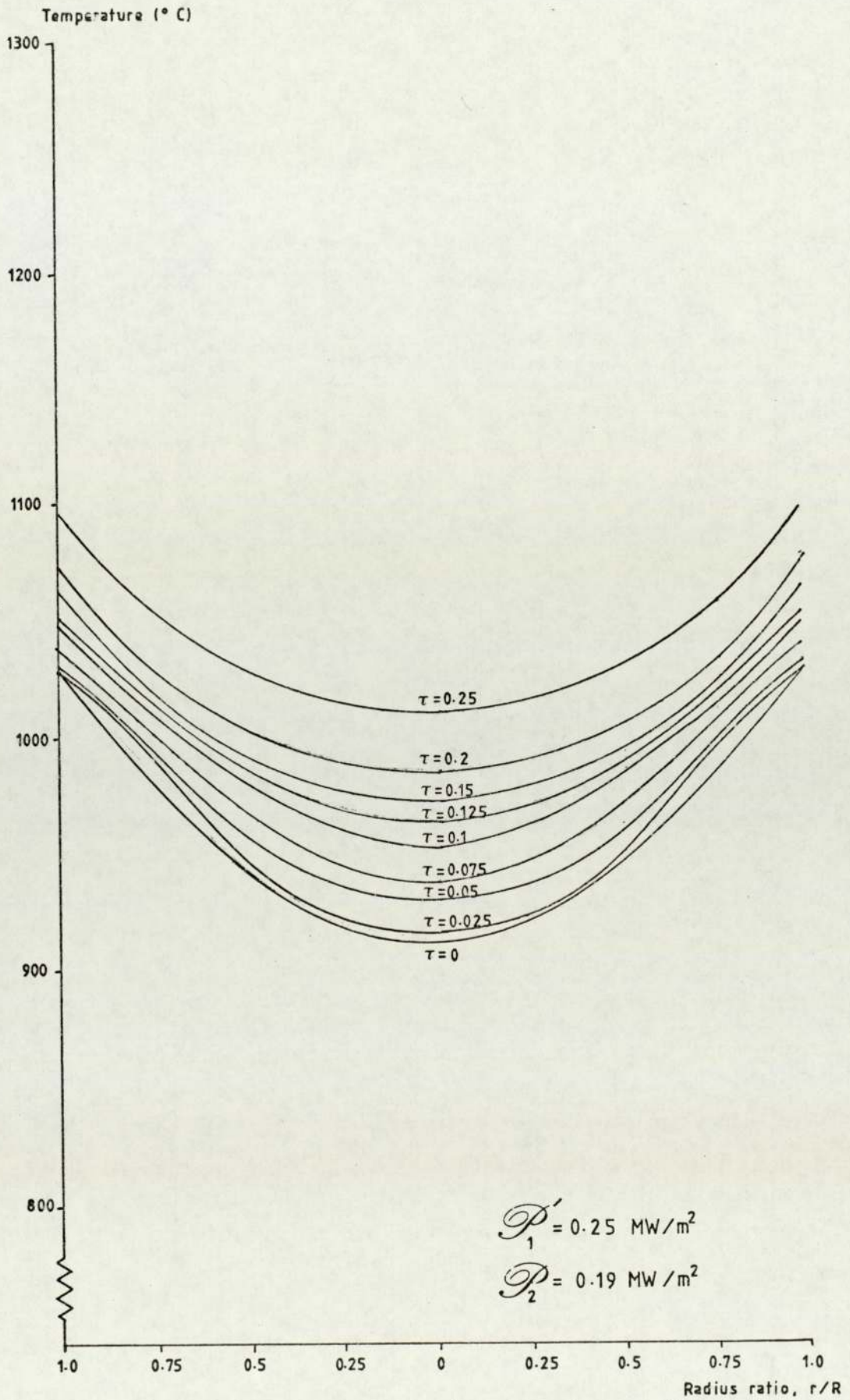


FIGURE A2.3: Example of the change in temperature profile during power input change at the transition from one coil section to another, not corrected for the effects of finite current depth.

APPENDIX 3 : DERIVATION OF EQUATION 5.13 for DETERMINING  
THERMAL CONDUCTIVITY k

Carslaw and Jaeger [24] consider the linear flow of heat in a rod of length  $l$ . The temperature at all parts of a transverse section through the rod of area  $A$  is the same, although each element of the rod loses heat by radiation from the surface, with surface thermal conductance  $k_m$ . The rod ends are maintained at fixed, steady temperature,  $T_1$  and  $T_2$ .

The equation

$$\frac{\partial T}{\partial t} = \frac{k}{c\gamma} \frac{\partial^2 T}{\partial x^2} - \frac{k_m p' T}{c\gamma A} \quad (A3.1)$$

may be solved, where  $p'$  is the rod section perimeter;  $k$ , the thermal conductivity,  $\gamma$  the density and  $c$  the specific heat of the rod material.  $T$  is the absolute temperature,  $\partial T / \partial t$  the first differential of temperature with respect to time and  $\partial^2 T / \partial x^2$  is the second differential of temperature with respect to distance along the bar. Omitting the second term on the right hand side of equation (A3.1) gives the heat diffusion equation without radiation. The second term describes heat loss to the external medium for small temperature differences between the bar and surroundings, setting the outside temperature to zero.



For steady conditions, the left hand side of equation (A3.1) becomes zero and the solution of

$$\frac{\partial^2 T}{\partial x^2} - \frac{k_m p' T}{k A} = 0 \quad (0 < x < l) \quad (\text{A3.2})$$

is found, where

$$\begin{aligned} T &= T_1 \text{ at } x = 0 \\ T &= T_2 \text{ at } x = l \end{aligned}$$

and

$$s^2 = \frac{k_m p'}{k A}$$

The solution of equation (A3.2) gives

$$T = C e^{s x} + B e^{-s x}$$

and

$$\begin{aligned} T_1 &= C + B \quad x = 0 \\ T_2 &= C e^{s l} + B e^{-s l} \quad x = l \end{aligned}$$

Thus the temperature is

$$T = \frac{T_1 \sinh s(l-x) + T_2 \sinh s x}{\sinh s l} \quad (\text{A3.3})$$

Let the temperature be  $T_a$ ,  $T_b$  and  $T_c$  at points  $x_a$ ,  $x_b$  and  $x_c$  along the bar, where  $x_c - x_b = x_b - x_a = a$ .

$$\frac{T_a + T_c}{T_b} = 2 \cosh s a = 2c \quad (\text{A3.4})$$

Hence,

$$e^{s c} = c^2 + \sqrt{(c^2 - 1)}$$

which is independent of  $T_1$  and  $T_2$ , the bar end temperatures. For two bars (1 and 2) of the same perimeter, cross-sectional area and surrounding medium conductivities, the ratio of their thermal conductivities is given by,

$$\sqrt{\frac{k_1}{k_2}} = \frac{m_2}{m_1} = \frac{\log [c_2 + (c_2^2 - 1)]}{\log [c_1 + (c_1^2 - 1)]} \quad (\text{A3.5})$$

A comparison of the thermal conductivities of two substances may be made, which is independent of the absolute temperatures of the bars and of radiation from the bars.  $k_1$  and  $c_1$  may be found by tests using a standard bar of known conductivity, (bar 1), thus equation (A3.5) and  $c_2$  may then be used to calculate  $k_2$  for the test bar under the same conditions.



APPENDIX 4 : SUMMARY OF CALCULATIONS FOR SINTERED  
BILLETS OF CHAPTER 7 by the method of CHAPTER 6

Abridged equivalent circuit calculations appear in the following tables for sintered billets of 0.74 (table A4.1), 0.79 (table A4.2) and 0.82 (table A4.3) relative density.

The resultant temperature distribution with time is summarized in tables A4.4 to A4.6 for  $\rho/\rho_0 = 0.74, 0.79$  and  $0.82$ , respectively.

FIRST COIL SECTION (sub-Curie)

Properties $\rho$ and $\mu_r$	Equivalent Impedances $m\Omega$	Work efficiency power factor and volt-amps	Volts/turn & Amp. turns	Magnetic field strength	Power Density (MW/m <sup>2</sup> )
$\rho = 1.28 \mu\Omega m$ $\mu_r = 13.8$	$R_w/N_c^2 = 2.375$ $R_c/N_c^2 = 0.259$ where $X_c/N_c^2 = 0.259$ $K = 77.7/m^2$ $X_w/N_c^2 = 2.524Z = 9.48$ $X_g/N_c^2 = 6.320$	$\eta = 0.872$ $\cos \phi = 0.278$ (VA) <sub>c</sub> = 98 kVA	$E/N = 9.8$ V $I_c N_c = 10.0$ kA	$H = 50.1$ kA/m	$\mathcal{P}_c = 0.587$

FIRST SECTION (Super-Curie)

Properties $\rho$ and $\mu_r$	Equivalent Impedances $m\Omega$	Work efficiency power factor and volt-amps	Volts/turn & Amp Turns	Magnetic field strength	Power Density (MW/m <sup>2</sup> )
$\rho = 2.73 \mu\Omega m$ $\mu_r = 1$	$R_w/N_c^2 = 0.777$ $R_c/N_c^2 = 0.259$ $X_c/N_c^2 = 0.259$ where $X_w/N_c^2 = 1.85$ $K = 77.7/m^2$ $X_g/N_c^2 = 6.320$ $Z = 7.83$	$\eta = 0.738$ $\cos \phi = 0.132$ (VA) <sub>c</sub> = 90 kVA	$E/N = 8.5$ V $I_c N_c = 10.5$ kA	$H = 98.7$ kA/m	$\mathcal{P}_c = 0.745$

SECOND COIL SECTION

Properties $\rho$ and $\mu_r$	Equivalent Impedances $m\Omega$	Work efficiency power factor and volt-amps	Volts/turn & Amp. turns	Magnetic field strength	Power Density (MW/m <sup>2</sup> )
$\rho = 2.73 \mu\Omega m$ $\mu_r = 1$	$R_w/N_c^2 = 0.756$ $R_c/N_c^2 = 0.276$ $X_c/N_c^2 = 0.276$ where $K = 77.7/m^2$ $X_w/N_c^2 = 1.20$ $Z = 7.84$ $X_g/N_c^2 = 6.32$	$\eta = 0.733$ $\cos \phi = 0.129$ (VA) <sub>c</sub> = 179 kVA	$E/N = 12.1$ V $I_c N_c = 14.8$ kA	$H = 47.7$ kA/m	$\mathcal{P}_c = 0.174$

Table A4.1 : Summary of Equivalent Circuit calculations for sintered billet workload  $\mathcal{V}/\mathcal{V}_c = 0.74$ .



FIRST COIL SECTION (sub-curie)

Properties $\rho$ and $\mu_r$	Equivalent Impedances $m\Omega$	Work efficiency, power, factor and volt-amps	Volts/turn & Amp. turns	Magnetic field strength	Power Density (MW/m <sup>2</sup> )
$\rho_{20-760}$ = $0.963\mu\Omega m$ $\mu_r=15.0$	$R_w/Nc_2^2=2.311$ $R_c/Nc_2^2=0.259$ where $X_c/Nc_2^2=0.259k=77.7/m^2$ $X_w/Nc_2^2=2.415Z=9.35$ $X_g/Nc_2^2=6.320$	$\eta=0.899$ $\cos\phi=0.275$ (VA) $c=108kA$	$V/N = 10.2V$	$H=54.2kA/m$	$\mathcal{P}_1=0.668$

FIRST SECTION (Super-Curie)

Properties $\rho$ and $\mu_r$	Equivalent Impedance $m\Omega$	Work efficiency power factor and Volt-amps	Volts/turn & Amp turn	Magnetic field strength	Power Density (MW/m <sup>2</sup> )
$\rho_{760-850} =$ $2.08\mu\Omega m$ $\mu_r=1.0$	$R_w/Nc_2^2=0.725$ $R_c/Nc_2^2=0.259$ $X_c/Nc_2^2=0.259$ where $X_w/Nc_2^2=0.934$ $K=7.77/m^2$ $X_g/Nc_2^2=6.320$ $Z=7.623$	$\eta=0.737$ $\cos\phi=0.129$ (VA) $c=99.9kVA$	$V/N = 8.9V$ $I_c Nc=11.3kA$	$H=102 kA/m$	$\mathcal{P}'_1=0.748$

SECOND COIL SECTION

Properties $\rho$ and $\mu_r$	Equivalent Impedances $m\Omega$	Work efficiency power factor and volt-amps.	Volts/Turn & Amp turns	Magnetic field strength	Power density (MW/m <sup>2</sup> )
$\rho_{850-1250}$ = $2.24\mu\Omega m$ $\mu_r=1.0$	$R_w/Nc_2^2=0.735$ $R_c/Nc_2^2=0.276$ $X_c/Nc_2^2=0.276$ where $X_w/Nc_2^2=1.028$ $K=77.7/m^2$ $X_g/Nc_2^2=6.320$ $Z=7.68$	$\eta=0.727$ $\cos\phi=0.132$ (VA) $c=192.2kVA$	$V/N = 12.4V$ $I_c Nc=15.5kA$	$H=50.9kA/m$	$\mathcal{P}_2=0.188$

Table A4.2 : Summary of Equivalent Circuit calculations for sintered billet workload,  $\gamma/\gamma_0=0.79$ .

FIRST COIL SECTION (sub-Curie)

Properties $\rho$ and $\mu_r$	Equivalent Impedances $m\Omega$	Work efficiency power factor and volt-amps	Volts/turn & Amp turns	Magnetic field strength	Power density (MW/m <sup>3</sup> )
$\rho_{20-760} = 0.84 \mu\Omega m$ $\mu_r = 11.7$	$\frac{R_w}{N_c^2} = 1.179$ $\frac{R_c}{N_c^2} = 0.259$ where $\frac{X_c}{N_c^2} = 0.259$ $K = 77.7/m^2$ $\frac{X_w}{N_c^2} = 1.213$ $Z =$ $\frac{X_g}{N_c^2} = 6.320$	$\eta = 0.820$ $\cos \phi = 0.182$ (VA) <sub>C</sub> = 184.4 kVA	$V/N = 12.3$ V $I_c N_c = 15.0$ kA	$H = 51.7$ kA/m	$\mathcal{P}_1 = 0.501$

FIRST SECTION (sub-curie)

Properties $\rho$ and $\mu_r$	Equivalent Impedances $m\Omega$	Work efficiency power factor and volt-amps	Volts/turn & Amp turns	Magnetic field strength	Power density (MW/m <sup>3</sup> )
$\rho_{760-850} = 1.81 \mu\Omega m$ $\mu_r = 1.0$	$\frac{R_w}{N_c^2} = 0.674$ $\frac{R_c}{N_c^2} = 0.259$ where $\frac{X_c}{N_c^2} = 0.259$ $K = 77.7/m^2$ $\frac{X_w}{N_c^2} = 0.878$ $Z = 7.52$ $\frac{X_g}{N_c^2} = 6.320$	$\eta = 0.722$ $\cos \phi = 0.124$ (VA) <sub>C</sub> = 110.5 kVA	$V/N = 9.3$ V $I_c N_c = 11.9$ kA	$H = 87.1$ kA/m	$\mathcal{P}_1' = 0.504$

SECOND COIL SECTION

Properties $\rho$ and $\mu_r$	Equivalent Impedances $m\Omega$	Work efficiency power factor and volt-amps	Volts/turn & Amp turns	Magnetic field strength	Power density (MW/m <sup>3</sup> )
$\rho_{850-1250} = 2.02 \mu\Omega m$ $\mu_r = 1.0$	$\frac{R_w}{N_c^2} = 0.674$ $\frac{R_c}{N_c^2} = 0.276$ where $\frac{X_c}{N_c^2} = 0.276$ $K = 77.7/m^2$ $\frac{X_w}{N_c^2} = 0.960$ $\frac{X_g}{N_c^2} = 6.320$ $Z = 7.62$	$\eta = 0.710$ $\cos \phi = 0.125$ (VA) <sub>C</sub> = 213.0 kVA	$V/N = 13.0$ V $I_c N_c = 16.4$ kA	$H = 54.2$ kA/m	$\mathcal{P}_2 = 0.195$

Table A4.3 : Summary of Equivalent Circuit calculations for sintered billet workload,  $\nu/\nu_0 = 0.82$ .



	POWER DENSITY (MW/m <sup>2</sup> )		average k (W/mK)	dθ dt (K/s)	TIME (s)	TEMPERATURE (°C)						
	INITIAL					INITIAL		FINAL		FINAL		
	φ	φ-φ <sub>c</sub>				θ <sub>c</sub>	θ <sub>m</sub>	θ <sub>s</sub>	θ <sub>c</sub>	θ <sub>m</sub>	θ <sub>s</sub>	
First Coil Section	Transient	0.587	0.587	19.6	-	23.9	100	100	100	290	480	613
		Steady state	0.587	0.582	14.4	20.4	4.9	290	480	613	323	580
	0.587		0.554	13.4	19.5	5.1	323	580	795	417	680	895
	0.587		0.532	13.5	15.0	6.7	417	680	895	466	760	910
	0.587		0.529	11.3	-	8.8	466	760	910	625	892	1006
	Transient	0.745	0.665	10.9	-	16.6	625	892	1006	802	1031	1086
		0.745	0.623	12.1	-	6.0	802	1031	1086	946	1072	1103
	Steady state	0.745	0.644	12.1	9.9	14.0	946	1072	1103	1085	1182	1190
		Transient	0.174	0.130	12.1	-	11.4	1085	1182	1190	1202	1270
	0.174		0.112	14.2	-	17.0	1202	1270	1292	1294	1325	1325
Second Coil Section	Steady state	0.174	0.112	14.2	2.3	7.5	1294	1325	1325	1311	1333	1339
		0.175	0.112	14.2	2.3	7.5	1311	1339	1339	1328	1341	1355
	0.175	0.112	14.2	2.3	7.5	1328	1341	1353	1345	1349	1367	

Table A4.4 : Summary of temperature distribution calculations for sintered billet ( $\nu/\nu_0 = 0.74$ ).

	POWER DENSITY (MW/m <sup>2</sup> )		average k (W/mK)	dθ dt (K/s)	TIME (s)	TEMPERATURE (°C)					
	φ	φ-φ <sub>c</sub>				INITIAL			FINAL		
						θ <sub>c</sub>	θ <sub>m</sub>	θ <sub>s</sub>	θ <sub>c</sub>	θ <sub>m</sub>	θ <sub>s</sub>
First Coil Section	Transient		25.6	-	13.8	30	30	30	166	332	498
	Steady state		0.668	0.668	21.9	166	332	498	243	432	621
	Sub-Curie		0.668	0.659	19.6	243	432	621	318	532	746
	Steady state		0.668	0.653	17.7	318	532	746	405	632	859
	Curie Transition		0.668	0.638	16.3	405	632	859	491	732	920
	Transient		0.668	0.636	13.7	491	732	920	525	760	950
	Curie Transition		0.668	0.630	13.1	525	760	950	589	854	994
	Transient		0.748	0.716	13.7	589	854	994	838	1050	1134
	Steady state		0.188	0.097	15.3	838	1050	1134	986	1082	1144
	Super-Curie		0.188	0.088	15.6	936	1082	1144	1111	1150	1188
Second Coil Section	Steady state		0.188	0.147	16.6	1111	1150	1188	1156	1181	1218
	Transient		0.188	0.144	17.1	1156	1181	1218	1181	1218	1254
	Steady state		0.188	0.139	17.5	1181	1218	1254	1248	1248	1314
	Steady state θ Rise		0.188	0.125	19.2	1248	1248	1314	1270	1301	1328

Table A4.5 : Summary of temperature distribution calculations for sintered billet ( $\nu/\nu_0=0.79$ ).



	POWER DENSITY		average k (W/mK)	dθ/dt (K/s)	TIME (s)	TEMPERATURE (°C)							
	(MW/m <sup>2</sup> )					INITIAL			FINAL				
	φ	φ-φ <sub>r</sub>				θ <sub>c</sub>	θ <sub>m</sub>	θ <sub>s</sub>	θ <sub>c</sub>	θ <sub>m</sub>	θ <sub>s</sub>		
First Coil Section	Transient	0.501	0.501	28.3	-	17.4	20	20	20	117	225	287	
		0.501	0.497	24.6	20.0	5.00	117	225	287	202	324	493	
	Steady state	0.501	0.494	23.6	13.6	7.38	202	324	493	276	424	587	
		0.501	0.494	21.8	13.0	7.67	276	424	587	366	525	698	
		0.501	0.489	21.0	12.2	5.34	366	525	698	381	550	760	
		0.501	0.484	19.9	11.2	8.90	381	550	760	516	650	920	
		0.501	0.475	18.2	10.6	9.45	516	650	920	530	750	980	
		0.504	0.479	18.2	-	7.67	530	750	980	601	788	956	
	Second Coil Section	Transient	0.504	0.473	15.1	-	8.14	601	788	956	760	947	1039
			0.504	0.392	16.4	-	13.98	760	947	1039	900	1073	1112
Steady state		0.504	0.392	16.4	-	8.99	900	1073	1112	990	1154	1159	
		-	-	-	-	-	-	-	-	-	-	-	-
Super -Curie	Transient	0.195	0.152	16.5	-	16.33	990	1154	1159	1160	1192	1207	
		0.195	0.152	19.2	-	34.97	1160	1192	1207	1212	1249	1268	
	Steady state	0.195	0.142	20.3	-	7.50	1212	1249	1268	1228	1265	1288	
		0.195	0.142	20.9	-	7.50	1228	1265	1288	1244	1278	1296	
		0.195	0.142	21.2	-	7.50	1244	1278	1296	1260	1291	1304	
		0.195	0.142	21.2	-	7.50	1260	1291	1304	1276	1304	1312	

Table A4.6 : Summary of temperature distribution calculations for sintered billet ( $\nu/\nu_0=0.82$ ).

APPENDIX 5: COST ANALYSIS OF INDUCTION HEATING OF  
POWDER-FORGING

A5.1 Introduction.

In this appendix, a quantitative assessment of the powder-forging route for sintered parts, using induction heating, is presented. Section A5.2 gives details of the cost advantages of using induction heating, compared with other furnace types. With the rapid rise in fuel cost over the last few years, induction heating presents a considerable saving over thermally-inefficient conventional furnaces. The capital expenditure and running costs are compared, using approximate figures for realistic production forging systems of the typical size used by G.K.N. Section A5.3 compares the powder-forging route with conventional forging methods. The powder-forging process has been developed by G.K.N. for over a decade, culminating in the establishment of a full commercial production plant for high volume production of ring and gear parts for automotive and agricultural equipment. Powder-forging has now reached maturity in a fiercely competitive, depressed market. The expansion of the process in the future depends on further cost reductions to improve competitiveness. Here, the critical factors in determining the economy of the forging route are identified. Apart from initial powder cost, the most expensive part of production of powder forged parts is the energy cost for sintering and heating for forging. This discussion concentrates on energy utilization since labour costs are so dependent on other factors, such as degree of automation and shift organization, considered further



in Chapter 11.

An economic assessment of the combination of induction heating and powder-forging appears in section A5.4. Information is drawn from the present experience of G.K.N. Powder-Forging Division on heating sintered parts and projected to future use of the process.

The figures used in sections A5.3 and A5.4 are approximate values for three reasons. First, since whenever possible much information has been derived from actual G.K.N. production, sensitive company information has been protected. Secondly, quoted figures have been found to vary widely depending on the source and date of the information. Finally, and especially in section A5.4, some arrangements combining induction heating and powder-forging have not as yet been subjected to the concrete test - the production line. This analysis represents the first stage in assessing the process from the Company's viewpoint. The hard economic facts derived here may be used in Chapter 11 to determine the coil type and design needed to heat preforms of various complex shapes with regard to other, more qualitative, environmental or convenience aspects, that do not lend themselves to critical financial consideration.

## A5.2 Induction Heating Versus Conventional Heating

### A5.2.1 Furnace Comparisons

For sintering, forging and annealing applications the major industrial furnances are of the following types:

- oil fired
- gas fired
- electric radiant
- induction heating.

Conventional furnaces suffer from poor energy efficiency because heat is applied by radiation and convection onto the metal surface and also into the surrounding atmosphere (table A5.1) [132]. Higher efficiencies are achieved during induction heating, where heat is generated and transported by conduction within the metal, and not subject to the associated heat transfer coefficient using external heat sources. General economic considerations are often difficult to assess due to changes in furnace capital cost and fluctuating fuel costs. Furnace efficiencies depend largely on their particular use, especially for induction heating where correct matching of the coil to work, and the heater to coil system, is required. For G.K.N. powder-forging applications, a medium frequency induction heater with an output of 100-160kW is compared with equivalent conventional furnaces, for heating solid steel billets, of 50mm typical diameter to 1250<sup>0</sup>C.



#### A5.2.1.1 Capital Costs

Table A5.2 indicates that equipment expenditure for induction heating are generally three times the cost of conventional oil, gas-fired or electric radiant furnaces of equivalent heating capacity. Some price variation occurs according to the frequency of the induction heater used [131], dictated by the metal size and magnetic state (table 2.2). The capital cost of induction heating equipment is increased if two units, at different frequencies, are required to heat the metal efficiently below and above the Curie temperature. For a particular application, the extra cost of installing a sub-Curie heater must be weighed against the benefits of greater efficiency and hence lower energy consumption. To achieve a uniform temperature distribution parts heated in conventional furnaces usually require longer soaking times at high temperature than induction installations. For heating powder preforms, the heating must be indirect within an inert atmosphere to avoid scaling and decarburization. These factors result in costly, larger capacity furnaces for an equivalent throughput. When increased installation costs and ancillary equipment charges, eg. atmosphere, have been added to the energy cost for longer heating times, the cost per tonne of heated parts is greater for electric, radiant, oil, and gas-fired types than for induction furnaces.

#### A5.2.1.2 Running Costs

Table A5.3 gives comparative fuel costs in May 1961 and equivalent direct conversion based on average furnace efficiencies. Heating by gas and oil can, exceptionally, reach 20%+ efficiency but for the indirect heating method required here 15% is more likely. Although induction heating furnaces are more efficient, electricity is considerably more expensive than fossil fuels and so the overall energy costs are comparable for all types or with a small advantage for induction heating, depending on the coil shape and workload coupling. The advantages of induction or conventional heating depend largely on how the heating units are operated. Oil and gas-fired furnaces require long "start-up" times before the furnace refractory walls reach operating temperature and acceptable atmosphere uniformity is achieved. Up to 15 hours start-up time is required (table A5.4) [133] to avoid excessive thermal shock to the furnace walls. Continuous production presents the optimum utilization of fossil-fuel furnaces, but is inconsistent with an industrial situation where shift changes, maintenance, lunch breaks, and breakdowns interrupt production.

In contrast, induction heating allows infinite variability in the heating process (figure A5.1). Full power is available seconds after energising the heating coil with minimal energy wastage. Within limits, the process is unaffected by any production halts.



During stand-by periods the induction heater power may be easily reduced to a value just sufficient to overcome radiation losses from the heated metal [94]. On resumption of forging, full power input is assumed and metal parts at the correct forging temperature emerge almost immediately from the coil. No billets are at an unacceptable temperature when leaving the furnace and rejects are minimized. Running costs are further reduced using induction coils by careful selection of frequency and power inputs, to give most rapid heating during the more efficient sub-Curie phase. A balance must be found between the lower cost of heating more rapidly for  $0^{\circ}\text{C}$  to  $760^{\circ}\text{C}$  at efficiencies approaching 80%, and increased energy loss by radiation incurred before forging, while equalizing the larger temperature differential produced in the billet.

Maintenance costs are reduced using induction heating. Fewer furnace parts are subjected to high temperature and cleaning operations are fewer, due to the purer heating atmosphere. Coils are easily disconnected for repair or replacement. Coil replacement time may be as little as 20 minutes [130]. Temperature uniformity over many parts ensures reduced wear on forging dies and press.

Few rejects and less scrap occur during induction heating as a result of the consistency of high quality part production.

Metallurgical properties can be more easily controlled in the absence of fossil-fuel combustion products by the use of protective atmospheres. For gas and oil furnaces, lack of adequate temperature and atmosphere control give oxidation or decarburization of the metal surface layers in contact with the atmosphere. This scale waste is typically six times the induction heating figure. High-output induction heaters, producing consistent quality parts with low scrap and reject rates, are well suited for automation. The more regular through-put gives a constant forging rhythm and forged output increases [130]. This is consistent with rapid forging and reduced costs since die life is improved as pressing time (billet time-in-press) falls and die temperature is lowered.

#### A5.2.2 Heating for Forging: Comparisons

Examples of simplified comparisons between induction heating and gas are given in tables A5.5 and A5.6. For the cost analyses of furnaces (table A5.5) and of a heating and forging suite (table A5.6), comparable equipment throughputs have been used for heating 50mm diameter billets to forging temperature. All figures are based on G.K.N. practice and existing equipment in May 1981 where applicable. As stated in Chapter 11, the important factors affecting profitability of heating for forging are:



- metal loss in heating and forging (scale and scrap)
- cost during down times
- die life
- labour costs
- forging rates.

Table A5.5 assesses the appropriate comparative equipment power rating, capital costs and running costs for through-heating 500kg/h of 50mm diameter steel billets to 1250°C for forging. One 8 hour shift for 250 days per annum produces 2000 tonnes a year, using a 160kW induction heater of 25% overall efficiency or an equivalent gas furnace (consuming 38.66 m<sup>3</sup>/h, which corresponds to 400kW approximately, and the best efficiency possible, 25%). Referring to the itemised descriptions in table A5.5, in brackets viz.( ), capital costs (1) are found using table A5.2. Here a single 3kHz induction unit has been used, which will not be as efficient below Curie as a 1kHz furnace.

The energy cost per tonne (13) and (14), is marginally in favour of the gas furnace. However, this is far out-weighed by the cost of greater scale loss (18) with the conventional furnace, due to decarburization. In general G.K.N. practice, the labour cost with induction heating is less than that for gas furnaces. Reduced scrap rates and automated furnace feed reduce the labour costs with the induction route.

Maintenance is here taken as the same for both furnaces; in practice, induction heaters are more reliable, but the costs of maintenance labour (24) is shown to be negligible. The overall cost per tonne is reduced by 27% (25), by the use of induction heaters rather than gas-fired furnaces. This is typical for many installations of other manufacturers. [18,134,135]. The difference in capital costs is £10 000 in favour of gas heating, but the running cost difference per year (26) is £14 820 in favour of induction heating; therefore the difference is recovered within a year.

Table A5.6 considers another production arrangement in more detail by including the complete forging installation, and compares the overall profitability of heating by induction and by gas over a typical ten hour period. Here, two 8 hour shifts for 250 days per year, producing 654kg/hr of forged billets, are considered. A 600kW induction heater is compared with a gas furnace (consuming  $66 \text{ m}^3/\text{h}$  gas, corresponding to 680kW approximately). Item (7) shows that the increased scrap rate for the gas furnace adds 6% to the cost of heating the greater initial quantity of metal required. Again, the energy cost (9) and (11) is in favour of gas heating but is not enough to overcome the greater cost of heating the scrap. Die costs (13) are considerably reduced with the induction furnace, accounting for about half of the overall works cost/hour (19).



It is during non-forging periods that the advantages of induction heating are strengthened. With reduced power input in the induction furnace, the energy lost in heating non-forged material is minimal. With gas however, the furnace must be maintained at temperature and with the loss of the contained metal. Overall, the induction route reduces costs over the 10 hour period by 6% (29) and increases profitability (34) by 52% of sale price.

### A5.2.3 Concluding Summary

The use of induction heating for forging is cheaper than conventional furnaces. The examples given show that cost may be reduced by between 6% and approximately one quarter, to give a 50% increase in profitability. It must be stressed that, in view of widely varying equipment capital and running costs, the only reliable method of obtaining a precise cost comparison is to carry out a rigorous analysis based on the specific requirements of the projected installation. Care must be taken to ensure that comparable units are considered and that no part of the production process has been omitted from the study.

## A5.3 Powder-Forging vs. Conventional Forging

### A5.3.1 Energy Consumption

A comparison is made between the conventional forging process from the starting point of a steel melting furnace, and the powder-forging route, starting with the powder plant.

This gives a realistic comparison by considering the manufacturing routes from similar raw material to the near finished component. (Any fine-finish machining and heat-treatment subsequent to machining have not been included).

#### A5.3.1.1 Conventional Forging

##### Steel Production

Steel is melted in large furnaces and cast into ingots. After various stages of reheating, rolling and removal of the decarburized surface layer, the billet is ready for forging. Most of the bars or billets purchased for conventional forges undergo one of three process combinations in the steel works. The route used depends on the supply sources, quantity and size. Table A5.7 [136] outlines these processes and gives details of the energy used by each route. Typical material utilisation is 40% [136,137] after removal of forging flash and machining. This is incorporated in table A5.7, by multiplying the energy used in kWh<sup>-1</sup> by a factor of 2.5 to give energy per tonne of finished product. Most powder-forgings are competing against parts made using Route 3.

##### Forging and Machining

Billets are forged (often in a number of stages) and the flash removed. The final shape and tolerances are achieved by machining. Table A5.8 gives a generalised analysis of energy used in forging and machining operations.



### A5.3.1.2 Powder-Forging

#### Powder Production

Steel is smelted in an induction furnace and then atomised with water jets to produce powder particles of the required size and shape. The powder is then dried and annealed to reduce internal stresses. Table A5.9 shows the energy consumption for powder production for the smaller scale of operation at current powder production levels.

#### Powder-Forging

In the powder-forging process, the powder is mixed and then sieved before compaction. The compacted "preform" is sintered to allow diffusion of alloying elements and improvement in inter-particle bonding. After cooling, the sintered preform is re-heated and then forged to give near 100% of theoretical density, and impart the desired mechanical properties to the part. Heat treatment and definning follow, resulting in the finished part. The energy utilization (table 5.10) assumes that the process is as used by G.K.N. Forgings at present.

### A5.3.2 Advantages of Powder-Forging

The powder-forging process has tangible cost advantages over conventional forging due to a reduction in machining. The improved material utilization results in reduced energy consumption in all stages of production.

The total energy consumption for conventional forging, using route 3, is  $4139 \text{ kWh t}^{-1}$  of the finished product (adding the totals from tables A5.7 and A5.8). Comparable powder-forging energy use is currently  $2839 \text{ kWh t}^{-1}$  (adding the totals from tables A5.9 and A5.10). Therefore, the powder-forging route consumes only about 70% of the energy for the conventional route. Some other benefits are outlined below. It is difficult to quantify the effects and implications of these factors, since, although some give improvements over conventional methods, others are unique to the powder forging process. These advantages may be summarised to be:

- Alloy systems may be made to precise compositions for particular applications demanding specific tensile strength, hardenability, wear resistance and fatigue performance properties [36].
- More complex shaped parts may be manufactured, within the constraints shown in figure A5.2, via one compaction and a single forging operation.
- Parts may be produced in a wide range of sizes to very close tolerances and finish.
- The mixing of powders which gives greater flexibility of alloy structure formation, than under conventional melting.
- Practices may create problems due to immiscibility of phases, and lack of solution.
- Controlled levels of porosity may be created by careful preform and die design, to reduce part weight in areas of the compacted metal part under reduced stress.



### A5.3.3 Other Factors

The powder cost is often a critical factor in deciding whether a powder-forging route is economic. The following methods ensure that this cost is minimized. It is advantageous to consider large production runs, since powder unit cost falls with increasing demand. The process lends itself well to high volume production of small parts. An automated system of die lubrication and die filling, compaction heating and forging, can achieve this, with labour costs kept to a minimum. Compaction die wear is improved by the reliability of automatic lubrication and accuracy of precise powder filling. Forging die life is increased as high temperature preforms are present for only a short time during high speed automatic operation. The use of re-cycled scrap for raw material production by direct comminution has been considered. It is estimated [138] that such a powder could replace about 20% of the existing market if it proved less expensive and energy consuming. If the energy required to make this 'scrap' atomised powder is reduced only by the energy needed to melt and refine steel for atomised powder, the average energy consumption of the overall process could be reduced by 4%.

### A5.3.4 Concluding Summary

At present, the powder-forging route offers considerable cost savings over conventional forging methods. Energy consumption is reduced to at least 70% of the previous requirement.

This comparison is typical for G.K.N. operations at present. However, within the foreseeable future, such advances as larger powder plants,\* and the use of a continuous furnace for both sintering and heating for forging, could reduce consumption to 40% of the current conventional forging figures. Similar reductions in energy use for powder-forging, compared with conventional forging, have been reported in the literature. An energy reduction of between 5% and 23%, depending on shape, occurs for hot isostatic pressing (H.I.P.) [137]. Precision part production from iron powder gives a 50% reduction in energy over conventional means [138]. A 15% cost reduction is possible for powder metal "superalloy" turbine discs [139]. Powder-metal automotive parts have been produced with energy savings between 40% and 60% [140]. Some of the examples given above do not consider the complete production process from steel or powder production plant. However the cost of these have incorporated within the respective steel billet or powder prices. The price of many powders, especially those of low production volumes or of specialized constituents, have fluctuated widely over the past ten years, [140] within the constraints of supply and demand. This may lead to an unrepresentatively low cost advantage for powder-forging in some cases.

\* These would decrease melting furnace energy use from 1000 kWh<sup>-1</sup> to 600 kWh<sup>-1</sup>, as for conventional steel plants.



## A5.4 Induction Heating of Sintered Metal Preforms for Forging

### A5.4.1 Billet Heating

The advantages of using induction heating for heating solid billets (Section A5.2) apply equally for heating simple shaped sintered powder preforms to forging temperature. It has been found in Chapter 7 that the process is even more efficient for powder parts since the metal resistivity is greater than for the solid metal, creating more  $I^2R$  heating. Control of heating time and atmosphere ensures that element diffusion, oxide reduction and temperature observed with powder billets accelerates diffusion and oxide reduction, minimizing the total heating time.

### A5.4.2 Heating of Shaped Parts

Conventional induction billet systems will not satisfactorily heat the total range of ring and gear components manufactured by G.K.N. Powder Forgings Division (Figure 8.6). Using solenoidal coils it was found that some portions of the preform heated preferentially. Also, long, inefficient soak times were necessary to even the temperature distribution before forging. Some difficulty was also experienced in adapting solenoidal coils for high-volume production. Linear "skate" coils have been developed to overcome some of these problems. The linear coil suffers from low electrical efficiency, due to poor coupling with the heated material (Figure A5.3), but preform transport through the coil is well suited to high-volume automated production.

Better atmosphere control in the linear coil ensures the correct metallurgical properties of the finished parts. Mesh belt transport prevents welding of preforms at high temperature, and gives flexibility to heat various shaped parts in one coil system. Examples from G.K.N. Powder-Forgings production of simple ring parts in Table A5.11 [114,145] shows the linear coil efficiency to be approximately 25-35%. It is difficult to make meaningful cost comparisons with heating for forging, using conventional furnaces, since practical production results with comparable sized furnaces are not available. However, Tables A5.12 and A5.13 [146] give a projected estimate of the cost saving per annum using induction heating for forging powder preforms, compared with a gas furnace of equivalent capacity. (Part production quantities are based on a 1978 sales forecast for 1981). For a single shift operation of this installation, running costs are reduced by 45-50%, using induction heating.



It must be noted however, that the gas furnaces in tables A5.12 and A5.13 are not of equivalent capacity to the respective induction units.

Empirical development work has continued (143) to improve the skate coil efficiency and heat distribution in more complex shaped parts by reducing the air-gap between the preform and coil turns. Typical efficiencies of arrangements tried in Chapter 9 are between 9% and 15%, but these could be improved by even closer coupling, the use of thermal insulation around the preform and coil, and higher power inputs to minimise radiation during soaking time at high temperature. The implications for G.K.N. of these cost analyses of coil design for induction heating powder-metal preforms for forging, are examined in Chapter 11.

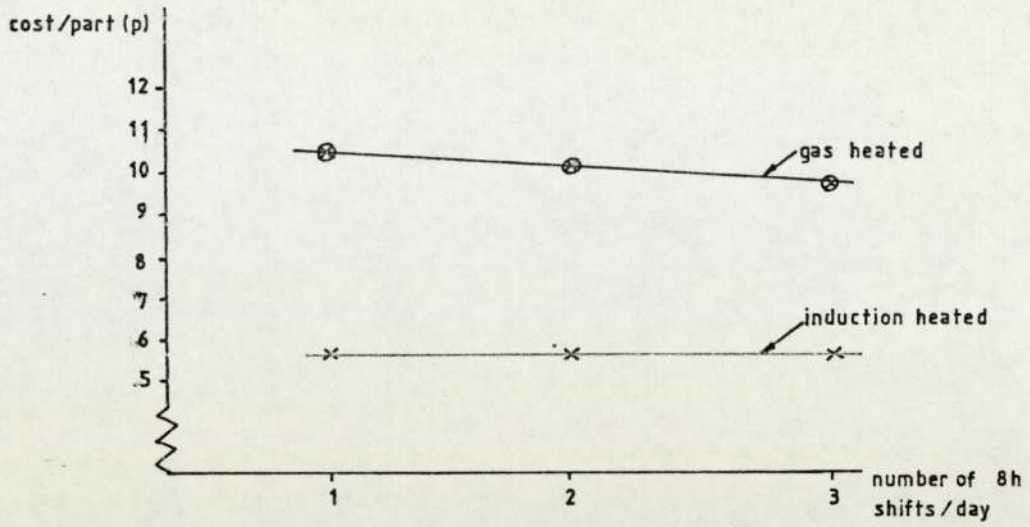


Figure A5.1 a

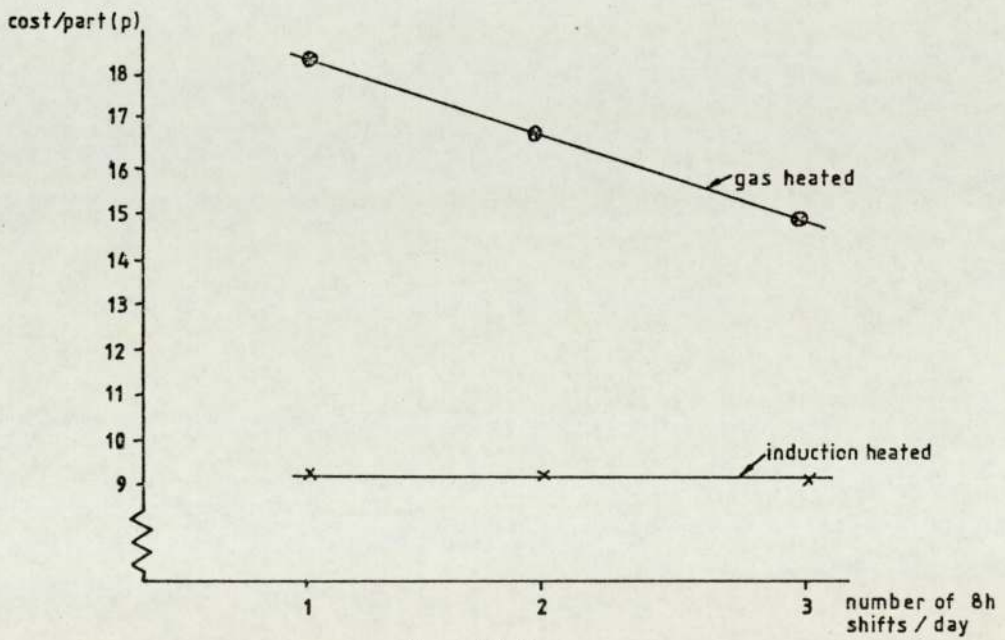
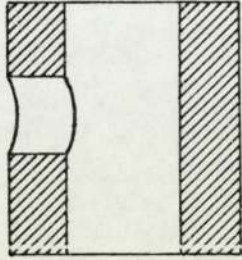


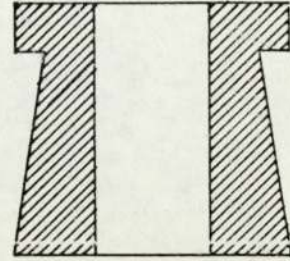
Figure A5.1 b

FIGURE A5.1: Cost comparison of induction heating and gas-fired furnaces with operation time. Figure A5.1a refers to the cost analysis of table A5.12 and figure A5.1b refers to table A5.13.

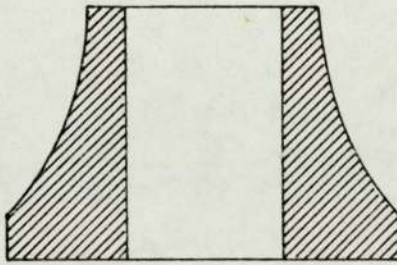




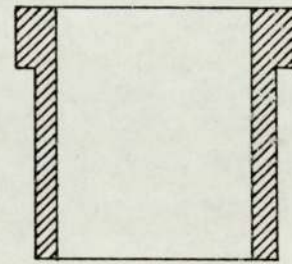
Holes in direction other than that of pressing



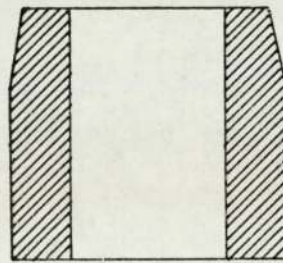
Re-entrant angles or necking



Very large radii



Long thin-walled sections



Small angled chamfering

FIGURE A5.2: Limitations of powder preform shape, -typical features that may not be incorporated, for press compaction [141,142].

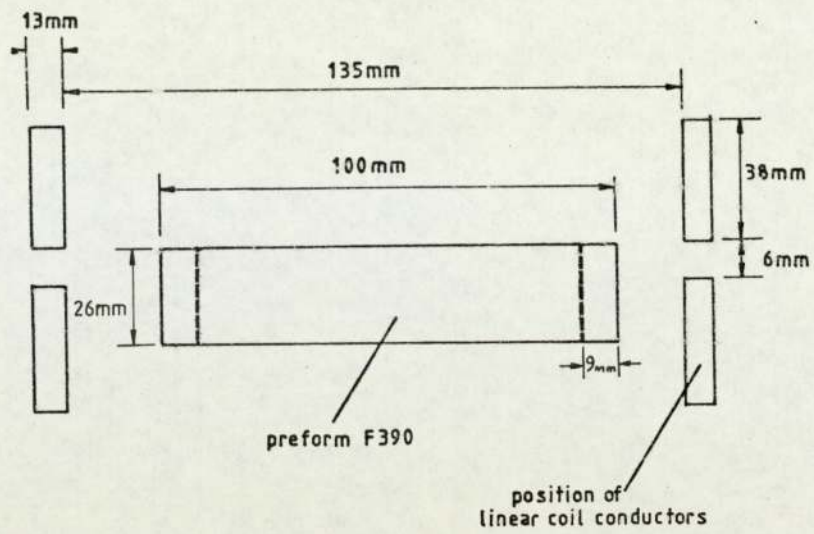


FIGURE A5.3: Linear coil configuration in use for heating preforms of Table A5.11.



METHOD OF HEAT TRANSFER	MW/m <sup>2</sup>
CONVECTION	0.005
RADIATION	0.1
CONDUCTION	0.2
FLAME	10
INDUCTION HEATING	30

Table A5.1 : Typical Power densities for various methods of heat transfer in metals [132].

FURNACE TYPE	CAPITAL COST (£/kW)	
GAS-FIRED	~ 50	
OIL-FIRED	~ 40	
ELECTRIC RADIANT	~ 60	
INDUCTION HEATERS	-Supply Systems (50Hz)	40-65
	-Motor Alternators (1-10kHz)	90-160
HEATERS	-Static Inverters (1-10kHz)	65-170

Table A5.2 : Capital cost comparisons for major furnace types, from manufacturers quotations in May 1981.

FUEL TYPE	COST (p/therm)	COST per 10 <sup>6</sup> kJ (£)	APPROXIMATE EFFICIENCY %	TOTAL FUEL COST per 10 <sup>6</sup> kJ (£)		
GAS	30.3	2.8	10 - 20	14 - 28		
OIL	34.9	3.3	10 - 20	17 - 33		
ELECTRICITY	Induction Heaters	-Radiant	15 - 20	39 - 52		
		-solenoid coils	82.0	7.8	50 - 80	10 - 16
		-other coil types	10 - 35	22 - 78		

Table A5.3 : Fuel cost and furnace efficiencies (May 1981) [155].

FURNACE TEMPERATURE (°C)	TIME TAKEN (h)	COMMENTS
0 - 700	3 - 4	start-up
700 - 800	1	mesh belt inserted
800 - 900	1	gas atmosphere introduced
900 - 950	1/2	
950 - 1150	4	furnace at forging temperature
1150	4	temperature and atmosphere stabilised.
TOTAL	<u>131-141</u> h 2 2	

#### ENERGY CONSUMPTION

Nominal Heating Capacity	280 kg/h
Heat Supplied to furnace	364 kW
Heat Supplied to Load	59 kW
Heat Lost To	-furnace casing 31 kW
	-open ends of furnace 0.4 kW
Heat Lost To	-gas atmosphere 22 kW
	-mesh transport belt 252 kW
Overall Efficiency	16 %
Load Temperature Uniformity	+5 %

Table A5.4 : Start-up sequence and energy consumption for an indirectly-fired gas furnace, used by G.K.N. [133].



ITEM No.	DESCRIPTION	CALCULATION METHOD	UNITS	INDUCTION HEATER	GAS FURNACE
1	Capital Cost	---	£	25 600	15 600
2	Annual Depreciation	(1) x 15%	£/year	3 840	2 340
3	Annual Throughput	---	t/year	2 000	2 000
4	Depreciation Cost/Tonne	(2)/(3)	£/t	1.92	1.17
5	Annual Hours	---	h/year	4 000	4 000
6	Hourly Throughput	(3)/(5)	t/h	0.5	0.5
7	Electrical Energy/Hour	---	kWh	160	---
8	Gas Consumption/Hour	---	m <sup>3</sup> /h	---	38.66
9	Energy Cost <sub>3</sub> per kWh	---	p/kWh	2.8	---
10	Fuel Cost/m	---	p/m	---	10.61
11	Energy Cost per Hour	(7)x(9)	£/h	4.48	---
12	Energy Cost per Hour	(8)x(10)	£/h	---	---
13	Energy Cost per Tonne	(11)/(6)	£/t	---	8.96
14	Energy Cost per Tonne	(12)/(6)	£/t	---	8.20
15	Scale Loss	---	%	0.5	3.0
16	Scale Loss per Tonne	---	t	0.005	0.03
17	Raw Steel Cost/Tonne	---	£/t	285	285
18	Scale Cost per Tonne	(16)x(17)	£/t	1.43	8.55
19	Manning Level	---	---	1	1.25
20	Labour Cost per Hour	@£3.60/h	£/h	3.60	4.50
21	Labour Cost per Tonne	(20)/(6)	£/t	7.20	9.0
22	Manning Level, maintenance	---	£/h	0.1	0.1
23	Maintenance Labour Cost	@£3.60/h	£/h	0.36	0.36
24	Maintenance Cost/Tonne	(23)/(6)	£/t	0.72	0.72
25	TOTAL COST per Tonne	(4)x(13)+(18)	£/t	20.23	27.64
26	Total Cost per Year	(3)x(25)	£/Year	40 460	55 280
27	Approximate Total Cost.	(26)x(5)	£/h	10.12	13.82

Table A5.5 : Cost analysis of induction heating and gas for billet heating at May 1981 charges [154].

ITEM No.	DESCRIPTION	CALCULATION METHOD	UNITS	INDUCTION HEATER	GAS FURNACE
1	Capital Cost-Forging Press	---	£	190 000	190 000
	-Heater	---	£	100 000	33 500
	-Total	---	£	290 000	213 500
2	Depreciation/Year	(1)x15%	£/year	43 500	32 000
3	Production per Year (Two Shifts)	---	h	4 000	4 000
4	Depreciation per Hour	(2)/(3)	£/h	10.88	8.00
COSTS PER HOUR, WHEN FORGING					
5	Throughput, Forged Weight	---	t/h	0.654	0.654
6	Losses in heating, Forging etc	[18], p303	%	25	32
7	Raw Steel Required	(5)x(100+(6))/100	t/h	0.817	0.863
8	Raw Steel Cost	£285/t x(7)	£/h	232.85	245.96
9	Electrical Energy/Tonne	---	kWh/t	385	---
10	Electricity Cost @2.8p/kWh	(9)x(10)/(7)	£/h	13.19	---
11	Gas Fuel Consumption/Tonne	---	m <sup>3</sup> /t	---	100.5
12	Gas Cost @ 10.61p/m <sup>3</sup>	(11)x(12)/(7)	£/h	---	12.36
13	Press Crew Wages	3 men @£3.60/h	£/h	10.80	10.80
14	Die Cost per Tonne	ave. die life	£/t	27	39
15	Die Cost per Hour	(14)x(5)	£/h	17.66	26.13
16	Additional Costs (cropping, handling & inspecting)	---	£/h	16.00	18.60
17	Additional Fixed Works Costs/Year (buildings land and services)	G.K.N accounting policy. Induction figure may be lower	£/year	43 825	43 825
18	Fixed Works Costs/hour	(17)/(3)	£/h	10.96	10.96
19	TOTAL WORKS COST/HOUR	(4)+(10)+(12)+(13)+(15)+(16)+(8)	£/h	312.36	332.81
20	Total Works Cost of 7 1/2 h of Forging in 10h	(19)x7 1/2	£	2 342.70	2 496.08
COSTS PER HOUR, WHEN NOT FORGING					
21	Wages of Press Crew (3)	@£3.60/h	£/h	7.34	7.34
22	Plant Depreciation	(4)	£/h	10.88	8.00
23	Heating Costs of Unforged Steel		£/h	1.51	5.89
24	Additional Fixed Works Costs/hour	(18)	£/h	10.96	10.96
25	TOTAL WORKS COST/HOUR	(21)+(22)+(24)	£/h	30.69	32.19
26	Total Works Cost for 2 1/2 Non-productive Hours	(25)x 2 1/2	£	76.73	80.48
27	TOTAL WORKS COST FOR 7 1/2 h FORGING and 2 1/2 h IDLE	(20)+(26)	£	2 419.43	2 576.56
28	Managerial and on-costs	(27) x 5%	£	121.17	128.83
29	TOTAL COSTS for 10 HOURS	(27)+(28)	£	2 544.50	2 705.39
30	Cost per hour	(29)/10	£/h	254.45	270.54
31	Saleable Forgings	(5)-1% scrap	t/h	0.648	0.648
32	Value of Forgings	(31) x £614/t	£/h	401.76	401.76
33	Sales per Hour	(32)x7 1/2 h/10h	£/h	301.32	301.32
34	Gross Profitability	(33)-(30)	£/h	46.87	30.78

Table A5.6 : Billet heating cost analysis for induction heating and gas-complete production process [154].



	<u>ROUTE 1</u>		<u>ROUTE 2</u>		<u>ROUTE 3</u>	
	kWh <sup>-1</sup>	kWh <sup>-1</sup> of finished product	kWh <sup>-1</sup>	kWh <sup>-1</sup> of finished product	kWh <sup>-1</sup>	kWh <sup>-1</sup> of finished product
MELTING FURNACE (sst arc furnace)	600	1500	600	1500	600	1500
SOAK	30	75	30	75	30	75
REHEAT	---	---	200	500	200	500
INGOT COGGING	30	75	30	75	30	75
BILLET MILL	20	50	20	50	20	50
REHEAT	---	---	---	---	200	500
REROLL	---	---	---	---	20	50
TOTALS		1700		2200		2750

Routes comprise :-

- ROUTE 1: The straight-through route. Ingots are passed through the cogging and billets mills without cooling after soaking.
- ROUTE 2: Ingots are allowed to cool after casting and are then reheated for the cogging and billet mills.
- ROUTE 3: As for route 2, with subsequent reheating and rerolling. This is usually for sizes of 50mm square maximum; most powder-forgings are competing against parts made from steel using this method.

Table A5.7 : Energy consumption for three routes of steel billet production used in conventional forging [136].

	kWht <sup>-1</sup>	kWht <sup>-1</sup> of finished products
COLD CROP	2	5
HEAT FOR FORGING @ 200 kW for 585 kg	338	845
FORGE : 1000t 40% MAXIMUM LOAD	43	79
: 350t 40% " "	22	41
SHOT BLAST	3	5
HEAT TREATMENT	200	340
MACHINING	---	74
<b>TOTAL</b>		<b>1389</b>

Table A5.8 : Energy consumption for conventional forging and machining [136].

	kWht <sup>-1</sup>
MELTING 20t HF UNIT	1000
ATOMIZING AND DRYING	57
ANNEALING	60
<b>TOTAL</b>	<b>1117</b>

Table A5.9 : Energy consumption for GKN powder production [136]



	kWh t <sup>-1</sup>
MIXING AND SIEVING	2
PREFORM PRESSING	55
SINTERING : @ 160kWh per 270 kg	590
3.7 kW MESH BELT PREFORM TRANSPORT	14
ENDOTHERMIC GAS	390
HEATING FOR FORGING : @ 200 kW for 585 kg	340
FORGING 350t press	21
HEAT TREATMENT	306
DEFINNING	4
	1722

Table A5.10 : Energy consumption for GKN powder-forging [136].

PREFORM NUMBER FURNACE			F 345		F 325		F 390	
			I.H.	GAS	I.H.	GAS	I.H.	GAS
Induction Heater conditions	Frequency	kHz	3	---	3	---	3	---
	Voltage	V	890	---	800	---	705	---
	Current	A	140	---	150	---	125	---
	Reactive Power	kVAr			46			
	Capacitors		14	---	14	---	14	---
	Power	kW	125	364	70	364	88	364
	Mesh Belt Speed	mm/sec	9.65	---	15.5	---	---	---
	Throughput	kg/h	253	280	179	240	220	272
	Energy Supplied/h	MJ	450	1300	252	1310	317	1310
Preform mass	kg	0.703	0.703	0.371	0.371	0.366	0.366	
Final temperature	°C	1090	1100	1090	1100	1090	1100	
Heating time	min	10		7		4		
Energy required/h	MJ	117	131	82.5	111	102	127	
Efficiency	%	26.0	10.1	33.0	8.5	32	9.7	

Table A5.11 : Performance of linear coil in heating preforms (Figure 8.6) using the coil arrangement of Figure A5.3 [144, 145].



ITEM	DESCRIPTION	UNITS	METHOD OF CALCULATION	INDUCTION HEATING	GAS FIRED
1	Quantity/year	---	---	220 000	220 000
2	Furnace Power	kW	---	124	70
3	Theoretical Production Hours	h	---	730	963
4	Tool Changes	h	---	352	352
5	Breakdowns	h	(6) x 10%	104	169
6	Actual Hours Production	h		1044	1691
7	Start-up Time (single shift)	h		---	3382
8	Fuel Consumption -Full Load	MWh	(6) x (2)	129	118
9	-Standby Load	MWh	(5)x(2)x7% ((4)+(5)+(7))x40kW	0.9	156
10	Fuel Cost -Full Load	£		3624	1222
11	-Standby Load	£		26	1616
12	Water cooling, endothermic gas and ancillaries	£		823	1038
13	Total Fuel Cost	£	(10+11+12)	4473	3876
14	Production -Labour	£	(6)x1x£3.60	3758	12175
15	-Supervision	£	(6)x2x£3.60 (14)x10%	376	1217
16	Total Labour	£	(14) + (15)	4134	13392
17	Replacement Parts	£	---	2000	5032
18	Maintenance Labour	£	((5)x2x£3.60	749	1217
19	Total Repair	£	(17) + (18)	2749	6249
20	Total Running Costs	£	(13)+(16)+(19)	11356	23517
21	Running Costs per part	p	(20) / (1)	5.2	11

Table A5.12 : Projected running cost estimates of induction heating of ring-shaped powder preforms for forging, compared with gas heating [129].

ITEM	DESCRIPTION	UNITS	METHOD OF CALCULATION	INDUCTION HEATING	GAS FIRED
1	Quantity/year	---	---	180 000	180 000
2	Furnace Power	kW	---	350	322
3	Theoretical Production Hours	h	---	486	841
4	Tool Changes	h	---	288	288
5	Breakdowns	h	(6) x 0.1	75	148
6	Actual Hours Production	h		747	1476
7	Start-up Time (single shift)	h		---	2952
8	Fuel Consumption -Full Load	MWh	(6) x (2)	261.5	475
9	-Standby Load	MWh	(5)x(2)x7% ((4)+(5)+(7) x175kW)	1.8	595
10	Fuel Cost -Full Load	£		7320	4920
11	-Standby Load	£		52	6159
12	Water cooling, endothermic gas and ancillaries	£		940	6097
13	Total Fuel Cost	£	(10+11+12)	8312	17176
14	Production -Labour	£	((6)x2x£3.60)	5378	8784
15	-Supervision	£	(14)x10%	538	878
16	Total Labour	£	(14) + (15)	5916	9662
17	Replacement Parts	£		2000	5000
18	Maintenance Labour	£	((5)x2x£3.60)	540	1065
19	Total Repair	£	(17) + (18)	2540	6065
20	Total Running Costs	£	(13)+(16)+(19)	16769	32903
21	Running Costs per part	p	(20) / (1)	9	18

Table A5.13 : Projected running cost estimates of induction heating gear-shaped powder preforms for forging, compared with gas heating [129].



LIST OF REFERENCES

## REFERENCES

- 1 G.K.N. Information sheet for employees.
- 2 Jones, P.K. The Powder-Forging Process, P.& P.D., G.K.N. Research Report, 1970.
- 3 Long G.R. Induction Heating of Powder Preforms, G.K.N. P.&P.D. Research Report, 1978.
- 4 Warren, P.H. Induction Heating of Powder Compacts, (E.C.R.C) Electricity Council Research Centre Report ECRC/M1250, May 1979.
- 5 Burch, C.R. and Davis, N.R. On the Quantitative theory of Induction Heating, Philosophical Magazine VI, pp768-783, 1926.
- 6 Jennings, R.E. Forging Heat by Induction?, American Machinist, pp98-99, November 1978.
- 7 Perkins, A.J. Electricity Supply Industry Assistance to the Drop Forger, National Association of Drop Forgers and Stampers Symposium, November 1978.
- 8 Osborn, H.B. Why Induction Heating?, Machinery, pp 61-67, June 1972.
- 9 Anon. A First Guide to Induction Heating, Intertherm Ltd.
- 10 Ingall, J.R. and Ellis, R.S. Induction Heating of Ferrous and Non-Ferrous Billets for Forging and Extrusion, Journal of the Institute of Metals, pp161-170, 1964.
- 11 Davies, E.J. & Simpson, P.G. Induction Heating for Industry, Electronics and Power, pp 508-515, July 1979.
- 12 Anon. Induction Heating Guidelines, Electrical Times, pp 37-38, April 1971.
- 13 Anon. Induction Heating of Billets and Bars, Electricity Council, Technical Information (IND 21),1977.



- 14 Hobson, L. Induction Heating Course Notes, April 19th-23rd, Electroheat Group, Loughborough University of Technology, 1982.
- 15 Tudbury, C.A. Basics of Induction Heating, Vols 1 & 2, Chapman and Hall, London 1960.
- 16 Brown, G.H.  
Hoyler, C.N.  
& Bierwirth, R.A. Theory and Application of Radio-Frequency Heating, Van Nostrand, New York, 1947.
- 17 Horn, H. Major Factors in the Design of Medium Frequency Induction Heating Furnaces, Eddycurrent Machinery Agents Ltd., Birmingham, 1971.
- 18 Davies, E.J. and P.G.Simpson, Induction Heating Handbook, M<sup>C</sup>.Graw-Hill, London, 1979.
- 19 Lozinskii, M.G. Industrial Applications of Induction Heating, Pergamon Press, Oxford, 1969.
- 20 Tasevski, Z. Inductive Billet, Bloom and Bar Heaters for Hot Working in Modern Forge Shops, Brown Boveri Review, V65,2, pp82-7, February 1978.
- 21 Simpson, P.G. Induction Heating, M<sup>C</sup>Graw-Hill, New York, 1960.
- 22 Tai, C.T. On the Presentation of Maxwell's Theory, Proc. I.E.E.E. V60 Number 8, August 1972.
- 23 Baker, R.M. Design and Calculation of Induction Heating Coils, A.I.E.E. Trans., V76 Pt 11, pp31-40, 1957.
- 24 Carslaw, H.S.and Jaeger, H.C. Conduction of Heat in Solids, Oxford University Press, Oxford, 1959.
- 25 Ede, A.J. An Induction to Heat Transfer, Pergamon Press, London, 1967.
- 26 Baker, R.M. Classical Heat Flow Problems Applied To Induction Heating, A.I.E.E. Trans., V77, pp106-112, 1958.
- 27 Warring,R.H., Hydraulic Fluids and Engineering Applications, Trade and Technical Press, 1961.

- 28 Hydraulic Power Transmission - Editors, Hydraulic Technical Data, Trade and Technical Press, 1966.
- 29 Vaughan, J.T. and J.W.Williamson Design of Induction Heating Coils for Cylindrical Non-Magnetic Loads, A.I.E.E. Trans., V64, pp587-92, 1945.
- 30 Vaughan, J.T. and Williamson, J.W. Design of Induction Heating Coils for Cylindrical Magnetic Loads, A.I.E.E. Trans., V65, pp887-92, 1946.
- 31 Anon. Capacitors for Power Factor Improvement, Bryce Capacitors Limited, Cheshire.
- 32 Dixon, R.H.T. and Clayton, A. Powder Metallurgy for Engineers, Machinery Publishing, Brighton, 1971.
- 33 Huppmann, W.J.and Hirschvogel,M. Powder Forging, Review 233 pp 209-239, International Metals Reviews, Number 5, 1978.
- 34 Thümmler & Thomma, W. The sintering Process, Review 115, Metals and Material, V1, Number 6., June 1967.
- 35 Anon. G.K.N. Powder Forging Materials Specification and Properties, G.K.N. Group Technological Centre Report, Issue Number 3, 1979.
- 36 Brown,G.T. High Duty Cost Conscious Parts by Powder Metallurgy Techniques, Chartered Mechanical Engineer, pp.49-51, July 1980.
- 37 James, W.B. G.K.N. Group Technological Centre, Confidential Report-Induction Heating for Powder Forging. part 11: Determination of mechanical Property data for induction heated W4 and W78 low alloy steels., (Memo no. 1083,) March 1980.
- 38 Brown, G.T. Development of Alloy Systems for Powder Forging, Metals Society Meeting on Alloy Composition and Microstructural Control in Relation to Processing, London, 1975.
- 39 Gray, W.A. The Packing of Solid Particles, Powder Technology Series, Chapman and Hall, 1968.



- 40 Tikkanen, M.H. On Some Basic Research Problems in Powder Metallurgy, Scandinavian Journal of Metallurgy, V9, pp 247-245, 1980.
- 41 Hausner, H.H. Editor, Modern Developments in Powder Metallurgy series, Vol.5 Materials and Properties, 1970. Vol.7 P/M Forging, 1974. Plenum Press, New York.
- 42 Jones, W.D. Principles of Powder Metallurgy, Edward Arnold, London, 1937.
- 43 Jones, W.D. Fundamental Principles of Powder Metallurgy, Edward Arnold, London 1960.
- 44 Hausner, H.H. Handbook of Powder Metallurgy, Chemical Publishing, New York, 1973.
- 45 Brown, G.T. The 'Core' Properties of a Range of Powder-metal Steels for Carburizing Applications, Powder Metallurgy, pp171-178, No,3, 1977.
- 46 Brown, G.T., and Steed, J.A. The Fatigue Performance of some Connecting Rods made by Powder Forging. Powder Metallurgy, V16 No,32 pp 405-415, 1973.
- 47 Brown, G.T. and Steed, J.A. A Comparison of the Mechanical Properties of some Powder Forged and Wrought Steels, Powder Metallurgy, V17, No 33. pp 157, 1974.
- 48 James, W.B. and Brown, J.T. Fatigue Testing of Connecting Rods, G.K.N. Group Technological Centre, Report, April 1979.
- 49 Jones, P.K. and Wisker, J.W. The Production of Precision Automotive Components by the Powder Forging Process - Present Situation and Future Prospects, Society of Automotive Engineers Congress and Exposition, Detroit, 1978.
- 50 Powell, R.W. A survey of Existing Data on the Thermal and Electrical Conductivities of Iron and Steels, Second Alloy Steels Report, Section 1X (4), 1939.

- 51 Griffiths, E. The Physical Properties of a Series of Steels, Second Report of the Alloy Steels Research Committee, Section 1X (3), 1939.
- 52 Griffiths, E. Resistivities of Steels up to 1300<sup>0</sup>C, Iron and Steel Institute Special Report, Alloy Steels Research Committee, Papers 23 and 24, 1946.
- 53 Vityaz, P.A. and Perelman, V.E. Porosity Distribution in Parts of Complex Shape and Methods of its Determination, Soviet Powder Metallurgy and Metal Ceramics, V10, 3 pp191-194, 1971.
- 54 Watanabe, M., Awano, Y., Danno, A., Onada, S. and Kimiwa, T. Deformation and Densification of P/M Forging Preforms, International Journal of Powder Metallurgy, V14, No 3, July 1978.
- 55 Smart, J., Reed, B.W. and Brown, P.R. Pressing and Sintering Methods to produce high grade tool steels, metal powder report, pp241-244, June 1980.
- 56 Mocariski, S. and Hall, D.W. Changes in Microstructure of Ferrous Powder Metal Compacts during High Temperature Sintering, Society of Automotive Engineers, Congress and Exposition, Detroit, 1980.
- 57 Bal'shin, M.Yu Control over the Properties of Sintered Ductile Materials, Soviet Powder Metallurgy and Metal Ceramics., V19 pp623-630, February 1980.
- 58 Grootenhuis, P., Powell R.W. and Tye R.P. Thermal and Electrical Conductivities of Porous Metals made by Powder Metallurgy Methods, Proc. Physical Society. V65, pp502-511, 1952.
- 59 Adlassig, K. and Fogler, O. Radexc-Rundschau, Pt. 2, V79, 1950.
- 60 Manegold, E. and Von Egnelhardt, W. Koll Z; V62, p285; V63,p12 and p149, 1933.



- 61 Koh, J.C.Y and Fortini, A. Thermal conductivity and Electrical Resistivity of Porous Materials, N.A.S.A. Report C.R. - 120854, 1972
- 62 Koh, J.C.Y. and Fortini, A. Prediction of Thermal Conductivity and Electrical Resistivity of Porous Metallic Materials, International Journal of Heat and Mass Transfer, V16, pp2013-2022, 1973.
- 63 Aivazov, M.I and Domashnev, I.A. Influence of Porosity On the Conductivity of Hot-Pressed Titanium Nitride Specimens Poroshkovaya Metallurgiya, V8, No9, pp51-54, 1968.
- 64 Odelevskii, V.I. Computation of the Generalised Conductivity of Heterogenous Systems, Zhurnal Tekhnicheskoy Fiziki, V21, No6, pp667-685, 1951.
- 65 Endo, I., Y. Kubo, H., Morioka, Y. and Itoh, S. Electrical Resistivity changes of Water-atomized Unreduced Steel Powder Compacts during Sintering, Journal of Japanese Society of Powders and Powder Metallurgy, V26, p201, 1979.
- 66 Endo, I., Kubo, H., Morioka, Y. and Itoh, S. Electrical Resistivity Changes of Iron Powder Compacts during Sintering, Journal of Japanese Society of Powders and Powder Metallurgy, V26, p195, 1979.
- 67 Goetzel, C.G. Treatise on Powder Metallurgy; Vol 11, 1950; Vol. 111, 1952 Interscience, New York.
- 68 Sands, R.L. and Shakespeare C.R. Powder Metallurgy, Newnes, London, 1966.
- 69 Leheup, E.R. and Moon, J.R. Powder Metallurgy, V21, p195, 1978.
- 70 Leheup, E.R. and Moon, J.R. Unpublished Report for G.K.N., Group Technological Centre, University of Nottingham 1979.
- 71 Conta, R.L. A Process for Improved Induction Heating of Powder Metal Compacts, I.E.E.E. Trans. on Industrial Applications, V1A-13, No4 1977.

- 72 Weissler, G.A. The Electrical Resistance of Metal Powder Compacts: The Influence of Surface Layers, Powder Metallurgy International, V11, No3, 1979.
- 73 Degtyareva, G.D. and Shvartzman, V.L. Magnetic Properties of some Iron Powder Concentrates, Soviet Powder Metallurgy and Metal Ceramics, V13, No6, pp443-6, 1974.
- 74 Pamasyuk, O.A. and Radomyselsky, I.D. Effect of P Additions on the Magnetic Properties of parts of Fe Powder, Soviet Powder Metallurgy and Metal Ceramics, V12, No4, pp289-292, 1973.
- 75 Moyer, K.H. Magnetic properties of Atomised Fe Powder Cores, Modern Developments in Powder Metallurgy V11, pp371-384, 1977.
- 76 Bolze, G.A. and Capus, J.M. Factors Affecting Properties of Sintered Fe, Modern Developments in Powder Metallurgy, V11, No.1, pp29-30, 1979.
- 77 Moyer, K.H. Effects of Porosity on Magnetic Properties, Powder Metallurgy International, V11, No.1, pp29-30, 1979.
- 78 Green, M.L., Herring, H. III, Sherwood, R.C., Robbins, M., Lambrecht, V.E. Jr. Properties of Fe - 50% Ni Alloys Prepared by Direct Hydrogen Reduction of Mixed Oxide Preforms, International Journal P/M and Powder Technology V16, No2, pp131-137, 1980.
- 79 Berkowitz, A.E. and Kneller, E. Magnetism and Metallurgy, Voll, part B. Experimental Methods Academic Press, 1969.
- 80 Bozorth, R.M. Ferromagnetism, Van Nostrand, London, 1951.
- 81 May, E., Industrial High Frequency Electric Power, Chapman and Hall, London, 1949.
- 82 Legg, V.E. and Given, F.J. Bell System Technical Journal, V19, p385, 1940.
- 83 Isserow, S. and Hatch, H.P. Magnetic Behaviour of High Density Bodies, International Journal of Powder Metallurgy, V13, No1, p51-53, 1977.



- 84 Huttig, G.F. and Rainer, H. Magnetic Properties of Iron Powder as affected by Changes in the Surface Conditions of the Particles, Powder Metallurgy Bulletin, V3, No3, pp48-60, 1948.
- 85 Steinitz, R. Magnetic Properties of Iron Powder Compacts, American Institute of Mining and Metal Engineers, T.P. 2334, Metals Technology, pp1-11, 1948.
- 86 Steinitz, R. Magnetic Properties of Iron Powder Compacts, American Institute of Mining and Metallurgy Engineers T.P. 2335, 1948.
- 87 Lenel, F.V. Metals Technology, Technical Paper 1788, 1945.
- 88 Polder D. and Santen, J.H. Physica, V12, p257, 1946.
- 89 Kir'yanov, Y.G. Syrkin, V.E. and Tolmasskii, I.S. Effect of some of the Process Parameters Involved in the Industrial Manufacture of R-10 and R-20 Carbonyl Iron Powders, Soviet Powder Metallurgy and Metal Ceramics, V16, No5, pp385-7, 1977.
- 90 Fluereșu, C. Chauffage par Induction d'Une Plaque en Acier, Revue Roumaines des Sciences Techniques Serie Electrotechiques et Energetique, V26, No1, pp15-26, Bucarest, 1981.
- 91 Capus, J.M. Magnetic Properties of Sintered Iron, Metal Powder Report, pp112-113, March 1981.
- 92 James, B.A. and Williams, G. Review of the Magnetic Properties of Sintered Iron, Session 3, pp74-85, Powder Metallurgy Group Annual Meeting, 1978.
- 93 Wilkes, D.J. Report on Induction Heating Exercise, G.K.N. Forgings Ltd. International Report, September 1980.
- 94 Clark, R.O.L. "Short Run Operation of High Output Induction Furnaces" V Congress International D'electrothermie. Paper No.311, 1963.

- 95 Shklyarov, I.N. and Orlovskii, A.E. Automated Equipment for Heat Treatment with Induction Heating. Metal Science and Heat Treatment, V19, pp758-762, 1977.
- 96 Summerhayes, B. Efficiency Improvement of Induction Heater Coils, Polypenco Ltd. Publication, Factory Publishing Ltd, London 1977.
- 97 G.K.N. Forgings Ltd Drawing Number A16218, Project Number F434, P&P. D, 1979.
- 98 G.K.N. Forgings Ltd Drawings, Adjustable Linear Coil, Drawing Numbers A16343, A16510 and B16557, Project Number F434, P&P. D, 1980.
- 99 Davies, E.J. and Das, S. Experimental Study of Eddy Currents Induced in the Solid Shells of D.C. Machines carrying Undulating Currents, I.E.E. Proc., V127, Pt.B, No.5, pp317-323, 1980.
- 100 Lavers, J.D. and Biringer, P.P. Induction Heating Calculations:- the effect of Coil Geometry, I.E.E.E. Industrial and General Applications Conference Record, pp299-305, 1970.
- 101 Lavers, J.D. and Biringer, P.P. An Improved Method of Calculating the Power Generated in an Inductively Heated Load, I.E.E.E. Trans. Industrial Applications, V1A-10, No2, pp273-278 March-April 1974.
- 102 Horoszko, E. Induction Heating of Rotating Bodies, Elektrowärme International, V36 (B2), p89-94, April 1978.
- 103 Ryff, P.E. Biringer, P.P. and Burke, P.E. Calculation Methods for Current Distribution in Single-turn Coils of Arbitrary Cross Section, I.E.E.E. Trans. Power Application and Systems, VPAS-89, No2 pp228-32, 1970.
- 104 Abramowitz, S. Handbook of Mathematical Functions, Dover Books Incorporated, p587, 1965.
- 105 Wilkinson, J.H. and Reinsch, C. Handbook for Automatic computation pp9-31, pp93-111, Volume 11: Linear Algebra, Springer - Verlag, 1971.



- 106 Reichert, K. A Numerical Method to Calculate Induction Heating Installations, Elektrowärme, V26, No4, pp113-123, 1968.
- 107 Kolbe, E. and Reiss, N. Distribution in Space of Current Density of Induction Heated bodies under Consideration of the Temperature Field, Elektrowärme, V25, 243-250, 1967.
- 108 Kolbe, E. and Reiss, N. A Mathematical Method of Determining the distribution of Current Density in Bodies of various Geometrical Shapes Heated by Induction, V Congres Internationale D'electotherme, paper N636, 1963.
- 109 Burke, P.E., Birke, P.P., Ryff, R.F. and Solger, E. The Prediction and Measurement of Current Distributions in Coaxial Geometries, Sixth PICA Conference Proceedings, 1969.
- 110 Dudley, R.F. and Burke, P.E. The Prediction of Current Distribution in Induction Heating Installations, I.E.E.E. Trans. Industrial Applications, VIA-8, pp565-71, 1972.
- 111 Weinstein, Bull. Bureau of Standards V3, No.1, p137, 1907.
- 112 Lyle Bulletin of the Bureau of Standards, V3, No1, p36, 1907.
- 113 Rosa, B. Bull. Bureau of Standards, V8, p101, 1912.
- 114 Lavers, J.D. An Efficient Method of Calculating Parameters for Induction and Resistance Heating Installations with Magnetic Loads, I.E.E.E. Industrial Applications, V1A-14, No5, 1972.
- 115 Renner, G. Computer Simulation of the Temperature and Electromagnetic Field in a Inductively Heated Semi-conductor, Mathematics and Computers in Simulation, V10, pp28-36, March 1978.

- 116 Gibson, R.C. SLEDDY, A Computer Program for Calculating the Induction and other Heating of Metal Slabs and Long Cylindrical Billets Electricity Council Research Centre, Capenhurst, Mathematical Memorandum ECRC/MM16, 1973.
- 117 Gibson, R.C. BIEDDY, A Computer Program for Calculating the Induction and other Heating of Long Rectangular and other Regularly Shaped Slabs and Billets, Electricity Council Research Centre, Capenhurst, Mathematical Memorandum. ECRC/MM20, March 1974.
- 118 Holmdahl, G. and Sundberg, Y. Calculation of Induction Heating with Digital Computers, 5th International Electroheat Conference, paper 633, Weibaden, 1963.
- 119 Dodd, C.V. Solutions to Electromagnetic Induction Problems, Report ORNL-TM-1842, Oak Ridge National Laboratory, Tennessee, U.S.A., June 1967.
- 120 Tunstall, N.J. and Dodd, C.V. Computer Program to Solve Eddy-Current Problems, Report K-1740, Oak Ridge National Laboratory, Tennessee, U.S.A., April 1968.
- 121 Michaels, T.B. and Streifer, W. Rapid Semi-analytic Method for Solving Laplace's Equation, I.E.E.E Trans. Industrial Applications, V1A-12, No2, March/April 1976.
- 122 Muñoz-Yagüe, A. and Leturcq, P. On a Semi-Analytic Method for Solving Laplace's Equation, I.E.E.E. Trans. Industrial Applications, V1A-14, No5, September/October 1978.
- 123 Heisler, M.P. Temperature Charts for Induction and constant temperature heating, Trans. ASME, V69, pp227-36, April 1947.
- 124 Anon. Industrial Heating, pp40-43, February 1974.
- 125 Ozişik, M.N. Boundary Value problems of Heat Conduction, International Textbook Co., Pennsylvania 1968.



- 126 Bayley, F.J., Owen, J.M. and Turner, A.B. Heat Transfer, Nelson, London 1972.
- 127 Crank, J. and Nicolson, P. A practical method for Numerical Evaluation of Solutions of Partial Differential Equations of the Heat Conduction Type, Proc. Cambridge Philosophical Society, Mathematical and Physical Science, V43, p50, 1947.
- 128 Thomas, R.F. and MacRoberts, M.D.J. RATH-Thermal Analysis Programs, Los Alamos Scientific Laboratories Report, L.A. 3264, University of California, New Mexico, 1965.
- 129 Gibson, R.C. A Computer Method of Calculating the Eddy Current Heating of Magnetic Materials, with a comparison between predicted and measured results in a 2MVA induction furnace, Electricity Council Research Centre, Capenhurst Report ECRC/N948, June 1976.
- 130 Burrett, C. How Europe's Largest Forge adopted Induction Heating and Profited by its Application, Paper presented to F.I.A. Heating Equipment Symposium, Chicago, Illinois, June 1975.
- 131 Bobart, G.F. Energy Saving Considerations in Mass Induction Heating, Iron and Steel Engineer 53, (5), p59-62, 1976.
- 132 Euler, K.J. and May, J. Powder Metallurgy International, V12, No3 pp138-140, 1980.
- 133 Private Communications with Manufacturers Burns Engineering Ltd, Rowley Regis, West Midlands.
- 134 G.K.N. Garringtons Ltd. Various Internal Reports on furnace performance.
- 135 Brearley, N.E. Electric Induction furnace replaces Oil - Fired units, Electrical Times March 6, pp6-7, 1981.

- 136 Wisker, J.W. Comparison of Energy Consumption: Powder Forging versus Conventional Forging, P.M. Group Annual Meeting 1976: Efficient Use of resources, Powder Metallurgy, No.2, pp126-7, 1977.
- 137 Wahlster, W., Stephen, H., and Ruthardt, R. Cost Estimates and Economic Considerations in the Production and Processing of High Quality Metal Powders, Powder Metallurgy International Vol.12, No4, 1980.
- 138 Kaufman, S.M. Energy Consumption in the Manufacture of Precision Metal Parts from Iron Powder, Metal Powder Report, pp444-8, October 1980.
- 139 Irving, R.R. All Systems are go for Powder Metallurgy, Iron Age, July 28, pp41-5, 1980.
- 140 James, P.J. Powder Metallurgy - Opportunities and new Developments, The Production Engineer, pp37-42, September 1980.
- 141 Gelsthorpe, D. Preform Die and Tool Design for the Powder Forging Process, Internal Report, R & D Division for G.K.N. Forgings Ltd, February 1970.
- 142 Anon Powder Metallurgy Design Guidebook, Metal Powder Industries Federation, Princeton, New Jersey, 1974.
- 143 Wilkes, D.J. Progress reports on Preform Induction Heating, G.K.N. Forging Ltd, internal Reports:- 1st October 1979, 30th January 1980, 30th May 1980, 30th September 1980.
- 144 Corrie, T.B. Preliminary trials - Mk 11 300kW Induction Forge Reheat Furnace, G.K.N. Forgings Ltd, Internal Report, April 1980.
- 145 Corrie, T.B. Operating parameters of the 300kHz Induction Forge Reheat Furnace, G.K.N. Forgings Ltd, Internal Report, January 1980.



- 146 Anon Estimated Cost Saving per annum using Induction Heating for Forging, G.K.N. Forgings Ltd. Internal Report, 1977.
- 147 Surveys conducted for G.K.N. Garringtons Ltd. by Mr J.A. Heathcock, M.E.B. Area Commercial Officer, Worcester; March 1980; June 1981.
- 148 Hermel W.  
Leitner, G. and  
Krumphold, R. Induction Sintering Fundamentals and Application, Powder Metallurgy, Group Meeting, Metals Society, 1979.
- 149 Vernia, P. Short Cycle Sintering by Induction Heating, Modern Developments in Powder Metallurgy, Vol 4, pp475-486, Plenum Press, New York 1971.
- 150 Johnson, R.H. The Efficient Use of Electricity as a Power Source in the P/M Process, Powder Metallurgy, No2, pp114-116, 1977.
- 151 Knopp, W. Furnace Heating versus Induction Heating of Powder-metal Performs, Fall Powder Metallurgy Conference Proceedings, pp104-118, 1971.
- 152 Hinsley, C.T. A Furnace for Liquid Phase Induction Sintering of Powder Metal Components, Electricity Council Research Report, ECRC.N702, 1974.
- 153 James, W.B. G.K.N. Group Technological Centre, Confidential Report - Induction Heating for Powder Forging, Part 1: Factors Influencing the Induction Heating of Powder Compacts, (Memo. No 1082), March 1980.
- 154 G.K.N. Garringtons Ltd. Company Accounts and internal reports.
- 155 National Industrial Fuel Efficiency Service (N.I.F.E.S.), Calthorpe Road, Birmingham.